New Technologies for Fluorescence Image-Guided Surgery

A thesis presented for the degree of Doctor of Philosophy

By:

Davide Volpi

Supervisor:

Professor Borivoj Vojnovic

Hertford College

CRUK/MRC Oxford Institute for Radiation Oncology

Department of Oncology

University of Oxford

Trinity Term 2014

Abstract

Davide Volpi Hertford College, University of Oxford
Doctor of Philosophy Trinity Term 2014

New Technologies for Fluorescence Image-Guided Surgery

To date, surgery is the most common and successful way to treat cancer. Tumour identification during surgery, however, can be challenging as it relies on the surgeon's ability to differentiate healthy from diseased tissue, based on visual appearance and palpation. Additional contrast mechanisms are needed to further improve cancer detection during surgery.

In this work, I explore the possibility of improving surgical outcomes by using intra-operative fluorescence imaging technologies to identify otherwise invisible lesions. A theoretical model is developed to quantify and characterise the imaging performance of fluorescence image-guided surgery (FIGS) and to guide the development of imaging systems. This model shows excellent potential for performance characterisation of FIGS devices, particularly when small lesions are involved.

The design, development and testing of FIGS devices for open and keyhole surgery are described. These devices exploit near infrared (NIR) wavelengths to achieve a superior depth penetration while minimising tissue autofluorescence. Unlike existing systems, the devices described in this work use a single miniaturised camera to simultaneously detect bright-field and fluorescence from multiple dyes. Practical tests indicate nano-molar detection of clinically approved fluorescence dyes.

The proposed technology is tested in a clinical study for detecting the sentinel lymph node (SLN) in gynaecological cancers. Results using two non-specific NIR dyes show excellent SLN detection rate in real time during open surgery and laparoscopy. In addition, multi-spectral fluorescence allows independent visualisation of different lymphatic pathways, crucial for understanding the mechanisms of metastasis through the lymphatic system. The FIGS devices are also used to test novel tumour-specific markers *in vivo*, *ex vivo* and *in vitro*. Promising results are reported, suggesting that this imaging technology is suitable for fluorescence molecular imaging.

In conclusion, I report the development and applications of a novel multi-spectral FIGS technology that can effectively improve outcomes in surgical oncology.

Contents

Acknowledgements

First and foremost I want to thank my supervisor, Professor Borivoj (Boris) Vojnovic, for his immense enthusiasm and knowledge, for having taught me how good research is done and for his contagious passion for science. I am enormously grateful to him for believing in my capabilities and for his continuous support throughout my D.Phil. Equally important, I would like to acknowledge the financial support of Cancer Research UK and the EPSRC that provided the necessary resources for conducting this work through the Oxford Cancer Imaging Centre grant.

I would like to acknowledge all my colleagues (present and former) of the Advanced Technology Development group. A special thank goes to Iain Tullis for his terrific help in all the technical aspects of my research and for his wise practical advice. I honestly believe that Google Search should provide an additional “ask Iain” button. Thank you to Paul Barber and Anthony Kavanagh for all their assistance during my project, Daniel Martins for his great support as fellow student and Linda Nemerofsky-Birks for her help in organising our work. Special thanks also to Robert Newman for sharing half of his precious Electronic Workshop with me and for the great help. Thank you to John Prentice and Gerry Shortland from the Mechanical Workshop for all the work spent building the essential bits for my project. Thank you all for being such great colleagues and, most importantly, devoted friends.

I would like to thank the numerous collaborators who made the clinical work possible. I gratefully acknowledge Professor Ahmed Ahmed from the Weatherall Institute of Molecular Medicine (WIMM) for the enormous amount of work that his group has devoted in exploiting our technology and for his wise and experienced suggestions. A special thank goes to Alex Laios for exposing me to the fascinating world of surgery and for being such a good friend and collaborator. I would like to thank Mr. Krishnayan Haldar and Mr. Pubudu Pathiraja for performing most of the surgical procedures, Kumar Gubbala, Hooman Soleymani, Martha Woodward and Riccardo Garruto for contributing to the clinical study. I also thank Professor Stephen Kennedy for his interest in the clinical use of

the fluorescence imaging systems. Most importantly, thanks to all the patients that participated in the study, which could not have been possible without their valuable consent.

I gratefully acknowledge our collaborators Yong Zheng, Muna El-Kasti and Christian Becker from the Nuffield Department of Surgical Sciences (NDSS) for the *in vivo* work, Trevor Yeung (also from NDSS) for the work on fluorescence lectin and for the numerous discussions, Professor Freddie Hamdy, Naomi Sharma and Helen Scott from NDSS and Oncology for the *in vitro* work. I also acknowledge our non-Oxford collaborators Professor Mark McGurk and Professor Tony Ng from King's College London for their interest in other clinical applications of the technology.

I would like to thank Selva and Angelos from the Oncology department for being such good friends and for all the moments we shared together. Many thanks to the staff from the Churchill Hospital in particular Jo, Dave, Lian, Giorgio and Federico for their relevant assistance during the course of the trial. Thanks to all my friends at Hertford College especially Kristian, Dan, Moritz and Rafael for making my D.Phil. even more fun. A special thank goes to Luca Mariotti from my former institution (University of Pavia, Italy) for being an excellent mentor and devoted friend.

Last, but by no means least, I want to thank Irina for her patience, care, affection and encouragement during my studies and for the wonderful time spent together. Thank you to my family for supporting me every day of my life and for allowing me to achieve all my dreams. To them I dedicate this thesis.

Davide Volpi

University of Oxford

September 2014

List of abbreviations

5-ALA	5-aminolevulinic acid
2PE	Two-photon excitation
ADU	Analogue to digital units
APSS	Albumin-enriched physiological salt solution
BMI	Body mass index
BSA	Bovine serum albumin
CAD	Computer-aided design
CCD	Charge-coupled device
CMOS	Complementary metal–oxide–semiconductor
CT	Computed tomography
CW	Continuous wave
dB	Decibel
DOT	Diffuse optical tomography
EMA	European medicine agencies
EPR	Enhanced permeability effect
FDA	Food and drug administration
FIFAC	Fluorescence imaging fast analytic calculator
FIGS	Fluorescence image-guided surgery
FLIM	Fluorescence lifetime imaging
FOV	Field of view
GPU	Graphic processing unit
GRIN	Gradient-index
GUI	Graphical user interface
HSA	Human serum albumin
Hb	Deoxyhaemoglobin
HbO_2	Haemoglobin
ICG	Indocyanine green
LED	Light-emitting diode
LN	Lymph node
MB	Methylene blue
MPE	Maximum permissible exposure
MRI	Magnetic resonance imaging
NA	Numerical aperture
NIR	Near infrared
NP	Nanoparticle

OCT	Optical coherence tomography
OD	Optical density
PMMA	Polymethyl methacrylate
QD	Quantum dot
QE	Quantum efficiency
PBS	Phosphate buffered saline
PET	Positron emission tomography
PpIX	Protoporphyrin IX
PSMA	Prostate-specific membrane antigen
ROI	Region of interest
RTE	Radiative transfer equation
SBR	Signal to background ratio
SLN	Sentinel lymph node
SNR	Signal to noise ratio
SPECT	Single-photon emission computed tomography
TBR	Tumour to background ratio
US	Ultrasound
UV	Ultra violet
WFA	Wisteria floribunda
WGA	Wheat germ agglutinin

List of Symbols

d	Entrance pupil diameter
D	Diffusion coefficient
e^-	Electron
ξ	Randomly-generated number between 0 and 1
ε	Molar extinction coefficient
f	Focal length
$f/\#$	F-number
F_{air}	Photon rate emerging from the tissue surface
F_M	Photon rate emitted from a fluorophore molecule
F_{pix}	Photon rate reaching a sensor's pixel
F_S	Photon rate emitted from the sample
F_V	Field of view
g	Anisotropy factor
G	Camera gain
η	Quantum yield
I	Pixel intensity level
$\boldsymbol{J}$	Light flux
$\boldsymbol{\lambda}$	Wavelength
l	Linear dimension of a tissue surface unit
l_t	Photon's mean free path
μ_a	Absorption coefficient
μ_{eff}	Effective attenuation coefficient
μ_s	Scattering coefficient
μ_s'	Reduced scattering coefficient
μ_t	Interaction coefficient
n	Refractive index
n_c	Number of cells in the sample
n_r	Number of fluorescently-labelled receptors per cell
ρ	Radial distance from the centre in cylindrical coordinates
R	Diffuse reflectance
R_{sp}	Specular reflectance
σ	Absorption cross section

s	Linear dimension of the image sensor
Ω	Solid angle of light collection
Φ	Excitation fluence rate
Φ_{air}	Photon flux density emerging from the tissue surface
Φ_S	Excitation power density at the tissue surface
T	Transmission factor
U	Light fluence rate
W	Weight factor
w_d	Working distance
z	Depth in tissue

List of Tables

List of Figures

Introduction

Background and motivation

Cancer is a major cause of death worldwide. On average, 910 people are diagnosed with cancer every day in the United Kingdom (Cancer Research UK, 2014). The total number of cancer cases is expected to increase by 55% in men and 35% in women between 2007 and 2030 (Mistry *et. al.*, 2011). This dramatic rise is due to a combination of higher incidence prediction of certain types of cancers (e.g. prostate and breast (Bray *et. al.*, 2012)) and due to the growing and aging of the population. Despite the increase in the total number of cases, the mortality rate has decreased over the last decades (Cancer Research UK, 2013) due to improvements in therapy and diagnostics. However, cancer still remains the second most common cause of death worldwide after hearth-related diseases (World Health Organization, 2013).

A key step towards a better management of the disease is the correct detection of a tumour, irrespectively on its size and stage. A number of imaging modalities are available to the oncologist for identifying a tumour and determining the most appropriate treatment for the patient. In the ideal scenario, a cancer imaging technique should detect a tumour of any size or type anywhere in the human body. In practice, the signal-to-background ratio generated by most imaging modalities is not sufficient for detection of certain types of lesions (Levin, 2005). This is particularly relevant for early cancer identification which, if successful, demonstrated significant benefits for the patients and reduced mortality rates (Etzioni *et al.*, 2003).

Despite the availability of techniques such as radiotherapy and chemotherapy, which are routinely used to treat many types of cancer, the principle and most successful approach for treatment of primary cancers is surgery (National Cancer Institute, 2008). This practice relies on the visual ability of the surgeon to intra-operatively identify and remove diseased tissues while leaving healthy tissues untouched. Correct tumour identification, however, is dependent on the contrast mechanisms employed; these are typically based on changes in the appearance (colour) and morphology (shape) of the tissues. The extent of such changes is very often related to the size of the tumour (i.e. contrast is lower for smaller tumours). In some cases, and in general for early stage cancer, distinction between diseased and healthy tissue during surgical operation can be significantly challenging. Differences might occur at a cellular or sub-cellular level, where tissue appearance is not affected macroscopically. This is translated as a lack of contrast that can lead to a potential failure in the identification of the disease. Because of the large number of cancers that are assessed and treated surgically, an imaging modality that can be used intra-operatively to improve tumour detection would be highly desirable.

Despite its limitations in terms of tissue penetration depth, optical imaging can offer tremendous advantages for early cancer detection due to its superior spatial resolution and molecular sensitivity (Weissleder & Pittet, 2008). Fluorescence imaging during surgery, in particular, is emerging as a powerful tool for detecting lesions otherwise invisible using conventional imaging modalities (Nguyen & Tsien, 2013). Moreover, its ability of detecting tumour cells in real time offers the possibility of surgically resecting cancerous lesions by fluorescence guidance (van Dam *et al.*, 2011). However, the success of this novel technique relies on the development of effective contrast agents and imaging systems suitable for use during surgery. In particular, the development of imaging devices is challenging, requiring appropriate design in detection systems, sensitive enough for

small tumour detection while able to operate in real time and within constraints imposed by surgery. This is even more relevant during minimally invasive surgery, given the significant light losses associated with laparoscopes and endoscopes.

A number of devices for fluorescence image-guided surgery (FIGS) have been described and some of them have been used in the clinic (Keereweer *et al.*, 2011). However, their use has been limited for a number of reasons, including poor surgical optimisation or restricted operation modality. In addition, the level of complexity of some systems developed by other research groups has resulted in large and bulky devices, thus restricting their use to open surgery only (Themelis *et al.*, 2009; Troyan *et al.*, 2009). There is a distinct need for simple, flexible and effective technology for FIGS, driven by the growing interest in the field.

Aims of this thesis

The primary goal of this work is to provide solutions to improve cancer detection during surgery by exploiting FIGS. Unlike existing published work in this field, I will pursue an approach that first analyses the problem theoretically with the aim of quantifying and predicting imaging performance, then use this knowledge to guide the design of instrumentation and finally apply this in the clinic. This will eventually enrich the knowledge on the factors that control a FIGS procedure and that are responsible for its success. In addition, this study aims to develop a generic technology and specific imaging devices that can overcome the limitations of existing FIGS systems in terms of usability, while maintaining detection sensitivity appropriate for molecular imaging. This thesis also seeks to demonstrate the usefulness of the technology during clinical and pre-clinical experiments.

Outline of this thesis

Despite the equally important part on the development of molecular markers, this thesis will focus primarily on imaging device development aspects of FIGS. The first chapter will summarise and compare the existing imaging modalities available in the clinic, with particular focus on optical imaging methods. The main concepts that underpin FIGS, including the availability of fluorescence markers, will be presented, along with the main applications. Chapter 2 will describe a theoretical model that I have developed, with the purpose of characterising and quantifying FIGS. The model was designed to simulate practical situations and to predict imaging performance using realistic imaging systems. Results will show theoretical evidence of the advantages of FIGS over conventional medical imaging modalities for detecting small numbers of cells. Chapter 3 will describe in detail the design and development of a FIGS technology that was developed in our research group. Imaging systems that use a *single* colour camera to simultaneously detect fluorescence and bright field images during open and keyhole surgery will be presented. One of the strengths of these systems is the simplicity of the technology used, in contrast to devices developed by other research groups. As I will show, this proved to be particularly important for a rapid clinical translation of the devices. Chapter 4 will focus on practical applications of the technology. Application to, and results from a clinical study on sentinel lymph node detection in gynaecological cancers will be presented. Results will be provided on the systems' detection performance during open surgery and laparoscopy, using two clinically approved fluorescence dyes. Pre-clinical applications of fluorescence molecular imaging of cancer using the FIGS systems will also be described. Finally, the impact of this work and future directions will be presented.

Personal contribution to this work

The FIGS systems described in this work were fully developed over the course of my D.Phil. studies in collaboration with my colleagues at the Advanced Technology Development Group. I guided the optical design of the systems and was involved in other aspects (electronics, software etc.). I fully developed and validated the theoretical model described in Chapter 2 and performed all the device testing and characterisation experiments. I actively contributed to all the practical applications of the devices described in this thesis, spending a significant amount of time in surgical theatres. The pre-clinical work was carried out in collaboration with the Weatherall Institute of Molecular Medicine (WIMM) and the Nuffield Department of Surgical Sciences (NDSS). The clinical study described in Chapter 4 was carried out in collaboration with the Gynaecological Oncology Unit at the Churchill Hospital and the WIMM in Oxford. *In vitro* and *ex vivo* imaging work, also described in Chapter 4, was carried out by me, with help with sample preparation from colleagues from NDSS and the Oxford Department of Oncology.

1. Background

1.1 Overview of cancer imaging modalities

1.1.1 Conventional imaging techniques

Medical imaging is critically important in numerous diseases and in cancer management, an area that this thesis is concerned with. Imaging is used to diagnose and stage cancer, to guide cancer treatments and to determine the success of such treatments. Different technologies can be used to detect cancer by exploiting contrast mechanisms that differentiate healthy from diseased tissue. Depending on the type of information gathered, cancer imaging techniques can be divided into two main categories (Weissleder & Pittet, 2008):

1- Anatomical or physiological information

2- Cellular or molecular information

The first group typically includes X-ray computed tomography (CT), magnetic resonance imaging (MRI) and ultrasound (US). The contrast exploited in CT results from differences in X-ray attenuation of tissue, in turn related to the physical properties of the tissue. MRI, on the other hand, does not rely on ionising radiation but most often images protons (i.e. water) concentrations. Protons are first aligned in an electromagnetic field and then allowed to relax: this relaxation is associated with electromagnetic emissions which are detected. Each XYZ position corresponds to a specific magnetic and electric field intensity and spatial information can thus be extracted. Another technique that does not rely on the use of ionising radiation is US. This uses high frequency sound waves that are made to

propagate in the body: reflections from tissue interfaces or regions of differing density are detected and mapped temporally and spatially.

In all these techniques, three-dimensional anatomic information can be obtained. In some cases, physiological information within the imaged volume can also be obtained: this is the domain of *functional imaging* that includes techniques such as functional MRI, diffusion MRI, CT perfusion imaging and, in particular, positron emission tomography (PET). In essence, these functional methods are able to detect changes in metabolism, blood flow and concentrations of specific biomolecules.

Molecular imaging is increasingly used due to its ability to monitor key molecular factors in carcinogenesis (Pysz *et al.*, 2010). This can be achieved by exploiting a number of existing imaging technologies, in particular PET (Gambhir, 2002) and single-photon emission computed tomography (SPECT) (Coleman, 1991). Molecular imaging is performed by using appropriate markers that target cellular receptors that may be over- or under-expressed in cancer. In the case of PET, information on the targeted tissue is obtained by detecting two gamma rays emitted in opposite directions from a positron-electron collision. In the case of SPECT, single gamma rays from a radionuclide are detected. The main disadvantages of these modalities include the use of ionising radiation, high cost and a limited spatial resolution (5-10 mm). PET and SPECT, however, lack of an anatomical reference frame, thus requiring integration with either CT or MRI for anatomical correlation (Pichler *et al.*, 2008).

Molecular imaging can also be achieved by conventional anatomical techniques used with appropriate contrast agents. One example is contrast-enhanced US imaging, which uses microbubbles to enhance the US signal (Deshpande *et al.*, 2010). Conventional anatomical

imaging techniques, however, suffer from fundamental limitations including poor detection sensitivity (MRI), large contrast agent dimensions (US) and often significant imaging agent concentration (US and CT), which eventually limit clinical translation (Jaffer & Weissleder, 2005).

Despite being able to detect a tumour deep in the body, the spatial resolution of most of the current imaging modalities is typically larger than 1 mm, using clinical imaging setups (James & Gambhir, 2012). Imaging resolution and contrast can in principle be increased: this comes at a cost of unacceptably high radiation doses, excessive contrast agent concentrations or inappropriately long imaging times. As a consequence, such imaging modalities are generally suitable to detect only large cancers at a relatively late stage, when mortality is highest (Jemal *et al.*, 2008).

1.1.2 Towards molecular imaging in oncology

Early cancer detection is a critical step towards successful disease treatment. It is generally accepted that a tumour can only grow up to ~2 mm in size using normal tissue vasculature (Folkman, 1971). The tumour has to then develop its own vasculature, through the 'angiogenesis' process (Weis & Cheresh, 2011). Following the angiogenic switch (Bergers & Benjamin, 2003), the tumour starts proliferating uncontrollably. The ultimate goal of early cancer detection is tumour identification before it undergoes this switch. This requires the development and application of highly sensitive, sub-millimetre resolution imaging modalities and of molecular markers to target one or more of the cancer 'hallmarks' (Hanahan & Weinberg, 2011).

The clinical detection threshold of well-established imaging techniques is theoretically of the order of a few cubic millimetres, though in practice can be as poor as ~1 cm^3 for solid

tumours (Weissleder, 2006). This is higher than the value corresponding to the angiogenic switch, suggesting that early detection with conventional techniques is questionable. For an average cell diameter of 10 μm, the angiogenic switch occurs when the tumour consists of ~10^6 cells, whereas current techniques are only capable of detecting above ~10^9 cells. This is a fundamental limitation that can only be overcome using an imaging technique that is able to detect a cell number ~3 orders of magnitude lower than that possible with conventional methods. Optical imaging has the potential to provide this level of sensitivity, provided that timely technique application is feasible.

1.1.3 Optical imaging

Optical imaging uses ultraviolet (UV), visible, near infrared (NIR) and infrared (IR) light to interrogate the tissue of interest. In comparison with other imaging modalities, the cost of optical imaging is low, under some circumstances imaging resolution can be high and anatomical and molecular information can be gathered without using ionising radiation. Moreover, its excellent molecular sensitivity makes optical imaging particularly appealing for early cancer detection. Optical methods are compared to other techniques in Table 1.

Technique	*Resolution*	*Depth*	*Type of information*	*Molar sensitivity*	*Cost*	*Ionising radiation*
CT	100 μm – 1 mm	Whole body	Anatomical	ND	$$	Yes
MRI	100 μm – 1 mm	Whole body	Anatomical, molecular	10^{-3} – 10^{-5} M	$$$	No
US	100 μm – 1 mm	< 10 cm	Anatomical, molecular	~10^{-12} M	$$	No
PET	~5 mm	Whole body	Molecular	10^{-11} – 10^{-12} M	$$$	Yes
SPECT	5 – 10 mm	Whole body	Molecular	10^{-10} – 10^{-11} M	$$	Yes
Optical	10 μm – 10 mm	< 5 cm	Anatomical, Molecular	10^{-9} – 10^{-17} M	$	No

Table 1: Comparison of imaging techniques in cancer. Adapted from (James & Gambhir, 2012; Weissleder & Pittet, 2008). ND: not determined.

The main limitation of optical imaging is its poor ability to interrogate tissues at depth, due to higher absorption and scattering of light in comparison with that of X-rays, gamma rays and US. This is particularly relevant when it comes to clinical translation, as the dimensions of human tissues and organs are much larger than the light mean free path (Ntziachristos, 2010). From this perspective, a superior result can be achieved by using near infrared (NIR) light. This is able to penetrate the tissue to depths considerably higher than for visible light, due to reduced NIR absorption and scattering coefficients (Jacques, 2013). However, penetration depths exceeding 25 mm are increasingly hard to achieve.

In a typical imaging setup, light is generated by an external source or internally by energy release from a chemical reaction (bioluminescence). Contrast can be obtained by changes in the optical properties of the tissue (i.e. refractive index, absorption and scattering) or by the ability of a molecule to absorb and emit light (i.e. fluorescence and phosphorescence).

Optical imaging techniques

A number of optical imaging techniques have been developed and can be used to detect cancer and other diseases. The lack of ionising radiation associated with optical imaging makes it worthy of continued research, and the range of applications is increasing as will be demonstrated in this thesis.

Fluorescence imaging is a rapidly evolving field that has been extensively used in biomedical research (Diaspro, 2011). Clinical studies have used fluorescence, for example, to image exogenous fluorophores during keyhole surgery (Cahill *et al.*, 2012) and confocal microendoscopy (Wang *et al.*, 2007). Alternatively, imaging of endogenous fluorophores (autofluorescence) can provide molecular information and improve contrast in comparison with white light reflectance (Farah *et al.*, 2012). Pre-clinical (Liu *et al.*, 2014) and clinical

(van Dam *et al.*, 2011) applications increasingly benefit from highly specific agents tagged with detectable fluorophores.

Diffuse optical tomography (DOT) has niche clinical applications (Eggebrecht *et al.*, 2014; Singh *et al.*, 2014), as has the analogous technique using fluorescence (FDOT) (Corlu *et al.*, 2007). Pre-clinical uses are more extensive (Bluestone *et al.*, 2004; Ntziachristos *et al.*, 2002), as this technique benefits from a low radius of curvature of the imaged volume.

The temporal decay of the fluorescence signal can also be used to gather information on the location of a fluorophore and its microenvironment (Elson *et al.*, 2004). This technique, known as fluorescence lifetime imaging (FLIM), has been used, for example, to detect *ex vivo* tissue autofluorescence from mucosal carcinomas (McGinty *et al.*, 2010). Two-photon (2PE) fluorescence microscopy can also be exploited because of its ability of penetrating relatively thick layers of tissue while maintaining sub-cellular resolution (Koehler *et al.*, 2011). While FLIM and 2PE are extensively used in the laboratory, the complex instrumentation associated with these techniques makes translation to the clinic awkward. Although attempts at miniaturising very complex optical apparatus have been made, the range of clinical applications is currently restricted.

In contrast to fluorescence emission, information on the molecular composition of the tissue can be obtained by exploiting inelastic light scattering. Raman spectroscopy can be used to determine the molecular composition of the tissue following continuous excitation with a NIR laser (Wachsmann-Hogiu *et al.*, 2009). Clinical applications have been carried out even during endoscopic surgery (Huang *et al.*, 2009) and to assess surgical margins in breast cancer (Haka *et al.*, 2006).

Optical coherence tomography (OCT), a technique based on optical interferometry, allows non-invasive imaging at a micrometre resolutions (Huang *et al.*, 1991). OCT has been widely used in the field of ophthalmology, due to the transparency of ocular structures (Gabriele *et al.*, 2011), and it is starting to be adopted in oncology (Vakoc *et al.*, 2012).

Finally, photoacoustic imaging is an increasingly popular technique that generates an image using sound waves produced by tissue thermal expansion following absorption of an optical pulse (Beard, 2011). Despite promising results *ex vivo* (Allen *et al.*, 2012), clinical applications of photoacoustic imaging are still being explored. A summary of the principle optical methods applied in the clinic, or close to clinical applications, is shown in Table 2.

Technique	***Resolution***	***Depth***	***Advantages***	***Disadvantages***
Wide-field fluorescence	50 µm - 5 mm	<10 - 20 mm	Cheap, real-time imaging, clinically used	2D only, low resolution at depth
DOT, FDOT	>>1 mm	~100 mm	3D possible	Slow, only certain geometries possible
FLIM	1 µm - 100 µm	~100 µm	Dye concentration independent, detects microenvironment	Expensive, needs pulsed laser
Two-photon microscopy	1 µm	1 - 2 mm	High resolution at depth	Restricted field of view, expensive
Raman[1]	-	1 µm – 1 mm	No contrast agent, high molecular specificity	Slow, limited penetration, hard to interpret
OCT	1 µm	~2 - 3 mm	Excellent spatial resolution, 3D imaging, endoscopy possible	Limited penetration, expensive, lack of specificity
Photoacoustic	50 µm - 1 mm	~50 mm	High resolution and penetration depth, 3D imaging	Expensive, needs coupling medium for use, hard to interpret

Table 2: Summary of the principle biomedical optical imaging techniques.

[1] Although Raman imaging is used in microscopy, in this instance the Raman technique provides only spectroscopic output from selected sub-millimetre regions of tissue.

1.2 Fluorescence image-guided surgery (FIGS)

When it comes to surgery, one of the greatest limitations of existing non-invasive imaging techniques is the difficulty of real-time co-registration with the surgeon's vision. Fluorescence image-guided surgery (FIGS) has emerged as a novel technique that can potentially fill this gap between imaging and surgical practice. This procedure images intra-operatively the distribution of a fluorescence marker. A new contrast mechanism is provided, effectively increasing the range of vision of the surgeon without significantly altering the surgeon's essential hand-to-eye coordination.

Contrast agents can be used to label tumour tissue (van Dam *et al.*, 2011) or non-specific agents can be used to detect relevant structures e.g. sentinel lymph nodes (Cahill *et al.*, 2012). Clinically used (and increasingly approved) fluorophores can be excited in the visible–NIR region of the electromagnetic spectrum. The main advantage here is that tissues of interest are highlighted in real time, making this technique suitable for live surgical navigation. This real-time operation, however, demands the use of very sensitive detectors, as the luxury of long-term signal integration is then not available.

Deep imaging is highly desirable and NIR fluorescence imaging has the potential to achieve this. The number of clinical applications using NIR fluorescence is rapidly increasing, as shown by a recent review (Vahrmeijer *et al.*, 2013). Biological tissues exhibit autofluorescence (e.g. from NADH, flavins, extracellular matrix etc.) when excited by visible light, particularly blue or UV light (Pavlova *et al.*, 2008). The use of NIR excitation significantly reduces these emissions, as well as providing imaging at depth. Moreover, the use of excitation wavelengths that are invisible by the human eye does not affect the conventional view of the surgeon during open surgery.

The clinical success that FIGS can potentially achieve is determined primarily by two equally important and interrelated factors: the development of effective contrast agents and the availability of sensitive imaging devices. The development of imaging devices for FIGS is a challenging process that relies on a trade-off between sensitivity, ergonomics, usability and cost. Imaging systems sensitive to femto-molar dye concentrations tend to be bulky, expensive and usually not suitable for integration in the operating theatre. Compact, low-cost systems, however, might not be adequate for the task. Unlike most of fluorescence imaging applications, FIGS devices must provide real-time surgical guidance and should preferably display fluorescence emission and the conventional visible colour image (bright field) simultaneously. This is particularly relevant when used in minimally invasive ‘keyhole’ surgical systems (i.e. laparoscopes and endoscopes), where the surgeon does not have direct visual access to the imaged area.

The tremendous potential of improving surgical outcomes by exploiting FIGS has been reported in a recent review (Nguyen & Tsien, 2013). However, controversy still exists on the ability of FIGS to detect small, pre-angiogenic cancer lesions. The work described in this thesis addresses this issue and attempts to provide technological solutions for future improvements.

1.3 Fluorescent contrast agents for FIGS

As this thesis principally focuses on the technological aspects of FIGS, a brief summary of the characteristics of the markers and the fluorophores typically used as FIGS contrast agents will be presented.

1.3.1 Types of fluorescence probes

In an ideal scenario, a contrast agent should target the tissue of interest without non-specifically binding to any other structures and should be cleared by the body after a period of time sufficient to allow fluorescence imaging. Depending on the targeting mechanism, the imaging probes for FIGS can be classified into three categories, as described below.

Non-specific dyes

Non-specific fluorophores, such as indocyanine green (ICG) and methylene blue (MB), are contrast agents that diffuse into the blood or the lymphatic system following topical or parental administration (Figure 1A). Labelling occurs as a consequence of dye retention in a particular tissue or organ. ICG, for example, has been used as a fluorescent dye perfusion angiography (Ris *et al.*, 2014) and for mapping lymph nodes in a variety of tumours including melanoma (Fujiwara *et al.*, 2009), breast cancer (Tagaya *et al.*, 2008), anal cancer (Hirche *et al.*, 2010a), colorectal neoplasia (Cahill *et al.*, 2012), gynaecological cancers (Crane *et al.*, 2011a; Furukawa *et al.*, 2010) and head & neck cancer (van der Vorst *et al.*, 2013). Alternatively, such non-specific contrast agents can be used to detect cancer tissue by exploiting the enhanced permeability and retention (EPR) effect (Maeda *et al.*, 2000). This derives from the ability of a tumour to rapidly develop blood vasculatures for oxygen supply. The abnormalities of such vasculature, together with a lack of effective lymphatic drainage, can produce accumulation and retention of this agent in the affected area. This phenomenon has been exploited in FIGS for detecting hepatocellular carcinoma following intravenous injection of ICG (Ishizawa *et al.*, 2009), for example.

Tumour-specific markers

Despite moderate success in a variety of surgical applications, non-specific fluorescence markers have had limited use in surgical oncology because of their lack of specificity. Interest has therefore grown towards the use of molecular markers that can specifically target over- or under- expressed receptors in cancer tissue (Figure 1B). Specific markers are developed by conjugating a fluorophore with targeting agents such as antibodies, peptides or, in general, small molecules that are specific to cell receptors. Clinical translation of tumour-specific markers requires full toxicity studies of the fluorophore-conjugated marker, and the use of established fluorophores (e.g. fluorescein) is preferred (Sturm *et al.*, 2013). MB and ICG do not have functional groups necessary for successful conjugation.

Smart probes

Activatable probes (also known as ‘smart’ probes) are an attractive type of fluorescence marker in which a quenched fluorophore undergoes a switching process in order to fluoresce. This switch usually occurs following interaction of a probe’s molecule with an enzyme present on the targeted tissue, which causes the release of free fluorophore molecules (Tung, 2004) (Figure 1C). These probes have a tremendous advantage over conventional markers as they provide superior tumour-to-background ratios, due to reduced non-specific binding and lack of unbound molecules. Similarly to smart probes, a non-fluorescent dye, 5-aminolevulininic acid (5-ALA), can be converted to fluorescent protoporphyrin IX (PpIX) through a series of molecular steps that occur in cancer tissue (Takahashi *et al.*, 2011). Following oral administration of 5-ALA and UV excitation, PpIX exhibits a strong red fluorescence that can be detected intra-operatively. This practice has

shown successful clinical outcomes in bladder cancer and, in particular, in gliomas with improved tumour-free survival (Stummer *et al.*, 2006).

A schematic representation of non-specific fluorophores, tumour-specific markers and smart probes is shown in Figure 1.

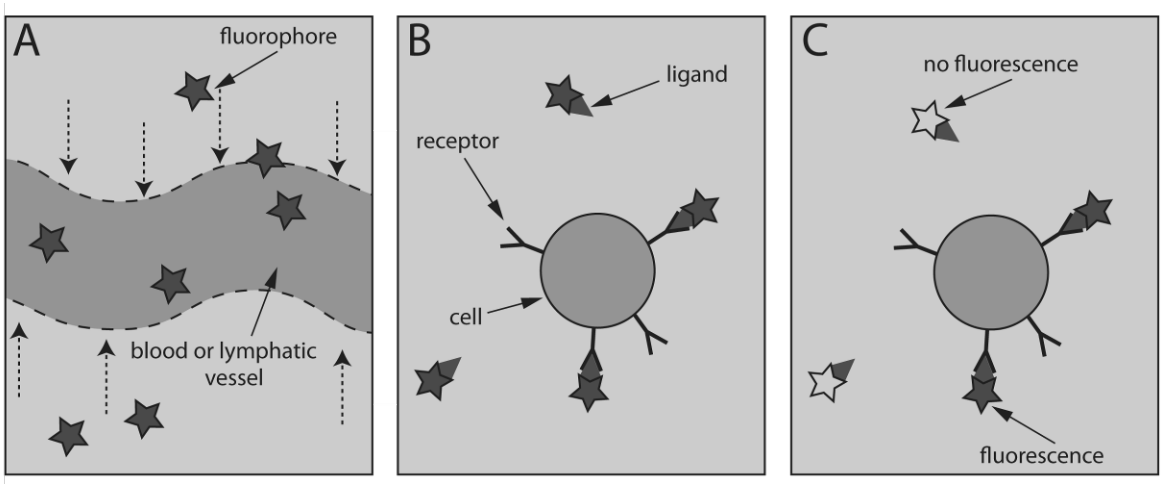

Figure 1: Schematic representation of different types of FIGS contrast agents. (A) Non-specific fluorescence dyes (e.g. ICG) diffusing to a blood or lymphatic vessel; (B) Tumour-specific markers and (C) smart probes targeting a cell.

1.3.2 Probes properties

Probe clearance

Fluorescence agents are excreted from the body typically through the liver and the kidneys. Excretion time varies depending on the water solubility of the drug and on the injected dose. Fluorescence imaging in proximity to the marker clearance path could be limited by the significant background. Nevertheless, dye clearance can be exploited to highlight organs that must be preserved and that are not clearly visible under white reflectance. For example, the ureter can be identified during lower abdominal surgery (Verbeek *et al.*, 2013) using MB, excreted through the urinary tract.

Fluorophore optical properties

A critical fluorophore property is its brightness: as will be highlighted in the next chapter, a fluorophore should have a quantum yield and an extinction coefficient as high as possible. In addition, its absorption peak should match the available wavelengths in high spectral intensity sources (e.g. lasers, or emission lines in arc lamps). A fluorophore should also have a large spectral gap between excitation and emission (Stokes shift) to allow optimal blocking of excitation light and maximum collection of emission. Dye photobleaching should be minimised in FIGS and, in particular, generation of toxic photoproducts must be negligible. Dye self-quenching should be limited and the fluorescence emission signal should increase with concentration.

Economic issues

A significant limiting factor in the development of new contrast agents for intra-operative fluorescence molecular imaging is the high cost associated with synthesis and testing. It has been estimated that imaging agent development costs between 50 and 100 million $ (Weissleder, 2006). As a consequence, pharmaceutical companies are reluctant to invest unless clear patient benefit is shown.

1.3.3 Available contrast agents

Fluorescence probes can be generally classified in two categories: inorganic and organic molecules. Inorganic molecules consist of quantum dots (QDs) and nanoparticles (NPs). Advantages of using this type of dyes include ability to tune the emission spectrum, high quantum yield and extinction coefficient, high resistance to photobleaching, large Stokes shift and improved photostability (He *et al.*, 2010). Moreover, up-conversion NPs can

absorb in the NIR – IR and emit fluorescence in the visible (Wang *et al.*, 2011). This can have a significant advantage as the excitation light does not cause autofluorescence and can penetrate deeper into tissue, while the fluorescence emission occurs at wavelengths where the quantum efficiency of detectors is highest. In addition, due to the typically very large anti-Stokes shift, a simple short-pass filter can be used for detection. Despite all these advantages, there remains concerns with inorganic molecules about their *in vivo* cytotoxicity (Nel *et al.*, 2006), since heavy metals are used. Clinical translation of these probes has been significantly slow.

In contrast to NPs and QDs, organic dyes (such as ICG, MB, cyanine dyes, fluorescein isothiocyanate *etc*.) exhibit much lower levels of toxicity. The doses typically used in FIGS are low, making these dyes relatively safe (Alford *et al.*, 2009). Many organic dyes can be readily conjugated to biomolecules, such as peptides or proteins, relevant for targeting cancer-related processes (Resch-Genger *et al.*, 2008). For these reasons, organic dyes are the best candidates for FIGS molecular contrast agent development.

Organic dyes for FIGS

A large number of organic dyes are available for fluorescence imaging, ranging from the visible to the NIR. Organic NIR dyes, in particular, are preferred for intra-operative fluorescence molecular imaging (Luo *et al.*, 2011). To date, the only fluorescence dyes that are approved by the U.S. Food and Drug Administration (FDA) and the European Medicine Agencies (EMA) are fluorescein, ICG and MB. Such dyes are often used off-label[2] to non-specifically visualise structures such as lymph nodes using fluorescence.

[2] Off-label use refers to the practice of using a drug for purposes different than the ones for which the drug was approved, as long as the surgeon considers them to be safe.

The Licor IRDye800-CW[3] has emerged as a preferred NIR dye because of its low toxicity (Marshall *et al.*, 2010) and straightforward conjugation to biomolecules (Kijanka *et al.*, 2013). There are a number of ongoing phase I clinical trials, both in Europe and in the U.S. involving fluorescence molecular imaging with IRDye800-CW. Cyanine dyes (e.g. Cy5.5 and Cy7) are also good candidates because of their high quantum yields and extinction coefficients along with relatively low toxicity (Alford *et al.*, 2009).

Table 3 summarises the principle fluorophores used so far in FIGS and those that have future potential.

	Absorption peak (nm)	***Emission peak (nm)***	***Quantum yield***	***Extinction coefficient ($M^{-1}cm^{-1}$ L^{-1})***	***Comments***	***References***
Fluorescein sodium	490	520	0.93	77,000	pH-dependent fluorescence intensity. Used clinically.	(Sjöback *et al.*, 1995)
ICG	780 (water) 800 (plasma)	810-820	0.027 (water) 0.04 (plasma)	150,000	Not suitable for bio-conjugation. Non-linear QY *vs.* concentration. Used clinically	(Philip *et al.*, 1996)
MB	665	685	0.05	80,000	Not suitable for bio-conjugation. Used clinically.	(Tuite & Kelly, 1993)
IRDye800-CW	785	830	0.034	180,000	Used in ongoing clinical trials	(Azhdarinia *et al.*, 2011)
Cy5.5	675	694	0.28	250,000		(Umezawa *et al.*, 2009)
Cy7	743	767	0.28	200,000		(Umezawa *et al.*, 2009)

Table 3: Summary of the main FIGS fluorophores.

[3] LI-COR Biosciences, Lincoln, NE, U.S.A.

1.4 The sentinel lymph node concept in oncology

Because of the availability of clinically approved non-specific contrast agents, one of the most common applications of FIGS is detection of sentinel lymph nodes (SLN) associated with a given tumour. The SLN concept is important in oncology for assessing cancer staging. In this section, a background on the lymphatic system and the role of lymph nodes will be provided. The SLN concept will then be introduced, along with conventional and novel techniques for detection of SLNs.

1.4.1 The lymphatic system

The lymphatic system is an organ of the circulation system consisting of a complex of vessels that collect and transport interstitial fluid (also known as 'lymph') through the body. Unlike the blood system, lymphatic vessels transport the lymph due to a pressure gradient (~ –1-2 mmHg), without a central pumping unit (Swartz, 2001). Another substantial difference is that the lymphatic vessels only carry fluid away from tissue. After the interstitial fluid has entered a vessel, backflow from the vessel to the tissue is prevented by means of specialised junctions (Dixon, 2010). The lymphatic system is a particularly important component of the immune system as it removes waste products from the cell interstitial space. Such products might include toxins, dead cells, pathogens and even cancer cells. Lymphatic vessels run roughly parallel to the blood vessels and deliver filtered fluid back into the blood stream.

Lymph nodes

Lymph nodes (LNs) are small organs of the lymphatic system distributed across the body along the route of the main lymphatic vasculatures (Weiss, 2009). The human body

contains around 600-700 LNs (typical diameter = 10 mm), mostly concentrated in the area of the groin, neck, axillae and thorax. LNs host white blood T- and B- cells (also known as lymphocytes) which attack and break down harmful compounds before being discarded by the body.

Lymph fluid enters the LN through the afferent lymphatic vessel and circulates through the sinuses which contain lymphocytes. The sinuses converge at the hilum where the lymph leaves the LN through the efferent lymphatic vessel. Valves at the surface of the LN are responsible for unidirectional movement of the lymph. The efferent lymphatic vessels of a LN can act as afferent vessels for a second LN, which can also be connected to a third LN and so on. In this way, a cluster of LNs in created where lymph is transported from the first to the last LN before being delivered to a more distant location through a larger lymphatic vessel. Figure 2 shows a two-dimensional cross-section diagram of a LN.

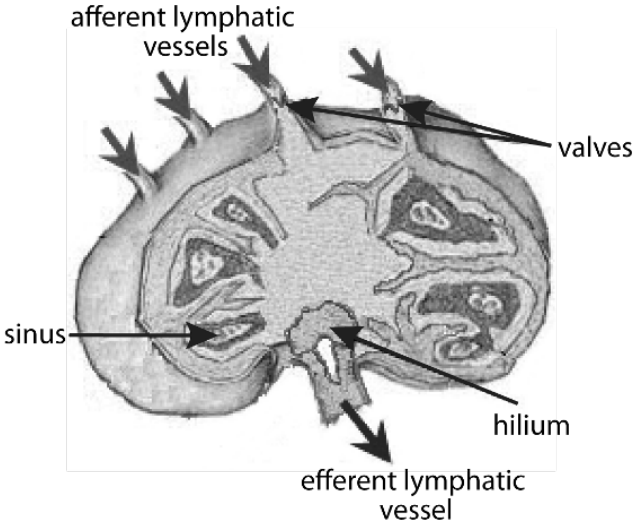

Figure 2: Cross-section of a lymph node. Afferent and efferent lymphatic vessels are shown as green and red arrows respectively. Adapted from (U.S. National Institutes of Health, 2014).

1.4.2 The sentinel lymph node

One of the main aspects that make cancer a relentless disease is that cancer cells can break away from the main tumour and travel to other locations. When a secondary tumour develops in such a location away from the primary tumour, the new cancer is known as a ‘metastasis’. Cancer cells can develop these at a distant organ after being transported through the blood or the lymphatic system (Chambers *et al.*, 2002). Although most of these cells are targeted and inactivated by the immune system, some may reach a distant location and start proliferating.

A clinically accepted, but controversial, way of preventing the spread of the disease to distant organs is to perform complete lymphadenectomy. This consists of removal of all the LNs that take up lymph from a tumour region (Briganti *et al.*, 2009). As one of the main functions of the lymphatic system is to regulate the pressure of the interstitial fluid, a systematic removal of LNs can cause unbalanced lymphatic drainage that can lead to lymphoedema (Stacker *et al.*, 2002).

When cancer cells detach from the primary tumour and drain into the lymphatic system, the reaction of the immune system first occurs within a group of LNs closest to the tumour. The sentinel lymph node (SLN) is defined as the first LN within this region that receives the lymphatic fluid draining from a primary tumour (Schauer *et al.*, 2005). A graphical representation of this effect is depicted in Figure 3.

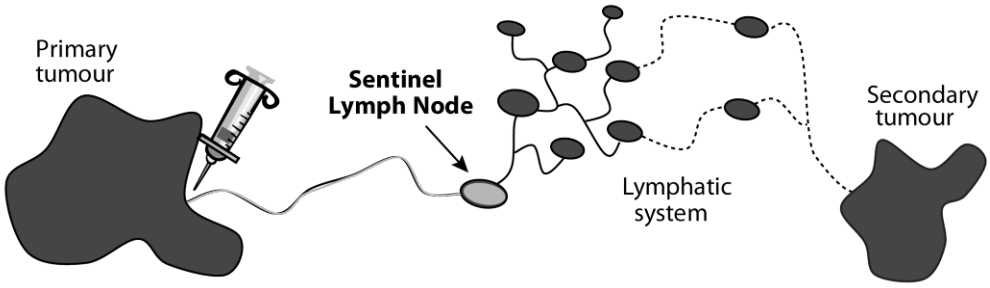

Figure 3: Schematics showing the SLN near a primary tumour. The peri-tumoural injection of a lymphatic tracer is highlighted, as will be discussed in §1.4.3.

The SLN concept, first introduced in 1990, assumes that the disease spreads in an orderly way from the primary tumour to the lymphatic system (Morton *et al.*, 1990). This concept relies on the assumption that if the SLN is negative for tumour metastasis (i.e. it does not contain any cancer cells), none of the other LNs will be positive. Provided the SLN is detected accurately, only patients with a positive SLN are likely to benefit from a radical lymphadenectomy (Morton *et al.*, 1992). The SLN method has been tested in a large number of cancer types (reviewed in (Chen *et al.*, 2008)), although convincing results have been obtained only in breast cancer (Veronesi *et al.*, 2003) and melanoma (Morton *et al.*, 2006), where this approach has become a standard of care.

1.4.3 SLN detection

As mentioned above, the relatively new paradigm of determining the tumour stage by examining the SLN depends on the accuracy of SLN detection. In order to be successful, the SLN method must rely on a procedure that can identify accurately the SLN associated with the primary tumour. It is important to note that in some cases, particularly when the

tumour is in the proximity of more than one lymphatic basin[4], multiple SLNs can be present. In this case, the detection technique should be able to identify all the SLNs related to the primary tumour.

Detection of the SLN is performed by injecting a contrast agent in a region close to the primary tumour, i.e. in an area that is believed to drain to the same SLN as the tumour (Figure 3). The contrast agent should rapidly drain to the lymphatic system and to the SLN, with no absorption into the bloodstream. In addition, this contrast agent should show high retention in the SLN for a period of time sufficiently long for intra-operative detection and biopsy, without reaching subsequent LNs.

Conventional SLN detection methods

Early contrast agents used for SLN detection were blue vital dyes such as isosulfan blue, patent blue V and MB (Morton *et al.*, 1992). These dyes are injected close to the main tumour and their diffusion through the lymphatic system observed intra-operatively. Direct injection in the tumour is not recommended because of the lack of vasculature typical of necrotic regions and the possibility of spreading tumour cells along the needle track (Loughran & Keeling, 2011). The first LN with a given degree of blue staining (subjectively assessed by the surgeon) is labelled as a SLN, removed and examined. One of the main disadvantages of this method is the relatively large volume of dye injected in order to produce sufficient staining of the SLN. A common practice is to repeat the injection at regular time intervals, thus increasing the risk of adverse reactions (Thevarajah

[4] The lymphatic basin is defined as a group of LNs in contact or in proximity to each other and that receive the lymph from the same region of the body.

et al., 2005). Another important limitation is that SLNs have to be surgically exposed in order to be detected, and that detection relies on the surgeon's vision.

The second technique for SLN mapping consists of injecting a radioisotope that continuously emits gamma rays that can be picked up using an appropriate detector (Alex & Krag, 1993). Take-up and retention in the SLN has been demonstrated using radioactive colloids (Sherman & Ter-Pogossian, 1953). The most common contrast agents for SLN mapping are sulphur colloids or nanocolloids, labelled with technetium-99m (^{99m}Tc) radioisotope. ^{99m}Tc has a relatively short half-life (~6 hs) and emits 140 keV gamma rays. A variety of gamma hand-held probes can be used to transcutaneously and intra-operatively detect the location of the emitted radiation (Tiourina *et al.*, 1998).

The main disadvantages of this method include the use of ionizing radiation, requiring access to nuclear medicine facilities, a lower spatial resolution when compared to the vital dye method and lack of integration with the surgical field (i.e. no co-registration with surgeon's view).

To date, the most common approach for SLN staging in a large variety of cancers uses a combination of vital blue dyes and radiocolloids. Gamma rays from radiocolloids are first detected and hotpots identified transcutaneously. Incisions are performed at such regions and the blue stained nodes surgically removed. In some cases, the procedure can be carried out during keyhole surgery using an endoscopic gamma probe (Barranger *et al.*, 2004). The combined tracer method was proved to be superior to the single injection of one tracer in terms of SLN detection rate[5] in a variety of cancers, thus becoming the gold standard

[5] In most studies, the SLN detection rate is defined as the ratio between the number of cases in which at least one SLN is detected and the total number of cases.

technique in SLN mapping (Cody, 2001; Meads *et al.*, 2014; Morton *et al.*, 1999). The success of this technique, however, relies on the correct injection of two contrast agents and, in particular, their propagation to the same lymphatic network.

Near infrared fluorescence method for detecting the SLN

SLN mapping using intra-operative NIR fluorescence has emerged as a potential alternative to these methods thanks to the good penetration depth and sensitivity of NIR fluorescence (Kitai *et al.*, 2005). To date, the only fluorescence contrast agent successfully used clinically for SLN mapping is ICG. In this work, however, the use of a second clinical fluorescence contrast agent is explored, as described later (Chapter 4).

Clinical results in a variety of cancers including breast, lung, colorectal, cervical, prostate and colon have shown encouraging results, with detection rates comparable to the radioactive method (Xiong *et al.*, 2014). Similarly to conventional methods, ICG is injected peri-tumourally and the fluorescence intensity is assessed intra-operatively. The intensity in the SLN depends on a number of factors, including dye concentration and injected volume, distance between injection site and SLN, dye diffusion in the lymphatic system and its retention in the SLN. Only the dye concentration and the injected volume can be controlled in practice.

The NIR fluorescence method has shown significant advantages in breast and vulval cancers, allowing transcutaneous visualisation of the lymphatic vessels and identification of the SLN (Hirche *et al.*, 2010b; Hutteman *et al.*, 2012). Fluorescence SLN mapping with ICG has also been successfully performed during keyhole surgery (Cahill *et al.*, 2012) and in robotically-assisted surgery (Rossi *et al.*, 2012). In this work, results from a clinical

study in gynaecological cancers will be shown, where the concept of SLN is still a matter of controversy.

2. Modelling fluorescence image-guided surgery

2.1 The need for a theoretical characterization

The usefulness and clinical impact of fluorescence image-guided surgery (FIGS) relies on the ability to target, to detect and to remove small clusters of tumour cells that would be missed using existing techniques. This ability is dependent on a number of aspects which include appropriate labelling of cancer cells, the generation and delivery of appropriate fluorescence excitation light, the use of efficient imaging systems for collecting the fluorescence emission and detectors responsive enough for real-time imaging.

Fluorescence microscopy has been extensively used in the biomedical sciences, therefore a comparison between this well established technique and FIGS was considered to be useful. When compared to fluorescence microscopy, the performance of FIGS is strongly limited by a number of factors, summarised in Table 4.

	FIGS	***Fluorescence microscopy***
Imaged area	~10^4 mm^2	~10^{-1} mm^2
Excitation power density	~0.01 W/cm^2	Up to 100 W/cm^2
Depth	< 20 mm	< 10 µm
Light collection solid angle	< 0.001 sr	2-4 sr
Typical range of exposure times	0.02 - 0.5 s	0.1 - 100 s
Typical signal collected	~10^4 photons/s	~10^{11} photons/s

Table 4: Typical imaging characteristics of FIGS and fluorescence microscopy.

Typical surgical field dimensions in FIGS are usually 3-4 orders of magnitude larger than in microscopy; as a result, the excitation power density is necessarily strongly reduced

when comparable light sources are used. Conventional fluorescence microscopy is based on superficial imaging of cellular and sub-cellular structures, where the light penetration is of the order of a few microns. Intra-operative fluorescence imaging, on the other hand, deals with 2D imaging of truly 3-dimensional structures in which the fluorophores may reside under several centimetres of tissue.

The light gathering power of a microscope objective is significantly superior compared to any optical system used for wide-field surgical imaging. Moreover, fluorescence microscopes often use sensitive, cooled and bulky imaging detectors that can operate at exposure times of the order of seconds or minutes. In contrast, compact imaging systems that operate at a 'live' imaging rate (25-200 ms typical exposure times) are required in FIGS. If fluorophores of similar quantum yields are assumed, this translates into collected photon numbers of $\sim 10^{11}$ /s in microscopy and $\sim 10^{4}$/s in FIGS images.

The ratio between collection and excitation photons in FIGS is thus poor. Despite this obvious qualitative observation, a more quantitative description of intra-operative fluorescence imaging is required. A complete, quantitative analysis of this complex process has to account for each step of the imaging procedure. A crucial point of this analysis is the correct description of the biological sample that is to be detected. Such a sample is typically a volume of tissue labelled with a fluorescent marker (e.g. labelled tumour cells) or one that contains unbound fluorophore molecules (e.g. in a sentinel lymph node).

The characteristics of the sample are expressed by a number of parameters which include the type of cellular receptor or molecular marker present, the affinity of the targeting process, the size and biological composition of the sample and its location within the tissue. As these parameters can vary within the same tissue, their exact value is often hard

to estimate and a degree of approximation is inevitable. Modelling a FIGS procedure can thus only be performed with limited accuracy.

In the case of a sample at depth, excitation light has to travel through the tissue in order to interact with the sample. The emission light has to travel back in order to reach the tissue surface. Light propagation in tissue has been meticulously described in the literature both theoretically (Prahl *et al.*, 1989) and experimentally (Okada *et al.*, 1997). Theoretical models can predict the photon flux (photons sec^{-1} cm^{-2}) at a given location in tissue. Such models are an essential tool for describing imaging procedures in the NIR, where light can penetrate for several millimetres in tissue.

Another challenging aspect that characterises a quantitative description of FIGS is the correct characterisation of the imaging devices used to gather fluorescence light. Such devices are generally optically complex (e.g. laparoscopes or endoscopes), and the manufacturers do not readily provide their light collection efficiencies. However, a complete theoretical description should consider all the parameters of the imaging system that influence the quality or signal-to-noise ratio of the output image.

The development of a theoretical model to characterise FIGS was thought to be useful, given a growing interest towards this field and the increasing number of applications. This description could be valuable to characterise existing systems and guide the development of new FIGS imaging devices. In this chapter, the theoretical aspects of FIGS will be presented. Key processes such as fluorescence and light propagation in tissue will be outlined. The theoretical model that I developed to quantify and predict the *imaging* performance of FIGS will then be described. The modelling results will be compared with data from validation experiments and used to predict biological imaging sensitivity.

2.2 Background on fluorescence

Although the phenomenon of fluorescence was known in the 16th Century, the term *fluorescence* was first adopted in 1852 by George Gabriel Stokes. In his work, Stokes discovered that fluorite could emit blue light when illuminated with ultraviolet radiation (Stokes, 1852). Since this mineral was used, he coined the term 'fluorescence' to describe this property. Following absorption of energy, a fluorescence molecule (also known as 'fluorophore') is excited from its singlet ground state to one of its singlet excited states. When the relaxation occurs through a radiative process, fluorescence photons of lower energy (i.e. longer wavelength) are emitted. Although excitation can raise a molecule to any of its excited states, fluorescence emission always occurs from the lowest one. This can be clearly illustrated using the ubiquitous *Jablonski diagram* which gives a visual representation of the energy levels of a system (Figure 4A) (Lakowicz, 1999).

The ground state S_0 and two excited states S_1 and S_2 are represented in the figure. At each of these states, the molecule can exist at several vibrational energy levels indicated with 0, 1 and 2. Absorption (upwards arrows) brings the system to any vibrational level of an excited state. Following absorption, the system typically relaxes to the lowest vibrational level of S_1 (dashed downwards arrows) before releasing its energy through a fluorescent photon (solid downwards arrows). The length of the arrows is proportional to the energy of the transaction. For simplicity, several processes such as intersystem crossing and phosphorescence have been excluded from this description. The wavelength or energy gap between the excited and the emitted photon is referred to as the 'Stokes shift'.

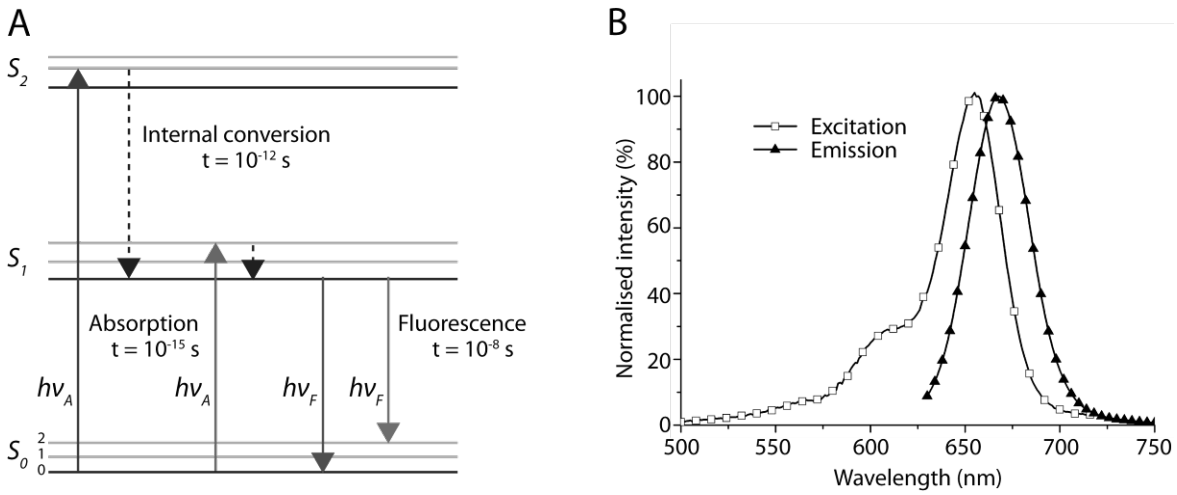

Figure 4: Principles of fluorescence. (A) Simplified Jablonski diagram indicating the time scale of each transaction (adapted from (Lakowicz, 1999)). (B) Example of excitation and emission spectra of a Cy5-derived fluorophore, as used in §4.2.

The relative probability of absorbing and emitting light at given wavelengths is represented by absorption[6] and emission spectra that are specific for each fluorophore in a given environment. An important observation is that emission wavelengths are independent on the wavelength of the absorbed photon that has caused the transition to the excited state. This is known as Kasha's rule (Kasha, 1950). The rule suggests that variations of the excitation wavelength for a given fluorophore will only affect the number of emitted photons according to the probability distribution represented by the absorption spectrum. Indeed absorption and emission spectra often overlap, as shown in Figure 4B. This apparent breakdown of conservation of energy is explained by the fact that, at room temperature, the energy level of some molecules can correspond to a high vibrational state of the ground level S_0.

[6] It should be noted that in the case of a fluorophore 'absorption' and 'excitation' are often used interchangeably. This is an approximation as absorption represents excitation only for cases when the relaxation process from S_1 to S_0 happens through emission of a fluorescence photon.

The ability of a molecule to absorb light is expressed by its molar extinction coefficient ε [$M^{-1}cm^{-1}$], which is related to the concentration and the absorbance of the compound (Pace *et al.*, 1995). Alternatively, the probability of absorbing a photon can be determined by using the *absorption cross section* σ (Lakowicz, 1999):

$$\sigma = 3.82 \times 10^{-21}\, \varepsilon \quad [cm^2]$$

The efficiency of the fluorescence process is described by the *quantum yield* which is defined as the ratio of the number of photons emitted to the number of photons absorbed. When this quantity is close to 1 (though 1 can never reached), most of the molecule's absorbed energy is released in the form of fluorescence photons. When the quantum yield is low, other relaxation processes (such as heat generation) dominate over fluorescence. The product of absorption cross section and quantum yield is known as fluorophore *brightness*. The brightness is the only truly representative quantity that describes the amount of light that a fluorophore can emit.

The number of fluorescence photons generated is proportional to the excitation fluence rate Φ [photons sec^{-1} cm^{-2}] at the fluorophore. For a given fluorophore molecule with absorption cross section σ and quantum yield η, the average emitted fluorescence rate (photons/s) is given by:

$$F_M = \Phi\, \sigma\, \eta \quad [\text{photons } s^{-1}] \qquad (1)$$

Because of the isotropic nature of the fluorescence process, all directions of photon emission are equally probable. However, the ability of a molecule to emit fluorescence photons is often affected by the intensity of excitation light. Photon-induced chemical damage can occur at prolonged excitation times or high light intensities. This effect, known as *photobleaching*, can cause the permanent loss of the ability of a molecule to emit

light. In practical FIGS photobleaching is never a problem and will not be considered in the model presented here.

2.3 Light propagation in tissue: theory

Light travelling in tissue undergoes a series of events that depend on the characteristics of the medium in which photons propagate. Such events are based on exchange of energy between light photons and particles in the medium. In a biological tissue, particles can vary in size from ~10 μm (cells) down to 0.1 nm or less (molecules). Because of this range of dimensions, light propagation is simplified by considering a statistical description of the processes involved.

When travelling in a medium, a photon can undergo absorption or scattering events, depending on the way an atom or molecule releases its energy. The absorption of a given compound is described by the *absorption coefficient* μ_a, defined as the product of the density of the molecules and the absorption cross section. The absorption coefficient is expressed as inverse of a distance (typically in cm^{-1}) and represents the average distance that light needs to travel in order to reduce its intensity to $1/e$ where e = Euler's number, 2.71828.

The probability of photon scattering in a medium is described by the *scattering coefficient* μ_s, which is also expressed as the inverse of a distance. A typical value of μ_s in tissue is 100 cm^{-1}, which indicates that on average a photon undergoes 100 scattering events when travelling through 1 cm of tissue, provided no absorption has occurred (Wang & Wu, 2007). The average scattering angle is related to the *anisotropy factor, g*, which assumes

values from 0 (isotropic scattering) to 1 (forward scattering). A quantity often used in biomedical optics to describe scattering is the *reduced scattering coefficient*, defined as:

$$\mu_s' = \mu_s (1 - g).$$

This quantity is widely preferred in the description of a given biological compound as it provides information on its transparency[7].

2.3.1 The near infrared optical window

The absorption and scattering coefficients for a given biological tissue represent the average values from distributions of all particles in the tissue. Because of differences in the excited levels, different molecules in the tissue will absorb at different energies. The energy gap between ground and excited states of most of the molecules found in biological tissues tends to be close to the energy of visible light. This results in increased probability of absorption for photons in the visible part of the spectrum.

As the wavelength is increased (energy decreased), the absorption rapidly decreases (Figure 5). For example, the absorption coefficient of oxyhemoglobin, which is one of the main light absorbers in the body, drops by 3 orders of magnitude from 420 nm to 700 nm light (Prahl, 1999). If however the wavelength is further increased, light absorption by water molecules (which account for approximately 65% of our body weight) starts to dominate. This results in an overall absorption spectrum that has a minimum in the near

[7] Two compounds with the same absorption and scattering coefficient will be more or less transmissive depending on their anisotropy factor.

infrared (NIR) region between ~650-900 nm (Figure 5). This spectral region is known as the *optical window* because of the superior light tissue penetration at these wavelengths[8].

The scattering coefficient also decreases as the wavelength increases. This is due to Rayleigh scattering (proportional to λ^{-4}), although for interaction with particles larger than the wavelength of light, Mie scattering must also be considered (Jacques, 2013). Given the much lower absorption coefficient, light scattering dominates in the NIR, making it the principal process affecting light transport. In addition, the anisotropy factor *g* for biological tissue is typically greater than 0.8 - 0.9, resulting in the high penetration depth that is characteristic of the NIR window.

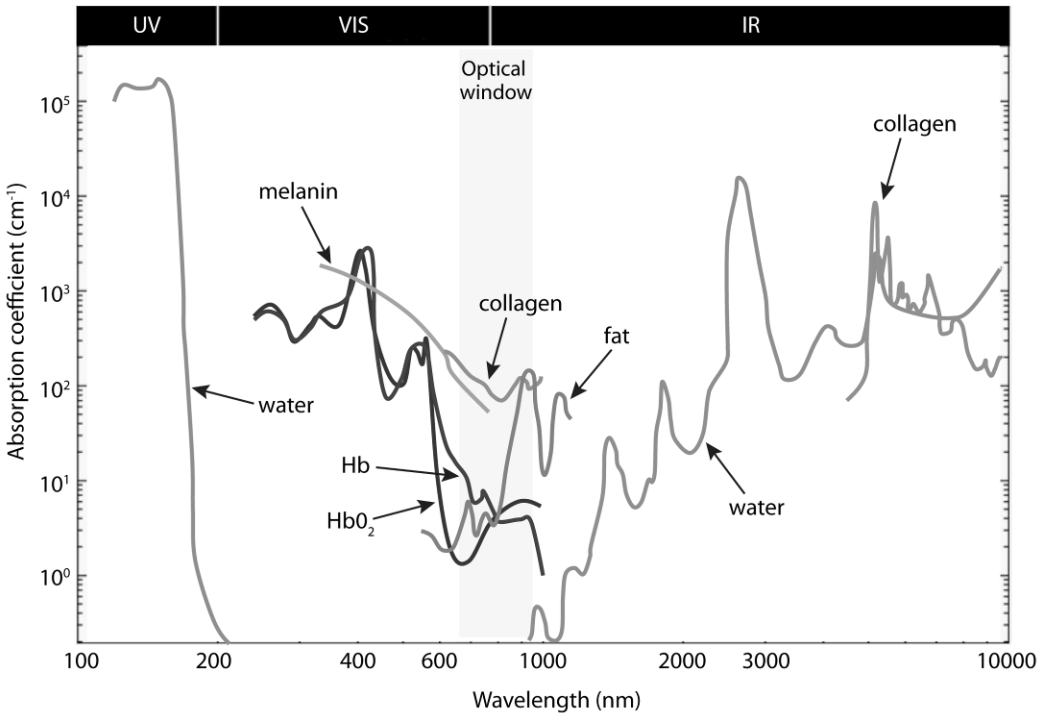

Figure 5: Absorption spectra for the main components of biological tissue. Note the logarithmic scale on the y-axis. Adapted from (Scholkmann *et al.*, 2014).

[8] This is sometimes referred as *first optical window*, as a second (1100-1350 nm) and a third one (1600-1870 nm) have also been described (Sordillo *et al.*, 2014), though these are less 'transparent'.

2.3.2 Modelling light propagation in tissue

The higher penetration depth of NIR light and its ability to investigate deep structures have contributed to the development of methods to describe light propagation in tissue. The aim of statistical models is to provide theoretical predictions of real situations with a given level of accuracy. For the purposes of this work, generic aspects of the most commonly used approaches (Monte Carlo simulation and diffusion theory) will be described. Hybrid models that combine the advantages of both have also been developed (Wang & Jacques, 1993) but will not be treated.

Monte Carlo simulation

Monte Carlo simulation is considered the gold standard for light propagation in tissue for its ability to meticulously describe a large variety of practical situations (Wilson & Adam, 1983). The Monte Carlo method (Metropolis & Ulam, 1949) is based on the random sampling of physical variables from known probability distributions. Such variables include for example the step size between two interactions and the deflection angle due to a scattering event. The step size s in a homogeneous medium is sampled by:

$$s = -\frac{\ln \xi}{\mu_t}$$

where ξ is a randomly generated number uniformly distributed between 0 and 1 and μ_t is the interaction coefficient, defined as the sum of absorption and scattering coefficients (Wang *et al.*, 1995). In a similar way, the deflection angle ϑ is sampled statistically according to:

$$\cos\vartheta = \frac{1}{2g}\left(1 + g^2 - \left(\frac{1-g^2}{1-g+2g\xi}\right)^2\right) \quad \text{if } g \neq 0$$

$$\cos\vartheta = 2\xi - 1 \quad \text{if } g = 0$$

where g is the anisotropy factor previously introduced.

In order to reduce computation time, photons are typically launched as a packet to which a weighting factor $W = 1$ is assigned. Following each interaction, W is reduced by a factor that depends on the optical properties of the tissue. When W reaches a given threshold, the photon package is normally terminated. In the more realistic scenario in which multiple media are considered, the optical properties have to be corrected accordingly. In addition, when crossing the boundary between two media, a photon is deflected according to Snell's law:

$$n_1 \sin \alpha_1 = n_2 \sin \alpha_2$$

where n_1 and n_2 represent the refractive indices of the two media and α_1 and α_2 the angles of the incident and transmitted photon.

To date, the Monte Carlo method still remains the most accurate way to describe light propagation in biological tissue. However, this comes at a price: as the scattering coefficient is typically much greater than the absorption coefficient, a photon undergoes a large number of interactions before being absorbed. As a consequence, the Monte Carlo method that simulates each interaction is computationally slow and requires several hours to compute even when using relatively simple geometries.

Diffusion approximation

As an alternative to the Monte Carlo method, an analytical description of photon propagation in tissue can be achieved by solving the so-called *radiative transfer equation* (RTE) (Arridge & Hebden, 1997). The RTE is a differential equation derived from the principle of conservation of energy that describes interaction of radiation with matter

following absorption and scattering. Because of its complexity, the RTE requires the assumption of some approximations in order for it to be solved. The most common one is the *diffusion approximation* (Contini *et al.*, 1997).

The diffusion approximation is based on the assumption that scattering is the principle mechanism responsible for light propagation in tissue. This is a typical characteristic of biological tissue in the NIR, where the absorption coefficient is much smaller than the scattering coefficient. Under these conditions, light does not have a preferential travelling direction and can be treated as optical energy that diffuses down a concentration gradient. This energy diffusion is described by Fick's first law, which in terms of light diffusion can be expressed as (Ripoll, 2012):

$$\boldsymbol{J}(\boldsymbol{r}) = -D\nabla U(\boldsymbol{r})$$

where $\boldsymbol{J}(\boldsymbol{r})$ is the light flux, D the diffusion coefficient and $U(\boldsymbol{r})$ the light fluence rate. The light flux represents the net energy flow per unit area and it points to the direction of prevalent flow. The light fluence rate is the energy flow per unit area regardless of the flow direction. Both quantities are expressed in units of W/cm^2. In this description, a steady-state regime was considered in which time dependence was excluded.

The expression of the diffusion coefficient for light transport is dependent on the optical properties of the tissue (Fishkin & Gratton, 1993):

$$D = \frac{1}{3(\mu_s(1-g)+\mu_a)}$$

In the case of absorbing media (i.e. absorption comparable to the scattering coefficient), a modified expression of D should be used instead (Aronson & Corngold, 1999). The diffusion equation for an infinite homogeneous medium is obtained by introducing Fick's

first law into the equation for energy conservation. The fundamental solution of the diffusion equation is the *Green function*, from which all the other solutions can be computed (Durduran *et al.*, 2010). For the purpose of this work, only solutions from a homogeneous semi-infinite medium will be considered.

The greatest limitation of this analytical approach is that, although computationally efficient, the diffusion approximation breaks down when propagation distances are smaller than the photon's mean free path $l_t = 1/(\mu_s (1 - g))$ (Yoo *et al.*, 1990). As a consequence, the accuracy in describing light propagation in tissue reduces when source and detector are close. Despite that, the diffusion approximation is often used to describe light propagation in tissue, for example for image reconstruction in diffuse optical tomography (Dehghani *et al.*, 2008).

2.4 Development of a theoretical model for FIGS

In this section the theoretical model that I developed to describe and quantify FIGS will be presented. Several assumptions and approximations have to be considered when modelling such a complex procedure. The purpose of this model is not to meticulously describe a particular aspect of the imaging process, but to give a 'rule of thumb' for practical situations. The schematic of the model is shown in Figure 6. A typical epi-illumination configuration in which the light source and the imaging system are located on the same side of the target object is assumed in the model. This represents the only practical geometry of illumination in FIGS, as dictated by the thickness of the human body.

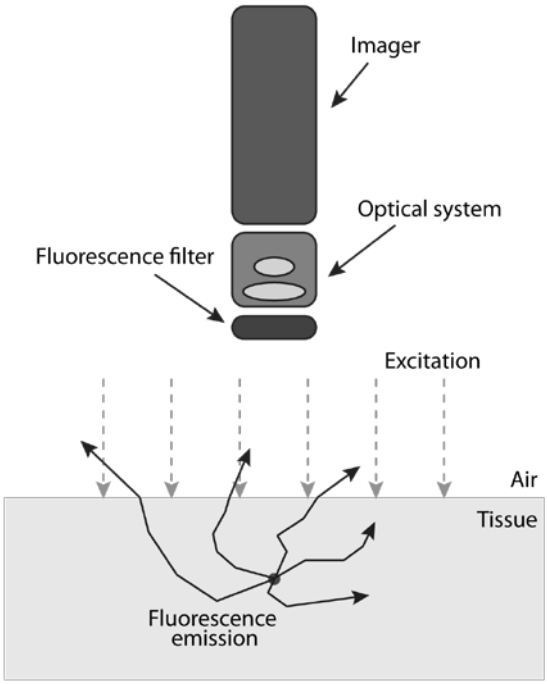

Figure 6: Schematic diagram of the theoretical model. Typical working distances between 100 to 400 mm and field of view of ~100 mm were considered.

The target object consists of a fluorescent sample located on the surface or at a depth in tissue. The sample dimensions are assumed to be much smaller than the imaging field. This is typical in practical applications, where fluorescence is used to detect small structures within larger surgical fields. Monochromatic excitation light is delivered in planes approximately orthogonal to the tissue surface. For simplicity, a beam of uniform intensity with a given surface power density is considered. Excitation light propagates in the tissue that, for convenience, is assumed to be homogeneous. The photon fluence rate at the sample is calculated to give an estimate of the total amount of light available for excitation. Fluorescence light is then emitted isotropically from a sample of given biological and fluorescence properties. Emitted photons propagate in the tissue before emerging from the surface. Part of the light escaping the tissue surface is collected by an

imaging device that consists of a fluorescence filter, an optical system (e.g. imaging lens, laparoscope or endoscope) and a camera.

2.4.1 Biological sample and fluorescence modelling

For simplicity, this model assumes that all of the fluorescence photons are generated only within the sample. The sample can either consist of fluorescently labelled cells or a volume that contains free dye molecules (Figure 7). The labelled sample comprises n_c cancer cells with an average number n_r of fluorescently labelled receptors per cell (Figure 7A). For simplicity, each cell contains an equivalent number of receptors and every receptor is labelled with a fluorophore molecule (i.e. highest affinity and specificity of the dye). This is, of course, a gross approximation, as in real situations, only a fraction of the receptors is labelled. Moreover, non-specific binding from free fluorophore molecules might also contribute to the overall fluorescence signal.

The sample dimensions are typically ~100 times smaller than the linear field of view. For sample sizes of the order of the mean free path of the photons in tissue (< 1 mm), the excitation fluence rate can be considered constant throughout the sample. Under these circumstances, the rate of the fluorescence light (photons/s) emitted from the sample can be expressed by:

$$F_S = F_M \, n_r \, n_c \tag{2}$$

where F_M is the average fluorescence rate from each molecule given by Eq. (1). In the case of a sample with free dye, the term $n_r \, n_c$ above is replaced by the total number of free fluorophore molecules in the sample volume (Figure 7B).

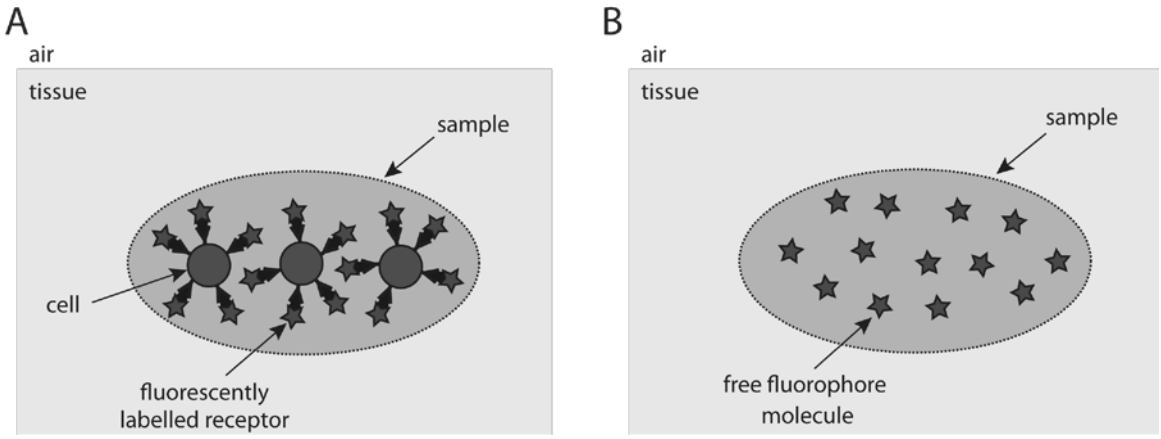

Figure 7: Schematic representation of the modelled fluorescence samples. (A) Sample containing fluorescently-labelled cells. (B) Sample containing free fluorophore molecules.

For simplicity, this model does not consider any effects of cross-excitation (i.e. photons that have been emitted do not excite other fluorophore molecules). However, a background light intensity level that takes into account non-specific binding and tissue autofluorescence can be added to the fluorescence signal. The level of inhomogeneity and the irregularities of a real biological sample are inevitably high and a more precise characterization goes beyond the aims of this model. This simple and approximate description of basic biological samples was thought to be accurate enough to assess a typical FIGS procedure.

2.4.2 Modelled light propagation in tissue

In a typical epi-illumination imaging scenario, where the fluorescent sample is embedded in tissue, excitation and emission photons have to travel from the tissue surface to the sample and back. In the case of NIR light, the penetration depth can be of the order of a centimetre or more and an accurate description of light propagation is required. For the purpose of reducing computation time, the proposed model uses a two-step approach where propagation of excitation and emission light are considered separately.

Excitation

A flat, homogeneous excitation beam propagates from air (n = 1) to a medium of refractive index n with normal incidence. The fraction of light directly reflected at the boundary between air and tissue (also known as *specular reflectance*) is computed by considering Fresnel equations for normal incidence. The specular reflectance is expressed as (Hecht, 1998):

$$R_{SP} = \left(\frac{1-n}{1+n}\right)^2$$

The excitation fluence rate Φ as a function of depth z in tissue is estimated using Beer's law:

$$\Phi(z) = \Phi_S (1 - R_{SP}) \mathrm{e}^{-\mu_{eff} z} \tag{3}$$

where Φ_S is the excitation power density on the tissue surface and μ_{eff} is the effective attenuation coefficient defined as (Kohl *et al.*, 1996):

$$\mu_{eff} = \sqrt{3\mu_a(\mu_a + \mu_s(1-g))}$$

A well-established Monte Carlo light propagation simulation package (MCML, (Wang *et al.*, 1995)) was used to test the accuracy of the analytical description of excitation. Photons (n = 10^7) were launched orthogonally to the tissue surface to simulate a broad excitation beam with diameter 100 mm (Figure 8A). Optical tissue parameters for NIR light typical of biological media were selected such that ($\mu_s >> \mu_a$). The same tissue parameters were used to solve Eq. (3). Figure 8B shows the decay of the excitation fluence rate at the lateral centre of the exciting beam as a function of depth in tissue. The analytical model based on Beer's law proved to be in agreement with the Monte Carlo simulation in describing the excitation fluence rate. Simulations were repeated across a wider range of

tissue optical properties and a similar level of accuracy was found (data not shown). As a result of this analysis, Beer's law was used in the model to propagate excitation light from the surface of the tissue to a deep sample.

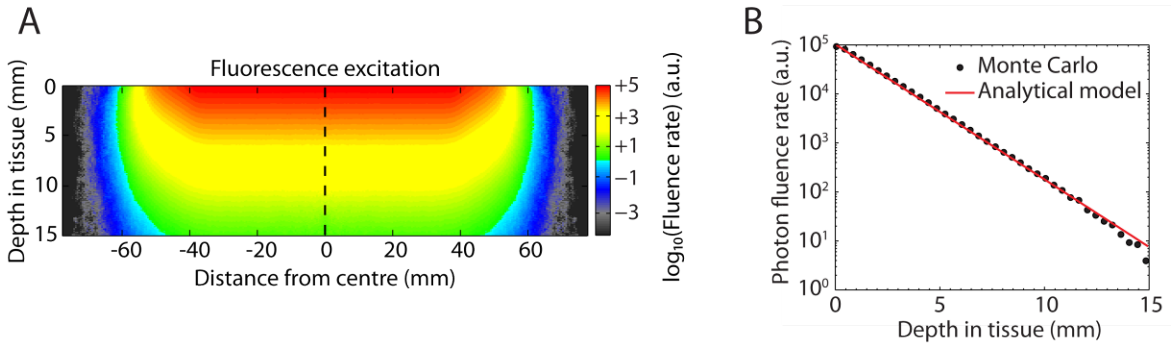

Figure 8: Modelling propagation of excitation light. (A) Colour intensity map representing Monte Carlo simulation of relative fluence rate as a function of distance from the centre and depth in tissue. (B) Intensity profile of excitation fluence rate along the dashed line in (A) compared with the analytical result obtained using Beer's law. Note the logarithmic scale on the ordinate. Tissue optical properties used: μ_a = 0.5 cm^{-1}, μ_s = 100 cm^{-1}, g = 0.675, n = 1.33; excitation beam diameter: 100 mm.

Emission

The amount of fluorescence light emitted by the sample is proportional to the excitation fluence rate at each fluorophore molecule. The rate of fluorescence emission (photons/s) was obtained by solving Eq. (1) and Eq. (2). Because of the isotropic characteristics of the fluorescence emission process, Beer's law is not adequate to describe the emitted light that travels from the sample and escapes the tissue surface. As a consequence, an analytical approach based on diffusion approximation was pursued.

The sample was approximated by an isotropic source embedded in a semi-infinite medium. The *diffuse reflectance* (i.e. the ratio between the photon rate at the source and the photon rate per unit area emerging from the tissue) was determined following the approach

described by Farrell *et al.*, (1992) and used to estimate the number of photons escaping the tissue surface from a source embedded at depth in tissue. Details of this approach are described in Appendix I.

Monte Carlo simulations were performed to test the accuracy of the analytical method in describing propagation in tissue of fluorescence emission. The original C code of the Monte Carlo package MCML was modified to simulate an isotropic source embedded in the medium (Figure 9A).

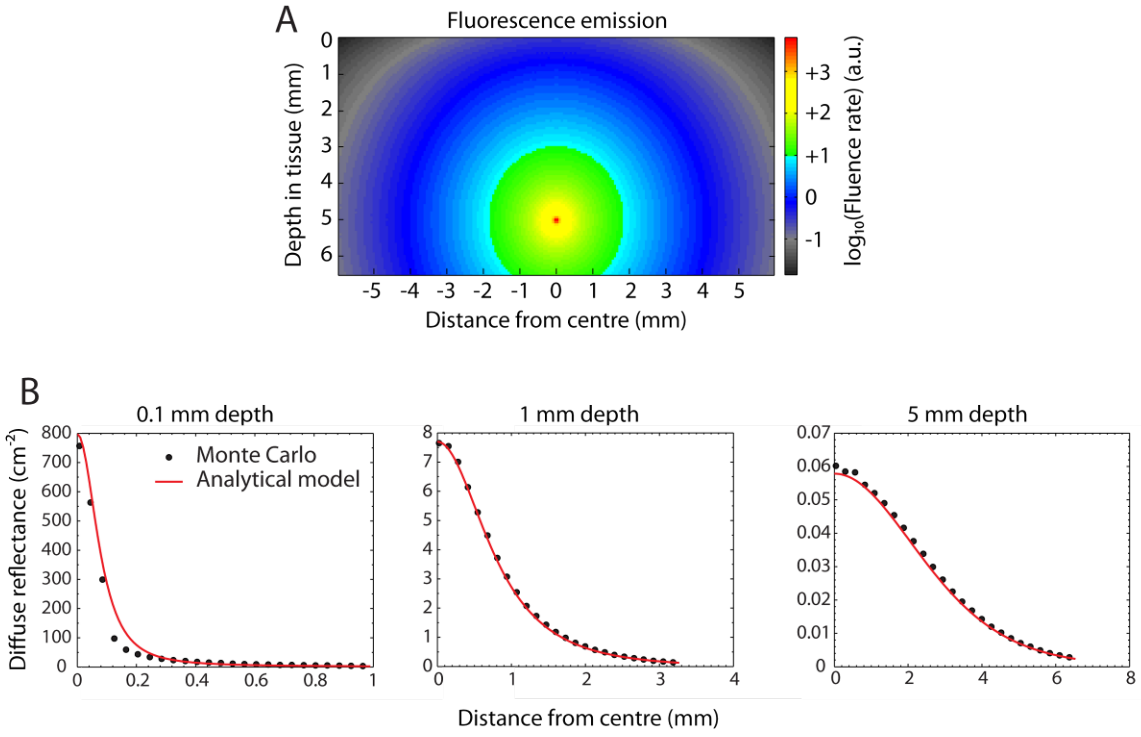

Figure 9: Modelling propagation of fluorescence emission. (A) Monte Carlo simulation of an isotropic source 5 mm deep in tissue. (B) Diffuse reflectance for an isotropic source at different depths in tissue from Monte Carlo simulations (dots) and using the analytical model (line). Tissue optical properties: μ_a = 0.5 cm^{-1}, μ_s = 100 cm^{-1}, g = 0.675, n = 1.33.

Simulations using a range of tissue parameters were carried out and the diffuse reflectance computed. Source depth in tissue was varied between 0.1 and 5 mm for each set of tissue

parameters. Figure 9B shows the diffuse reflectance values obtained with Monte Carlo simulation for depths of 0.1, 1 and 5 mm in comparison with the ones calculated analytically from the diffusion approximation.

As already reported in the literature (Wang & Jacques, 2000), the accuracy of the analytical model in predicting diffuse reflectance decreases at depths of the order of the photon's mean free path (i.e. < 0.1 mm). Despite that, the analytical approach based on the diffusion approximation is used in this model at any sample depth in order to decrease complexity and improve computation time.

For a sample at a given depth in tissue, the average photon flux density (photons s^{-1} cm^{-2}) escaping the tissue surface at a distance ρ from the centre is expressed by:

$$\Phi_{air}(\rho) = F_S R(\rho) \tag{4}$$

where $R(\rho)$ is the diffuse reflectance (Appendix I) and F_S the total number of photons/s emitted by the sample as in Eq. (2). The angle at which each photon escapes the tissue surface is related to the propagation direction before striking the surface and on the refractive index mismatch tissue/air. Monte Carlo simulations (Kienle *et al.*, 1996) and experimental measurements (Xia & Yao, 2007) have shown that the angular distribution of the diffuse reflectance $R(\rho)$ in diffuse media is close to a Lambertian distribution (i.e. light leaves a point on the tissue surface with equal intensity in all directions). As a result, all photon directions were considered equally probable.

2.4.3 Light collection and imaging

In a typical imaging setup, light from the object plane (in this case the tissue surface) is projected on the image plane (image sensor) by an optical system (e.g. a lens). The final image is related to the number of photons that strike each sensor pixel during the imager

exposure time. This is proportional to the number of photons emitted by a small surface that corresponds to the surface pixel as projected on the object plane. Based on this consideration, an algorithm was developed where, depending on the specific imaging parameters, the tissue surface is divided into squared units that correspond to the sensor pixels projected on the object plane. Photon collection efficiency is computed by considering the light gathering power of the optical system. Photons reaching the sensor's pixels are converted into electrons and their value digitised to produce the output intensity at a given pixel.

Pixel sampling

Given a square image sensor of dimension $s \times s$ and an optical system with effective focal length f, the lateral field of view F_V at a working distance w_d can be approximated using rectilinear projection by:

$$F_V = \frac{w_d s}{f} \tag{5}$$

Figure 10 provides a visual representation of all the parameters in this equation. A thin lens approximation is used such that the working distance is considered as the distance from the principal point of the lens to the object plane. The size l of each virtual pixel projected on the object plane is obtained by dividing the lateral field of view by the number of lateral sensor pixels. For simplicity, the pixels are assumed to be square. The average photon rate (photons/s) emerging from an arbitrary Lambertian square unit (i,j) on the tissue surface is given by:

$$F_{air}(i, j) = \Phi_{air}(i, j) \times l^2 \tag{6}$$

where Φ_{air} is the photon flux density obtained by converting Eq. (4) to Cartesian coordinates. A quantised distribution of photons emerging the tissue surface is calculated by computing Eq. (6) for each surface pixel.

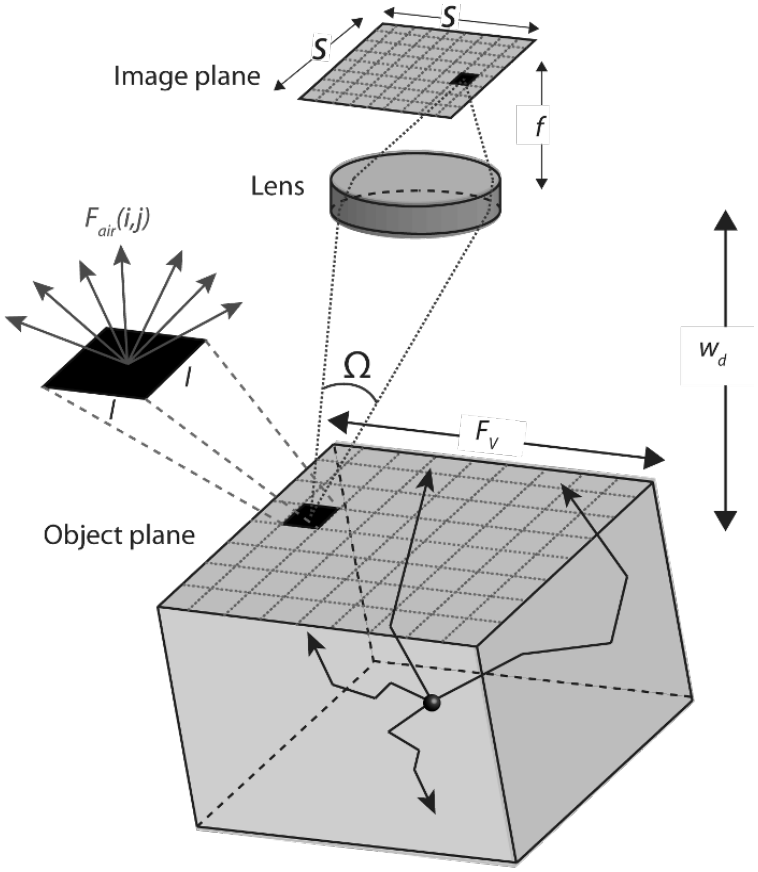

Figure 10: Schematic representation of the model imaging parameters.

Light collection

In a typical FIGS procedure, only a small fraction of the fluorescence emitted light is collected by the imaging system. The photon collection rate (also known as light gathering power) is related to the solid angle Ω that the entrance pupil of the optical system subtends with the tissue surface (Figure 11). In the case of a Lambertian emitter, the light gathering power of the system is given by $\Omega/2\pi$, where Ω can be expressed as:

$$\Omega = 2\pi(1-\cos\vartheta) = 2\pi\left(1-\cos\left(\arctan\left(d/2w_d\right)\right)\right)$$

where d is the diameter of the entrance pupil, as shown in Figure 11.

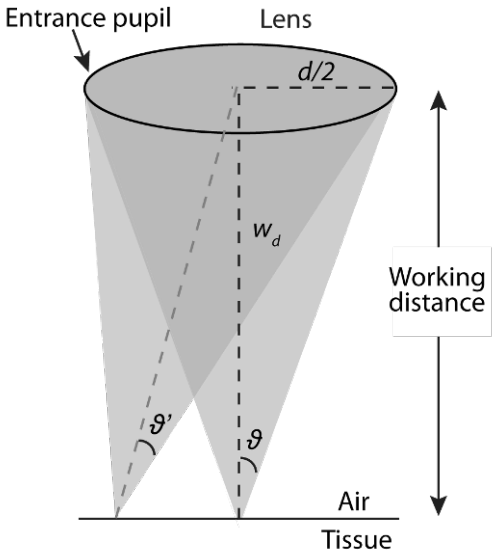

Figure 11: Schematic representation of the modelled optical system. The two cones indicate the light gathering power of the system. The angles ϑ and ϑ' are assumed to be equal.

The diameter of the entrance pupil is given by the ratio of the effective focal length f and the f-number $f/\#$ of the optical system. For a given working distance, the solid angle of collection Ω decreases as the field of view increases due to the falloff caused by the cosine-fourth law of illumination[9]. This is particularly evident when large pupil sizes (low f-numbers) and short working distances are used. In the case of this model, a uniform solid angle throughout the object plane was used to compute light gathering power. This approximation is adequate for a typical imaging setup and for a sample at the centre of the field of view.

[9] The cosine-fourth law of illumination states that the light gathering power of an optical system is proportional to the fourth power of the cosine of the angle between a ray from the periphery of the field of view and the optical axis (Hecht, 1998).

The photon rate reaching a given pixel (i,j) of the image sensor is expressed by:

$$F_{pix}(i,\, j) = F_{air}(i,\, j)\frac{\Omega}{2\pi}T$$

where the T is a transmission factor that accounts for optical losses in the system (lenses and filters). The transmission factor T is particularly relevant when modelling fluorescence as optical filters usually collect only part of the broad emission spectrum of a fluorophore. Moreover, optical transmission especially in the NIR can be quite poor in the case of complex systems such as laparoscopes and endoscopes. To account for the statistical nature of photons, the photon rate $F_{pix}(i,j)$ is replaced by a value generated using a Poisson distribution with expected value $F_{pix}(i,j)$.

Digitization and output

The photons that strike a sensor pixel are converted into electrons according to the quantum efficiency (QE) of the sensor. Given the wavelength-dependency of QE, different values that correspond to the distribution of wavelengths of the emission spectrum should be used. For simplicity, this model assumes that all emission wavelengths are detected with equal probability. For a narrow emission spectrum, this is a valid approximation.

The number of electrons generated at each pixel during an exposure time t (in seconds) is:

$$n_{e^-}(i,\, j) = F_{pix}(i,\, j)\, t\, \mathrm{QE}$$

A sensor fill factor of 100 % is assumed in this formula in order to reduce the complexity of the model. An additional electron signal was added to account for thermal noise, dark current and readout noise typical for non-ideal detectors. The total electron signal is multiplied by the gain G of the on-chip amplifier before being converted into pixel

intensity levels. The intensity level $I(i,j)$ in a given pixel expressed in terms of digital counts is given by:

$$I(i,j) = \frac{\left(n_{e^-}(i,j) + n_{e^-_{noise}}(i,j)\right)G}{\mathrm{e}^-/\mathrm{ADU}} \tag{7}$$

where e^-/ADU represents the number of electrons associated to each quantised intensity level. The variable $I(i,j)$ assumes only integer values from 0 to 2^n-1, where n is the bit depth of the digitisation process. The final output image is calculated by computing Eq. (7) for each sensor pixel.

2.5 Model graphical user interface

The analytical model includes a large number of variables that are typical in practical situations. These variables are related to several characteristics of the imaging process which include tissue optical properties, fluorophore and sample characteristics, imaging geometry, photodetector and image processing. Figure 12 shows a flowchart of the theoretical model with all the variables that contribute to the final image.

Given the large range of values that each variable can assume, a way to dynamically change all the imaging parameters while simultaneously providing a visual representation of the results was thought to be useful. For this reason, a graphical user interface (GUI) of the analytical model was developed to allow full control of all the free parameters. The GUI was created with the intent of providing an open-source tool that anyone can use to apply the analytical model to characterise an imaging system or as guidance for future device development and requirements. The GUI was developed using Phyton programming language.

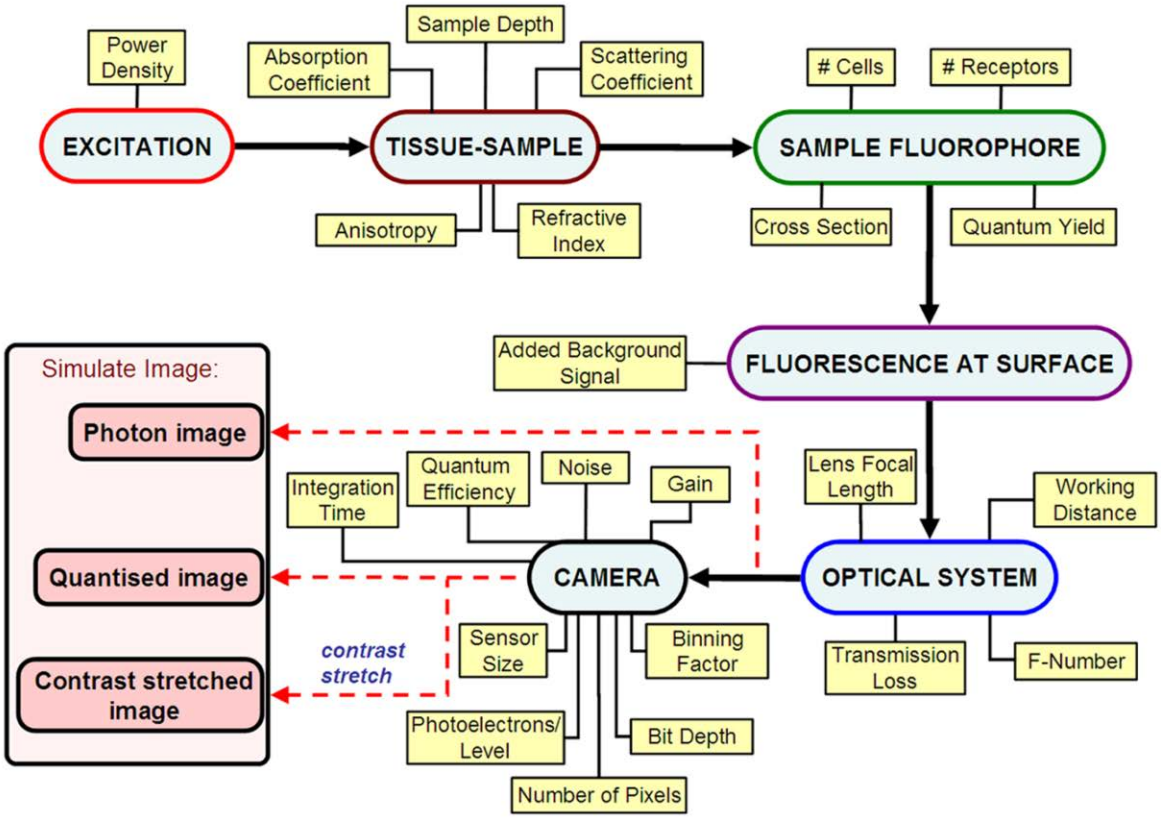

Figure 12: Flowchart of the theoretical model. The parameters in the yellow boxes represent the variables of the model.

A standalone executable for Microsoft Windows platforms named *FIFAC* (Fluorescence Imaging Fast Analytic Calculator) was developed and made available for download from our research group's website (*http://users.ox.ac.uk/~atdgroup/software*). Details on the development and operation of this software tool are described in Appendix II. The software was designed to display all the imaging parameters in the same window. The modelled output image is provided and can be saved for further image analysis. A screen capture of the *FIFAC* software tool is shown in Figure 13.

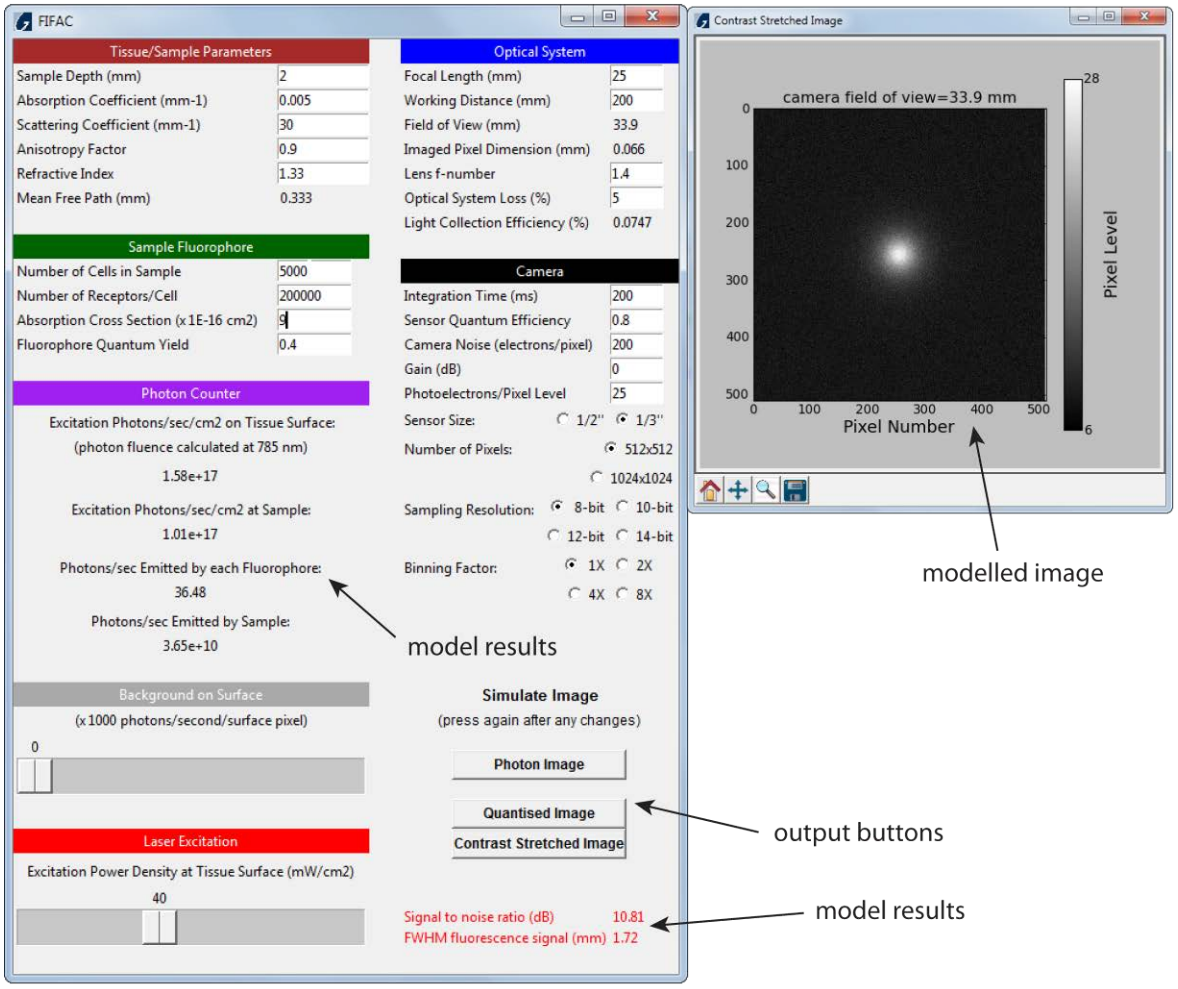

Figure 13: *FIFAC* graphical user interface. The main control panel is shown on the left and the output modelled image on the right.

One of the greatest advantages of this software tool is that the output image is generated almost instantaneously, thus allowing rapid analysis of imaging performance when any of the parameter(s) is changed. Apart from predicting the output image, useful quantities such as signal-to-noise ratio (SNR) and sample resolution are provided. Details on how these quantities are computed are also described in Appendix II.

2.6 Experimental validation of the model

The analytical model described in the previous section was designed to predict fluorescence imaging performance from practical situations. Because of the high number of free parameters in the model and the difficulties in estimating their true values, an experimental validation of the model is not straightforward. Despite the fact that some aspects of the model have already been validated (e.g. light propagation in tissue), other aspects (e.g. imaging performance of surgical systems) need to be experimentally characterised. In this section, experiments to determine the level of accuracy of the FIGS model in predicting results from practical situations will be described.

A conventional wide-field imaging system and a surgical laparoscope were used to test the model. The laparoscope was optically characterized in order to determine the imaging parameters necessary for the analytical calculations (i.e. focal length, f-number and optical transmission). Imaging tests using indocyanine green (ICG) fluorescent dye at depth in a liquid phantom were performed. Such tests were carried out using free fluorophore molecules diluted in small volumes.

2.6.1 Laparoscope optical characterization

Unlike conventional imaging lenses, the optical characteristics of laparoscopes and endoscopes are not easily available. Key imaging parameters such as light gathering power and light transmission are not specified. This is particularly relevant when NIR wavelengths are used, since these devices are generally designed to operate only in the visible part of the spectrum. A detailed experimental analysis of the optical properties of surgical systems for minimally invasive surgery was considered to be necessary for determining the required parameters of the model. For this purpose, a 10 mm diameter,

310 mm long rigid laparoscope (Storz Hopkins II, Karl Storz) typically used for abdominal keyhole surgery was considered (Figure 14A). The laparoscope imaging channel consists of an objective lens, a rod lens relay system and an eyepiece at the output, as shown following X-ray imaging (Figure 14B). Light collection efficiency depends on the gathering power of the optical system and on the optical transmission through the detection channel. These quantities need to be determined experimentally to derive both the system f-number and, in effect, the system T-number (Ray, 2002).

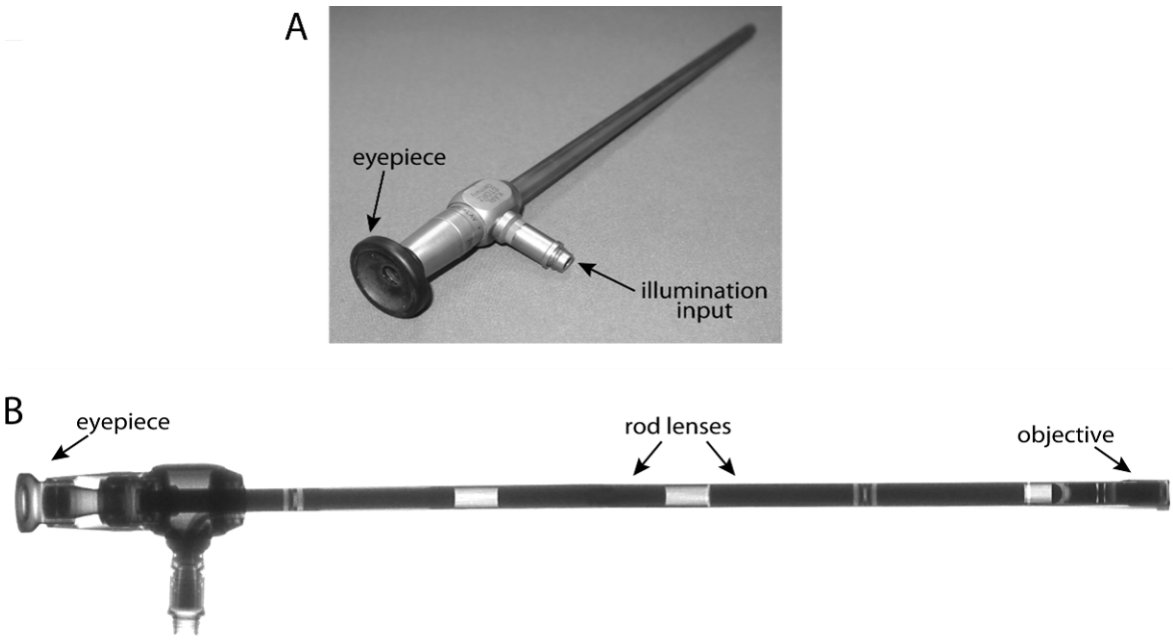

Figure 14: Storz Hopkins II, 10 mm diameter laparoscope. (A) Actual image and (B) X-ray image obtained using an X-ray imaging system (45 kVp energy) available in our laboratory. X-ray image courtesy of A. Kavanagh.

Methods I: laparoscope f-number

The light gathering power of an optical system is expressed by the f-number (Born *et al.*, 2002):

$$f/\# = \frac{f}{d}$$

where f is the focal length of the system and d the diameter of the entrance pupil (i.e. the image of the aperture stop as seen from the front of the optical system). The focal length can be estimated by inverting Eq. (5):

$$f = \frac{w_d s}{F_V} \tag{8}$$

where w_d is the working distance, s the diagonal size of the sensor and F_V the diagonal field of view (FOV).

As the eyepiece of the laparoscope produces near-collimated light, a lens is required in order to focus this light on the sensor. A 25 mm focal length imaging lens (67-715, Edmund Optics) was used in conjunction with a 1/3” sensor CCD camera (XC505P, Sony). This combination proved to be optimal for viewing a circular image on a 4:3 aspect ratio sensor. The equivalent focal length of the system laparoscope-lens-camera was calculated by solving Eq. (8) for a range of working distances and averaging the results. The FOV was measured by placing a ruler on the object plane. Video output from the camera was digitised using a video-to-USB 8-bit resolution converter (DFG/USB2PROPCB, The Imaging Source).

The diameter d of the entrance pupil was measured using a separate FOV-calibrated imaging system. This consisted of the same lens and camera described above, with the lens used at f/1.4 and the object plane at a distance of ~50 mm from the lens. The short working distance allowed imaging of the entrance pupil over a significant number of pixels (typically >2000) and thus reduced measurement errors. In addition, a high aperture and a short working distance provided a very shallow depth of field that resulted in precise

estimation of both the pupil diameter and its position. Without varying imager position or focus, a ruler replaced the laparoscope and provided, when in focus, a conversion factor pixels/unit length. Image analysis was performed with ImageJ software (U.S. National Institutes of Health).

Methods II: laparoscope optical transmission

The optical transmission of the laparoscope's imaging channel was measured using the setup illustrated in Figure 15. The laparoscope eyepiece was illuminated using small diameter (100-200 μm) monochromatic, collimated light beam. Laser sources operating at five wavelengths (532, 660, 732, 785, 830 nm) from the visible to the NIR were used to provide this collimated light. Each laser was collimated independently and coupled to the input of a 10× Galilean beam expander (BE10M, Thorlabs). Small diameter apertures were placed at the output of the expander to produce a re-collimated beam of diameter much smaller than the laparoscope exit pupil. An XY translation stage (ST1XY, Thorlabs) aligned apertures to the system axis, such that the small beam, laparoscope eyepiece and laparoscope imaging port were all coaxial.

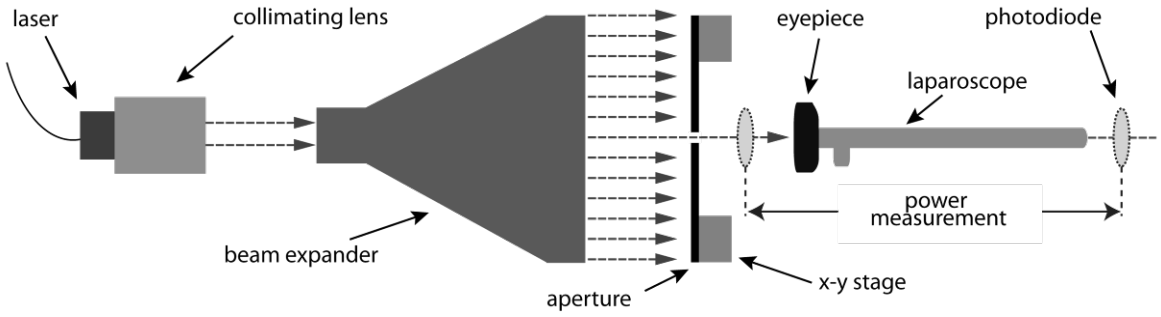

Figure 15: Experimental setup for measuring the laparoscope optical transmission.

The optical transmission was determined through measurement of the intensities of the beam entering the eyepiece and leaving the laparoscope tip. A large area photodiode

detector measured the relative intensities of the input and output light. The same procedure was repeated for all the laser wavelengths and for different aperture sizes (< 200 μm).

Results

The effective focal length of the system that includes the laparoscope, the 25 mm focal length lens and the camera was measured to be 4.02 ± 0.01 mm. The laparoscope entrance pupil (shown in Figure 16A) was measured to have a diameter of 0.45 ± 0.03 mm. By using Eq. (8) the f-number of the system was estimated to be 8.91 ± 0.06.

The absolute spectral transmission through the imaging channel of the laparoscope is shown in Figure 16B for wavelengths ranging from the visible to the NIR. Results suggest that optical transmission of this laparoscope decreases significantly in the NIR portion of the spectrum.

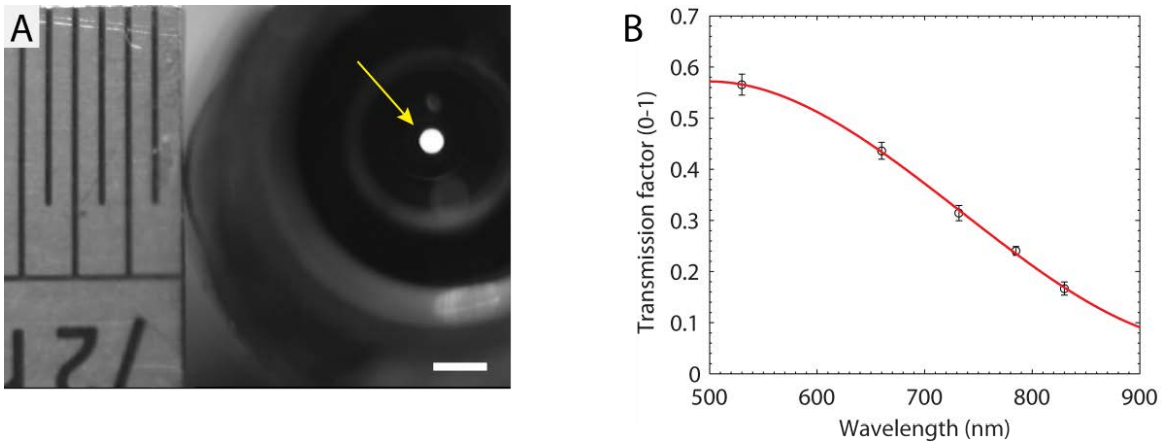

Figure 16: Characterisation of the laparoscope optical system. (A) Image of the entrance pupil of the laparoscope (yellow arrow). Scale bar: 1 mm. (B) Absolute light transmission of the laparoscope imaging channel. Error bars represent the standard deviation of measurements performed in triplicate, using different laser spot sizes. Adapted from (Volpi *et al.*, 2014).

2.6.2 Experimental analysis of laparoscope optical performance

The measured f-number and optical transmission of the laparoscope were validated by comparing its imaging performance with a conventional wide-field system. The wide-field system and the laparoscope used the same lens and camera as previously described (i.e. 25 mm focal length lens and 1/3” CCD camera). This allowed determination of the ratio of the light gathering powers by comparing the effective apertures of the wide-field and laparoscopic systems.

The effective aperture of the wide-field system was calculated by correcting the infinity-set f-number for image and pupil magnification. The f-number of the laparoscope was ~f/8.9, as previously calculated. Given the low image magnification of the laparoscope (m ~ 0.04) when used at a typical working distance of 100 mm, this f-number was assumed to represent the effective aperture stop of the system.

The 25 mm focal length lens was used in the laparoscopic configuration with an aperture sufficiently large to collect all the light from the eyepiece. Operating the lens at f/2.8 or lower proved to be adequate for this purpose. A laser rejection filter (785-nm StopLine single-notch filter, NF03–785E-25, Semrock) was placed in front of the 25 mm focal length imaging lens for filtering out excitation light. As will be shown in more detail in the next chapter, this configuration provided optimal rejection of excitation light.

The fluorescence sample was made by diluting ICG dye in a plasma-equivalent solution (albumin-enriched physiological salt solution (APSS)) that was prepared using the recipe described in Appendix III. ICG was diluted at concentrations ranging from 200 nM to 20 μM in 1 ml volume solution. Following spectroscopic measurement to determine the emission peak of ICG:APSS (data not shown), the laparoscope transmission value

corresponding to 830 nm (~18%) was used in the calculations. The ICG:APSS sample was placed in a 1 ml Eppendorf tube and excited using a homogeneous beam of monochromatic light with 15 mW/cm^2 power density at the sample. This light was produced by a custom-made light source with a 785 nm laser module (K78S04F-1.60W, BTW). Figure 17 shows a schematic of the imaging procedure for the wide-field system and for the laparoscope.

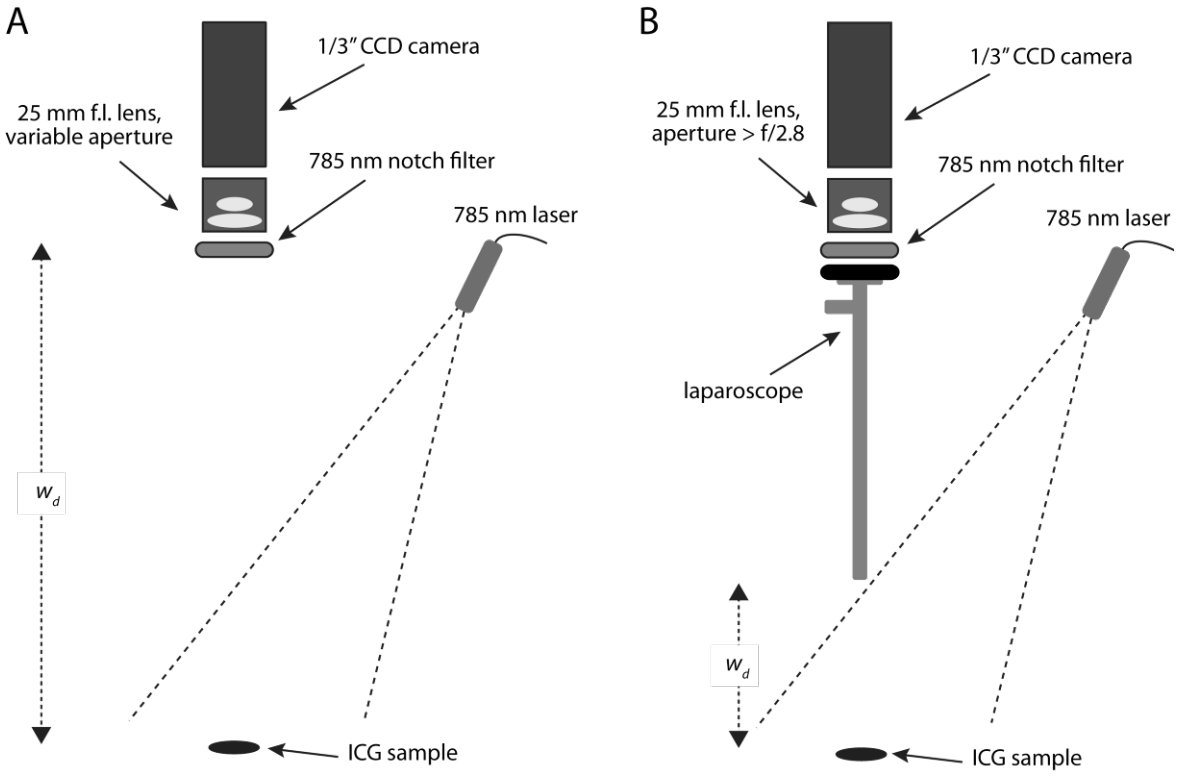

Figure 17: Experimental setup to validate the modelled imaging performance. Schematics of the wide-field (A) and laparoscopic (B) systems configuration are shown. Working distances are indicated as w_d.

Imaging was performed at a working distance of 320 mm for the wide-field system and 100 mm for the laparoscope. Ambient light intensity was negligible during imaging. Relative sensitivity was calculated as a ratio of the average fluorescence intensities from equivalent sample imaged areas. For this purpose, the camera output was digitized using

the video-to-USB converter previously noted. Data from >1000 pixels were typically used for intensity measurements. Image analysis was performed using ImageJ software. Results from the image analysis were compared with relative sensitivity computed from the laparoscope transmission and f-number that were determined in the previous section.

Figure 18 shows the sensitivity ratio wide-field:laparoscope as a function of the wide-field effective f-number. Results show good agreement between measurement-predicted and experimental values, suggesting accurate characterization of the laparoscope imaging channel was achieved. Experiments indicate that, when the laparoscope is used in the NIR, it is equivalent to a conventional wide-field system operating at ~f/20.

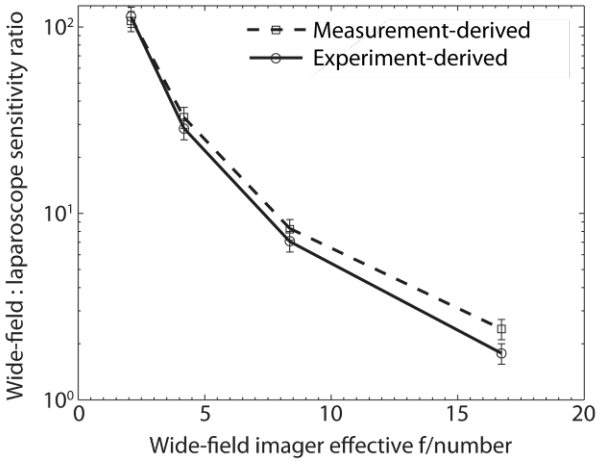

Figure 18: Laparoscope optical performance relative to a wide-field system. Measurements-derived (dashed line) and experiments-derived (solid line) sensitivity ratio wide-field:laparoscope for fluorescence imaging of ICG solution. Note the logarithmic scale of the y-axis. Error bars in the experiment data represent the standard deviation of experiments conducted in triplicate using different concentrations of ICG:APSS (20 , 2 and 0.2 µM).

Differences between the measurement-derived and experiment-derived curves can be explained by the approximation of the broad emission spectrum to a single monochromatic wavelength. Further results, separately obtained using another fluorophore emitting in the

far-red spectrum (methylene blue), confirmed the level of accuracy reported (data not shown).

2.6.3 Fluorescence imaging of deep ICG samples: model *vs.* experiments

The optical properties of the laparoscope were used for a full experimental validation of the theoretical model. Due to the large number of variables involved, some of the free parameters of the model were experimentally measured or calculated (e.g. number of fluorophore molecules, imaging system optical transmission, collection efficiency, excitation power) and others were obtained from the literature (e.g. dye quantum efficiency and tissue optical properties). Because of its relevance in FIGS, ICG was used as fluorescent dye in these experiments. This dye was diluted to specific concentrations and the total number of free molecules estimated. The wide-field and laparoscopic systems as well as the excitation laser source described for the previous experiment were used.

A sample containing free fluorophore molecules was created by diluting ICG in 50 µl of distilled water to produce a 4 µM solution. A relatively low ICG concentration was adopted to avoid fluorescence quenching effects (Mordon *et al.*, 1998) that are not considered in the model. The total number of fluorophore molecules in the sample, as required by the analytical model, was calculated by computing the concentration, volume and molecular mass (775 g/mol) of the ICG solution. Distilled water was used as solvent instead of APSS as quantum yield data (also required by the model) were then available from the literature (Benson & Kues, 1978). The ICG solution was placed in a 50 µl Eppendorf tube at the bottom of a deep Petri dish filled with a solution of 5% milk in water. This solution was used to simulate a highly scattering medium typical of biological

tissue. The volume of solution was adjusted to create depths ranging from 5 to 15 mm as measured from the middle of the sample to the surface of the medium.

The optical properties of the milk solution described in Wabnitz *et al.,* 1993 were used in the model. Excitation power density at the surface of the phantom was set to 7 mW/cm^2. The experimental- and the model-generated images were compared and analysed using ImageJ. SNR was calculated as the ratio between the average intensity of the peak of the image and the standard deviation of the noise in regions where no sample was present.

In a first experiment, fluorescence from a 15 mm deep sample was acquired both with the wide-field system and the laparoscope. The same sample and imaging systems were then modelled using *FIFAC*. The number of sample fluorophore molecules in the model was adjusted to provide a signal comparable with the experiments for the wide-field system. This was a necessary adjustment as the correct number of molecules that contributed to the fluorescence signal from the sample was almost impossible to estimate.

The wide-field system operated at f/5.6 with an exposure time 80 ms. The laparoscopic system imaged the same sample at 320 ms exposure and 4× electronic gain. Figure 19A shows the results obtained by imaging (left) and by generating an image with the analytical model (right). As shown from the intensity profiles (Figure 19B), the analytical model proved to be accurate in predicting the output signal from the laparoscopic system.

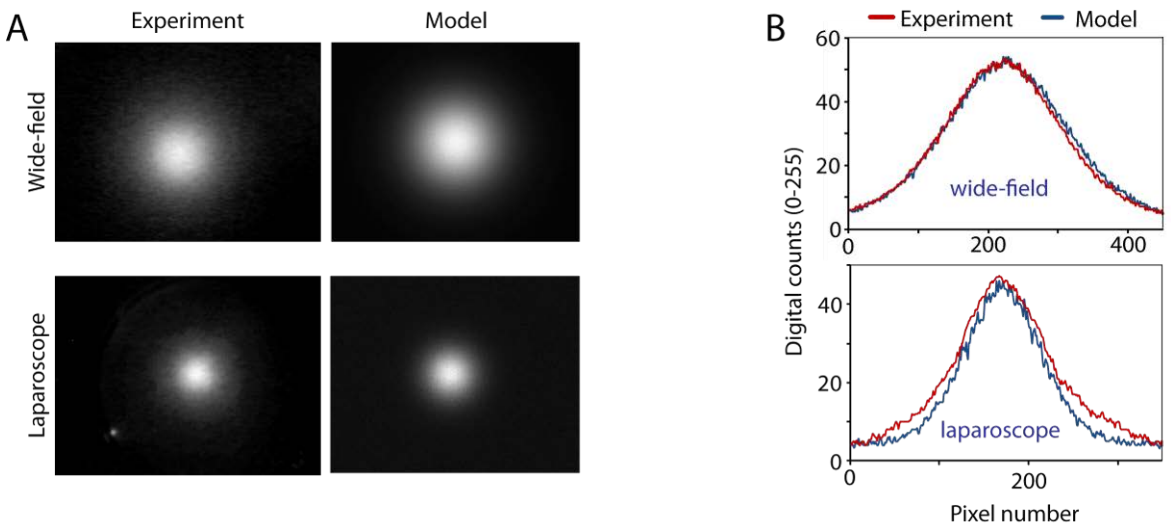

Figure 19: Experimental validation of modelled laparoscopic imaging. (A) Experimental and modelled images from a 15 mm deep fluorescent sample imaged with the wide-field (top) and laparoscope (bottom) systems. The scale of the graymap was stretched to the minimum and maximum image pixel count for display purpose. (B) Intensity profiles across the centres.

In a second experiment, the ability of the model to predict fluorescence intensities from samples at different depths in tissue was tested. Only the wide-field system was used in this test. As in the previous experiment, the imaging lens was set to f/5.6. Results from samples at depths of 5, 7 and 9 mm are shown in Figure 20A. Similarly to the previous experiment, the number of sample molecules in the model was adjusted when the sample was placed at a 5 mm depth in order to provide a modelled output signal peak comparable to that of the experiment. Results from the profile analysis showed that the model could predict the drop in image resolution (i.e. increase in the blurriness at depth) with reasonable accuracy (Figure 20B).

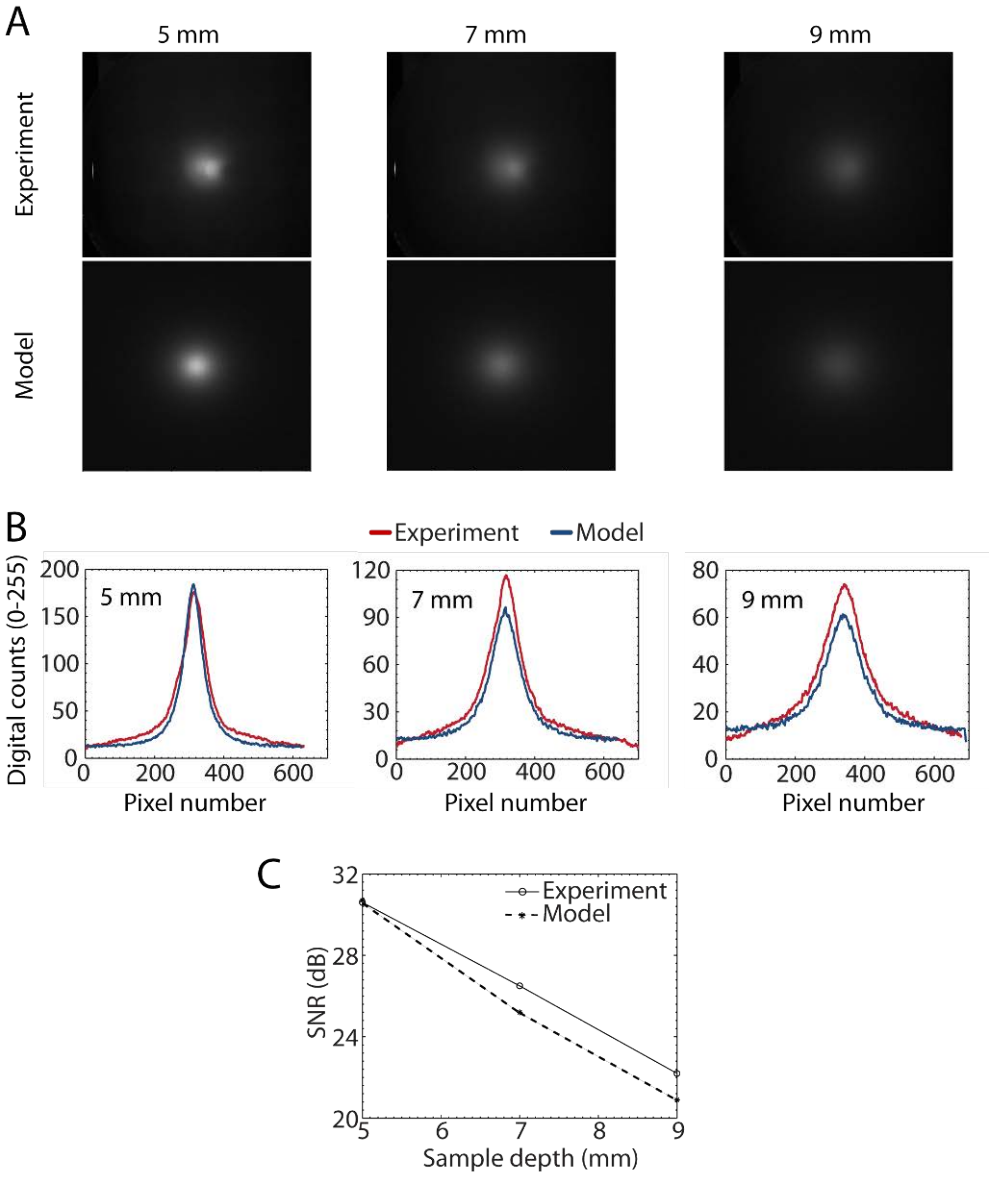

Figure 20: Experimental validation of deep fluorescent samples modelling. (A) Experimental and modelled images using the wide-field system at different imaging depths and (B) corresponding intensity profiles. SNRs of the images are plotted in (C).

Differences in the intensity levels and SNR between modelled and experimental results were observed (Figure 20C). Presumably, this variation was caused by the use of imprecise tissue optical parameters and the point source approximation of the model. Shorter

working distances were not considered as the dimensions of the sample was too large to be approximated by a point source.

Despite the uncertainty and approximation of some of the imaging parameters required by the model, comparison with practical imaging results seemed to provide reasonably correct predictions.

2.7 Performance prediction in fluorescence molecular imaging

Performance prediction of fluorescence imaging of cellular samples using the analytical model will be presented in this section. Only results that are based on theoretical considerations will be shown.

In order to quantify the ability of an imaging system to detect fluorescence from small cellular samples, the model was used in 'reverse': starting from a given image SNR, the minimum number of cells necessary to produce an image was determined. Realistic imaging parameters were used in the calculations (Table 5).

Excitation (mW cm^{-2})	10
Working distance (mm)	200
Focal length (mm)	25
Imaging *f/#*	f/1.4
Sensor size	1/3"
Exposure time (ms)	200
e^-/ADU	25
Quantum efficiency	0.8

Absorption coefficient (cm^{-1})	0.05
Scattering coefficient (cm^{-1})	300
Anisotropy factor	0.9
Refractive index	1.33
No. Receptors/Cell	10^5
Fluorophore quantum yield	0.2
Absorption cross section (cm^2)	8×10^{-16}

Table 5: Typical imaging parameters for modelling cellular sensitivity.

Figure 21A shows the modelled number of cells required to generate an image with SNRs of 20, 30 and 40 dB in the case of a wide-field system. Results from the model suggested that an f/1.4 system should be capable of detecting approximately 10, 10^4 and 10^7 fluorescently labelled cells at 10 µm, 1 mm and 10 mm depths respectively. These numbers refer to an SNR of 20 dB, (i.e. a signal:noise ratio of 10).

When a rigid laparoscope was modelled, the minimum number of cells at 10 µm depth increased to ~5000 (Figure 21B). This is not accounting for variations of excitation power density which, particularly for short working distances, can be higher than the 10 mW/cm^2 used in the calculations.

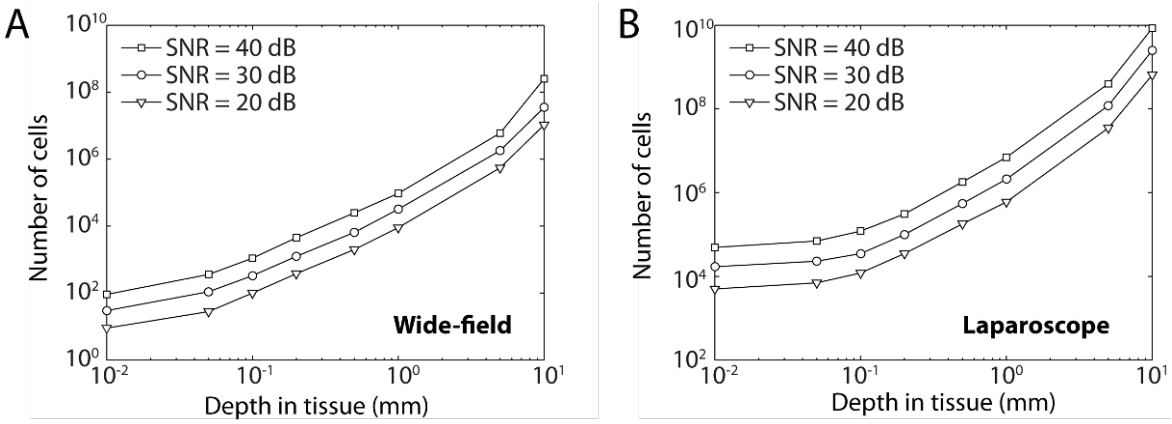

Figure 21: Model predictions of cellular sensitivity in FIGS. Minimum number of fluorescently-labelled cells detectable at given SNRs as a function of sample depth in the case of wide-field (A) and laparoscopic (B) systems. Note the logarithmic scale on the *x* and *y* axes.

A maximum exposure time of 200 ms was used in the modelling, as much longer times are inappropriate for real-time use. Detection of lower number of cells can also be achieved, for example, by means of pixel binning. The *FIFAC* software interface allows setting 2×, 4× or 8× image binning to increase SNR and reduce spatial resolution; however no binning

was assumed in the results shown here. For deeper samples, where spatial resolution is inherently poor, binning would indeed be preferable.

The apparent fluorescent sample size as a function of depth in tissue is shown in Figure 22. This sample was assumed to be smaller than the imaged pixel, as projected on the object plane (i.e. <0.07 mm). The imaging parameters shown in Table 5 were used.

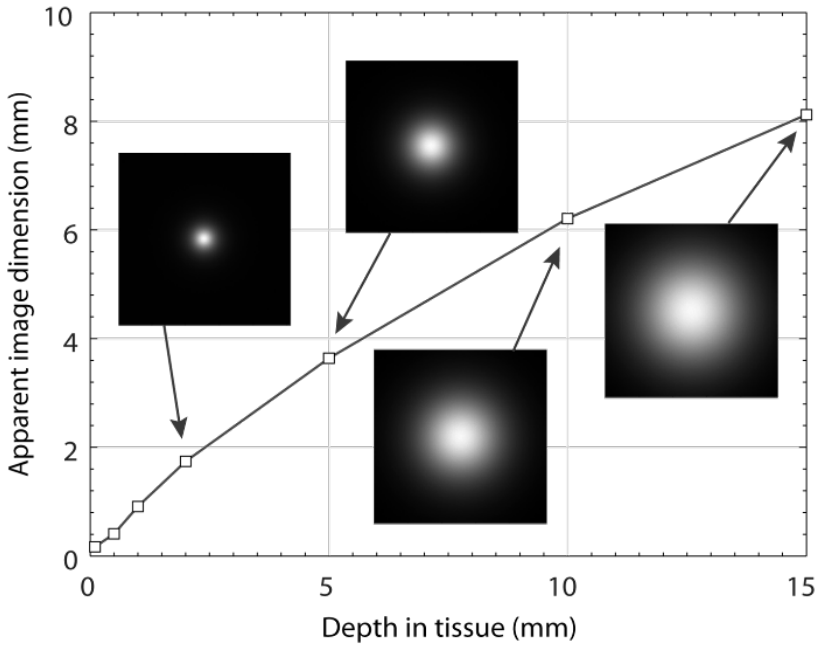

Figure 22: Model resolution predictions for deep fluorescent samples, showing the variation of the apparent sample dimensions as a function of depth in tissue. Modelled images at different depths are also shown. In each image, the scale of the graymap was stretched to the minimum and maximum image pixel count for display purpose.

Degradation of spatial resolution with depth was relatively linear up to ~2 mm below the surface. At a depth of 15 mm the sample appeared ~8 mm wide, i.e. the depth response becomes increasingly non-linear. This is inevitable since the light is increasingly absorbed with depth.

2.8 Discussion of Chapter 2

Despite promising results in detecting both tumour and sentinel lymph nodes, imaging devices are typically not standardised and their performance is rarely known. As a result, important biological questions (such as the minimum detectable lesion dimensions) remain unanswered. This chapter has described the development and practical testing of a theoretical model that quantifies FIGS and that acts as a useful tool for imaging standardisation.

The model was designed to simulate practical situations in which small fluorescent samples embedded in tissue are excited and imaged. The samples were modelled based on biological considerations which included cell and receptor numbers. Analytical equations were used to describe propagation of excitation and emission light in tissue. Fluorescence light collection was modelled using a geometrical approach that took into account all the relevant optical quantities, such as f-number, working distance and light transmission. The final image was generated by modelling a real camera system and calculating the number of digital counts produced for each pixel.

The analytical description of light propagation in tissue proved to be in agreement with gold-standard Monte Carlo simulations, at fluorescent sample depths ranging from 100 μm to 10 mm. Although not truly representative of real situations, the use of approximations using isotropic sources in homogeneous medium results in short computation times, particularly useful when model with a high number of free parameters is applied. Other parameters typical for practical situations have been excluded from the calculations (e.g. depth of field, vignetting, optical aberrations, sensor fill factor etc.) as their contribution to the final result was thought to be either minimal or readily accounted for.

Despite the use of well-characterized analytical equations, the real novelty of this theoretical model is its capacity to provide fast and practically accurate predictions of device performance. This was accomplished by considering a large number of imaging parameters that contribute to the output image. A graphical user interface of the model was developed with the intent of offering full control of such parameters and providing open source software available to the community.

This model is potentially relevant in the field of fluorescence molecular imaging as it represents both a tool to quantify performance of existing systems and a guideline for development of new devices.

Laparoscope optical characterisation

Conventional systems for minimally invasive surgery are generally optimised for operation in the visible part of the spectrum. NIR performance of the *illumination* channel has been previously assessed for a number of laparoscopes (Glatz *et al.*, 2013). However, no quantitative analyses are available in the literature for the *detection* channel. The approach that was pursued in this chapter allowed absolute measurement of light gathering power (f-number) and optical transmission.

The transmission of the laparoscope was measured 'in reverse', using the eyepiece as the input, as it allowed to use a collimated test beam of practical dimensions[10], in a portion of the system which would conventionally deliver nearly collimated light. Although this arrangement only determines the on-axis transmission, the transmission at larger angles could be inferred when operating the laparoscope in its conventional imaging mode. This

[10] As the exit pupil of the laparoscope is of larger diameter than the entrance pupil, larger beam sizes can be used when the eyepiece is used as the input.

effect was of course indistinguishable from vignetting. The laparoscope imaging channel is equivalent to a system with aperture stop ~f/8.9 and overall light transmission that drops from ~55% in the visible to ~18% at 830 nm. As the f-number depends on the focal length and size of image sensor used, the estimated value is referred to the particular setup used. A similar experimental approach can be followed to determine the f-number in case a different camera and/or laparoscope is used.

The poor NIR transmission is an indication that the imaging channel incorporates several optical components that are not optimised for such wavelengths, probably due to the use of visible-only anti-reflection coatings on the optical surfaces. A number of NIR-optimised laparoscopes are commercially available (e.g., Storz FL series and Novadaq PINPOINT), although their absolute optical performance has not yet been determined.

Experimental validation and cellular sensitivity

Experimental tests to validate the accuracy of the model were also performed. The success of such tests was, of course, strictly dependent on a correct estimation of the parameters values. Results showed that the model was accurate to within ~±10% in describing imaging of deep samples in homogeneous media and when comparing laparoscope and wide-field system performance. Despite the approximations and assumptions in the model, the level of accuracy was proved to be satisfactory for the purposes of a theoretical characterization and quantification of FIGS.

Using realistic imaging and biological parameters, the model estimated that detection of superficial samples containing as few as ~10 cells is feasible during open surgery, although several practical factors may undoubtedly increase this figure. The model also suggests that a laparoscopic system should be capable of detecting ~5000 cells, although lower

numbers can be detected by increasing the excitation power. These numbers are well below the estimated threshold of ~10^6 cells required for angiogenic switch that was presented in §1.1.2. As a result, the findings from the theoretical model confirm that intra-operative fluorescence molecular imaging can have a significant potential to improve detection of microscopic lesions.

3. A new FIGS imaging technology

The theoretical basis of FIGS was shown in the previous chapter, with focus on the potential of FIGS for detecting small clusters of cells, as required in intra-operative molecular imaging. The analytical model presented guides the selection of excitation power, imaging optics and camera sensitivity needed in order to achieve a given fluorescence detection capability.

In this chapter the practical aspects of FIGS will be described, with particular focus on the development of imaging devices that are based on the results of the model. A technological background of FIGS will be presented, which will focus on the main system components such as light sources, delivery systems, imaging optics, filters and detectors. This will be followed by a brief description of existing FIGS devices developed by others, focusing on their practical applications and imaging limitations. In the second part of this chapter, the FIGS technology that was developed in our research group will be introduced and the imaging devices that were designed based on this technology will be described. As the development of such devices required complementary expertise present in our research group, only the aspects in which I was more actively involved will be discussed in more detail. These included device development, testing, optimisation and improvements.

3.1 Background on FIGS imaging systems

The clinical translation of fluorescence imaging is guided primarily by the development of effective contrast agents and sensitive imaging devices. As recently suggested (Zhu *et al.*,

2014), new targeted agents for human use can be translated in the clinic only when a suitable detection technology is available. For this reason, the development of imaging systems is one of the driving forces towards a successful clinical use of fluorescence imaging.

3.1.1 Overview of the available technologies

The development of devices for FIGS is a process that requires appropriate selection, testing and optimisation of a large number of components. In this section, such components and their relevancy in FIGS will be briefly described.

Light sources

Light sources that are typically used in FIGS instruments can be divided into three main categories: arc lamps, light-emitting diodes (LED) and lasers. Arc lamps are the most common light sources in medical applications due to their high optical power output and broad emission spectrum, making them an ideal illumination source for keyhole surgery. However, they have a short lifespan and low optical efficiency, are difficult to control and thus require a mechanical shutter for fast on/off switching. Moreover, their large radiant area and angle of emission result in exceptionally high étendue. Because étendue must be conserved (see Appendix IV), only a small fraction of light from an arc lamp can be collected and coupled to a light delivery system.

LEDs have recently emerged as an alternative source of white light illumination and fluorescence excitation in FIGS (Gioux *et al.*, 2009). Despite their lower optical output, LEDs can be more effectively coupled to a given illumination system because of their lower étendue compared to arc lamps. In addition, LEDs can also be used as excitation

sources because of their availability at most wavelengths and, in particular, their relatively high spectral radiant flux (≳10 mW/nm).

Finally, laser diodes are optimal light sources for fluorescence excitation because of their exceptionally high spectral radiant flux, that can reach in excess of ~1000 mW/nm in continuous-wave (CW) operation. Moreover, their low étendue in addition to the very narrow spectral bandwidth facilitate both light delivery to the surgical field and fluorescence filtering. Bright-field imaging can also be achieved. Noonan *et. al.* used a supercontinuum fibre laser as a source of white light illumination for a robotic device (Noonan *et al.*, 2009). This had the significant advantage that the same laser source can also be used to provide a range of monochromatic excitation wavelengths.

The main characteristics of these three types of light sources are compared in Table 6.

	Arc lamp	***LED***	***Laser***
Étendue	High	Medium	Low
Spectral radiant flux	~1 mW/nm	~10 mW/nm	~1000 mW/nm
Spectral bandwidth	Broad source	~30-50 nm	<5 nm
Wavelength selection	Selectable	Limited	Limited
Lifespan	~1,000 hrs	>10,000 hrs	~10,000 hrs
Switching speed	Slow	Fast	Fast
Cost	Moderate	Low	High

Table 6: Main properties of light sources used in FIGS.

Although arc lamps are still the gold standard in illumination for medical devices, comparable or superior results can be achieved using LEDs and lasers, as indicated in a recent publication that compared these sources (Clancy *et al.*, 2012).

Light delivery system

Based on the findings from the theoretical model presented in Chapter 2, a FIGS device should be designed to deliver at least ~10 mW/cm^2 of excitation power at the tissue surface. It is rarely possible to deliver light from the source to the tissue without some form of light delivery system. One exception is in endoscopy with LED illumination at the tip (Lee *et al.*, 2009). Although optimal in terms of optical transfer efficiency and illumination geometry, this configuration is not always suitable for FIGS. For example, a distance of ~2-3 m is typically present between the light source and the surgical field in keyhole surgery systems. Here, light is delivered by means of 'light cables' that consist of optical fibre bundles or liquid-filled light guides. Table 7 summarises the main advantages and disadvantages of these two solutions.

	Fibre bundles	***Liquid light guides***
Flexibility	High	Moderate
Autoclavable	Yes	No
Typical light transmission	~75%	~85%
Packing fraction losses	Yes	No
Average life span	3-5 years (limited by bend number)	3 years (limited by bubble formation)

Table 7: Main properties of fibre bundles and liquid light guides for FIGS.

Both light delivery systems rely on the principle of total internal reflection[11] to constrain light to the core(s) and transmit it over large distances. The acceptance angle of light guides depends on the refractive index mismatch between the core and its surrounding layer (cladding) and in most cases it is ~±30 deg. Despite liquid light guides having

[11] Total internal reflection occurs when light strikes the boundary between two media at an angle that is higher than a critical angle given by Snell's law of refraction.

superior transmission, no packing fraction and a more homogeneous light output, fibre bundles are often preferred in keyhole surgery for their greater flexibility and compatibility with sterilisation.

Imaging optics

The type of optical imaging system for FIGS is related to the type of surgical procedure. In open surgery, imaging lenses are used to collect light with required fields of view at sufficiently long working distances to allow surgical access. The light gathering power is controlled by the effective aperture of the optical system. Large apertures allow greater light collection at the expenses of a reduced depth of field.

In keyhole surgery, the inside of the body is visualised using surgical instruments such as laparoscopes. The limited apertures of keyhole surgery systems results in much lower light gathering power compared to that of open surgery systems (see §2.6.1). The relay system used in a classical flexible endoscope uses a coherent optical fibre bundle to transfer the image from the distal to the proximal end of the endoscope. Modern flexible endoscopes, however, do not have a relay system as the camera is located at the tip of the instrument. A rigid endoscope (or laparoscope) uses a system of thick relay lenses (Hopkins, 1966) or gradient-index (GRIN) lenses (Moore, 1980).

Fluorescence filters

Optical filters are necessary in FIGS to reject excitation light while transmitting fluorescence emission. Based on the calculations from the analytical model previously described, when 10^{14} photons/sec/mm^2 (~2.5 mW/cm^2) of excitation light is delivered to a 1 mm^2 sample containing 100 cells, around 10^8 photons/s are emitted. Considering a

worst-case scenario in which all the excitation photons are reflected by specular and diffuse reflectance, the ratio excitation/emission photons that are collected by the imaging system is ~10^6. This result suggests that emission filters with optical densities (OD) greater than 6 must be used in order to separate weak emissions from the more intense excitation signal. Moreover, since Stokes shifts are generally small in organic fluorophores, steep edges are required between transmission and attenuation regions. Interference filters (Hadley & Dennison, 1947) can, in practice, just satisfy these requirements. However, they have the disadvantage that, unlike absorptive glass filters, a high stop-band attenuation is only obtained at narrow angles of incidence (Semrock, 2014). Fluorescence filters can be constructed to perform high pass, low pass, band pass and band stop functions. Of these, the high pass or band pass responses have been traditionally used for detecting fluorescence emission. The use of such filters limits imaging to fluorescence emission spectrum wavelengths. In this work, the use of band stop filters (notch filters) is explored.

Detectors

The most common imaging detectors used in FIGS use charge-coupled devices (CCD) or complementary metal–oxide–semiconductor (CMOS). Although CCDs are still preferred for their lower noise and higher quantum efficiency, CMOS sensors with comparable performance are becoming available. Alternatively, more complex types of detectors such as Electron Multiplying CCD (EMCCD) or Intensified CCD (ICCD) cameras can be used to provide superior signal-to-noise ratio (SNR) (Dussault & Hoess, 2004). However, the typical volume and weight of such cameras make them often impractical for intra-operative use. Bright-field colour information from the surgical field must also be

collected, thus requiring the use of colour cameras, multiple cameras or alternatively monochrome ones with sequential red, green and blue illumination.

3.1.2 Imaging requirements in FIGS

Fluorescence and bright-field imaging

One of the main imaging requirements of a FIGS device is the simultaneous visualisation of fluorescence emission with white reflectance light (i.e. conventional colour imaging). This is a crucial aspect as the surgeon needs to view the distribution of the contrast agent, the morphology of the tissue and the position of the surgical tools, preferably at the same time. Achieving such multi-modality imaging is made possible by the judicious combination of light sources, filters, imaging and detectors that operate together to display a weak fluorescence emission signal superimposed on white reflectance images. To date, a number of solutions have been proposed to solve this problem.

The most common approach is to split the white reflectance from the fluorescence emission and to use at least two cameras to detect independently both channels. In the case of a NIR fluorescence, a dichromatic beam splitter can be used to separate long wavelengths (fluorescence emission) from short wavelengths (white reflectance) (Themelis *et al.*, 2009; Troyan *et al.*, 2009). For fluorescence imaging in the visible, the emission light is not spectrally distinguished from the ‘white light’ field and beam separation can be achieved using neutral beam splitter with uneven division ratio to account for different signal intensities. In such multiple-detectors approaches, a colour camera usually detects strong white light reflectance signals, while a high sensitivity monochrome detects weak fluorescence emission. Filters are required in both channels to block the excitation light and to transmit the desired wavelengths. A fast image processing

unit thresholds the fluorescence image before overlaying it in false-colour (typically lime green) onto the white reflectance images (Glatz *et al.*, 2014). A similar approach has been implemented using a dual imager where the imagers and a beam splitting prism are contained in a single housing (Venugopal *et al.*, 2013).

A single imager can also be used with stacked pixel design whereby blue, green, red and NIR are acquired at different depths in the sensor (Fengler & Westwick, 2009). This of course restricts the range of fluorescence wavelengths to the NIR region only. A further method to achieve a near-concurrent fluorescence and bright-field with a single sensor is obtained by time-multiplexing illumination and excitation while using a filter to block excitation light (Gray *et al.*, 2012). A very high dynamic range sensor and real-time video processing is required for simultaneous display of the two channels, but the short integration times limit the achievable sensitivity.

Multi-spectral fluorescence imaging

The use of multiple fluorescence excitation wavelengths is an attractive feature in FIGS due to the increasing number of spectrally distinguished fluorescence markers that are becoming available for clinical use. In addition, the possibility of colour-coding fluorescence emission from such markers can lead to independent visualisation of multiple structures or biological processes. A solution has been proposed in which two NIR dyes emitting at different wavelengths are separated with a dichroic mirror and independently detected using two separate cameras (Troyan *et al.*, 2009). A false-colour overlay scheme is used to display the signal from the two cameras and distinguish between emissions from two fluorophores. An arrangement in which a single NIR camera with a dual band-pass filter for detection of two emission channels has also been proposed (Ashitate *et al.*, 2012).

Multi-spectral fluorescence in the visible is a more challenging task due to the cross-talk between dye emissions and bright-field illumination. To the best of my knowledge, no FIGS systems that use a single camera for both multi-spectral fluorescence and bright–field imaging are available. This chapter will show how this feature is achieved in our imaging technology.

3.1.3 Imaging sensitivity in FIGS

The performance of a FIGS device is assessed by its ability to detect, with an appropriately high SNR, low volume samples containing a low number of fluorophore molecules (i.e. high spatial resolution and sensitivity). Fluorescence sensitivity, in particular, is a trade-off between several factors summarised in this section.

Sensitivity can be increased by integrating the light reaching the detector over a longer period of time. For surgical safety, however, camera exposure times should be limited to ~100-300 ms to allow real-time surgical navigation. This is particularly crucial during keyhole surgery, where there is no direct access to the surgical field, and the surgeon relies completely on images displayed on a screen.

A crucially important practical issue is that a high depth of field is, in general, required. In the case of endoscopes, flexible or otherwise, a small pupil diameter guarantees a high depth of field. When using a wide-field system, stopping down the lens to a diameter larger than f/4 is problematic with small area sensors due to depth of field reduction at working distances relevant to surgery. This inevitably limits the light gathering power of the optics.

As previously mentioned, large image sensors and cooled cameras increase imaging SNR, but limit the practicality of the system. Imaging noise and resolution can be traded against

each other by applying imaging gain and pixel binning. All such factors have to be considered when developing a FIGS system that is sufficiently sensitive for fluorescence molecular imaging and at the same time practical for clinical translation and intra-operative use. As will be shown later, the technology presented in this work is also a compromise between sensitivity and practicality.

3.1.4 Ergonomics and safety of FIGS systems

For practicality, small and compact FIGS devices that can be hand-held and that interfere minimally with the standard surgical practice are preferred. This is relevant both for keyhole surgery, where endoscopes are conventionally hand-operated, and for open surgery, where small devices can, in principle, be inserted into surgical cavities.

From the safety perspective, an important aspect to consider is the amount of excitation light that can be delivered to the patient without causing damage. The maximum permissible exposure (MPE) given by the light exposure standards (ANSI, 2014a) is 200 mW/cm^2 for 400-700 nm wavelengths. At longer wavelengths the MPE increases (e.g. ~300 mW/cm^2 at 800 nm) because of higher penetration depth and consequent deposition of energy over a larger volume. However, power densities not greater than ~50 mW/cm^2 are recommended due to potential phototoxicity in some fluorophores (Bäumler *et al.*, 1999; Nakayama *et al.*, 2003). This is an important issue to address in keyhole surgery where very short working distances can result in significant power densities at the tissue.

Finally, a FIGS system must also comply with technical standards and regulatory safety for medical electrical equipment. This ensures that it is insensitive to other electrical sources and that it does not itself radiate interference. In the case of a laser light source, laser safety rules must also be considered.

3.1.5 Existing clinical FIGS devices

A large number of fluorescence imaging devices intended for FIGS have been developed by various companies and research groups. Because of poor optimization for surgical use and compliance with regulation, to date only a fraction of these devices have been used clinically. A detailed review of all the existing clinical FIGS devices is reported in Appendix V. The most popular commercially available FIGS devices for open surgery are the Photodynamic Eye (PDE) from Hamamatsu (Furukawa *et al.*, 2010) and the SPY from Novadaq Technologies (Gurtner *et al.*, 2013). The so called 'surgical microscopes' (e.g. Leica FL400 and Zeiss OPMI Pentero) are also very popular FIGS systems that are typically used for 5-aminolevulinic acid fluorescence imaging of malignant gliomas (Stummer *et al.*, 2006). A number of laparoscopic systems intended for FIGS is also available from Storz, Olympus and Novadaq. All these devices are designed to work only with ICG, and are not compatible with other excitation/emission wavelengths.

A number of clinical FIGS devices have also been developed by academic research groups. To my knowledge, only devices for open surgery have been used clinically. The most well-known wide-field imaging systems are the FLARE, developed by the Frangioni's group at Harvard Medical School (USA) (Troyan *et al.*, 2009), and a system developed by the Ntziachristos' group at Technical University of Munich (Germany) (Themelis *et al.*, 2009). More technical information on the technology used in these devices is available in Appendix V. Both systems have been used primarily in the Netherlands for SLN imaging in a variety of cancers (Crane *et al.*, 2011a; Troyan *et al.*, 2009), to visualise the ureters (Verbeek *et al.*, 2013) and to assist detection of ovarian cancer deposits (van Dam *et al.*,

2011). Multiple excitation channels are supported, although most of the clinical studies were performed with ICG.

Limitations of current systems

Commercial systems operate at video-rates and require relatively high fluorophore concentrations. Moreover, the lack of pre-clinical tumour-specific marker data suggests that the sensitivity of these systems might not be adequate for fluorescence molecular imaging (Zhu *et al.*, 2014). This is even more significant for minimally invasive surgery devices because of the increased detection light losses.

Research systems tend to use more sensitive detectors to increase fluorescence sensitivity. For example, the FLARE and Munich systems use separate cameras to detect fluorescence and bright-field images. Despite the advantages in terms of fluorescence SNR, these systems are not compatible with hand-held operation and their use has been limited to open surgery. This is a significant constraint due to the growing interest towards FIGS in minimally invasive surgical procedures. In addition, the popular approach of using a dichroic mirror to split fluorescence emission from white reflectance light limits the usability of the systems to NIR fluorophores only. This is an important drawback, as some of the fluorophores suitable for clinical use are excited in the visible (e.g. FITC and Protoporphyrin IX). Another limitation of multi-camera systems is the need of software to re-combine the fluorescence and bright-field images. As this software has to comply with specific medical device regulations, its development can further hinder clinical translation.

3.2 Development of FIGS technologies: our approach

In this section, the technology designed and developed by our research group for use in imaging devices for FIGS will be described. Given the large variety of surgical procedures that can benefit from intra-operative fluorescence, in contrast to existing systems, our approach focussed on developing a flexible technology that can be integrated with both keyhole surgical devices and customised wide-field systems. Based on this technology, we developed a wide-field imaging system for open surgery and a camera attachment for laparoscopic (keyhole) surgery. Both systems can operate at multiple excitation wavelengths to exploit part of the range of available fluorescence markers. Unlike the multi-spectral systems mentioned in the previous sections, we concentrated on minimising the complexity of the technology to allow simple operation and rapid clinical translation, while maintaining a level of sensitivity suitable for cancer molecular imaging.

3.2.1 Overview of the technology

The surgical field is illuminated with white light for bright-field imaging and monochromatic red or NIR wavelengths for fluorescence imaging. White light from a bright LED and red-NIR light from multiple laser diodes are combined and delivered through a light guide.

A *single* colour CCD camera is used to provide white-reflectance (colour) and fluorescence images either separately or simultaneously. This is accomplished by using notch filters in the detection channel that match the excitation wavelengths and reject the narrow-band laser lines. Camera sensitivity and LED intensity are synchronously adjusted to ensure visualisation of a typically weak fluorescence emission together with conventional bright-field.

Membrane-operated and foot switches are used to control the devices. No software or PC unit is required for device operation and no image processing is necessary, nor is used. A diagram representing the outline of this technology is shown in Figure 23.

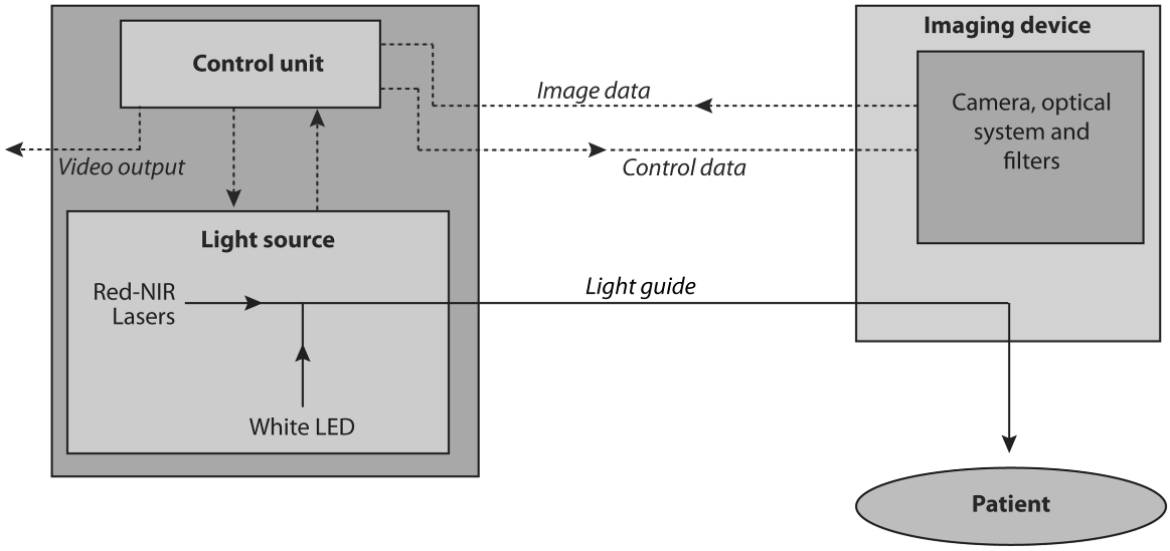

Figure 23: Schematic representation of the FIGS technology described in this work.

3.2.2 Illumination and excitation systems

Because of its higher coupling efficiency and switching speed, an LED source was selected over arc lamps for bright-field illumination. The LED (LZ1-10CW00, LED Engine) operated at a typical maximum forward current of 1 A, producing a luminous flux of 227 lm of cool white light from a 4.4 × 4.4 mm footprint emitter with effective emitting area of ~1.5 × 1.5 mm and ± ~60 deg emission angle. Laser diodes (K66S09F-0.80W and K78S09F-1.60W, BWT-Beijing Ltd.) were used to generate monochromatic excitation in the far red (660 nm) and NIR (785 nm) wavelengths. These wavelengths were optimal for excitation of the clinically approved dyes methylene blue (MB) and indocyanine green (ICG) (Figure 24). A secondary reason was the availability of high-power laser diodes and off-the-shelf narrow-band laser rejection filters at these wavelengths.

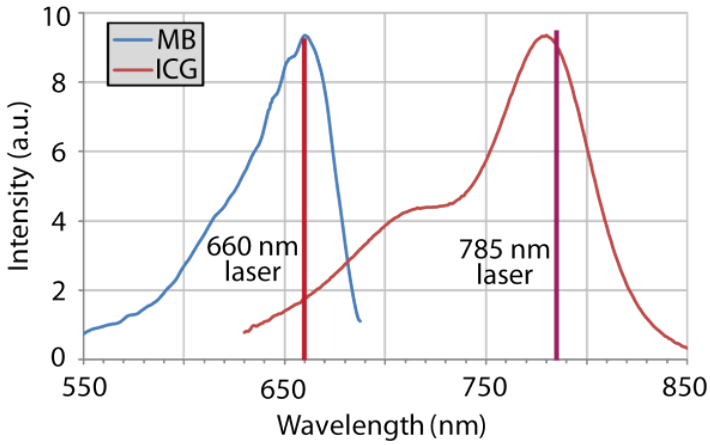

Figure 24: Excitation spectra of MB and ICG and laser lines used in the technology. Dyes were diluted in distilled water at a concentration of ~100 µM. Spectroscopic measurements were performed using a spectrophotometer (8453, Hewlett Packard).

The laser modules were mounted on Eurocard printed circuit boards with custom-made driver and thermoelectric cooling (Vojnovic, 2011), as shown in Figure 25. Laser light is emitted from a 100 µm core diameter multimode optical fibre with ~ 0.15 – 0.2 NA. The optical power in CW mode was measured to be 800 mW and 1600 mW for the 660 nm and 785 nm laser respectively.

Because of significant differences in the étendue of the lasers and of the LED, the laser fibre NA was first increased to ~0.3, using a pair of aspheric lenses (focal lengths of 15 mm and 11 mm) and injected into a multimode 300 µm diameter optical fibre (Figure 25). A significant advantage of this design is that spurious emissions from the laser can be eliminated by placing specific 'clean-up' filters in the infinity space between the pair of lenses[12]. The design allowed combining up to 7 × 300 µm laser fibres into an array of 1

[12] Although semiconductor laser sources are considered to be monochromatic, there is a weak, broad emission around the peak emission, due to LED action within the laser chip.

mm diameter. Details on the development of this fibre bundle are described in Appendix VI.

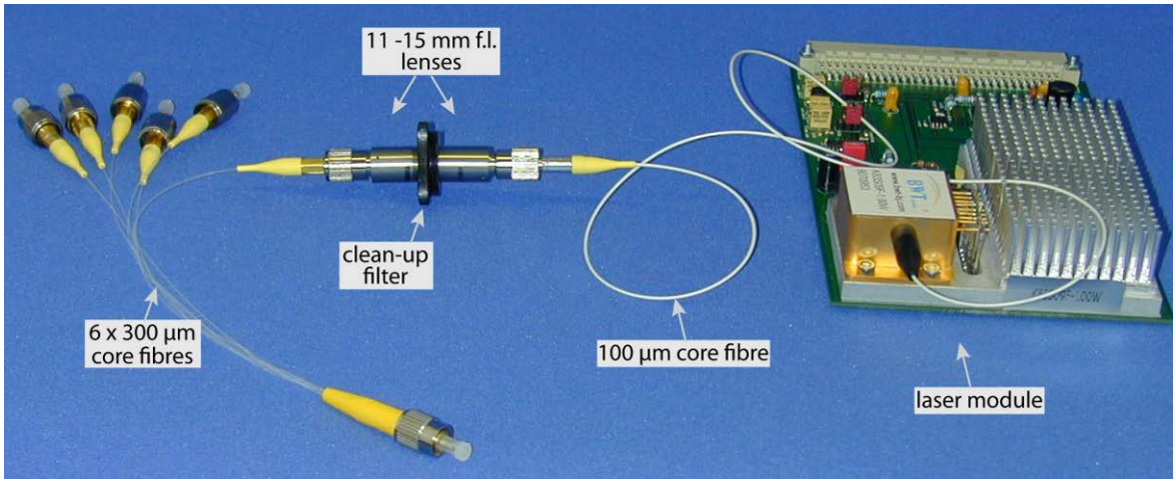

Figure 25: Laser source and delivery system. Custom-made laser module and optical arrangement used to combine up to 7 laser fibres (although only 6 are shown) into one fibre connector.

Excitation and illumination sources were combined and delivered to the output guide through a customised optical arrangement that was first modelled using optical ray tracing software (Optic Lab, Science Lab Software), as shown in Figure 26.

A dichromatic beam-splitter (FF649-Di01, Semrock) was used to combine visible light from the LED with far red – NIR light from the combined laser fibres. An NIR-coated 40 mm focal length lens (NT48-769, Edmund Optics) and a polymer collimation optic and holder (FA10784_LE1-RS, Ledil) were used to collimate laser and LED light respectively, as required for beam combination with a dichromatic mirror. A pair of visible-NIR coated lenses (NT45-508-INK and NT49-784-INK, Edmund Optics) was used to focus the combined illumination/excitation beam to a spot with ~0.5 NA, launched into the light guide.

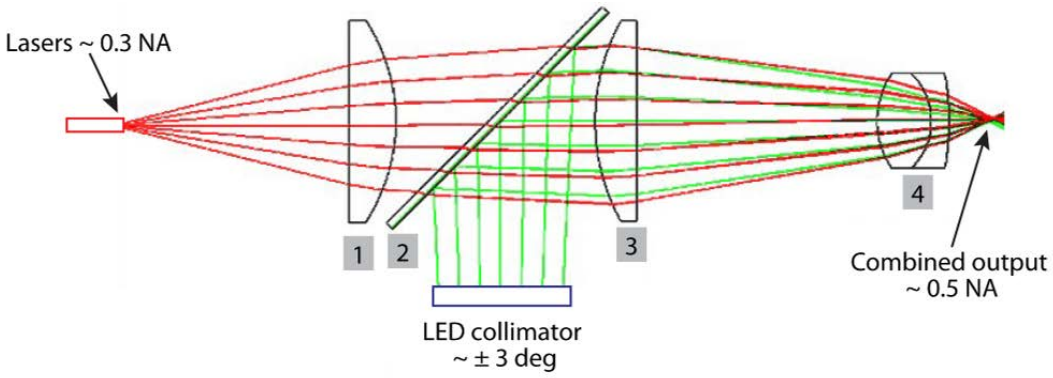

Figure 26: Ray tracing modelling of light combination and delivery. 1: plano-convex lens, 40 mm focal length; 2: dichromatic mirror; 3: plano-convex lens, 50 mm focal length; 4: achromatic lens, 15 mm focal length.

3.2.3 Fluorescence filtering technique and imaging

The proposed technology used high optical density (OD ~6) narrow-band notch filters to reject laser excitation wavelengths while allowing simultaneous imaging of white reflectance (shorter wavelengths) and fluorescence emission (longer wavelengths). Another advantage of this setup is that several filters can be placed in series for rejection of multiple laser lines. Two filters (NF03-658E-25 and NF03-785E-25, Semrock) were used in the detection channel to block 660 nm (~647-672 nm band) and 785 nm (~767-800 nm band) excitation wavelengths respectively. Figure 27 shows the spectral characteristics of the output light (illumination and excitation) overlaid on the filters' response.

The main disadvantage of using an interference type of filter, as mentioned, is that correct filtering is achieved only with incident angles <5 deg. Although ideal for keyhole surgical systems in which near-collimated light is produced from the eyepiece, this constrains the design of a wide-field imaging system in terms of aperture size and field of view.

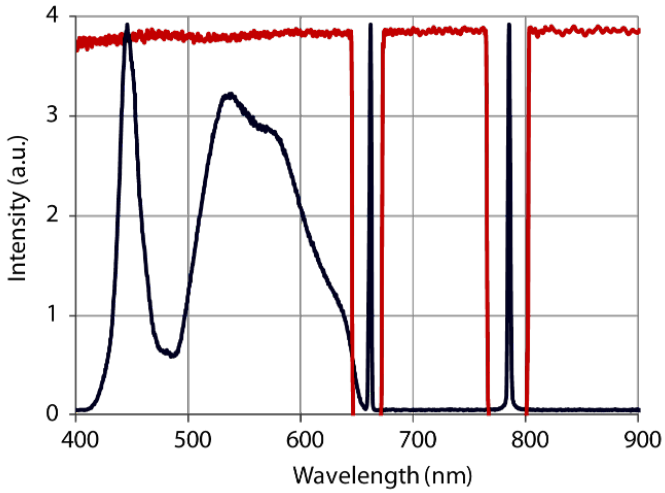

Figure 27: System output light and filters response spectra. Combined illumination and excitation spectra are shown in blue; spectral response of two notch filters is shown in red. The blue spectrum was obtained by summing heavily attenuated individual laser outputs (OD 4) with the LED illumination spectrum.

Laser clean-up filters

The laser blocking efficiency of the notch filters was tested using spectroscopic measurements in a four-light-port cuvette holder (CVH100, Thorlabs). The two laser sources (660 and 785 nm) described above were used at 75% their maximum output power. Light from the 100 µm laser fibre was collimated using an 18 mm focal length fibre collimating lens (F280FC-B, Thorlabs) and delivered to a 4 ml cuvette containing a 10% milk solution, again in order to simulate highly scattering biological tissue. The collimated beam size did not exceed the linear size of the cuvette, ensuring that all the light was delivered to the milk solution. The notch filter and the spectrometer fibre collected light from an adjacent port at 90 deg, collecting scattered light only. A pair of 1 mm diameter apertures was placed before the notch filter to ensure transmission of collimated light. Filtered light was detected using a 600 µm diameter multimode optical fibre (FT600EMT, Thorlabs) connected to a calibrated USB-controlled spectrometer (HR2000, Ocean

Optics). Spectra were collected before and after adding a clean-up filter between the laser collimating lens and the cuvette. The experiment was repeated for the 660 and 785 nm laser. Figure 28A shows an image and a diagram of the experimental setup. The tests were conducted in the dark to eliminate contributions from external light sources.

Figure 28B shows spectroscopic measurements in the 660 nm channel, suggesting that a clean-up filter is necessary to remove out-of-band excitation components and reduce the background signal. A comparable improvement was also observed at 785 nm, but the wings were not as pronounced due to the wider 785 nm band-stop region.

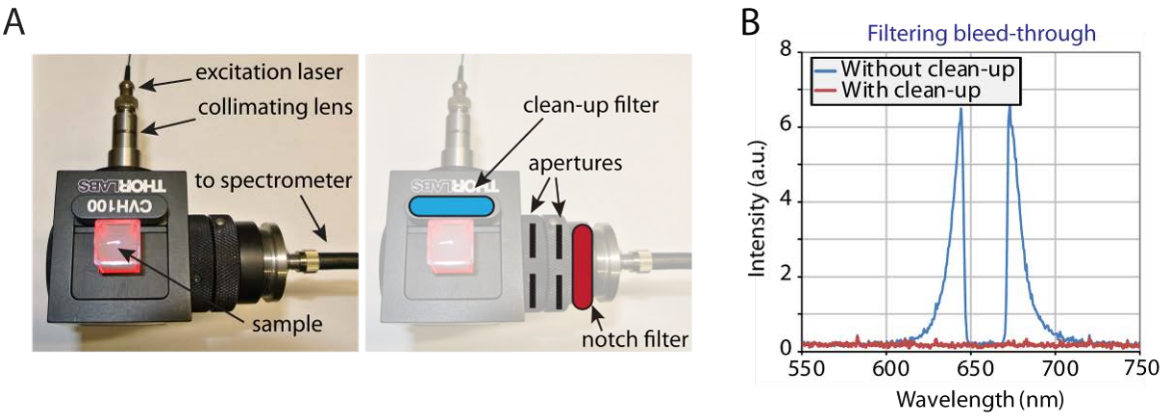

Figure 28: Laser clean-up filters performance testing. (A) Experimental setup showing the milk solution in a four-light-port cuvette holder. (B) Spectroscopic measurement of 660 nm laser light bleeding through the notch filter with and without the clean-up filter.

3.2.4 Detection

A miniature 1/3” image sensor format CCD colour camera (XC505P, Sony) was chosen as the optimal imager for this technology (Figure 29A). To ensure NIR sensitivity, the sensor’s short-pass filter was removed and replaced with a 450-1000 nm anti-reflection coated window of equivalent dimensions. The camera uses a Sony Super HAD CCD II ™

sensor[13] with on-chip microlenses to achieve a high level of sensitivity. It provides interlaced video (PAL standard) and allows integration of several seconds, if required. The camera electronic gain and integration time are manually controlled and adjusted depending on the intensity of the fluorescence signal. Camera control is performed through serial communication interface (RS232). The main characteristics of the camera, as provided by the manufacturer, are listed in Figure 29A.

Camera responsivity

The camera relative spectral responsivity was assessed by comparing its performance with a well-characterised scientific-grade camera. A monochrome 2/3" CCD camera (Orca-ER, Hamamatsu) with 1344 × 1024 effective pixels of size 6.45 × 6.45 µm was used for this comparison. A picture of the camera and its main characteristics are shown in Figure 29B.

The spectral response of the two cameras was compared by mounting each camera on a dual-port microscope (Eclipse E600FN, Nikon), set up for Köhler illumination. A standard 100W DC-powered filament lamp provided illumination. The imaged sample consisted of an aluminium foil placed between a microscope slide and a coverslip. The position of the foil was adjusted to occupy half of the coverslip. The sample was imaged using a 20× objective such that ~30% of the field of view was occupied by the aluminium foil. This allowed focussing of the foil edge. Absorption band-pass filters (FKB-VIS-40 kit, Thorlabs) were mounted between the light source and the condenser to select 40 nm wide spectral regions ranging from 400 to 850 nm.

[13] http://www.sony.net/Products/SC-HP/datasheet/01/data/E08Z22D9Z.pdf

A

Image sensor	Sony ICX639BKA 1/3″
Number of effective pixels	752 x 582
Pixel size	6.50 µm x 6.25 µm
Signal to noise ratio	46 dB (1:200)
Bit depth	8 bit
Dimensions (H x W x D)	22 x 22 x 64 mm
Weight	51 g

B

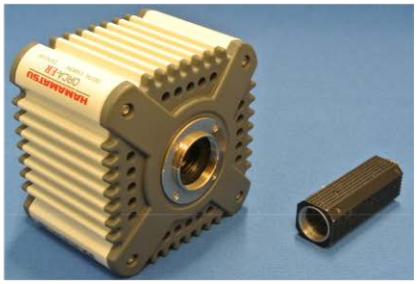

Image sensor	ER-150 CCD 2/3″
Number of effective pixels	1344 x 1024
Pixel size	6.45 µm x 6.45 µm
Dynamic range	1:3000
Full well capacity	18,000 e^-
Bit depth	12 bit
Dimensions (H x W x D)	95 x 95 x 75 mm
Weight	1300 g

Figure 29: CCD cameras specifications. (A) Sony XC505P camera used in this work. (B) The Orca-ER camera next to the Sony one and specifications of the Orca-ER.

A region of interest (ROI) equivalent to the field of view in the case of a 1/3” sensor was selected using a customised camera control software interface. The similarity in the pixel dimensions (6.45 × 6.45 µm *vs*. 6.50 × 6.25 µm) allowed accurate comparison between the Orca and the Sony cameras. Imaging was performed with both cameras set to 10 ms exposure time and minimum electronic gain. The images were corrected by subtracting a ‘black’ frame (light off and same exposure time). The mean signal was calculated by selecting a region in the bright portion of the image (i.e. where the foil is not present) corresponding to 200 × 200 pixels. At each selected wavelength, the experiment was repeated for different illumination levels to improve the statistical significance of the results.

Figure 30 shows the variation of the ratio between the average signal in the ROI generated by the Sony and the Orca as a function of wavelength. Since the ORCA is back-illuminated, it is more responsive in the blue and not very responsive in the NIR. It is

important to note that these results refer to the output signal only, and that the SNR (superior, as expected, for the Orca camera) was not considered in this comparison. Results suggest that the ICX639BKA sensor used in the Sony camera has high responsivity, particularly in the NIR (Vojnovic, 2012a).

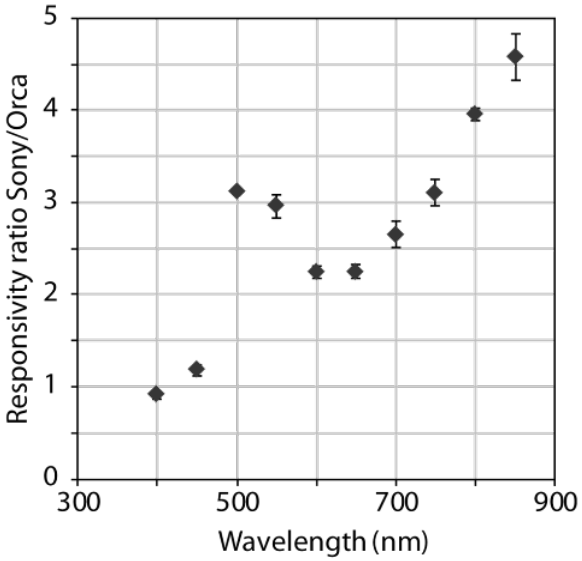

Figure 30: Sony camera evaluation results. Relative responsivity ratio indicating the mean signal of the Sony divided by the mean signal of the Orca as a function of wavelength. Error bars refer to the standard deviation of two measurements acquired at different illumination light levels.

3.3 Wide-field imaging system

In this section, the development and testing of the FIGS wide-field imaging device will be described. This system comprises two parts: a control unit that includes the light sources and the device head. The system was optimised for use during open surgical procedures.

3.3.1 Control unit

The control unit consists of a 4U, 63HP steel case (360 × 330 × 190 mm) that includes a combination of commercial and in-house developed printed circuit boards and various

optical/mechanical assemblies (Figure 31). The NIR laser sources are constructed on standard Eurocard boards (100 × 160 mm) and housed in the control unit. Space for up to six NIR sources (wavelength > 650 nm), of similar or different wavelengths, is provided. All the laser fibres are combined in a single fibre bundle for common output, as previously described. The white LED for illumination is also housed on a Eurocard board which is included in an optical assembly that contains the lenses and dichromatic mirror to combine visible with NIR light. The operation of the system is controlled by a processor board through an internal Inter-Integrated Circuit bus (I^2C bus). External access to the processor is provided, if required, through a USB 2.0 interface. A second board is dedicated for video processing. Here the camera video signal is used to control the illumination intensity of the LED light through on-board digital-to-analogue converters. This maintains a constant camera output signal under white light illumination by varying the light intensity as a result of changes in device's working distance and/or tissue reflectance.

The front part of the unit houses a customised optical/electrical connector and a panel of membrane-operated switches for device control (Figure 31B). The connector socket is recessed to make it accessible only to the imaging devices' plug. A safety switch adjacent to the connector is used to disable all the light sources at any time during operation. A key switch is also used to enable/disable the lasers. The control panel membrane switches allow the user to select excitation wavelengths and to set the camera sensitivity during fluorescence. The rear part of the control unit (Figure 31C) houses sockets for the foot switches (used to toggle between fluorescence and bright-field mode), external video connection, auxiliary outputs and power connection. As the device outputs a video signal, a video-to-USB converter module (DFG/USB2propcb, the Imaging Source) is included to provide, if required, USB image data to an external PC/laptop.

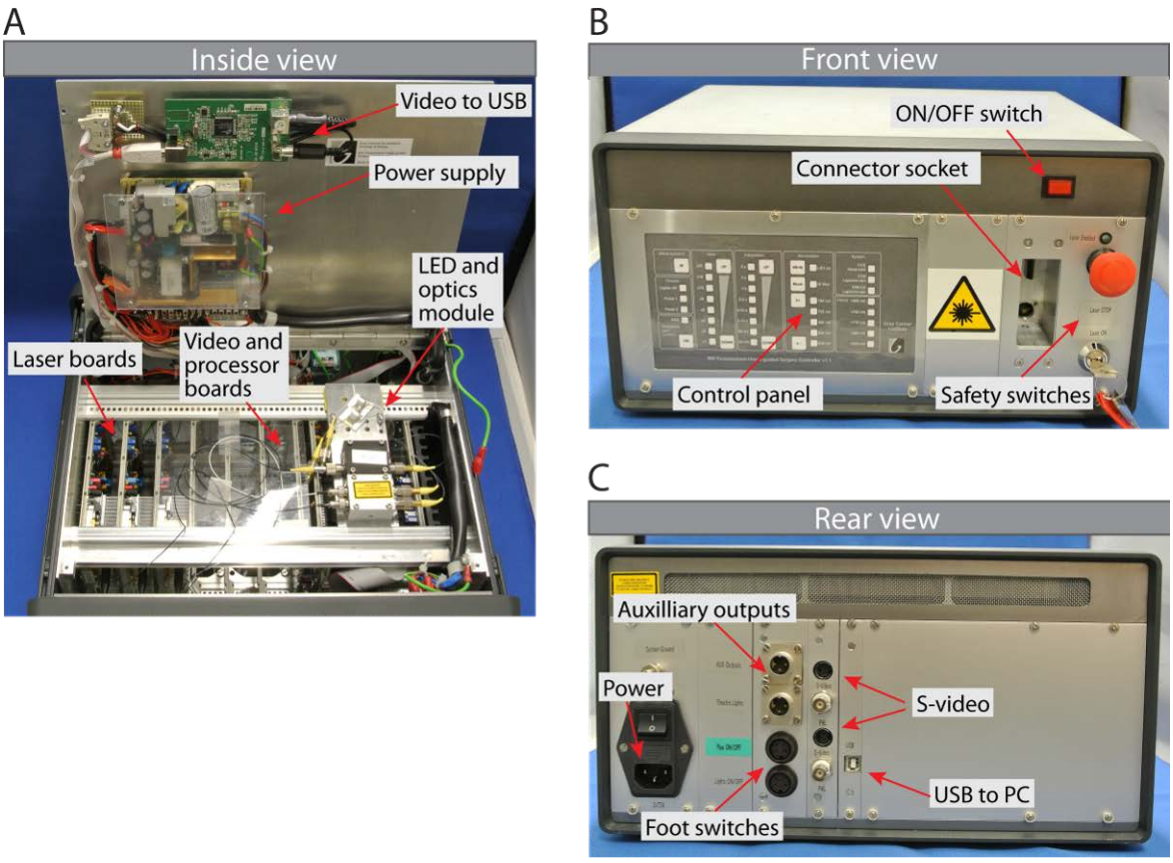

Figure 31: System control unit. (A) Open view, (B) front view and (C) rear view.

3.3.2 Imaging head: design and development

The imaging head was designed with consideration for practical dimensions appropriate for hand-held operation during open surgery. Light is delivered from the optical output port of the control unit to the imaging head using a 2 m long, 3 mm core diameter liquid light guide (77567, Newport), designed for high throughput of both visible and NIR light. Imaging is performed by a 25 mm focal length imaging lens (NT67-715, Edmund Optics) in conjunction with the 1/3” CCD described. Although capable of operating at lower f-numbers for higher sensitivity, the aperture is set to f/5.6 to ensure sufficient depth of field, as required by non-flat surgical fields. A DC motor is used to rotate the lens focus ring to allow manual focus control during operation. The notch filters are placed in a

custom-made tube screwed on the front of the lens barrel. As the narrow angle of view (~±6 deg) is not compatible with the cone of light that is produced from the light guide (~±30 deg), a pair of lenses (NT63-663 and NT49-917, Edmund Optics) is used to reduce the NA from ~0.5 to ~0.15. Modelling of this optical arrangement with Optics Lab ray tracing software is shown in Figure 32A. A wedge prism (10 deg deviation angle, 10 JW 25, Comar Optics, custom-coated) is used to deviate the reduced-NA light, as required in a system where illumination and imaging are not concentric.

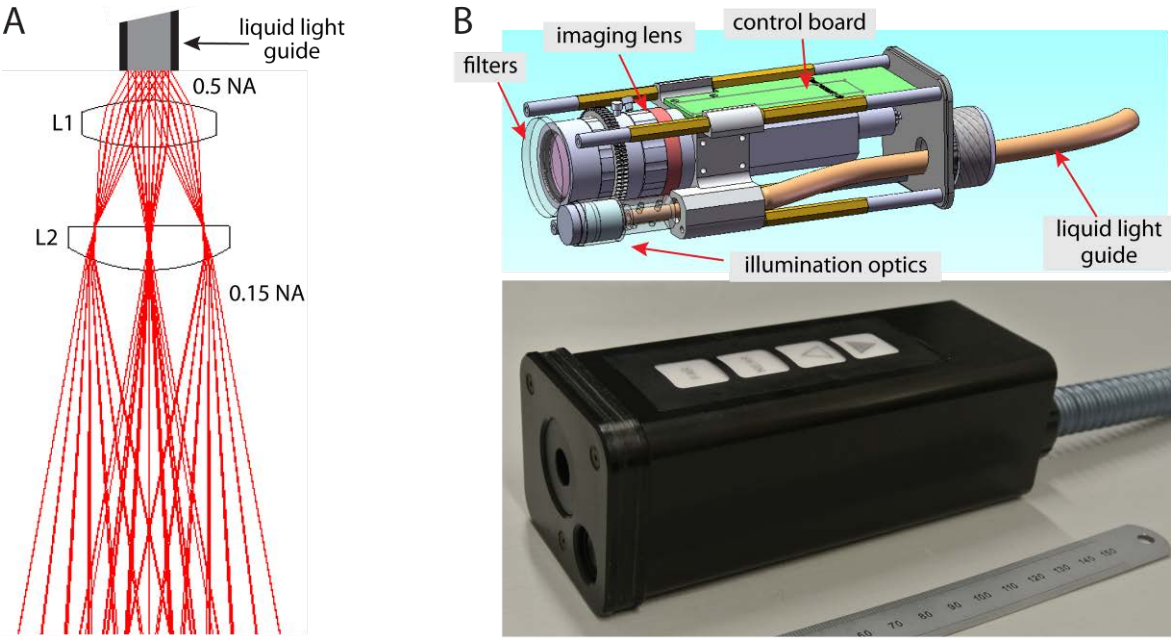

Figure 32: Wide-field device head design and development. (A) Ray tracing modelling of the optical system used to reduce the illumination/excitation NA from the device head. L1: 10 mm focal length, 10 mm diameter lens; L2: 20 mm focal length, 12 mm diameter lens. (B) CAD model and final design of the wide-field imaging system.

The illumination and detection systems are housed in a custom-made polyoxymethylene case measuring 150 × 60 × 50 mm (Figure 32B). The device cannot be sterilised and the size of this case was chosen to fit existing camera drapes conventionally used in the clinic. A visible-NIR anti-reflection coated window (40 GJ 03, Comar Optics) is placed on the

front face of the case to protect the filters and to form a flat end suitable for routine cleaning. The top side of the case includes a panel of membrane switches used to operate the motor for manual focus control (near and far) and to increase/decrease camera sensitivity during fluorescence imaging.

A custom-made connector with a 2 m long, 16 mm diameter flexible conduit is used to optically and electrically connect the device head to the control unit (Figure 33A). The wide-field imaging system plugged into the control unit is shown in Figure 33B.

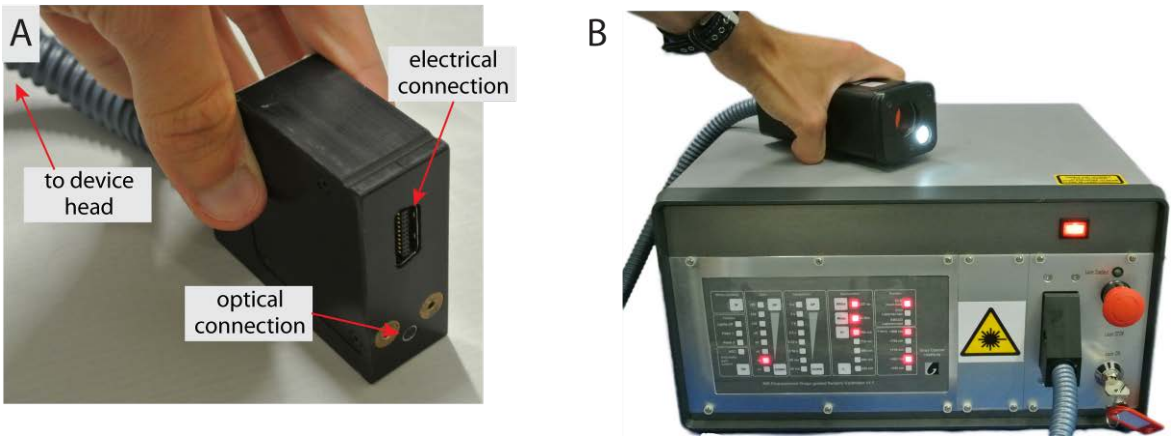

Figure 33: Wide-field imaging system development. (A) Custom-made device connector for optical and electrical connection to the control unit. (B) Wide-field imaging system energised and plugged in the control unit.

3.3.3 Testing

Device operation

The wide-field imaging system generated a diagonal field of view of ~120 mm at a typical working distance of 350 mm (Figure 34A). At the same distance, it delivered up to 2 mW/cm^2 of white light illumination and 3-7 mW/cm^2 of 660 nm and 785 nm excitation (Figure 34A). These values refer to the use of a single laser per wavelength. Higher power can be achieved by adding more lasers (up to 6 in total).

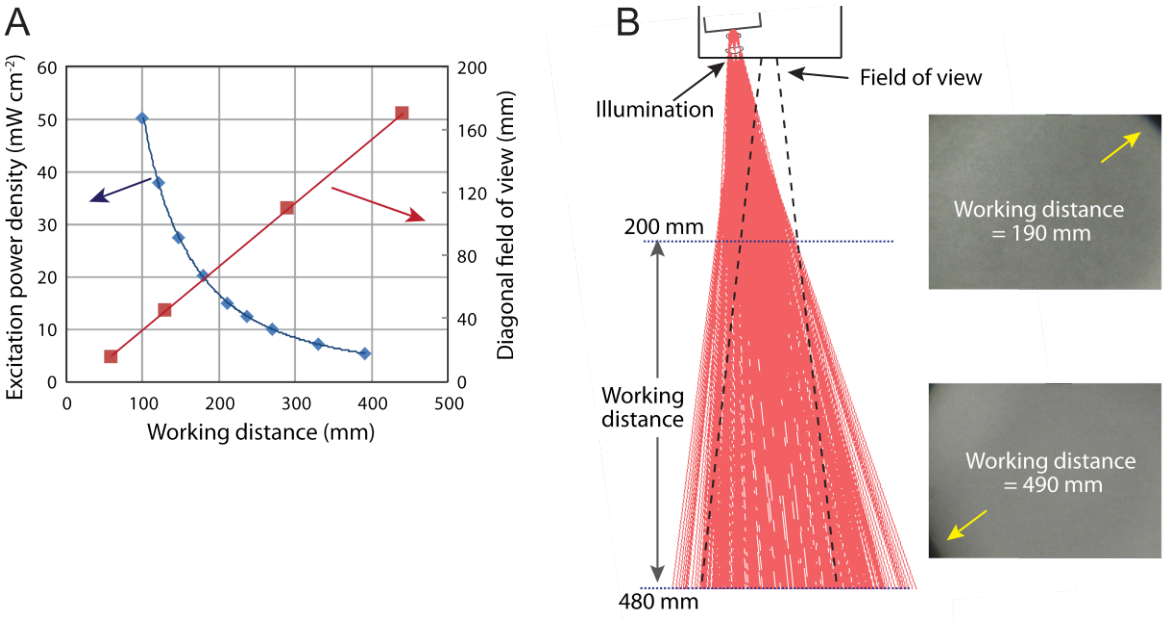

Figure 34: Wide-field device illumination and excitation testing. (A) 785 nm laser excitation power density and diagonal field of view of the wide-field device as a function of working distance. (B) Geometry of illumination showing working distance limits for even illumination. The two images represent the uneven corner illumination (yellow arrows) at two working distances outside the 200-480 mm range.

Flat illumination is provided for working distances ranging from 200 to 480 mm due to the tilt angle of the illumination beam (Figure 34B). Shorter and longer distances are supported but result in somewhat uneven illumination. This was demonstrated by imaging a flat Lambertian surface at 190 mm and 490 mm working distance. As expected, results show uneven corner illumination when the system is used at such working distances (yellow arrows in Figure 34B).

The ability of the system to simultaneously detect white reflectance and fluorescence was tested using ICG dye. Figure 35 shows imaging results of a sample of 100 nM of ICG in a capillary tube (inner diameter 500 µm) and a colour chart (87-423, Edmund Optics). The intensity of the fluorescence signal changed with camera sensitivity, while the white

reflectance signal was maintained constant by automatic adjustment of LED current. The laser excitation power was not affected by changes in camera sensitivity.

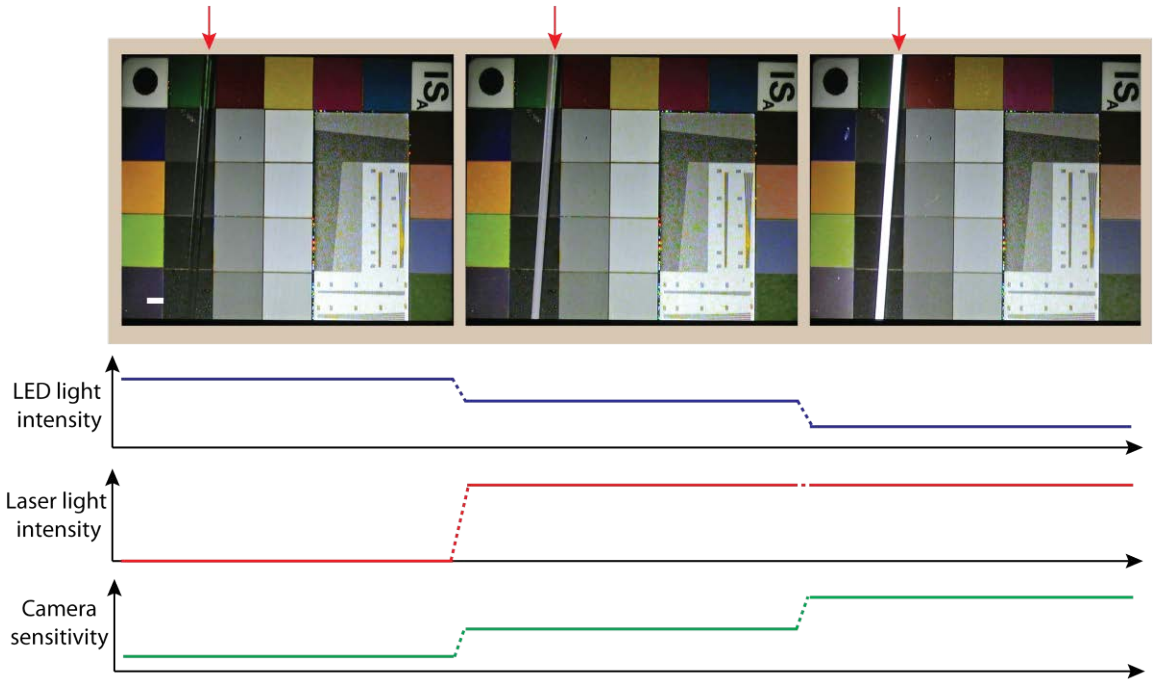

Figure 35: Wide-field system operation modes. Bright-field only (left) and simultaneous bright-field and fluorescence imaging (centre and right) of a colour chart and ICG solution in a capillary tube (indicated with the red arrows). Working distance: 200 mm. Scalebar: 2 mm. A diagram shows the corresponding variation of LED and laser intensity and camera sensitivity. Note that this graph is for qualitative representation only and that the vertical scales are not linear.

Filtering optimisation

Despite the relatively small field of view and aperture chosen to ensure optimal rejection by the filter, a small amount of laser excitation bleed-through was observed during the first practical tests. Spectroscopic measurements and the use of a second rejection filter to double the overall OD confirmed that this bleed-through was due to in-band laser wavelengths leaking through the imaging filters at larger angles. This effect was

particularly evident when imaging high-scattering solutions at close working distances, suggesting that diffusely reflected light was not fully blocked by the notch filter.

An improvement in the laser rejection efficiency was attempted by placing a customised 10 mm aperture in front of the imaging channel in order to prevent scattered light from getting through the filters at great angles (Figure 36A). The size of this aperture was selected such that the light gathering power of the f/5.6-set imaging lens was not affected.

The usefulness of the aperture was tested by imaging a solution of MB fluorescence dye in a scattering medium and exciting using the 660 nm laser channel. The scattering medium was prepared by diluting 10% milk in distilled water and placed in a 100 mm diameter Petri dish. The imaging device was set at a working distance of 200 mm from the surface of the medium to ensure that its field of view did not exceed the size of the Petri dish. The same milk solution was used as solvent to prepare a solution of 3 nM of MB in a 4 ml cuvette. This cuvette was placed vertically at the field of view centre, simulating a possible imaging scenario in which a low-concentration fluorescence sample is surrounded by highly scattering media. A schematic of the experimental setup is shown in Figure 36B. A black reference object was also placed on the surface of the milk solution in the imager field of view.

White reflectance images and fluorescence images were acquired before and after adding the aperture at exposure times of 4 ms and 320 ms respectively. A combined image was also acquired at 320 ms exposure (Figure 36C). Despite no obvious differences in the white reflectance images, fluorescence and combined images showed improved contrast between the MB solution and the black object. Two regions of interest (ROI) of ~10,000 pixels corresponding to the MB sample and the reference object were considered for the

fluorescence images (Figure 36C). The mean and standard deviation in each ROI were determined using ImageJ software.

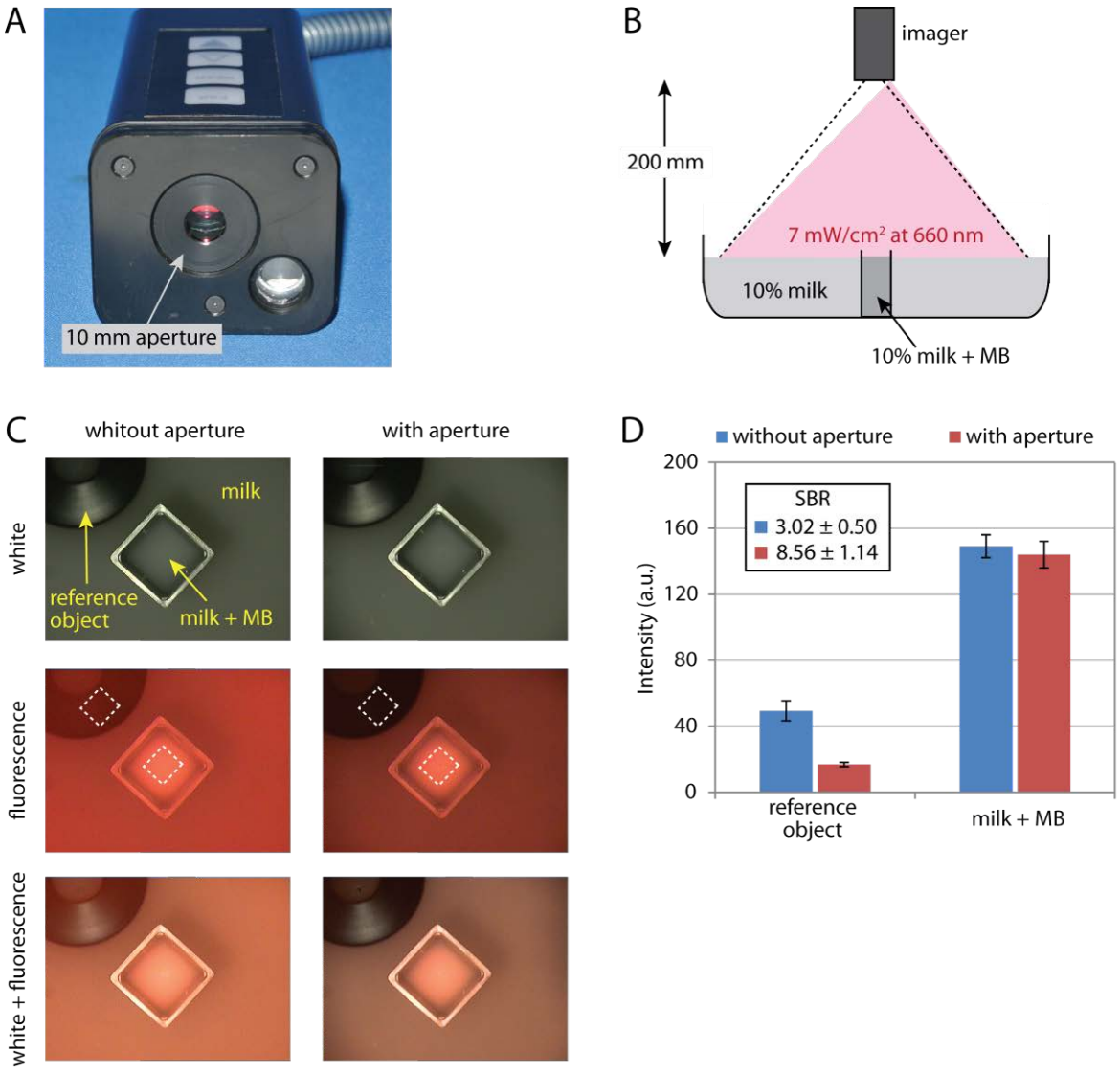

Figure 36: Wide-field imaging system filtering optimisation. (A) Device head with 10 mm diameter front aperture. (B) Schematic of the experimental setup to test the filtering performance with the added aperture. (C) Imaging results showing the effect of the aperture on white reflectance and fluorescence images following 660 nm excitation. (D) Mean signal measured in the ROIs indicated in (C) and results of signal-to-background ratio (inset). Error bars represent the standard deviation of the signal.

Figure 36D shows the results of the image analysis expressed in terms of average signal in the ROIs in the cases with and without the aperture. Signal-to-background ratio (SBR) was calculated by dividing the ROI average signal corresponding to the cuvette by the equivalent one for the reference black object. The SBR at 660 nm excitation improved from 3.02 ± 0.50 with the original design to 8.56 ± 1.14 when the aperture was used. A smaller improvement in the SBR was observed using ICG dye and exciting at 785 nm (results not shown). This was most likely due to the wider stop-band of the 785 nm notch filter. Following these results, the aperture was added to the original design of the wide-field system and placed in front of the entrance window that protects the filters.

Fluorescence detection sensitivity

The fluorescence detection sensitivity of the wide-field imaging system was assessed using samples of MB and ICG diluted in an albumin-enriched physiological salt solution (APSS). This solvent was chosen to simulate practical situations where the dyes bind to albumin proteins of the lymphatic system (i.e. for sentinel lymph node mapping). The procedure to prepare this solution is described in Appendix III. Two ml solutions of MB and ICG ranging from ~100 nM to ~1.5 μM were placed in a multi-well plate (780271, Greiner Bio-One). Imaging was performed at a 350 mm working distance from the top of the plate (without lid) and an exposure time of 40 ms was used. The electronic gain of the camera was set to its minimum. The average fluorescence signal was estimated over ROIs of 50 × 50 pixels. Image analysis was performed using ImageJ. The average fluorescence signal expressed in pixel intensity levels is shown in Figure 37. Results show detection linearity over the range of dilutions and the ability of detecting nano-molar concentrations in real time.

Longer exposures and greater camera sensitivity can of course be used to achieve higher fluorescence detection limits. Further dye dilutions were performed to assess the minimum detectable concentrations at a given signal-to-noise ratio (SNR). The SNR was calculated by dividing the average signal from the fluorescent sample by the standard deviation of the signal in a control well (APSS only). The same size of ROI as in the previous test was considered. In this case, imaging was performed at 200 mm working distance, 320 ms exposure time and maximum electronic gain (10×). Concentrations as low as ~130 pM for ICG and ~300 pM for MB were detected with SNR ~4 (12 dB), suggesting high fluorescence sensitivity of the device in near-real time.

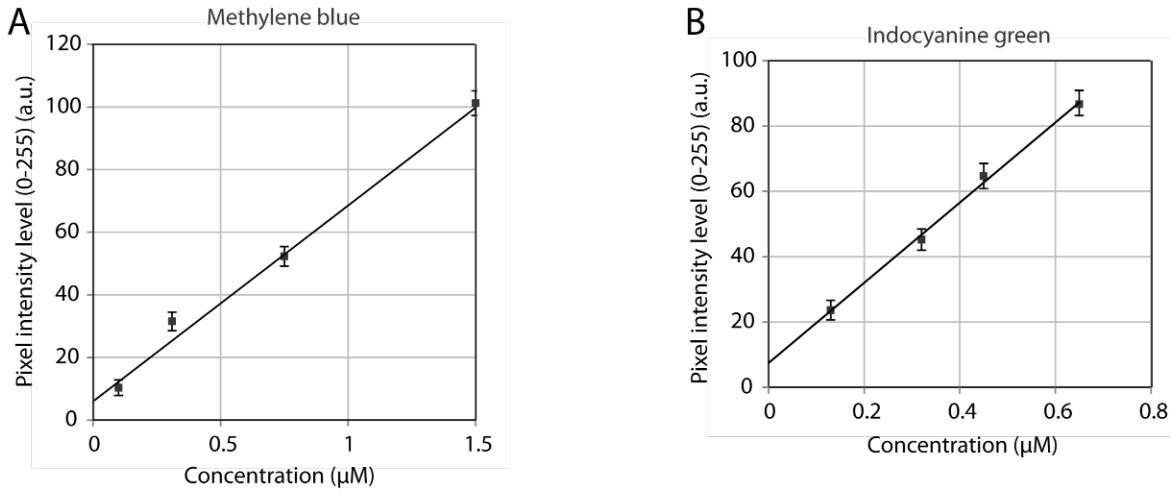

Figure 37: Wide-field imaging system fluorescence sensitivity. Results are shown for different concentrations of MB (A) and ICG (B) solutions. Exposure time: 40 ms.

3.4 Laparoscopic imaging system

The same novel FIGS technology can also be used in conjunction with devices for keyhole surgery. In this section, the development and testing of an imaging device for intra-operative fluorescence during keyhole surgery using conventional rigid laparoscopes is described.

The Storz Hopkins II 10 mm diameter laparoscope described in §2.6.1 was mainly used in this work. During conventional laparoscopy, a colour camera equipped with a lens is used to collect and display in real time light emerging from the eyepiece. As internal body cavities need to be illuminated, the light is provided using optical fibres that deliver light from the input port of the laparoscope to its distal end. The illumination fibres are arranged to surround the imaging channel or to be adjacent to it. The output light is emitted with a maximum NA of ~0.6, equivalent to ~±37 degrees.

The optical transmission through the imaging channel was determined to be poor in the NIR, as described in §2.6.1. Optical transmission through the illumination channel of the laparoscope was assessed by using collimated light at different wavelengths. This transmission was found to be independent of wavelength, over the range 532 nm - 830 nm but varied with laparoscope model. Testing of two nominally identical Storz laparoscopes (i.e. with the same part number) revealed that the transmission varied between ~31% and ~37%. It is probable that even larger variations exist from device-to-device, resulting from a combination of manufacturing tolerances and sterilization history. The substantial light losses in the illumination and imaging channels suggest that a high level of optimisation is required when integrating conventional laparoscopes into a FIGS system.

3.4.1 Design and development

The laparoscopic imaging system was designed to be attached, similarly to a conventional laparoscope camera, to the eyepiece of the instrument. Light output from the eyepiece was collected using a 25 mm focal length imaging lens (NT67-715, Edmund Optics) and focussed on the 1/3” image sensor of the Sony XC505P camera. Although a 25 mm focal length provided the largest field of view when used with 1/3” image format, longer focal

lengths can also be used to increase the overall image magnification. Most commercial systems use a 27 mm focal length lens for such imaging, but this was not available to us with an achromatic visible-NIR performance, while the 25 mm lens we used was relatively achromatic. Narrow-band laser rejection filters were again placed between the eyepiece and the imaging lens. Figure 38 shows a schematic of the imaging system used at the output of the eyepiece.

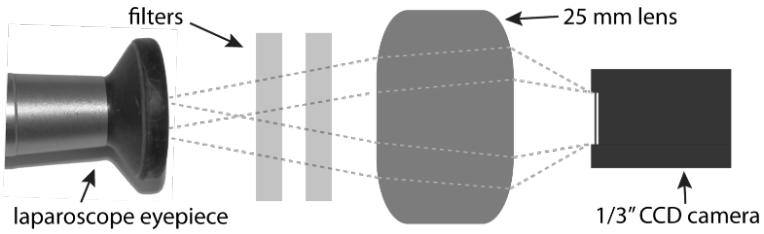

Figure 38: Schematic representation of the FIGS laparoscopic system.

The ability of the filters to reject excitation light is dependent, as previously mentioned, on the maximum incidence angle of light emerging from the eyepiece. This angle was calculated by measuring the dimensions of the image beam produced by the eyepiece as a function of the distance from the laparoscope eyepiece. For this purpose, the laparoscope tip was placed at a typical working distance of 100 mm from a Lambertian surface of area greater than the laparoscope field of view. The output beam from the eyepiece, representing the imaged field, was observed by projecting it on a white sheet of paper and its diameter measured using a ruler.

Figure 39 shows the increase of the radius of this output beam as a function of distance from the laparoscope eyepiece, which corresponds to a maximum divergence angle of ~6.6 degrees. This angle proved to be sufficiently low for correct filtering of the excitation light. With the lens used at its maximum aperture (f/1.4), the distance between the eyepiece and the edge of the lens barrel was limited to ~45 mm in order to avoid image vignetting.

This was demonstrated by imaging a colour chart with the 25 mm, f/1.4 lens placed at (1) 15 mm, (2) 45 mm and (3) 55 mm distance from the laparoscope eyepiece (Figure 39). In the case of images (1) and (2), the dark edges are caused by uneven illumination and image fall-off due to the cosine-fourth law. In image (3) the dark edges are primarily due to image vignetting as the entrance pupil of the lens is not sufficiently large to capture light from the edges of the object plane.

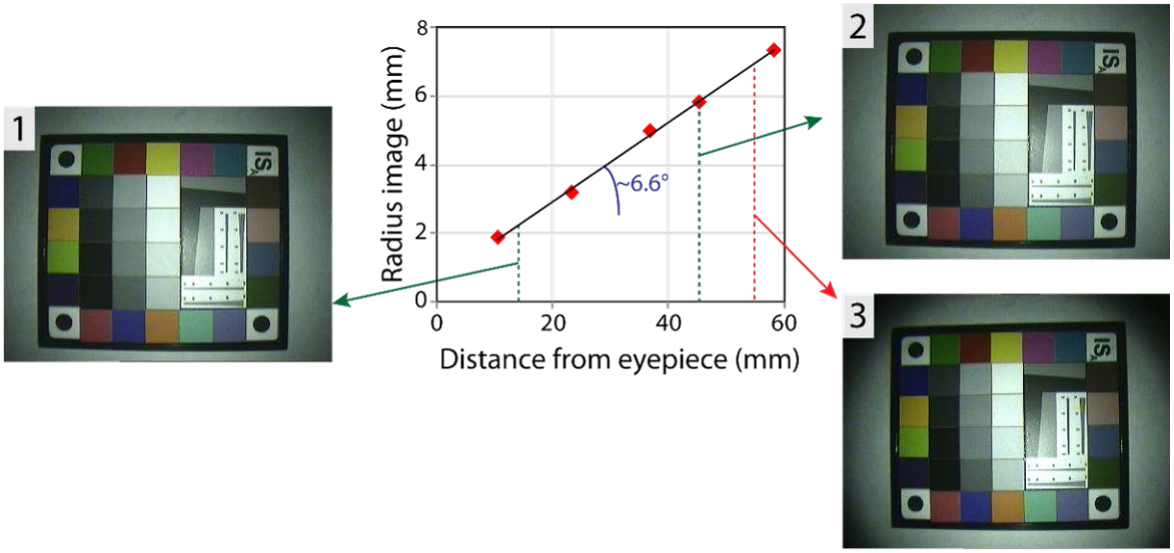

Figure 39: Imaging field size as a function of distance from the laparoscope eyepiece. The three images show a colour chart illuminated with white LED light from the laparoscope. The chart was imaged with the 25 mm focal length imaging lens placed at 15 mm (image 1), 45 mm (image 2) and 55 mm (image 3) distance from the laparoscope eyepiece.

A customised eyepiece clamp was manufactured, leaving sufficient space to house up to 5 filters (each in a 3.5 mm thick holder) in front of the 25 mm lens. A 181 mm long, 38 mm diameter case was developed to house the camera, the lens and the filters. Polyoxymethylene was used as material to minimise weight while maintaining adequate rigidity. The case was equipped with an external ring to allow manual focus control of the lens, similar to that provided in standard cameras. Figure 40A-B show model and final

design of the camera attachment. As for the wide-field system, the device was connected to the control unit through an optical-electrical custom-made connector (Figure 40C).

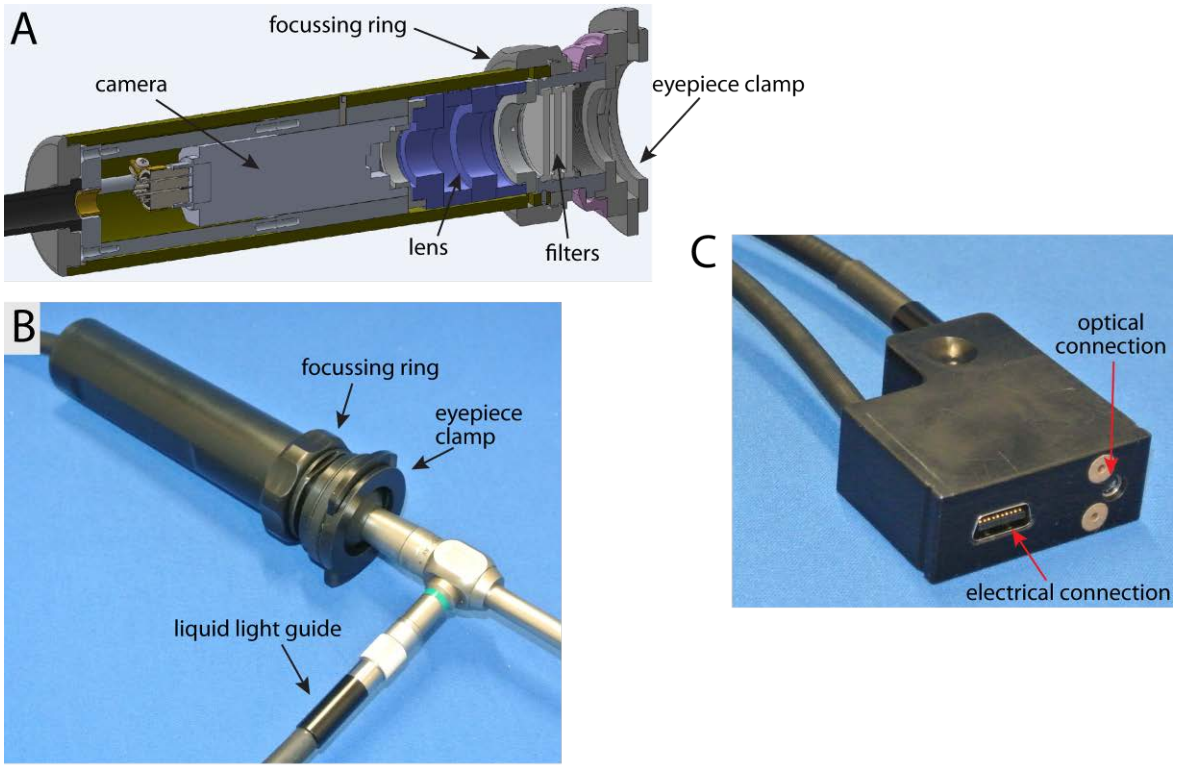

Figure 40: Design and development of the FIGS laparoscopic system. (A) CAD model and (B) final design of the camera attachment. (C) Electrical-optical connector that is plugged in the same control unit as for the wide-field.

A liquid light guide (LLG20.530, Ultrafine Technology Ltd.) was used to deliver illumination and excitation light to the laparoscope. This allowed beam homogenisation and superior light throughput compared to that possible with optical fibre bundles (~85% *vs.* ~78% transmission). However, as the liquid light guide cannot be sterilised, a sterile drape was needed to cover the cable.

3.4.2 Laparoscopic system testing

The output power of the laparoscopic system was measured using a digital power meter (Gentec DUO, Gentec-EO). When the system operated with 2 × 785 nm lasers, the total power output from the laparoscope was measured to be ~620 mW. This resulted in ~10 mW/cm^2 of excitation power density at a typical working distance of 100 mm. At this distance, the diagonal field of view was measured to be ~135 mm. Figure 41A shows both 785 nm excitation power density and diagonal field of view as a function of working distance measured from the tip of the laparoscope.

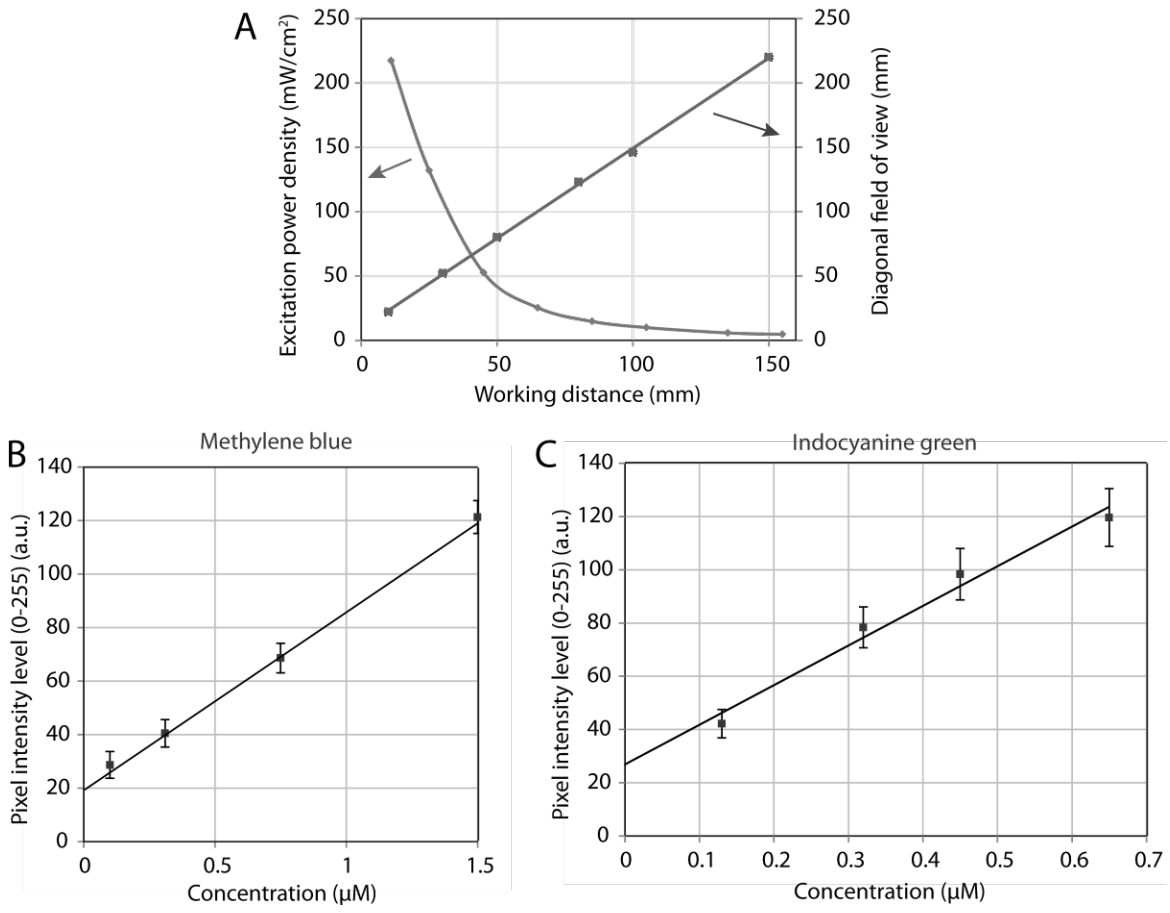

Figure 41: Laparoscopic system testing. (A) 785 nm excitation power density and diagonal FOV as a function of working distance of the laparoscope. Camera pixel counts as a function of MB (B) and ICG (C) concentration. Exposure time: 40 ms; electronic gain: 10×; working distance: 100 mm.

The total output power from the laparoscope in the case of 1 × 660 nm laser was ~150 mW, although higher values could be achieved by adding more lasers.

Fluorescence sensitivity was again tested by imaging MB and ICG samples, but at a working distance of 100 mm. The exposure time of the camera was set to 40 ms for real-time imaging and maximum electronic gain (10×) was used. The same dilutions in APSS as for the previous experiment with the wide-field system were performed (§3.3.3). Figure 41B-C shows the average fluorescence signal at a given range of dilutions of MB and ICG, suggesting that nano-molar sensitivity could be obtained with the laparoscope, in real time. When the camera is used at 500 ms exposure time, the lowest detectable concentration with SNR=3 (9.5 dB) was measured to be 260 pM and 600 pM for ICG and MB respectively.

3.4.3 Laparoscopic system: future developments

One of the main issues of the laparoscopic system described here (as with other laparoscopes) is the uneven brightness profile, due to a contribution of bell-shaped illumination and imaging sensitivity fall-off due to the cosine-fourth law (Hecht, 1998). This is particularly evident in the configuration using a 25 mm focal length lens that maximised the laparoscope field of view on a 1/3” sensor.

The possibility of improving the field flatness was tested by modelling bright-field imaging using longer focal length lenses. A white-reflectance image was acquired using the laparoscopic system as described earlier (which uses a 25 mm focal length lens), with the instrument placed orthogonal to a Lambertian surface at 100 mm distance. Images using 29 mm and 31 mm focal length lenses were modelled and compared to images acquired with the 25 mm lens. Figure 42 shows the bright-field modelling images when

the 3 lenses are used and the corresponding diagonal profiles. As expected, results suggest improvements in the image flatness when longer focal length lenses are used.

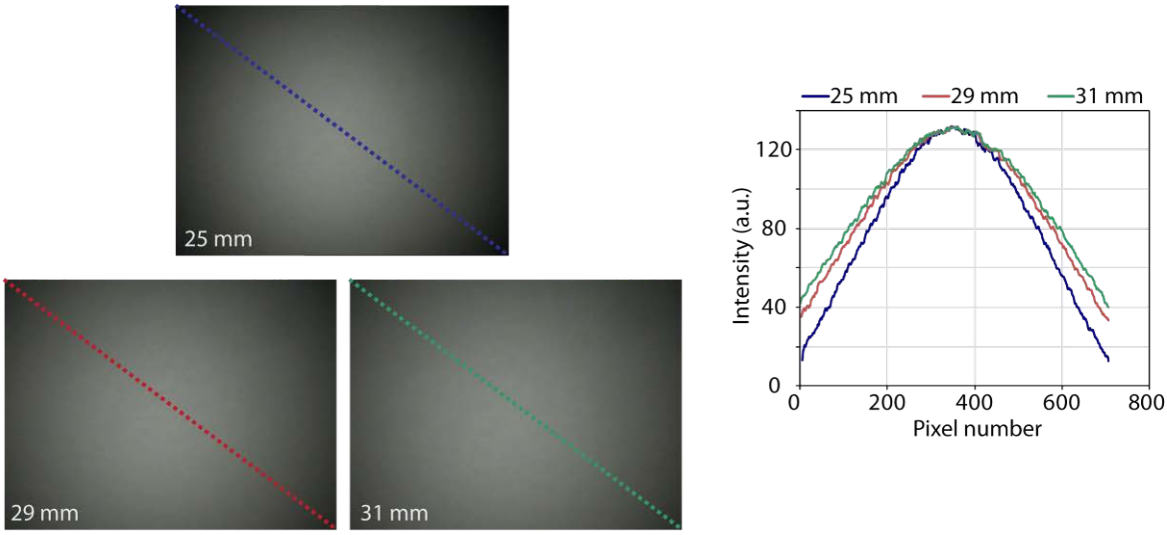

Figure 42: Laparoscope field flatness testing. Illumination field using the 25 mm imaging lens (top) at the output of the eyepiece. Simulated fields using 29 mm and 31 mm focal length lenses (bottom). The graph shows the profiles along the images diagonals.

The focal length, however, has to be limited as small field of views are not always practical in laparoscopy. Most importantly, narrower field of views result in longer working distances required in order to generate the same image. This has important consequences for fluorescence imaging as the excitation power density at the target decreases dramatically with distance (Figure 41A).

Another potential development of the laparoscopic system will consist in exploring the possibility of implementing a zoom system, as already available in conventional laparoscopes.

3.5 Focus-tuneable wide-field imaging system

Despite being successfully used clinically, as will be shown in Chapter 4, the performance of the wide-field imaging system described in §3.3 was limited by several factors. As the illumination was not equally distributed around the detection channel, the field of view was evenly illuminated only over a range of working distances. In addition, the current unit used a relatively large motor to control the lens focus, making further miniaturisation awkward. Lastly, focussing using this motor proved to be rather slow, particularly during rapid changes of working distance.

3.5.1 Electrically focus-tuneable lens

We tried to overcome the limitation of focussing with conventional lenses by exploring the possibility of using electrically focus-tuneable lenses (Ren *et al.*, 2006). Such lenses are constructed using a thin polymer membrane that separates two chambers filled with optical fluid and air. By providing current to a solenoid, the pressure difference between the two chambers changes and consequently the membrane bends (Figure 43A). When no current is applied the membrane is almost flat, resulting in long focal lengths. As the current is increased, the radius of curvature (and consequently the focal length) of the lens decreases. The electrically focus-tuneable lens that was used in this work is the Optotune EL-10-30-VIS-LD (83-921, Edmund Optics). This is a plano-convex lens with an outer diameter of 30 mm and clear aperture[14] of 10 mm. The lens operates at 5 V DC with a control current ranging from 0 (+140 mm focal length) to 300 mA (+45 mm focal length). A customised driver designed to accurately regulate output current was developed for testing the lens

[14] The diameter of the clear aperture in such type of lens is limited aberration caused by gravity.

(Vojnovic, 2012b). The lens and the customised driver are shown in Figure 43B. The optical transmission of the lens in the wavelengths of interest (visible-NIR) was assessed by shining collimated laser light normally to the lens and measuring the current in a photodiode at the input and output of the lens. Transmission ranged from ~95% in the visible to ~88% in the NIR (830 nm) (Figure 43C).

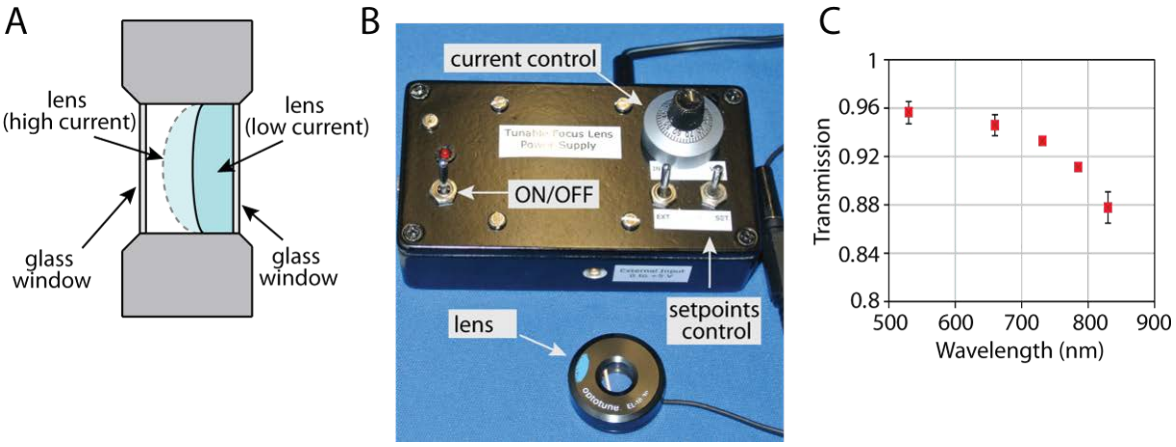

Figure 43: Fluid focus-tuneable lens. (A) Schematics of the lens. (B) Focus-tuneable lens used in this work and custom-made lens driver. (C) Measured spectral transmission of the lens.

3.5.2 Optical system design

Because of its operation at focal lengths longer than required, the focus-tuneable lens is not suitable as a single element for a wide-field device in FIGS. This lens was thus used as one element in an optical system, where it provided focus control in an arrangement where the physical space between all the optical components is kept constant. Figure 44 shows a diagram of this arrangement. The focus-tuneable lens (L2) was used in conjunction with a 60 mm focal length achromatic lens (L3) (49954, Edmund Optics) to produce an equivalent focal length range of ~ +25 to +40 mm. This lens pair was placed at a given distance from a 25 mm imaging lens (L1) (NT67-715, Edmund Optics) such that light collected and focussed by the imaging lens is re-collimated by the lens pair. This

configuration allowed placing the notch filters required for laser rejection in the collimated light path. A second 25 mm lens (L4) (NT67-715, Edmund Optics) focussed the filtered light on a 1/3" format imager. Since the focus of the 25 mm objective lens L1 is set to a fixed position, objects at different distances from the lens (shown in blue and red in Figure 44) are focussed on different virtual image planes located at given distances from the back of the lens. By selecting the right focal length of the focus-tuneable lens, light from a specific image plane of the objective lens is collected and collimated by the pair tuneable-achromatic lens. When the second 25 mm imaging lens focuses the light on the image sensor, the final result is that the focus of the optical system can be controlled by varying the current on the focus-tuneable lens. The position of the lenses can be arranged to generate a focal range between infinity and ~30 mm, although working distances < 100 mm would be excluded as not practical in FIGS.

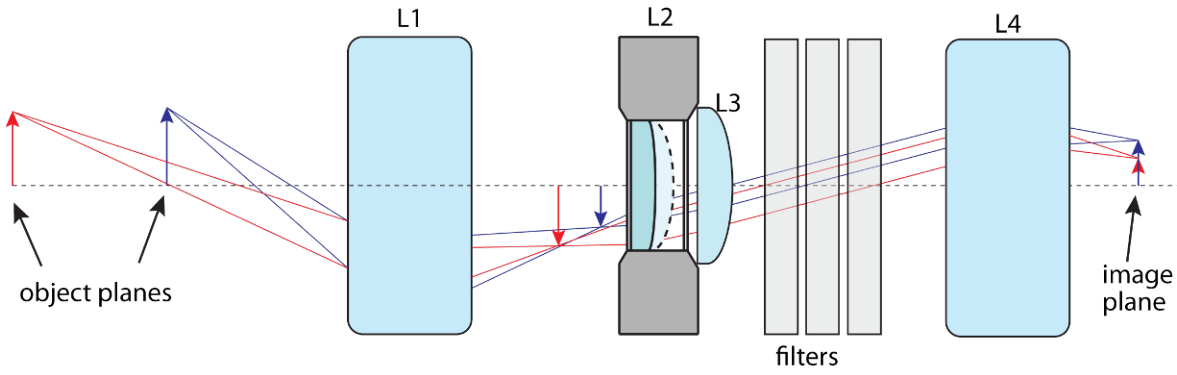

Figure 44: Schematic representation of the focus-tuneable optical system. By adjusting the current at the focus-tuneable lens (indicated as L2), the system allowed to focus at a range of working distances (red and blue optical paths).

3.5.3 Optical system testing

The proposed optical system was tested using the same 1/3” CCD Sony camera as the wide-field system described previously (§3.3). The current to the focus-tuneable lens was manually adjusted to vary the focus of the imaging system with working distance.

Figure 45A shows the current required and the resultant field of view as a function of working distance (measured from the end of the objective lens). A typical field of view of ~120 mm is produced at a working distance of 300 mm with the lens operating at ~60 mA.

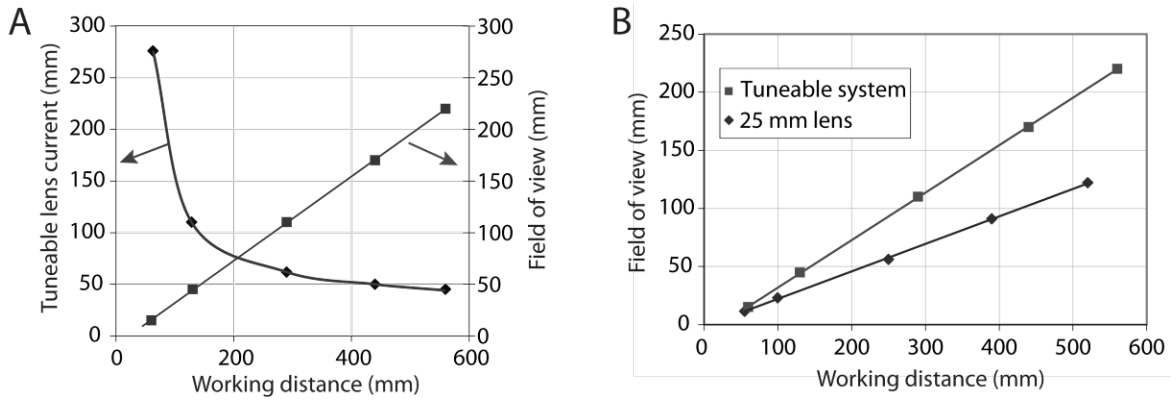

Figure 45: Focus-tuneable system testing. (A) Focus-tuneable lens operating current and system field of view as a function of working distance. (B) Field of view comparison between the focus-tuneable wide-field system (red) and the conventional one described in §3.3 (blue).

When compared with the conventional use of the 25 mm imaging lens on a 1/3” image sensor, as for the previous wide-field system, the field of view increased more rapidly as a function of working distance (Figure 45B). This desirable effect is due to variations in the dimensions of the image plane of the objective lens as a function of object plane distance from the lens. The focus-tuneable system therefore behaves as a 25 mm focal length system with sensor size dynamically changing from ~1/3” at short working distances to ~2/3” at long working distances. At a typical working distance of 300 mm, the diagonal field of view increases from ~70 mm to ~120 mm, despite the fact that the same image

sensor and objective lens were used. This has important consequences in FIGS, since the conventional configuration restricts the field of view to that determined by the filters' acceptance angle.

Aperture stop

The aperture stop of this optical system was controlled by placing an aperture between the tuneable-achromatic lens pair and the filters. Although the aperture stop is placed in the infinity space of the system, its optimal position varies with overall focal length. Nevertheless, this variation is small and its diameter was empirically set to 4.5 mm, making the system operate with light gathering power equivalent to the f/5.6 wide-field system previously described. In addition, this aperture significantly improved the achromatic performance of the system, as shown in Figure 46A. In this test, a resolution target (EIA-1956 Resolution Video Test Chart) was illuminated with visible light from a white LED and NIR light from an 830 nm LED. Images were acquired before and after adding the 4.5 mm aperture to the system. The camera sensitivity was adjusted to generate a comparable signal in both cases.

Bright-field and fluorescence testing

The focus-tuneable optical system was compared to the wide-field system described in §3.3 and its performance assessed during bright-field and fluorescence imaging. A colour chart (87-423, Edmund Optics) and two vials containing 2 ml of ICG (right) and MB (left) were used as a target. Both dyes were used as 1 μM solutions in distilled water. The working distances of the two systems (380 mm for the conventional wide-field and 250 mm for the focus-tuneable device) were set to achieve the same field of view. The comparison was performed under the same lighting conditions. White reflectance imaging

at 4 ms exposure time showed no significant image quality differences between the conventional and the focus-tuneable systems (Figure 46B).

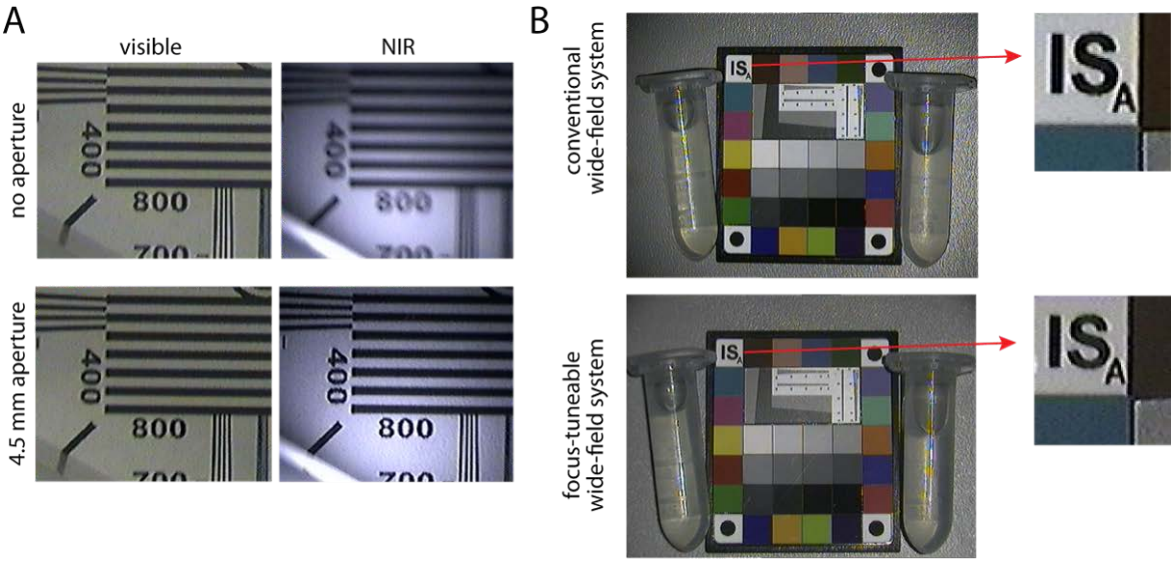

Figure 46: Focus-tuneable system imaging performance. (A) Visible and NIR (830 nm) imaging with and without the 4.5 mm aperture showing improvement in the achromatic performance of the focus-tuneable system. (B) White reflectance imaging with the conventional (top) and focus-tuneable (bottom) systems showing comparable imaging performance.

Simultaneous fluorescence and bright-field images acquired at 80 ms exposure time are shown in Figure 47A for 785 nm (left) and 660 nm (right) excitation light. The fluorescence emission signal was quantified by imaging the same object without white light illumination and selecting 70 × 70 pixels ROIs corresponding to the vials. The results, shown in Figure 47B, suggest comparable detection sensitivity for MB but ~7% lower sensitivity of the focus-tuneable system for ICG fluorescence emission. This difference is compatible with the lower NIR transmission relative to the visible that was measured for the fluid lens (see Figure 43C).

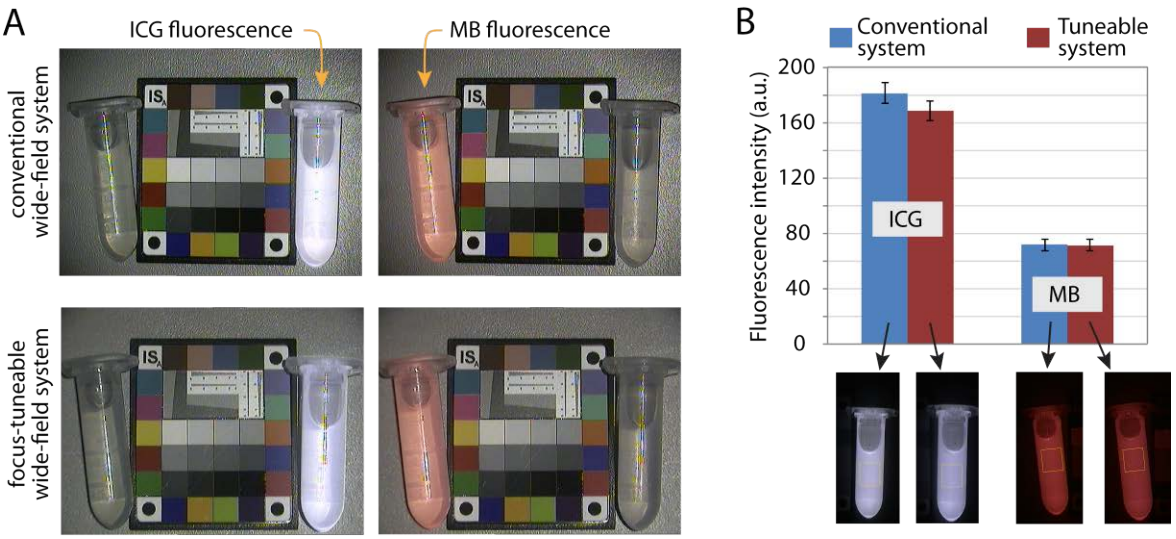

Figure 47: Focus-tuneable system fluorescence performance. (A) Simultaneous bright-field and fluorescence imaging with the conventional (top) and focus-tuneable (bottom) systems. (B) Quantification of the fluorescence signal from ICG and MB for the two systems.

3.5.4 Illumination system design

Based on the experience from the previous wide-field FIGS device, a design was developed for an illumination system that was concentrically distributed around the imaging channel. A multi-furcated fibre optic bundle was designed and assembled. This collects light from a light guide and splits it into multiple sources around the imaging channel (Figure 48A). Polymethyl methacrylate (PMMA) fibres were used because of their low cost, high acceptance NA (~0.5) and simplicity in polishing and terminating. Due to poorer transmission in the far red – NIR, relative to the visible (Schubert, 2006), the length of the fibre bundle was limited to ~300 mm. At one end of the bundle, 28 × 0.5 mm diameter fibres were tightly packed in a 3 mm diameter custom-made brass ferrule. When placed against the surface of a 3 mm core diameter liquid light guide, this resulted in a packing fraction of ~78%. At the distal end, the fibres were arranged to form 4 bundles of

7 fibres each, packed in a hexagonal pattern in 1.5 mm diameter brass ferrules. The procedure for manufacturing the fibre bundle is described in Appendix VI.

As the fibres operated at ~0.5 NA and the required illumination cone has a ~0.2 NA, each output bundle was fitted with a lens to reduce the angular extent of the beam. It was considered desirable to reduce the diameter of this lens as much as possible. One way to do this is to place dielectric material between the lens and the fibre, effectively reducing the fibre NA at the expense of spherical aberration. A 5 mm diameter, 4.6 mm focal length lens (32-403, Edmund Optics) was preceded by a 3 mm thick layer of acrylic and placed in contact with the output fibre bundle. The illumination beam from the lens had the required ~0.2 NA. Flat illumination over the working distance range of interest (~100-400 mm) was achieved by tilting the 0.2 NA illumination beam from each port. The optimal tilting angle was modelled using 3D CAD software and determined to be ~6 deg (Figure 48B).

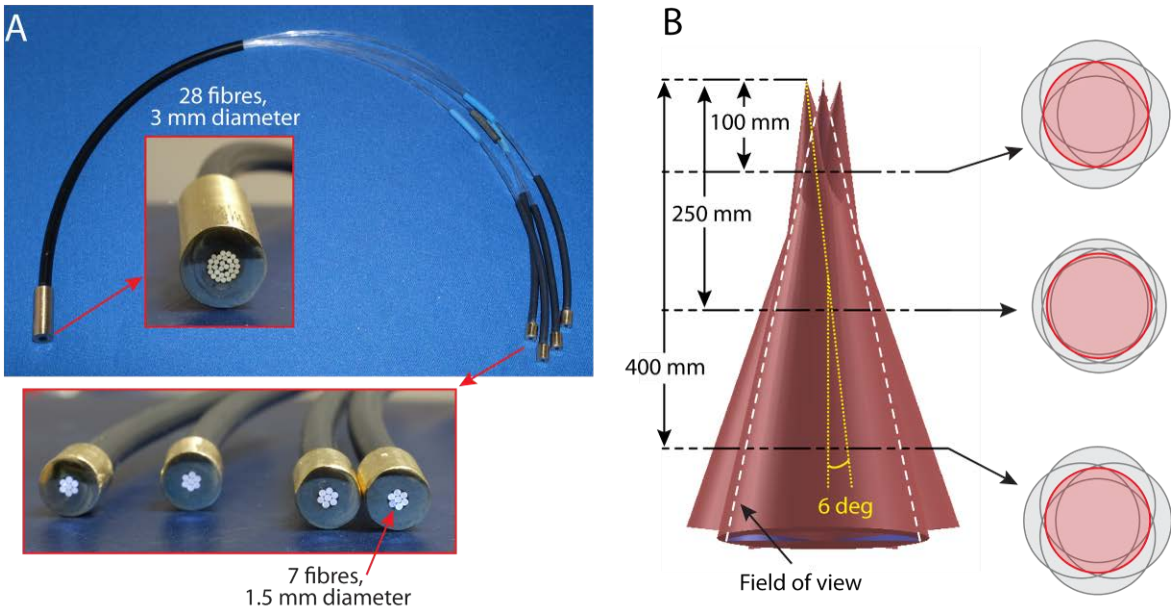

Figure 48: Custom-made fibre optic bundle (A) and required illumination (B). CAD modelling in (B) shows the cones of light from the fibres and the wide-field focus-tuneable system FOV. Cross sections at different working distances are also shown, with the FOV highlighted in red and the illumination beams in grey.

One additional and important advantage of the use of the 3 mm acrylic is that the 5 mm lens diameter is now more than large enough to allow de-centring of the fibre bundle. The illumination beam could thus be 'tilted' by de-centring the fibre bundle relative to the lens, while all the illumination components remain perpendicular to the imaging channel (Figure 49A). The extent of the tilting angle was modelled as a function of fibre bundle distance from the lens axis using ray tracing software. The 6 deg angle required is achieved when the fibre bundle is de-centred by ~0.5 mm relative to the axis of the condenser lens (Figure 49B).

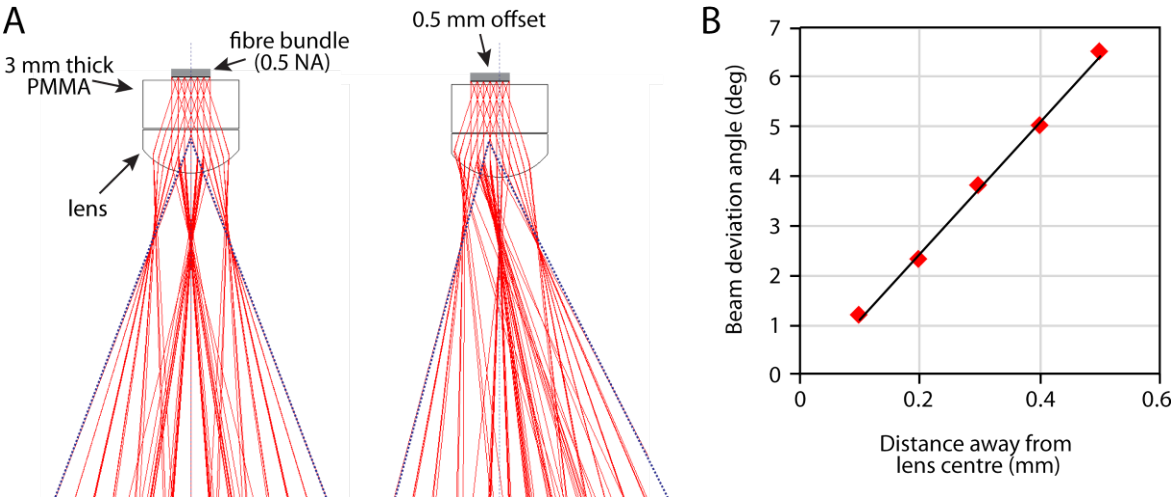

Figure 49: Focus-tuneable system illumination modelling. (A) Ray tracing modelling showing the effect of de-centring the fibre bundle about the lens. (B) Tilting angle of the illumination beam as a function of position of the fibre bundle relative to the axis of the lens.

3.5.5 Illumination system development and testing

The illumination system was tested in conjunction with the focus-tuneable system. The imaging system described in §3.5.2 was housed in a 160 mm long, 35 mm diameter tube screwed into the camera (Figure 50A). In the case of the standard Sony XC505P camera[15],

[15] The Sony XC505P camera can also be used with its sensor at 90° relative to the body.

the overall length of the system as measured from the camera connector to the front of the objective lens was 235 mm.

A custom made holder was placed around the objective lens to house the illumination fibre bundle ferrules. The fibre bundles were distributed around the imaging channel to form a square array (Figure 50B). To ensure uniform illumination, the orientation of the four illumination ports (i.e. the rotation of the custom made holder) was adjusted to be aligned with the rectangular field of view of the system. The condenser lenses and the 3 mm thick acrylic layer were glued together using UV curing optical adhesive (NOA68, Norland). This resulted in a ring-shaped structure that is placed around the objective lens in front of the ferrule holder. The relative position of the ferrule and lens holders was adjusted to ensure the required 0.5 mm de-centring between fibre bundle and condenser lens. The overall diameter of the system was 51 mm.

The evenness of the illumination was tested by coupling the common end of the multi-furcated bundle to a 3 mm diameter, 0.5 NA liquid light guide from a halogen lamp (Model 21AC, Thorlabs). For this purpose, a customised coupler was used to centre the bundle to the light guide and keep the two against each other. A white sheet of paper was illuminated at a range of working distances. Images of the illuminated field were acquired using an independent imaging system and the illumination profile analysed using ImageJ. Figure 50C shows false-colour intensity maps of the illumination over the field of view at a short (100 mm), medium (250 mm) and long (400 mm) working distances. As expected from the CAD modelling, short and long working distances resulted in slightly uneven illumination, with a more prominent bell-shaped light profile.

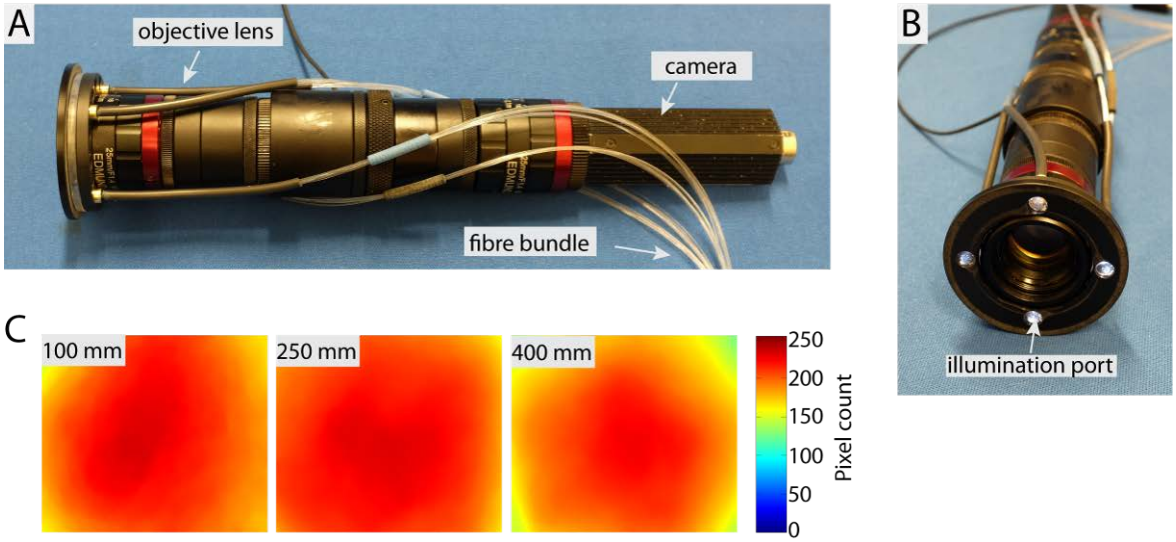

Figure 50: Focus-tuneable system final design and illumination testing. (A) Top view of the focus-tuneable imaging system. (B) Front view of the system highlighting the illumination ports. (C) Illumination profile false-colour intensity map corresponding to short, medium and long working distances.

3.6 Future technology development

The wide-field imaging system (§3.3) and the laparoscopic device (§3.4) have been successfully used clinically, as will be shown in the following chapter. Development research, however, has continued with the aim of improving the performance of the current systems, based on limitations observed during clinical use. In this section, some potential improvements and new solutions for future developments of FIGS systems will be described.

3.6.1 Light sources in FIGS

Multi-spectral excitation

One of the greatest limitations of the technology described in this work is that the light source is limited to excitation wavelengths >650 nm. Although NIR wavelengths are

optimal for higher tissue penetration and result in lower tissue autofluorescence, some of the clinically approved fluorophores (i.e. 5-aminolevulinic acid and fluorescein) are excited in the UV-visible regions. A FIGS device capable of exciting from the UV to the NIR is therefore particularly attractive.

A possible way to achieve this wide excitation range is to use a longer optical system with a series of dichromatic beam splitters to combine light from separate sources. For example, a high-power UV LED and a 488 nm laser can be combined to the white light by using a single-edge and a notch dichromatic beam splitter respectively. In practice, the relatively large étendue of LEDs requires larger diameter optical components as the length of the system increases. Although larger diameter lenses can be used, the dimensions of off-the-shelf dichromatic beam splitters are insufficient for capturing diverging light rays coming from regions of the LED around the centre.

A potential solution to this problem can be achieved by using a pair of relay lenses between two dichromatic beam splitters to reduce the overall diameter of the beam. An example of an optical system to combine different light sources and focus the resulting beam to an output light guide is shown in Figure 51. In this design, a white LED (L1) is coupled to a UV one (L2) (e.g. 405 nm) using a single-edge dichromatic beam splitter (D1) that reflects and transmits short and long wavelengths respectively. Narrow-band laser light (L3) (e.g. 488 nm) is combined with the UV-visible beam using a notch dichroic beam splitter (D2). A pair of lenses is then used to reduce the beam diameter and allow coupling with NIR excitation wavelength(s) (L4) by means of a third beam splitter (D3). Finally, a system of lenses is used to focus the UV-visible-NIR beam to an output light guide. This design was modelled with optical ray tracing software, optimised and tested.

Preliminary results (performed without the 488 nm laser) suggested that a correct beam combination was achieved and that the output beam focussed with ~0.5 NA, as required by the light guide.

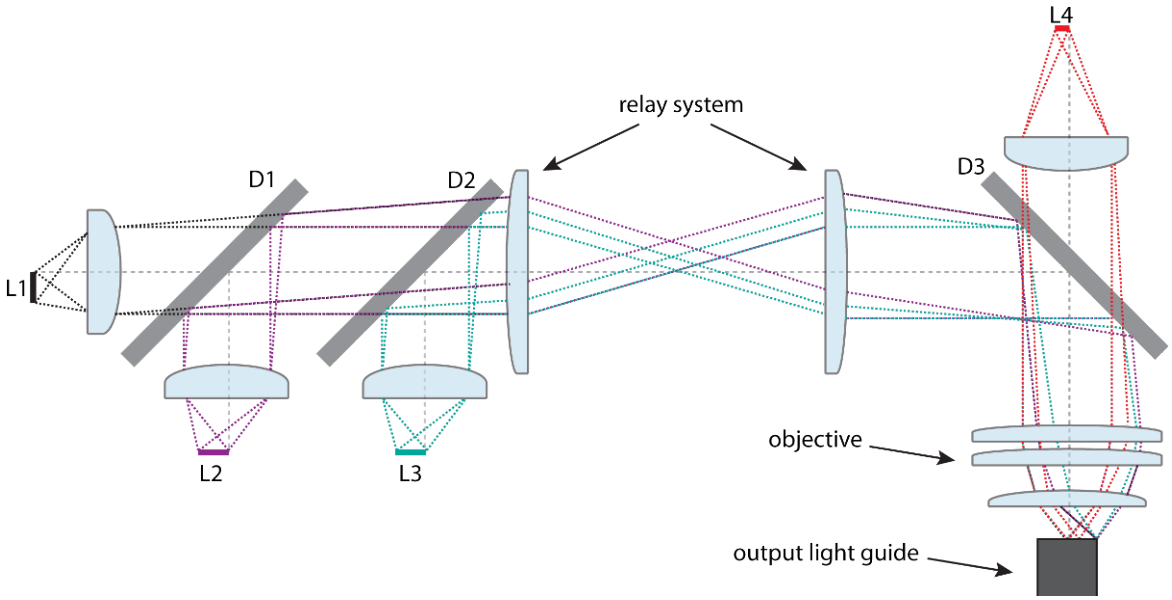

Figure 51: Future developments of multi-spectral excitation system. Shown is a schematic of a possible design for combining bright-field illumination and UV, visible and NIR excitation.

RGB illumination

Alternatively to a white LED, illumination can be achieved by combining light from red (R), green (G) and blue (B) LEDs using, for example, a cross dichroic prism ('X-cube') (Okuyama, 2001). When compared to the spectrum of a white LED, an RGB system lacks spectral components between ~550-620 nm (Figure 52A), which can potentially influence image quality during white reflectance imaging. However, the transmission band of the red channel of a typical X-cube was measured using a spectrometer and it was found that wavelengths > ~560 nm are transmitted. As a result, a high-power white LED can in principle be used instead of the red one to account for the missing wavelengths.

A significant advantage of an RGB illumination system over a white LED is that the colour balance of the illumination light can be controlled by changing the relative contribution of each LED source. This can be particularly useful in the case of spectral overlap of fluorescence emission and bright-field illumination (e.g. in the case of red-purple fluorescence emission from 5-ALA), as the relative contribution of illumination wavelengths can be adjusted to maximise fluorescence contrast during simultaneous imaging with bright-field. Figure 52B shows an example of this approach in the case of 5-ALA fluorescence imaging in malignant glioma.

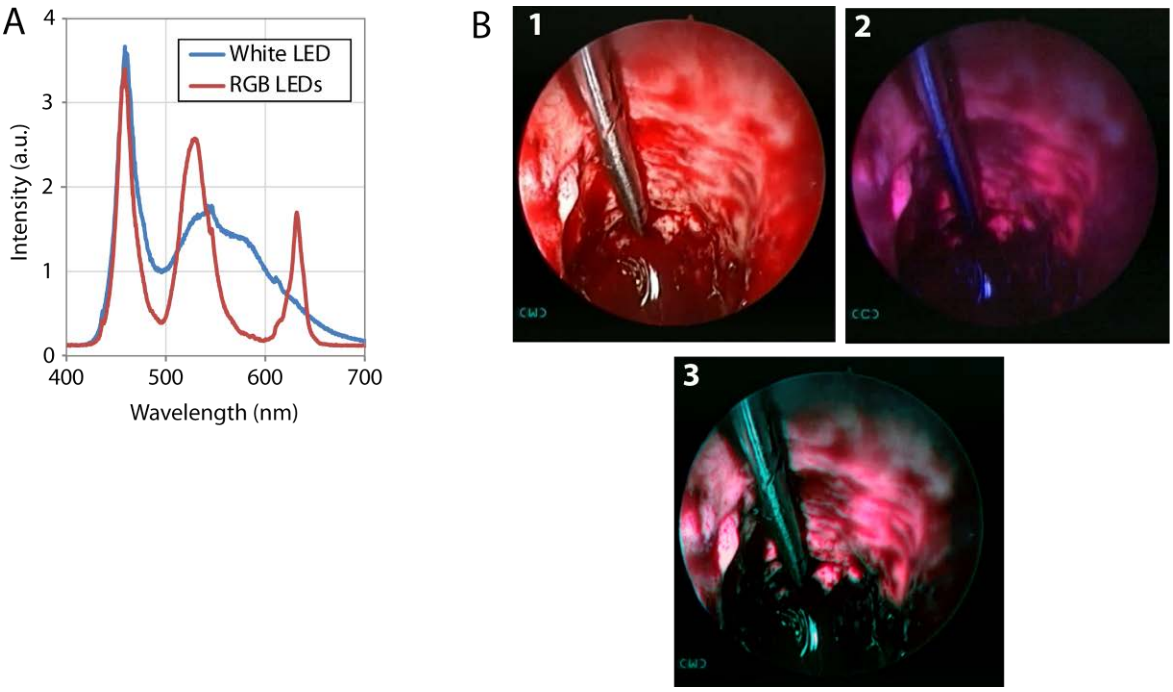

Figure 52: Future developments of illumination system. (A) Visible spectra from a white LED and from combined red, green and blue (RGB) LEDs. (B) Fluorescence-guided surgery of malignant glioma using 5-ALA. 1: bright-field image; 2: fluorescence from 5-ALA; 3: simulated fluorescence and bright-field image as obtained using green and blue illumination. Endoscopy images courtesy of N. de Pennington, John Radcliffe Hospital, Oxford.

Images 1 and 2 are stills from a surgical video of bright-field and fluorescence respectively, acquired by our collaborators using the Storz D-Light system for endoscopy.

This system can display fluorescence emission with a faint blue signal from the excitation light, resulting in loss of information from the conventional bright-field. Image 3 simulates the result of superimposed fluorescence and bright-field using an RGB illumination source with the red channel suppressed. As a result, reflectance details can be preserved and displayed in false-colour together with fluorescence from 5-ALA.

3.6.2 Light homogenisation in a fibre bundle

Optical fibre bundles are the most common way of delivering illumination light in keyhole surgical devices due to their compatibility with conventional sterilisation process. In this work, however, liquid light guides were preferred over optical fibre bundles because of their ability to homogenise the output beam. This indeed proved to be necessary for laser light due to its much lower étendue compared to the LED illumination light. The laser light thus illuminated only a small area of the light guide.

An alternative approach was examined using a hexagonal rod homogeniser ahead of the light guide. A fibre bundle (4.8 mm diameter, 2500 mm long; 495 NCS, Karl Storz) was used in this experiment to test the effectiveness of the rod homogeniser. A 100 µm multimode fibre, ~0.2 NA delivered 660 nm laser light. A 50 mm focal length plano-convex lens (48-770, Edmund Optics) was used to collimate the laser light and a microscope objective (S Fluor 10×/0.5, Nikon, focal length 20 mm) focussed this light with the ~0.5 NA required by the fibre bundle. This light illuminated either the fibre bundle (defocused spot diameter ~1 mm) or the 25 mm long (high NA) hexagonal rod (63-082, Edmund Optics), with the same spot diameter. The opposite face of the homogeniser was butted up to the fibre bundle. The flat-flat homogeniser distance was

4 mm with a 4.62 mm apex-apex distance, appropriately filling the 4.8 mm diameter light guide. A schematic of the optical setup is shown in Figure 53.

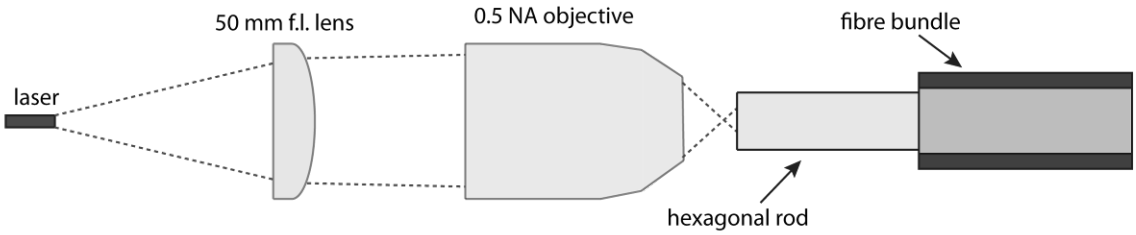

Figure 53: Schematic of the experimental setup to test the homogenising rod. The same test was repeated with the rod replaced by the fibre bundle.

Relative light power output at the distal end of the fibre bundle was measured using a digital power meter (Gentec DUO, Gentec-EO). Figure 54 shows the two experimental setups in case of (A) laser light directly on the surface of the fibre bundle and (B) when the homogenising rod is used in front of the bundle.

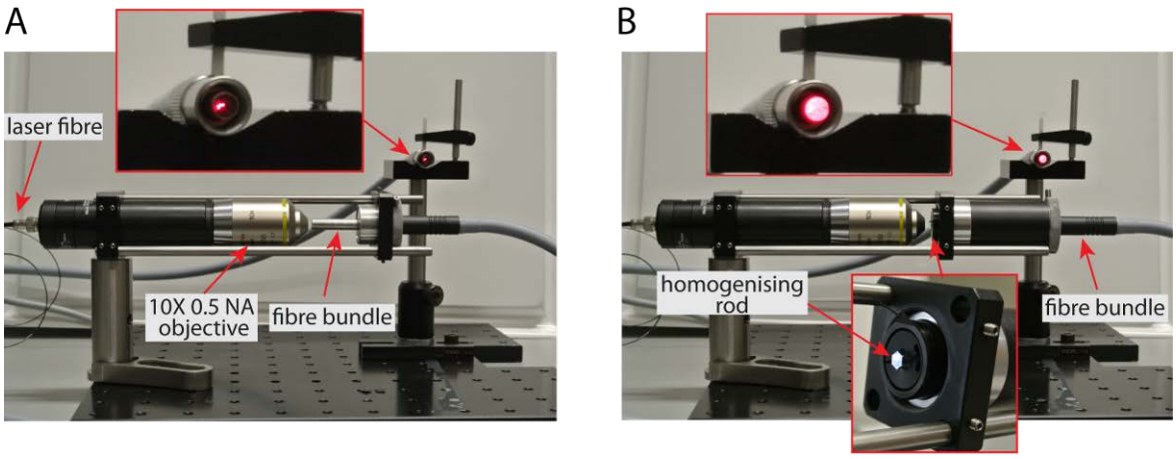

Figure 54: Experimental setup for testing the homogenising rod. Light was delivered to (A) the fibre bundle and to (B) the homogenising rod butted up to the fibre bundle. The images in the top insets show a close-up of the distal end of the bundle. The bottom inset in (B) shows the custom-made rod holder.

A rod mount (64-907, Edmund Optics) and a custom-made mechanical arrangement were used to place the microscope objective, the rod and the fibre bundle concentric relative to each other (bottom inset of Figure 54B). Close-up analysis of the output from the fibre bundle (top insets in Figure 54) shows that the hexagonal rod is adequate to homogenise 0.5 NA light. The relative transmission when the homogeniser is used was measured to be 87%. A ~92% transmission is expected as the homogeniser was not antireflection coated. The additional 5% losses are expected to be due to imperfect hexagon vertices and possible dust or dirt on the surfaces. Nevertheless, the homogeniser is extremely effective at reducing fibre bundle hotspots. Future FIGS system can potentially make use of this approach and adopt more flexible and autoclave-compatible optical fibre bundles at the expense of slightly lower light transmission.

3.6.3 Endoscopic systems

The development of a laparoscopic attachment that was used with a 10 mm rigid laparoscope was described in §3.4. The same attachment could in principle be used with a conventional fibre-based flexible endoscope that transmits light from the objective lens to the eyepiece using a coherent fibre bundle. Despite a lower light gathering power dictated by a limited aperture size, NIR light transmission relative to the visible is superior in fibre-based endoscopes compared to rod lens-based laparoscopes. This was confirmed by imaging the same scene with a laparoscope and a gastroscope and using a diffusive 830 nm LED as a source of NIR light.

Figure 55 shows the results using the camera attachment previously described in conjunction with a rigid laparoscope (A) and a flexible gastroscope (B). The working distance of the gastroscope was adjusted to produce a visible (white-reflectance) signal and

field of view comparable to the ones obtained with the laparoscope. For the purpose of this test, the imaging channel only was considered. Results showed higher signal from the 830 nm LED in the case of the gastroscope, demonstrating the superior relative NIR transmission of the coherent fibre bundle when compared to rod lenses. This is an important advantage for developing NIR fluorescence systems that operate with fibre-based endoscopes.

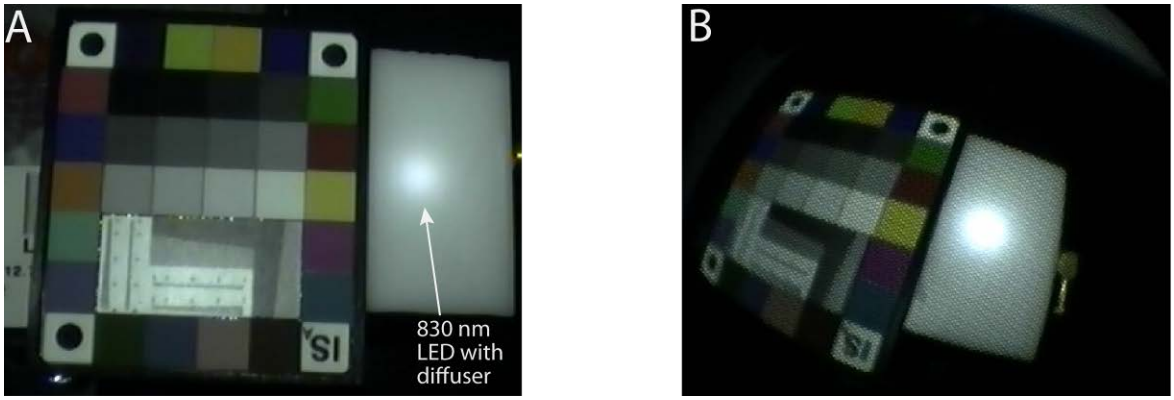

Figure 55: Visible-NIR imaging with two types of endoscopes. A rigid laparoscope (A) and a flexible gastroscope (B) are shown.

Modern video endoscopes, however, are designed to house the image sensor near the distal end of the instrument (Edmonson, 1991). This has the important advantage that greater image resolution can be achieved, as the number of image pixels is set by the sensor and not by the number of fibres in the coherent bundle. This significant development of endoscopic systems, however, comes at a price. As the image sensor is incorporated in the endoscope main body, a FIGS implementation becomes challenging. Significant (and impractical) modifications of the instrument are required to fit the fluorescence filters. Possible solutions to overcome this difficulty might include the addition of a coherent fibre optic bundle in an endoscope with a free working channel. This bundle would be used to

collect exclusively fluorescence emission light, while bright-field is provided as conventionally using the imaging channel of the instrument.

3.6.4 Distance sensing during laparoscopy

One of the crucial safety issues concerning intra-operative fluorescence in keyhole surgery is the level of tissue exposure with excitation light that, particularly at very close working distances, can induce photo-damage. As the power density could potentially go above the allowed maximum permissible exposure of ~200-300 mW/cm^2 (ANSI, 2014b), a way to dynamically adjust and limit the output power as a function of distance of the instrument tip from the surgical field would be highly desirable. To date, no surgical system with this feature is available.

A possible solution for this problem is to estimate the device working distance from the amount of light diffusely reflected at the tissue and collected by the laparoscope. This can in principle be accomplished by adding an additional light source and measuring the diffuse reflectance on the imaging side using a photodetector. As the signal detected depends both on the working distance and on the tissue diffuse reflectance, wavelengths that are equally reflected across different types of tissues are preferred.

The visible light (white LED) reflectance and that at three different NIR wavelengths was measured with *ex vivo* animal tissue (bacon). The sample was illuminated with a flat illumination beam generated from LED and laser sources available in our laboratory. The Sony XC505P camera was used in conjunction with a 25 mm lens (NT67-715, Edmund Optics) set to f/8 at a working distance of 350 mm. A small amount of red food dye was added to the tissue to simulate blood: a visible high absorbance solution. Figure 56A shows monochromatic images of the tissue illuminated with the visible and NIR

wavelengths. Profile analysis of the images are shown in Figure 56B. Results suggest that wavelengths in the region 660 - 785 nm provide a relatively flat response across the tissue in comparison with visible and 980 nm light.

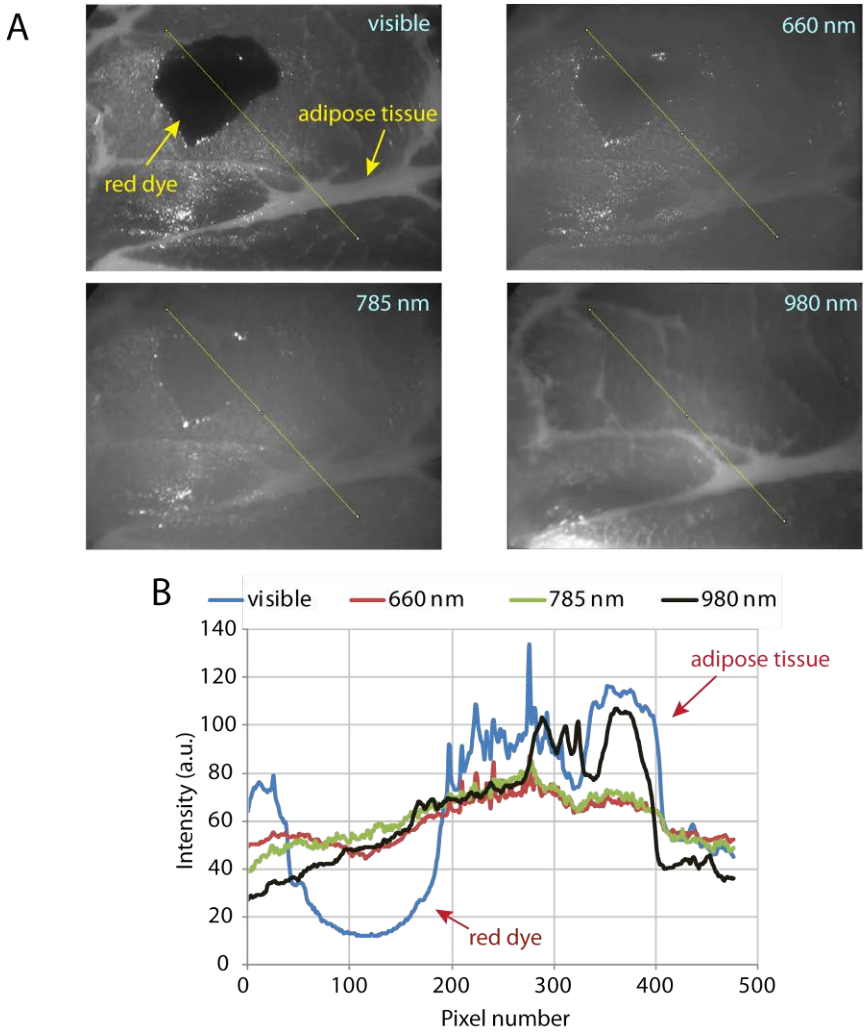

Figure 56: Reflectance from different wavelengths of *ex vivo* pig tissue. A red dye was used to simulate blood absorption. (A) Imaging results at different illumination wavelengths. (B) Image profiles across the yellow lines in (A) show a near-flat response at 660-785 nm.

As the light used to sense the laparoscope working distance has to be filtered out before reaching the image sensor, a practical solution would be to use wavelengths that can be easily blocked using a short-pass filter in front of the camera. This filter, however, needs to

transmit light corresponding to the emission spectrum of NIR fluorophores, inevitably limiting the range of wavelengths for distance sensing to the ~900 nm region. A further advantage of a distance-sensing device is that the fluorescence intensity can be related to the excitation power density by measuring the working distance of the laparoscope during imaging. This will eventually allow the comparison of the fluorescence signal from different fields of view and, most importantly, to set an intensity threshold for surgical resection of a fluorescent specimen.

3.7 Discussion of Chapter 3

In this chapter, the developments of several novel technologies that can be exploited for developing FIGS devices were described. Multi-spectral fluorescence imaging and bright-field using a single camera was achieved, thus improving flexibility in comparison with many of the existing systems. A tremendous advantage of this approach is that different types of imaging devices can be used based on the same technology. To the best of my knowledge, this is the first multi-spectral fluorescence system that can operate both in open surgery and in keyhole surgery.

A wide-field imaging device and a laparoscope attachment that generate a typical excitation power density of ~10 mW/cm^2, as required following theoretical modelling (Chapter 2), were presented. The systems are compact, lightweight and suitable for hand-held operation. The development and testing of the two devices, along with solutions for performance improvements, was described. Both the laparoscope and the wide-field system proved to be capable of detecting nano-molar concentrations of two clinically approved NIR dyes in real time. Unlike most existing technologies, no image processing

software is used for simultaneous display of fluorescence and bright-field images. This proved to be a significant advantage for prompt clinical translation, as will be shown in the next chapter.

One of the strengths of our design is the relatively simple technology that is used for simultaneous bright-field and multi-spectral fluorescence detection. Although more complex features such as spectral unmixing and absorption correction can in principle be implemented, our approach focussed primarily on developing a useful and practical tool for the clinician. Although results were presented with two NIR wavelengths, the systems can in principle operate at any excitation wavelength from the visible to the NIR, provided that appropriate light sources and filters are added.

The design and development of a prototype of wide-field imaging system for FIGS capable of focussing without moving parts has also been described. In comparison with the ‘conventional’ wide-field system, this device is smaller, has concentric illumination and detection channels and its focus can be adjusted very rapidly. In addition, its field of view, at a typical working distance of 300 mm, is almost twice as large (four times the area) compared to the previous system. Despite being only a prototype, an enclosure will be constructed and control buttons will be added to create a final design suitable for clinical use. This device will be connected optically and electrically using a similar connection as for the conventional wide-field system.

A highly significant advantage of using an electrically focus-tuneable lens for focussing is that fast autofocus algorithms can be conveniently implemented (Krotkov, 1988). This is particularly beneficial in a hand-operated FIGS device. Future developments of this device will include a fast autofocus system that will facilitate its surgical usability.

In the last part of this chapter, future technological developments were introduced. These included improvements in coupling and delivering light from different sources, development of endoscopic systems and distance-sensing during laparoscopy. Such development will be crucial for the design of future systems for fluorescence molecular imaging. In the next chapter, practical applications of the FIGS systems will be described.

4. Clinical and pre-clinical FIGS applications

In the previous two chapters, the exceptional detection sensitivity of FIGS as predicted by theoretical modelling was demonstrated, along with the development of imaging systems designed for intra-operative fluorescence imaging. *In vitro* tests have shown nano-molar fluorescence sensitivity of the imaging devices using clinically approved NIR fluorescence dyes (§3.3.3 and §3.4.2). Despite the encouraging results, one of the most challenging aspects of FIGS is the translation of the imaging devices from the bench to the clinic. As previously discussed, this required the imaging devices to be compliant with relevant electrical standards, laser safety rules, ergonomics and sterility.

In this chapter, practical imaging results using the FIGS devices described earlier will be shown. Results from a clinical study involving sentinel lymph node fluorescence detection in gynaecological cancers, using clinically approved non-specific dyes, will be presented. As this was the first clinical use of our FIGS devices, the main purposes of this study were to (1) assess the usefulness and reliability of the technology and (2) to determine limitations and issues that can be addressed in future device development. *In vivo* imaging results using tumour-specific markers to detect ovarian cancer cells will then be presented. Finally, additional *ex vivo* and *in vitro* preliminary results using other novel tumour-specific markers will be presented.

4.1 Fluorescence imaging of SLNs in gynaecological cancers

Although the concept of sentinel lymph node (SLN) and its clinical relevance have been clearly demonstrated in breast cancer (Veronesi *et al.*, 2003) and melanoma (Morton *et al.*, 2006), it is still unproven in other cancer types. In gynaecological cancers, for example, the role of the SLN biopsy is still an evolving concept, not without controversy. In this section, a clinical study will be presented in which the FIGS imaging systems described in this work were used to detect SLNs in gynaecological cancers. The study was conducted in collaboration with the Gynaecological Oncology Unit, with Professor Ahmed A. Ahmed and others at Oxford.

4.1.1 Fluorescence properties of MB and ICG

Two of the clinically approved fluorescence markers, methylene blue (MB) and indocyanine green (ICG) were used as contrast agents in this clinical study. Despite the fact that anatomical differences between individuals may cause difficulties with the visualisation of the SLN, the fluorescence signal is ultimately dependent on the dye concentration at the target and on dye binding to lymph proteins.

The relationship between dye concentration and fluorescence intensity was assessed using the FIGS technology prior to clinical translation. As albumin is the most common protein in the lymph to which ICG binds, the fluorescence signal as a function of albumin concentration for this dye was also measured. Despite the fact that MB has been successfully used as a vital dye for SLN mapping (Li *et al.*, 2009), it does not bind to lymph proteins (Tsopelas & Sutton, 2002).

Methods

In the first experiment, MB (Methylthioninium chloride, Proveblue 5 mg/ml, Provepharm SAS) and ICG (25 mg vials, Pulsion Medical Systems) were diluted in water solutions containing 20% human serum albumin (HSA) (#100-512, Gemini Bio-Products) at concentrations ranging from 200 nM to 0.8 mM. 300 µl solution for each dilution value per well of a 96-well plate was used. Images were acquired using the wide-field imaging system at a working distance of 400 mm and 40 ms exposure times.

In the second experiment, ICG was diluted in solutions of different HSA content, resulting in 10 µM ICG concentration. Aliquots of 300 µl ranging from 0% HSA (water for injection only) to 100% HSA (stock solution) and 10 µM ICG were placed in a 96-well plate and imaged similarly to the previous experiment. Quantitative image analysis for both tests was performed by measuring the average signal in regions of interest corresponding to each well. The image analysis was performed with ImageJ software.

Results

Figure 57A shows the variation of the fluorescence signal for different concentrations of ICG and MB in 20% HSA. Coincidentally, both dyes generate the greatest fluorescence signal at similar concentrations (~ 10 µM). As the concentration increases from the optimal one, the intensity of the fluorescence signal decreases due to the contributions from self-absorption (Benson & Kues, 1978) and due to quantum yield reduction caused by dye dimerization (Philip *et al.*, 1996).

The variation of the fluorescence signal as a function of HSA content of the solution is shown in Figure 57B. Results suggest that the fluorescence signal from ICG in 40% HSA is ~4-fold higher than when the same number of fluorophore molecules are diluted in

water. This signal increase with lymph protein binding has been extensively reported in the literature (Desmettre *et al.*, 2000). However, the test also showed that the intensity of the fluorescence signal appears to reach a plateau above ~30% dilution of HSA. This suggests that further increase of albumin concentration does not improve the fluorescence emission signal, as expected when the number of albumin proteins exceeds the number of fluorophore molecules. This experiment was performed with ICG only as MB did not bind to lymph proteins.

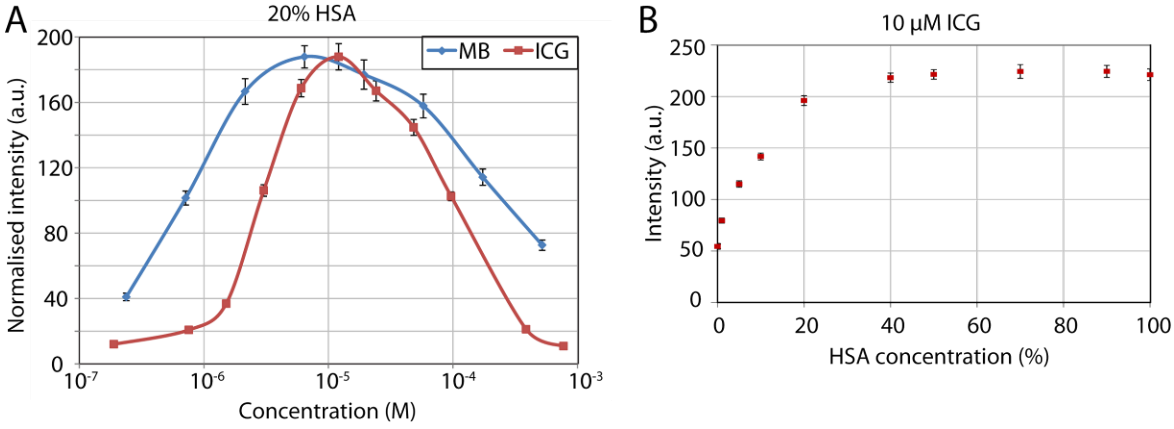

Figure 57: *In vitro* fluorescence properties of ICG and MB. (A) Normalised fluorescence intensities for MB and ICG in 20% HSA as a function of dye concentration. Note the abscissa's logarithmic scale. (B) Fluorescence intensity of ICG (10 µM concentration) as a function of HSA content of the solution. Note that 100% HSA corresponds to the stock solution (albumin content: 3 g/dl).

The results shown here demonstrated that both the concentration and the microenvironment dramatically affect the fluorescence signal, suggesting that careful optimisation of the injection method (i.e. dye concentration and volume) is required.

4.1.2 Background of SLN mapping in gynaecological cancers

Endometrial cancer

Endometrial[16] cancer is the most common type of gynaecological tumour in developed countries, with raising incidence with life expectancy increase (Amant *et al.*, 2005). The main surgical procedure for the treatment of this disease consists of the complete removal of the uterus (hysterectomy). As the incidence of lymph node metastasis in early stage patients is around 10% (Creasman *et al.*, 1987), it is debatable whether a complete removal of the regional lymph nodes (lymphadenectomy) should be also performed. Since most women with early stage endometrial cancer are not likely to benefit from lymphadenectomy, the assessment of the SLN status is crucial to avoid unnecessary LN dissection. Previous results on the ability of the SLN to predict LN metastasis have shown 100% sensitivity and specificity, indicating high usefulness of the SLN practice (Niikura *et al.*, 2004). However, a detection rate of 82% was obtained using a combination of blue and radioactive dyes, suggesting that more effective ways of detecting SLNs are desirable.

Cervical cancer

Cervical[17] cancer is a rare disease that accounts for 0.9% of all the cancer cases in the UK (Cancer Research UK, 2011a). Similarly to endometrial cancer, the treatment of choice for patients with early stage cervical cancer is radical hysterectomy and pelvic lymph node dissection (Averette *et al.*, 1993). Lymph node metastasis, however, is more common, with positive lymph nodes in the pelvic area in around 25% of the cases (Sakuragi *et al.*, 1999).

[16] The endometrium is the inner mucous membrane of the uterus.

[17] The cervix is the lower part of the uterus.

Conventional SLN detection techniques have shown detection rates ranging from ~85% using blue dye to ~90-95% when combined with the radioactive tracer, with sensitivity and specificity greater than 90% (Frumovitz *et al.*, 2008).

Vulval cancer

Vulval cancer is the rarest of the gynaecological malignancies, accounting for 0.4% of all the cancer cases (Cancer Research UK, 2011b). Treatment of early stage vulval cancer patients consists of excision of the tumour and groin lymph node dissection. In such patients, the incidence of LN metastasis is around 30% (Burger *et al.*, 1995). SLN detection rate has been reported to be ~98% using the combined dye/radioactive method, with ~92% sensitivity and specificity in predicting LN metastasis (Hampl *et al.*, 2008). A multi-centre observational study in which lymphadenectomy was omitted in patients with a negative SLN has shown dramatic decrease in morbidity over patients that underwent complete groin LN dissection (Van der Zee *et al.*, 2008). This result, in addition to optimal conditions for peri-tumoural injection and convenient location of the first LN basins, suggests that SLN dissection can potentially become a standard of care in women with early stage vulval cancer.

4.1.3 The PIONIR study

Despite evidence of potential benefits of SLN mapping in gynaecological cancers, at the time of writing this thesis this mapping has not been accepted as a standard of care in the UK for a number of reasons. These include the need of a nuclear medicine unit, the relatively low cancer incidence and the lack of consistent data on lymphatic drainage. In order to address these issues, a clinical study was designed by our colleagues to assess the

feasibility of SLN mapping in patients with endometrial, cervical and vulval cancer, using the fluorescence imaging systems previously described.

Study design and objectives

The clinical study is still taking place in Oxford, starting in 10/2012, but results only up to 9/2014 are presented here. The study was named PIONIR (An observational **PI**lot Study **O**f **N**ear **I**nfra**R**ed imaging), aimed at sentinel nodes, in early stage vulval, cervical and endometrial cancers using ICG and MB as fluorophores. The study included early stage cancer patients that were routinely scheduled to undergo lymphadenectomy. Patients that had previous chemotherapy, radiotherapy or surgery to the LNs of interest were excluded from the study. As this was a proof of principle study, clinical decisions were not made based on the outcomes of the SLN detection procedure. The main objective of this study was to investigate the feasibility of using the custom-made imaging devices to detect SLNs. Reporting the SLN detection rate and sensitivity/specificity of the technique was among the secondary objectives of the study. As an exploratory objective, the relationship between injection site and lymphatic drainage was also assessed in selected women with endometrial cancer following injection of two spectrally-distinguishable fluorescence dyes. A flowchart representing the main steps of the study is shown in Figure 58.

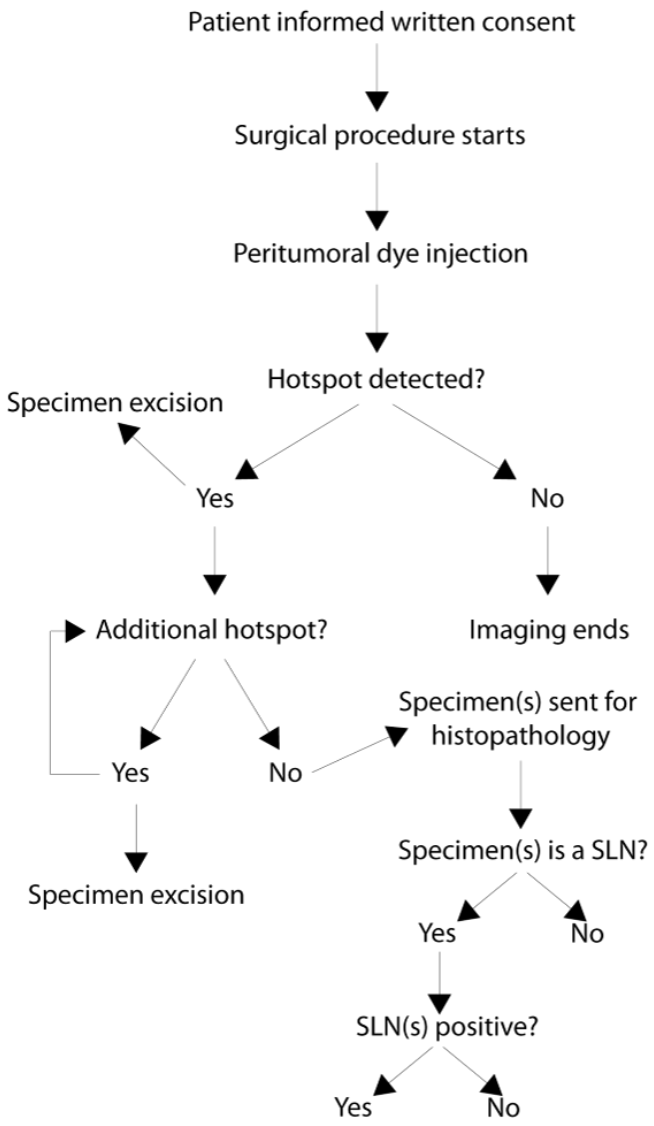

Figure 58: Flowchart of the PIONIR study.

Injection technique

Clinically approved NIR fluorescence dyes, ICG (25 mg vials, Pulsion Medical Systems) and MB (Methylthioninium chloride, Proveblue 5 mg/ml, Provepharm SAS), were injected peri-tumourally at the start of the surgical procedure. The dyes were re-suspended (ICG) or diluted (MB) in water for injection to obtain concentrations suitable for fluorescence imaging. Dose and total injected volume were set initially to 5 mg/ml and 1 ml

respectively, and then adjusted during the course of the study to improve detection rate until a satisfactory level was achieved. The dyes were freshly prepared on the day of surgery and a single vial was used for each procedure in order to account for rapid degradation in aqueous solutions (Saxena *et al.*, 2003). For the endometrial cancer group, ICG was injected in both sides of the cervix corresponding to the 3 and 9 o'clock positions. In a sub-group of selected patients, this was followed by injection of MB into the uterine fundus using an epidural needle. For the cervical cancer group, injection of ICG in both sides of the cervix was performed as described for the endometrial cancer group. For the vulval cancer group, ICG was injected in four peri-scarring/tumoural margins. These procedures were, of course, undertaken by the surgeons and their assistants.

Surgical technique, intra-operative detection and specimen examination

In endometrial and cervical cancer cases, laparoscopic and/or open surgery procedures were performed at the surgeons' discretion, while all the vulval cancer patients underwent open surgery. Fluorescence imaging was attempted in all procedures. The surgeon estimated whether the fluorescence signal was sufficient to warrant resection based on subjective observation. Exposure time per frame, during fluorescence acquisition, ranged between 40 ms and 320 ms, depending on the emission intensity and imaging depth. During open surgery procedures, the theatre lights were dimmed to minimise background illumination. In a sub-group of vulval cancer patients, transcutaneous NIR fluorescence imaging was performed suprapubically prior to surgical procedure.

The fluorescence 'hotspots' detected with the imaging system were removed, labelled and dispatched, along with all the other LNs, to Pathology. Hotspots were assessed by a

responsible pathologist to verify presence of a SLN and to determine metastatic involvement. All the other LNs were also examined to assess cancer cell presence.

Statistical analysis

The hotspot detection rate was calculated as the ratio between the number of cases in which at least one hotspot was detected and the total number of cases. The SLN confirmation rate was calculated as the ratio between the number of hotspots that contained a SLN[18] and the total number of hotspots removed.

Whether the SLN determined the metastatic status of all the other LNs was estimated by calculating sensitivity and specificity according to the definitions described in (Lalkhen & McCluskey, 2008) and summarised in Table 8. 'Positive' and 'negative' refer to a LN with and without cancer cells respectively.

True positives:	Number of cases in which the SLN(s) is positive and at least one LN is positive
False positives:	Number of cases in which the SLN(s) is positive and all the LNs are negative
True negatives:	Number of cases in which all the LNs are negative and the SLN(s) is negative
False negatives:	Number of cases in which at least one LN is positive and the SLN(s) is negative

$$Sensitivity = \frac{True\ positives}{True\ positives\ +\ False\ negatives} \qquad Specificity = \frac{True\ negatives}{True\ negatives\ +\ False\ positives}$$

Table 8: Definition of sensitivity and specificity for SLN mapping.

[18] As assessed by histopathological examination.

4.1.4 Integration of the imaging system in the operating theatre

Following local ethics approval, the wide-field imaging system and the laparoscope attachment were introduced at the Churchill Hospital in Oxford. The main control unit was placed on a medical trolley with lockable wheels for convenient transport and stable positioning during the surgical procedure (Figure 59A). Given the limited distance (~2 m) between the imaging probes and the control unit, the trolley was placed ~1 m away from the surgical bed. This arrangement was not in the way of the surgeon and did not affect conventional surgical practice.

During open surgery, the wide-field imaging head and umbilical cord were covered using a sterile drape normally used to achieve laparoscopic camera sterility. The imaging head was connected to a sterile flexible arm (StrongArm 73000, Mediflex) for positioning above the patient and for rotational and translational adjustments (Figure 59B). For this purpose, a custom-made clamp was developed that ‘clicks’ into the distal end of the arm and holds the imaging head with a bracket system. The flexible arm was mounted prior to surgery on the side of the surgical bed using a rail clamp and its height adjusted at the start of the operation. A typical working distance of ~350 mm between the device head and the surgical cavity was adopted in most situations (Figure 59D), although shorter distances were used in some cases (i.e. during transcutaneous imaging). When fluorescence imaging was not performed, the positioning wheel of the arm was released and the imaging head moved away from the patient. At the end of the procedure, the surgical arm was removed and sent for sterilisation, while the rest of the equipment was cleaned using surgical wipes.

During laparoscopy, the same control unit as for the wide-field was used (Figure 59A), with the camera attachment and light delivery guide plugged in.

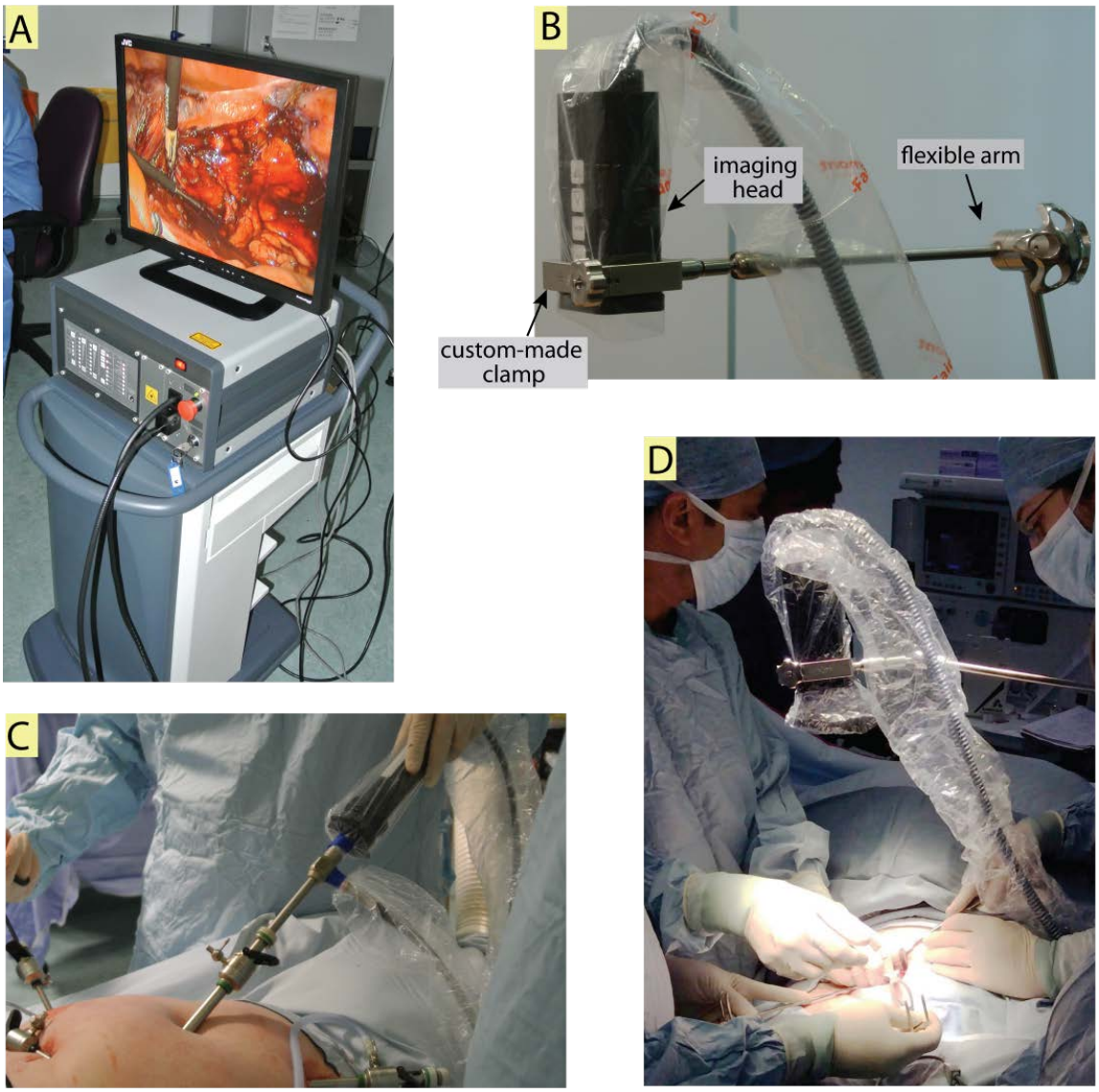

Figure 59: FIGS imaging systems in the operating theatre. (A) Surgical trolley with the system control unit and monitor. (B) Detail of the wide-field imaging head clamped on the flexible arm. (C) Laparoscopic camera attachment used in conjunction to a rigid laparoscope. (D) Intra-operative use of the wide-field system during open surgery.

A conventional camera drape was taped to the laparoscope eyepiece and the imaging head clamped onto it. The drape was then slid to fully cover the imaging head and the camera connection. A second drape was then placed on the laparoscope illumination port to cover the liquid light guide used for light delivery. This was necessary as the liquid light guide is

not autoclavable. Figure 59C shows the laparoscope, with camera attachment and liquid light guide. As for conventional use, the laparoscope was placed before the start of the operation in a sterilised ‘thermos flask’ filled with hot water, in order to prevent laparoscope objective lens fogging during the procedure. At the end of the procedure, the drapes were removed and the imaging head and light guide wiped.

Toggling between (a) white light only, (b) white light and fluorescence and (c) fluorescence-only imaging was controlled in both devices by operating a foot switch. The imaging sensitivity during fluorescence mode was manually adjusted. Since the laparoscope attachment did not include control buttons, the camera sensitivity was set from the control unit by another operator, following instructions from the surgeon. The video output from the control unit (S-video) was connected to the auxiliary input of the operating theatre’s multimedia platform. This allowed simultaneous video recording and live display on theatre monitors. The full imaging procedure was recorded as MPEG-compressed data and stored on the multimedia platform’s hard drive.

4.1.5 Clinical study results

The fluorescence imaging systems proved to be reliable in all the 46 cases considered in this work. Fluorescence-guided SLN dissection was achieved (Figure 60A), as well as visualisation of the lymphatic system (Figure 60B). Among the 46 women included, 25 had endometrial cancer (54%), 10 had cervical cancer (22%) and 11 had vulval cancer (24%). Laparoscopy was performed in 28 cases (endometrial and cervical cancers only) while open surgery was performed in 17 cases. One operation (endometrial cancer) was planned to be performed laparoscopically; however, the complexity of the procedure ultimately required an open surgery approach. ICG was injected in all except one case, in

which MB only was used. Although the dye concentration/injected volume were initially set to 5 mg/ml and 1 ml respectively, they were gradually optimised to 1 mg/ml and 4 ml. Dose escalation or changes were performed on the first 33 patients, while for the remaining 13, the dosage was set to 1 mg/ml and 4 ml. Out of these 13 cases, 3 endometrial cancer patients had simultaneous injections of ICG and MB.

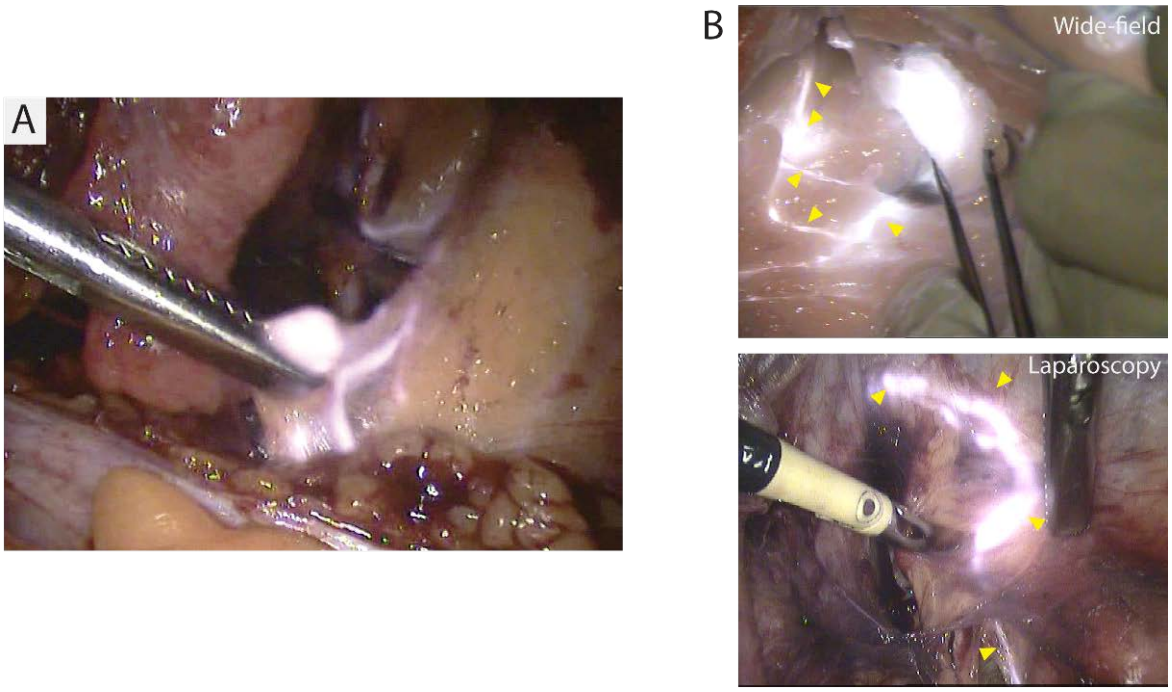

Figure 60: Examples of intra-operative fluorescence imaging with ICG. (A) Detection of an internal iliac SLN during laparoscopy in endometrial cancer. (B) Visualisation of the lymphatic vessels (arrowheads) during open surgery (top) and laparoscopy (bottom). Imaging exposure time: 40 ms.

Detection rate and histopathological analysis

The main results of the PIONIR study are summarised in Table 9. When all the cases were considered, at least one hotspot was detected in 38 patients, leading to a detection rate of ~83%. A total of 70 hotspots were removed intra-operatively. Out of these hotspots, 61 were confirmed to be SLN by histopathological examination (87% confirmation rate).

When only the optimised dose group was considered (the last 13 cases), the hotspot detection rate increased to 100% and 27 out of the 29 (93%) hotspots removed were confirmed to be SLNs.

Out of the 35 cases with detected (and confirmed) SLN, 5 had at least one SLN with metastasis (14%). The sensitivity and specificity of the SLN method, when all cases are considered, were only 50% and 90% respectively. In contrast, when the optimised dose group was considered, the specificity increased to 92% while the sensitivity could not be calculated due to the absence of cases with positive LNs in these 13 patients.

	All cases (n = 46)	***Optimised dose only (n = 13)***
Hotspot detection rate	83%	100%
SLN confirmation rate	87%	93%
Sensitivity	50%	N/A
Specificity	90%	92%

Table 9: Main results of the PIONIR study.

Results for cancer type

When data from all the cases in the study were examined for individual cancer types, the hotspot detection rate was 72% for endometrial cancer, 100% for cervical cancer and 91% for vulval cancer. The most common anatomical site for SLN detection in endometrial and cervical cancer was the external iliac group of LNs, followed by obturator, common iliac and internal iliac.

In vulval cancer, transcutaneous inguinal SLN detection using ICG was successfully achieved in 5 out of 7 cases (71%) (Figure 61). A maximum imaging depth of ~20 mm was obtained using a camera exposure time of only 80 ms.

Figure 61: Transcutaneous SLN detection in a patient with vulval cancer. SLN depth ~20 mm. Exposure time during transcutaneous imaging: 80 ms. Electronic gain: 10×. SLN detected ~6 min after dye injection.

Multi-wavelength detection

Out of 70 hotspots, 68 were detected with ICG, 1 with MB and 1 with both dyes. In one endometrial cancer case of the optimised dose group, an external iliac SLN was taken up by ICG injected near the cervix and by MB injected in the uterine fundus, suggesting common lymphatic drainage. Two-wavelength detection was achieved by switching between 785 nm and 660 nm excitation, as shown in Figure 62.

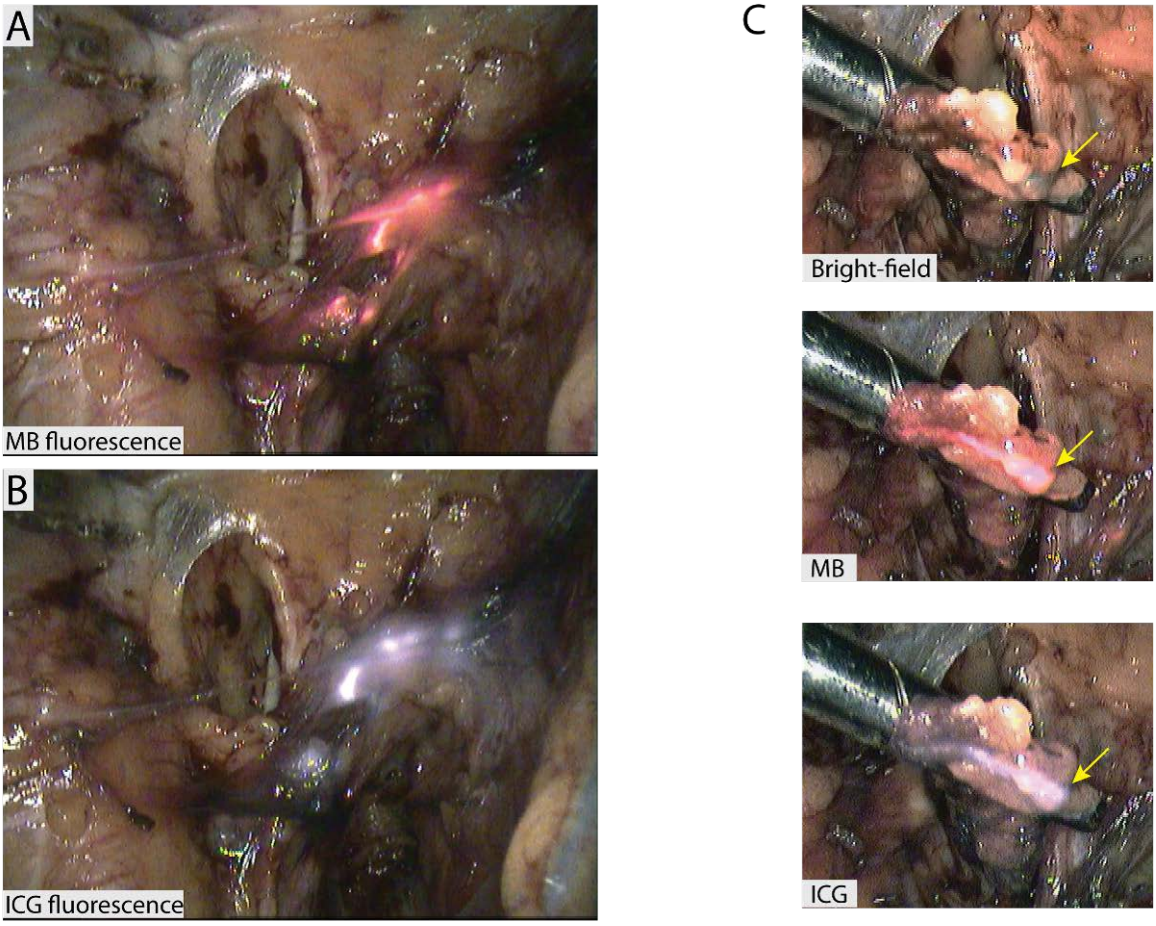

Figure 62: Multi-spectral fluorescence imaging during laparoscopy. Fluorescence detection of lymphatic vessels with MB (A) and ICG (B) in a patient with endometrial cancer. (C) Further excision showed co-localisation of the two dyes in an external iliac SLN (yellow lines). All images were acquired at 40 ms exposure time.

4.1.6 PIONIR study: discussion

The main purpose of this clinical study was to assess the feasibility of using the FIGS imaging devices to intra-operatively detect SLNs, using non-specific fluorescence dyes. The imaging system proved to be reliable both during laparoscopy and open surgery. Its ability of operating with a laparoscope or with a wide-field system proved to be particularly beneficial in at least one case where the surgical procedure was first attempted laparoscopically and then converted to open. The use of the fluorescence imaging devices

did not hinder the surgeon and only marginally prolonged the operation time by ~5-20 min, depending on the procedure and location of the SLN(s).

Because of the lack of consistent early results on the optimal injected dose, the dye concentration and volume varied across the study and reached 1 mg/ml and 4 ml after 33 cases. Furthermore, a SLN biopsy is a relatively difficult procedure to master: previous studies have shown that at least ~30 cases are necessary as part of the 'learning curve' of the technique (Morton *et al.*, 1999). For these reasons, only the 13 cases with optimised dose should be considered for a fair evaluation of this method.

At least one SLN was detected in each patient from the optimised dose group for each cancer type. Two of the 29 hotspots excised from this group were not confirmed to be a LN and contained adipose tissue instead. This is not uncommon in SLN biopsy particularly when the imaging technique (fluorescence) is capable of detecting relatively low dye concentrations, and it can be related to the dye escaping the lymphatic system as a consequence of surgical manipulation (van der Vorst *et al.*, 2011). Interestingly, the two non-SLN hotpots were detected in women with high BMI (>30), indicating that careful selection of eligible patients should perhaps be re-considered.

Transcutaneous detection of SLNs in vulval cancer patients following ICG injection proved to be accurate up to a depth of ~20-25 mm below the skin. As SLNs in vulval cancer are located superficially, NIR fluorescence imaging has a definite potential to reduce invasiveness, since excision could be guided by transcutaneous fluorescence signal. However, difficulties were observed in two women with a high BMI (>30) as the excitation light could not penetrate the higher adipose tissue thickness. This was in agreement with the findings from a similar study on vulval cancer (Crane *et al.*, 2011a).

Nevertheless, the greatest limitation for successful transcutaneous fluorescence imaging was the presence of background light in the operating theatre, which reduced the available camera sensitivity.

Simultaneous MB and ICG injection was attempted in selected endometrial cancer cases with the aim of investigating the relationship between injection site and lymphatic basin. SLN detection rates with MB were significantly lower than with ICG, suggesting poorer uptake by the lymphatic system. This could be caused by the lack of sulphonic acid groups which bind to lymph proteins, causing MB to rapidly migrate to blood capillaries (Tsopelas & Sutton, 2002). However, improvements in the detection rate were achieved when a 4 ml MB volume was injected. Co-localisation of ICG and MB in a SLN was detected in a patient with endometrial cancer following ICG injection in the periphery of the cervix and MB injection in the uterine fundus. In this case, two-wavelength imaging suggested a common draining path from the two injection sites to a SLN from the external iliac group. Further evidence is required to determine consistent lymphatic basin involvement from the two locations. Further data will ultimately provide useful information on the optimal injection practice for SLN detection in endometrial cancer. To the best of my knowledge, this is the only clinical study that used fluorescence from MB for detecting SLNs[19] and, most importantly, the first one that used a combination of two spectrally distinguishable fluorescence dyes. This was achieved thanks to the significant advantages of our custom-made imaging system over commercially available devices.

The ability of the SLN to predict the nodal involvement of metastasis was assessed by standard histopathological examination. Considering all the cases in the study in which a

[19] MB has been previously used as a vital dye for SLN detection in endometrial cancer (Li *et al.*, 2009).

SLN was found (n = 35), five cases (14%) had a positive SLN. In three of these cases, the SLN was positive and all the other LNs were negative. Although this is considered as `false positive`, a small number of cancer cells could be trapped in the first LN only, due to the expected orderly spread of the disease through the lymphatic system. Patients with a false positive SLN would therefore be likely to benefit from lymphadenectomy.

In this study, two false negatives were observed in endometrial and vulval cancer, both in the group of cases considered as part of the learning curve. In the endometrial case, the patient was morbidly obese, with previous history of abdominal surgeries, which might have affected the normal lymphatic supply. In the vulval cancer case, the false negative SLN could not be clearly justified. A plausible speculation for this failure may be attributable to the lower detection rate that was observed for the non-optimised dose group.

Comparison with previous work

NIR fluorescence detection of SLN using ICG has been performed, by others, in a number of studies in gynaecological cancers. These studies, updated to September 2014, are summarised in Table 10. Unlike previous work by other groups, our study combined endometrial, cervical and vulval cancer using the same imaging system. The detection rate (100%) reported in this work for the group with optimised injected dose was comparable to some of the other studies. However, the SLN detection rate reported by other groups varied across different studies that used the same imaging system, suggesting that a standardisation of this technique is needed. The approach presented in this work proposes a standardised method that uses the same imaging device and that provides a satisfactory detection rate using the fluorescence technique.

Reference	*Cancer type*	*Surgical procedure*	*Imaging device*	*No. of cases*	*SLN detection rate*
(Furukawa *et al.*, 2010)	Cervical	Open	Photodynamic Eye	12	83%
(Crane *et al.*, 2011b)	Cervical	Open	Munich system	10	60%
(Crane *et al.*, 2011a)	Vulval	Open	Munich system	10	100%
(van der Vorst *et al.*, 2011)	Cervical	Open	Mini-FLARE	9	100%
(Rossi *et al.*, 2012)	Endometrial/ Cervical	Robotic-assisted laparoscopy	Da Vinci + FIREFLY	20	85%
(Holloway *et al.*, 2012)	Endometrial	Robotic-assisted laparoscopy	Da Vinci + FIREFLY	35	100%
(Hutteman *et al.*, 2012)	Vulval	Open	Mini-FLARE	9	100%
(Schaafsma *et al.*, 2012)	Cervical	Open	Mini-FLARE	18	78%.
(Schaafsma *et al.*, 2013)	Vulval	Open	Mini-FLARE	24	79%
(Rossi *et al.*, 2013)	Endometrial	Robotic-assisted laparoscopy	Da Vinci + FIREFLY	29	62%
(Mathéron *et al.*, 2013)	Vulval	Open	Photodynamic Eye	15	100%
(Jewell *et al.*, 2014)	Endometrial/ Cervical	Robotic-assisted laparoscopy	Da Vinci + FIREFLY	227	95%
(Sinno *et al.*, 2014)	Endometrial	Robotic-assisted laparoscopy	Da Vinci + FIREFLY	38	92%

Table 10: Other gynaecological cancer studies on SLN fluorescence imaging.

Future directions

Despite the fact that the technique has been optimised to achieve ~100% SLN detection rate, patients outcomes can be improved only if the detected SLN is capable of predicting the metastatic status of all the other LNs. As the incidence of metastatic disease in the lymphatic system is around 15-20% (Novak & Berek, 2007), a large number of cases is needed in order to determine the rate of false negative SLNs using the fluorescence method. Determination of sensitivity and specificity and their comparison with values

obtained with the combined radiocolloid-blue dye method will be crucial towards the use of fluorescence SLN mapping in gynaecological cancers as a standard of care.

4.2 *In vivo* imaging of ovarian cancer by targeting c-Met receptors

Although its fluorescence detection sensitivity proved to be adequate for non-specific imaging of lymph nodes, the proposed technology for FIGS needed to be validated *in vivo* for fluorescence molecular imaging of cancer. For this purpose, the wide-field imaging system was used to pre-clinically image ovarian tumour xenografts using a fluorescently tagged peptide, recently developed by GE Healthcare. In this section, the results of these tests will be presented and potential clinical translation of fluorescence molecular imaging in FIGS will be described. As this work was the result of combined effort of several research groups (Professor Ahmed A. Ahmed *et. al*., Dr Christian Becker *et. al.*), I will only describe the aspects in which I was mainly involved.

4.2.1 Background

Ovarian cancer is the most common cause of death among women with gynaecological malignancies, accounting for almost 3% of all cancer deaths (Cancer Research UK, 2011c). In ovarian cancer, chemotherapy shows response in about 70% of the patients (Muggia *et al.*, 2000). Second-look laparoscopic evaluation of the disease has been widely performed in cases with evidence of complete chemotherapy response to determine which patients are free of residual disease. Follow-up of women with negative second-look examination has shown a recurrence rate of nearly 50% after 18 months (Gadducci *et al.*, 1998). A plausible explanation for recurrence is the presence of microscopic deposits that are not detectable with conventional laparoscopy. A distinctive molecular feature that

characterises such deposits is essential for designing a targeted-therapy specific for cancerous cells.

The trans-membrane human growth factor receptor, c-Met, plays an important role in tumourigenesis, effectively driving tumour growth in a variety of cancers (Comoglio, 2001). The c-Met receptor has been shown to be over-expressed in almost a third of ovarian cancer patients (Di Renzo *et al.*, 1994), although these data have been obtained using histological procedures, and expression may in fact be higher. This property, together with the availability of molecules that inhibit c-Met function (Comoglio *et al.*, 2008), makes it a potential biomarker for targeted therapy in patients with chemotherapy-resistant disease.

A crucial step towards a successful implementation of such therapy is the analysis of c-Met expression in the residual disease. Detection of c-Met expression in microscopic tumour deposits, however, can be challenging using conventional techniques. Because of its superior sensitivity, intra-operative fluorescence imaging is the most suitable candidate for detecting c-Met in chemotherapy-resistant disease. The ability of a novel fluorescence marker to bind to c-Met receptors was tested and the feasibility of fluorescence molecular imaging *in vivo* using the imaging system described in this work was assessed.

4.2.2 Methods

Fluorescence agent

A novel fluorescently tagged peptide (GE137, GE Healthcare) with high affinity to human c-Met was used in this study as a biomarker. The reagent consisted of a peptide conjugated to a Cy5-derived fluorophore (also known as AH114444 or Cy5.7). The fluorescence

properties of this dye were assessed by placing a 3 ml aliquot at 70 μg/ml concentration in a fluorescence spectrometer (LS-50B, Perkin Elmer). The fluorescence spectra of the GE137 marker are shown in Figure 63A. Excitation and emission peaks were measured to be around 653 nm and 675 nm respectively. Fluorescence characteristics of the agent were compatible with the 660 nm excitation channel of the imaging device, as verified *in vitro* (results not shown).

In vivo model

In vivo experiments were performed using a human ovarian cancer cell line (SKOV3) and a mouse ovarian cancer cell line (MUKA). The expression of c-Met was accurately measured using flow cytometry analysis by our collaborators (Liu *et al.*, 2014). Results showed strong c-Met expression in SKOV3 cells and no expression in MUKA cells. Although more ovarian cancer cell lines were tested for measurements of c-Met expression, only SKOV3 and MUKA were used for the *in vivo* experiments.

Seven to eight week old female Balb/C nude mice (Charles River, UK) were used in this study. The animals were treated according to the standards set and permitted by the UK Home Office and Oxford Ethical Review Committee. Mice were injected subcutaneously in the dorsal side with 2×10^6 cells (SKOV3 and MUKA) suspended in 200 μl PBS. Due to immune system inhibition, all animals developed tumours after ~20 days. The fluorescently tagged peptide GE137 and the Cy5.7 dye were injected in the mouse tail at 48 μg/ml concentration (0.08-0.1 ml/20g mouse). Fluorescence uptake by the tumour was observed transcutaneously up to 8 hs after injection using the wide-field imaging system.

Imaging setup

The wide-field imaging system was placed on top of the anesthetised mouse at ~350 mm working distance using a flexible arm (Figure 63B). Images were acquired at 660 nm excitation and 40 ms camera exposure times. Room lights were switched off to reduce unwanted illumination. Image acquisition was performed using IC Capture (The Imaging Source) while live video was displayed on a monitor for real-time fluorescence-guided tumour excision.

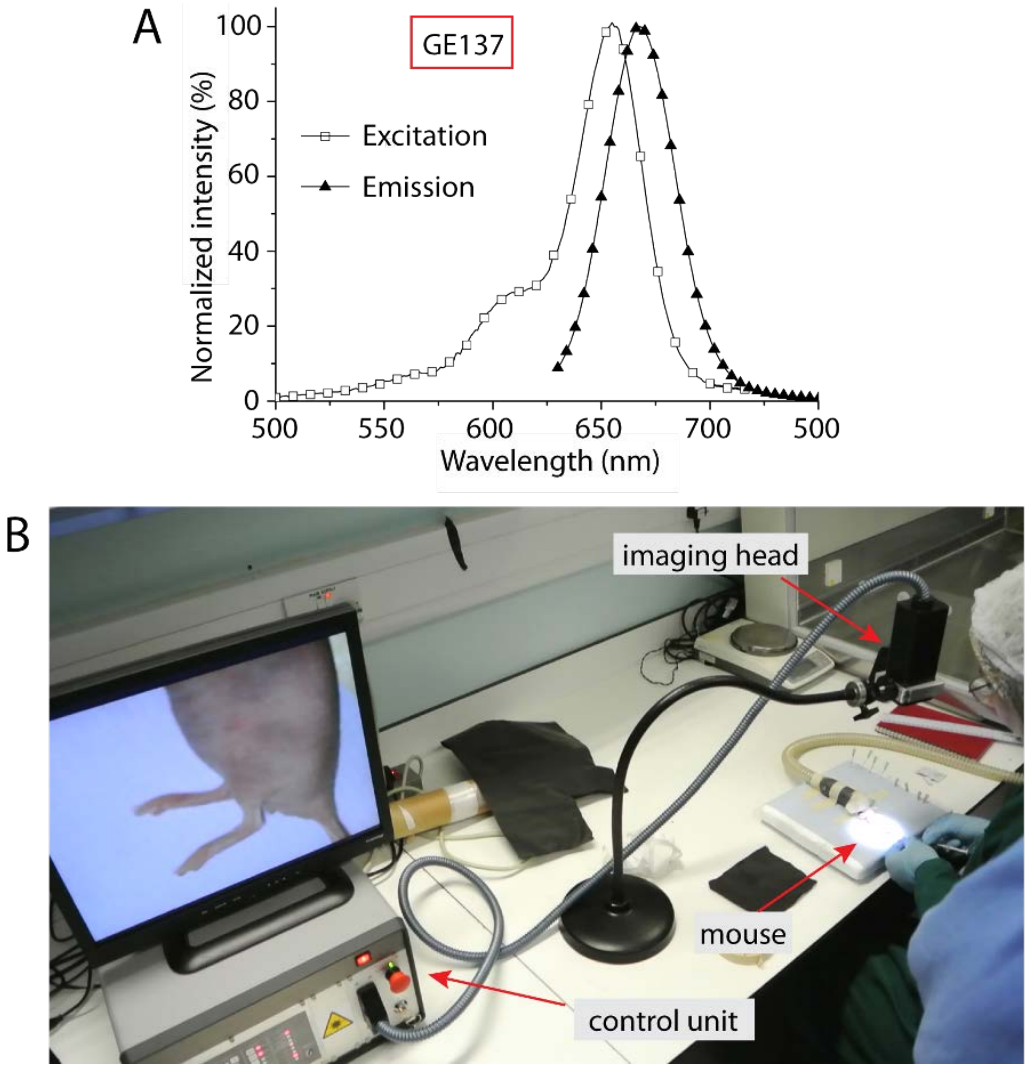

Figure 63: GE137 fluorescence spectra (A) and *in vivo* imaging setup (B).

Image analysis

Quantitative image analysis was performed using ImageJ. The tumour-to-background ratios (TBR) were calculated by dividing the average fluorescence signal in a region of interest (ROI) corresponding to the tumour by the same value from a ROI surrounding the tumour. Both ROIs included at least 2000 image pixels. Results were expressed as the mean TBR from 3 mice.

4.2.3 *In vivo* imaging results

Tissue autofluorescence

During the first imaging experiments, a strong autofluorescence signal was observed in the mouse bowel prior to injection of the agent (Figure 64A). The intensity of the autofluorescence caused saturation of the image signal, even with the system used at its lowest sensitivity. This was a significant limiting factor in the detection of intentionally added fluorophores using the 660 nm excitation wavelength. As the source of this unwanted signal was likely to be associated with the diet, a sample of food used to feed the mice (RM3 (E) DU, Special Diet Services, UK) was imaged with the same system. Results confirmed a very strong autofluorescence at 660 nm (Figure 64A), with no signal observed following excitation in the NIR (785 nm) (not shown).

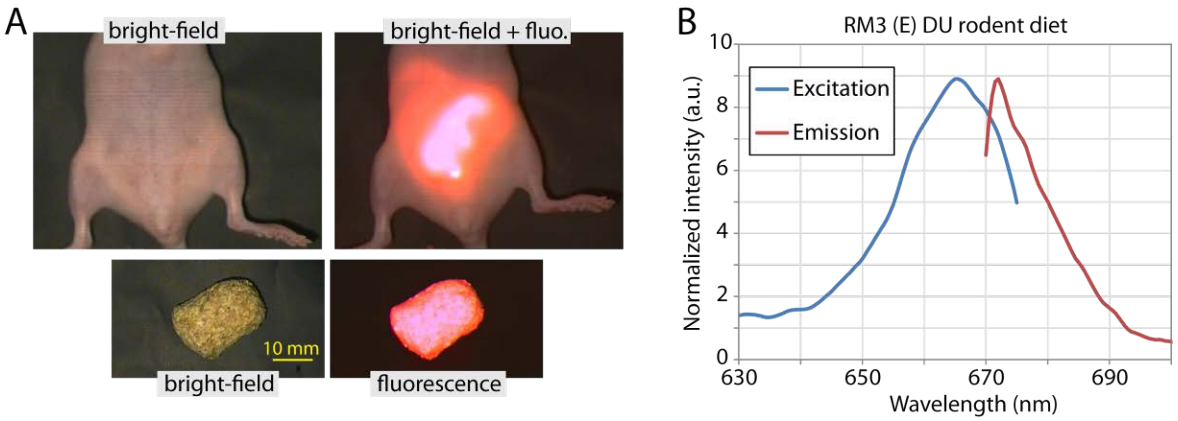

Figure 64: Autofluorescence using conventional rodent diet. (A) Autofluorescence from the mouse bowel (top) and fluorescence imaging of a sample of the diet (bottom). (B) Fluorescence spectra of the rodent diet used.

The fluorescence spectra of the diet were assessed by spectroscopic measurements. The food pellet was broken up and placed in a beaker containing 5 ml of ethanol. The mixture was stirred at room temperature for 2-3 hs and then centrifuged at 10,000 rpm for 200 s to remove the solid material. Spectroscopic measurements obtained with the fluorescence spectrometer showed excitation and emission spectrum peaked at 665 nm and 672 nm respectively (Figure 64B). The close match to the fluorescence imaging system excitation channel explained the strong signal observed *in vivo*. The fluorescence signal originating from the diet was likely to be due to the chlorophyll of alfalfa, a perennial flowering plant present in food rich of vitamin D (Troy *et al.*, 2004).

An alfalfa-free rodent diet (2919, Harlan) was purchased to attempt reducing *in vivo* autofluorescence. This new diet provided a significantly lower autofluorescence signal when directly imaged in its original form (Figure 65A).

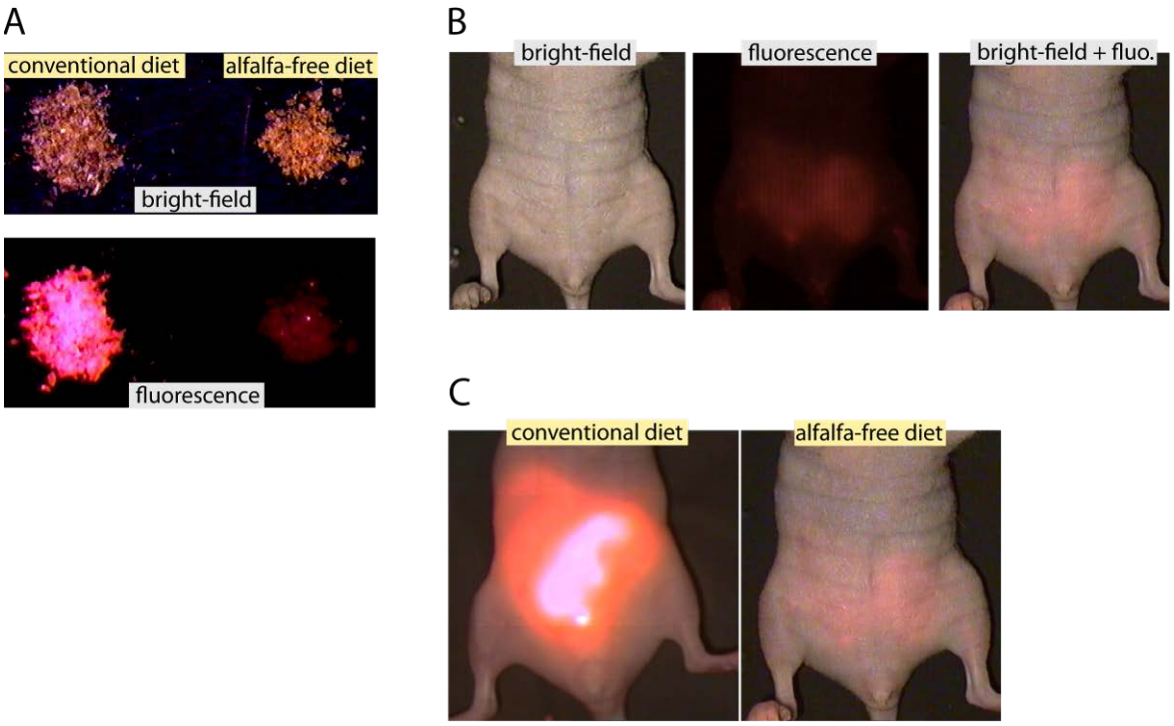

Figure 65: Autofluorescence using alfalfa-free rodent diet. (A) Fluorescence comparison between conventional (left) and alfalfa-free (right) diets. (B) Autofluorescence from a mouse fed with the new alfalfa-free diet. (C) *In vivo* autofluorescence comparison between the two diets. All the fluorescence images were acquired with 40 ms camera exposure time.

Following this test, mice were subsequently fed with an alfalfa-free diet for 11 days before imaging. Figure 65B shows the strongly reduced autofluorescence signal from a mouse at 660 nm excitation.

When compared with the conventional diet (Figure 65C), the alfalfa-free diet significantly decreased the background, thus ultimately improving detection of exogenous fluorescence contrast agents.

Fluorescence imaging of c-Met

Following intravenous GE137 injection, the fluorescence rapidly increased in the urinary bladder and kidneys before being discharged (data not shown). The wide-field imaging system detected SKOV3 tumour deposits in real time (40 ms exposure), both transcutaneously and post-excision (Figure 66). No tumour uptake was observed when only the Cy5.7 dye was injected.

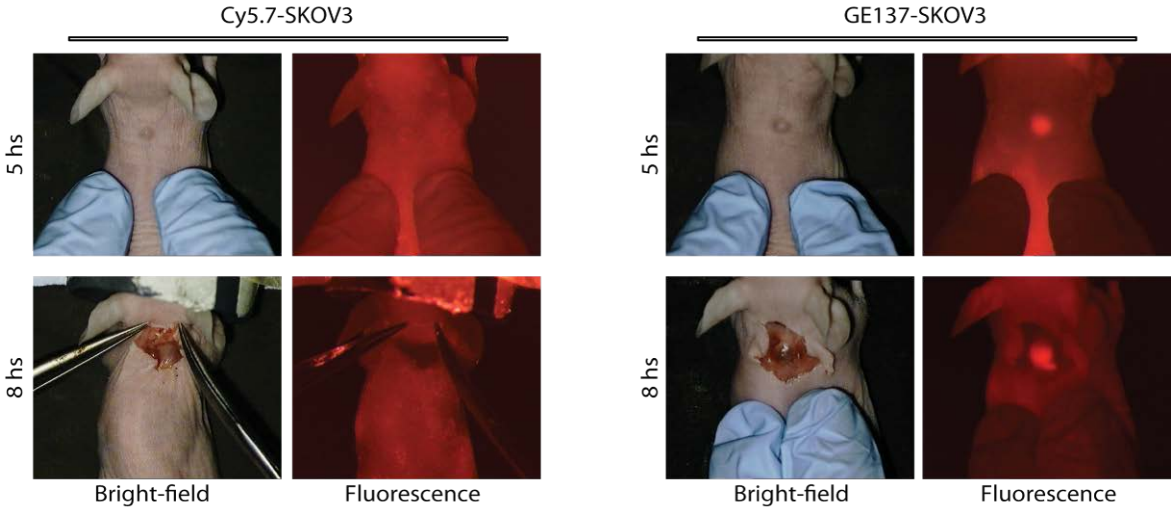

Figure 66: Subcutaneous SKOV3 xenografts imaging results. Fluorescence and bright-field images obtained 5 and 8 hs following intravenous injection of Cy5.7 (left) or GE137 (right). Adapted from (Liu *et al.*, 2014).

The fluorescence intensity expressed in TBR was superior for the SKOV3 xenografts compared to the MUKA xenografts, confirming the different c-Met expression of the two cell lines (Figure 67A).

Transcutaneous imaging of SKOV3 xenografts showed that TBR reached a plateau at ~3 hs following tracer injection (Figure 67B). This plateau persisted throughout the experiment duration (8 hs). Sub-millimetre tumour deposits were observed

transcutaneously and in real time, confirming the ability of the imaging system in detecting c-Met with high sensitivity (Figure 67C).

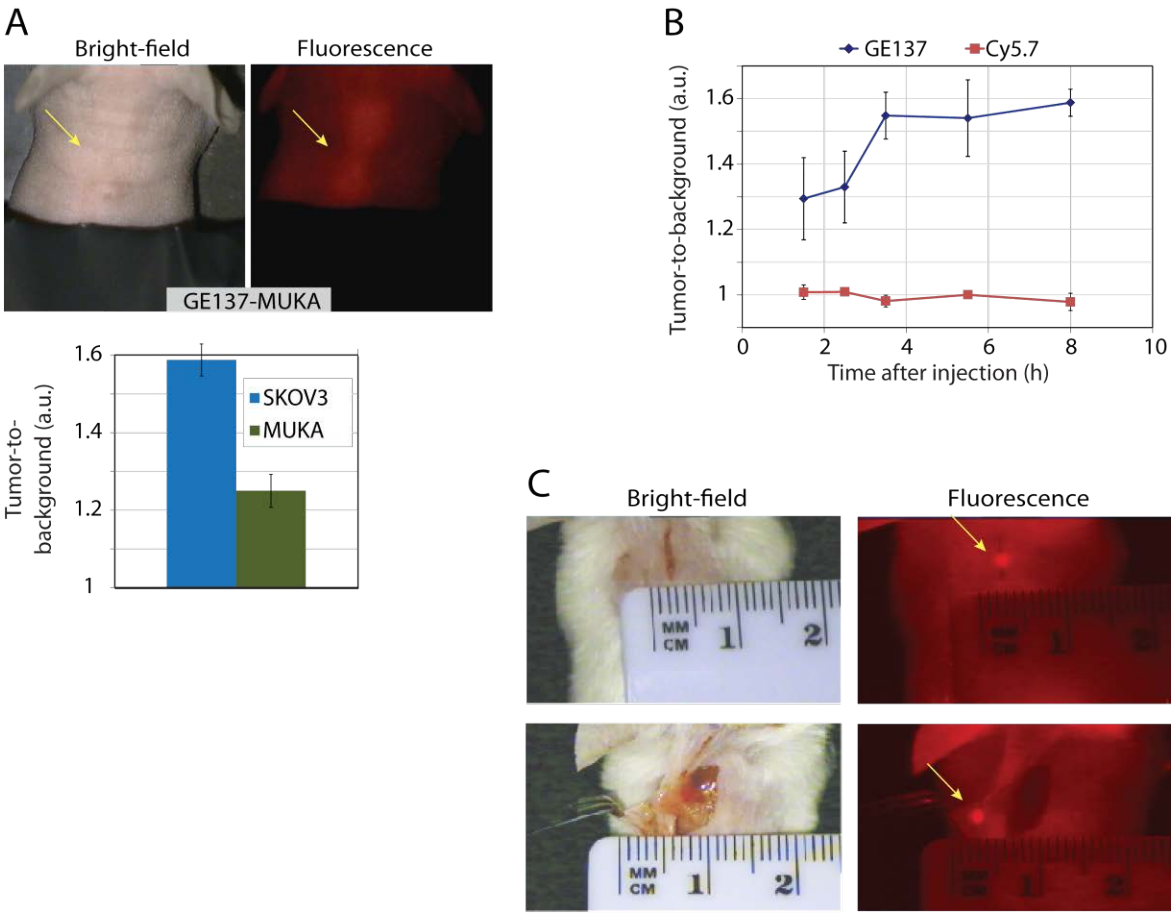

Figure 67: *In vivo* fluorescence imaging results. (A) Fluorescence and bright-field images of subcutaneous MUKA xenografts at 8 hs after GE137 injection. Also shown is the TBR at 8 hs for SKOV3 and MUKA xenografts. (B) Variation of TBR following injection of GE137 and Cy5.7 in SKOV3 xenografts over a time period of 8 hs. Error bars represent the standard deviation of the mean of measurements on 3 mice. (C) Transcutaneous and intra-operative fluorescence detection of a sub-millimetre SKOV3 deposit. Adapted from (Liu *et al.*, 2014).

4.3 Other practical experience with fluorescence molecular imaging

In the previous sections, the successful use of the FIGS imaging systems in both clinical and pre-clinical studies was demonstrated. The principle results from further additional FIGS imaging work, in which I was involved, will be introduced and presented here.

4.3.1 Targeting colorectal dysplasia using fluorescently-labelled lectins

In the UK, over 40,000 patients are diagnosed each year with colorectal cancer, accounting for nearly 10% of all cancer deaths (Cancer Research UK, 2011d). Colonoscopy is an essential diagnostic and therapeutic procedure in the management of colorectal cancer. White-light endoscopy, in particular, has remained the gold standard for screening and surveillance. Early detection of colorectal lesions, however, presents a significant challenge when no distinguishing features are present. For this reason, the development of a fluorescence molecular marker that can identify pre-cancerous lesions or dysplasia has the potential to improve early cancer detection rates and to reduce false-negative colonoscopies.

‘Wheat germ agglutinin’ (WGA) is a lectin that has been used to highlight dysplasia areas in Barrett's oesophagus (Bird-Lieberman *et al.*, 2012). Some of our collaborators investigated the possibility of using a different fluorescently labelled lectin as a probe to detect dysplasia and pre-cancerous lesions in colorectal cancer. *Ex vivo* imaging experiments to test the binding of a novel lectin using the FIGS imaging systems will be described here.

Methods

Our collaborator, Dr. Trevor M Yeung, Nuffield Department of Surgical Sciences, University of Oxford, demonstrated that the lectin '*Wisteria floribunda*' (WFA) specifically binds to MUC2 proteins that are the predominant component of mucus. For this reason, he investigated the possibility of using WFA as a fluorescence marker to label healthy tissue and create a negative contrast agent for dysplasia. WFA was labelled with Cy5 dye (PA25001, mono-reactive dye, GE Healthcare) to exploit the 660 nm excitation channel of the FIGS devices. For the *ex vivo* experiments, freshly excised tissue samples were sprayed with Cy5-labelled WFA lectin at a concentration of 5 µg/ml and rinsed twice with PBSA. Baseline white light and autofluorescence images were acquired prior to dye application. Exposure times ranged from 40 ms to 160 ms. All imaging procedures were performed in the dark to minimise background signals.

Results

Following topical application of the Cy5-labelled WFA, fluorescence laparoscopy showed clear distinction between non-dysplastic tissue and cancer in a freshly excised tissue, as confirmed by H&E stained histological analysis (Figure 68A). A 10 min period of time between topical administration of the dye and first cycle of washing was allowed to elapse in order to secure binding.

The second specimen was obtained from transanal endoscopic microsurgery, and fluorescence was able to distinguish normal mucosa from cancer (Figure 68B). Unlike the previous specimen, the cancer was not clearly visible under bright-field illumination, and the variation of the fluorescence signal could noticeably highlight the boundary with healthy tissue.

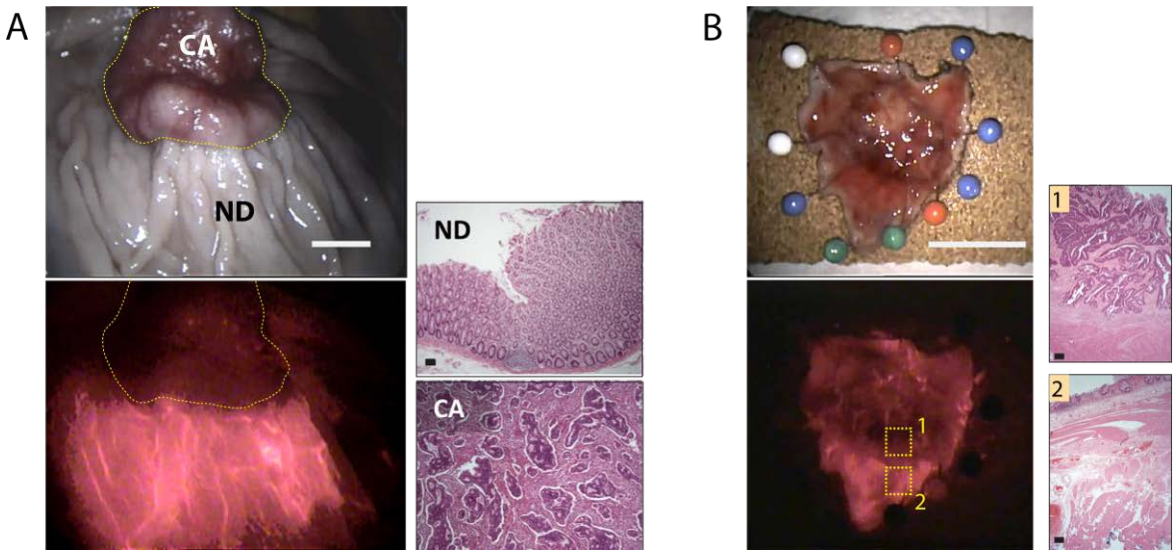

Figure 68: Fluorescence laparoscopic imaging of freshly excised tissues. Bright-field images and histological validation (4× objective) are also shown. (A) Imaging of normal and cancer tissue (encircled in dashed yellow line). Scale bars: 10 mm (laparoscopy) and 200 µm (histology). (B) Imaging of a specimen from transanal endoscopic microsurgery. Scale bars: 50 mm (laparoscopy) and 200 µm (histology). Histology images courtesy of TM Yeung and LM Wang.

The third specimen was an anterior resection with multiple colonic polyps (tubular adenomas). Given the large size of this specimen, imaging was performed using the wide-field device. Fluorescence imaging showed clear differences between the polyps and the normal mucosa (Figure 69A).

In a fourth specimen, simulated fluorescence colonoscopy was performed by insufflating and intubating the excised tissue and imaging with the rigid laparoscope. Differences in fluorescence emission signal showed two cancerous lesions: one that was visible under bright-field imaging (CA1 region in Figure 69B) and another flat lesion (CA2, encircled in blue) that was not apparent with conventional endoscopy. Quantitative image analysis showed an average normal to cancerous tissue ratio of 3.6 calculated considering all imaging results.

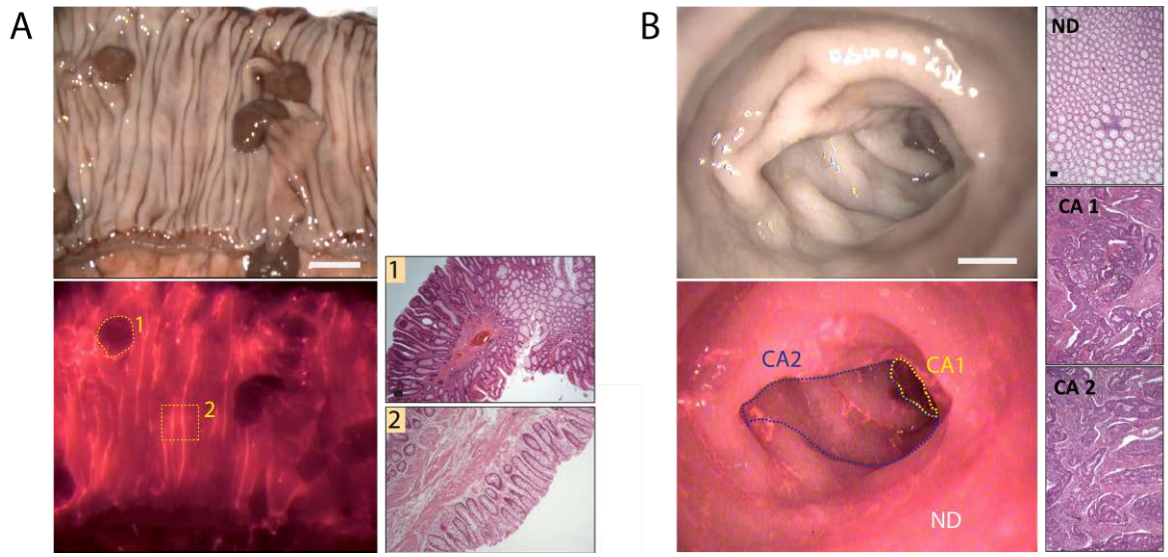

Figure 69: Wide-field imaging and simulated endoscopy of freshly excised tissue. (A) Large excised specimen imaged with the wide-field system. Scale bars: 10 mm (wide-field) and 200 µm (histology). (B) Simulated fluorescence colonoscopy on *ex vivo* tissue under insufflation showing a flat lesion (CA2) not detectable with bright-field. Scale bars: 10 mm (laparoscopy) and 200 µm (histology). Histology images courtesy of TM. Yeung and LM Wang.

4.3.2 Imaging prostate cancer with NIR fluorescence

Prostate cancer is the most common cancer in men, responsible for over 10,000 deaths in the UK each year (Cancer Research UK, 2011e). One of the main issues that contribute to the rate of mortality is the inability to clearly assess surgical margins during prostatectomy[20] (Swindle *et al.*, 2005). Current methods for prostate cancer detection include ultrasound (Hodge *et al.*, 1989) and MRI (Roethke *et al.*, 2012) for biopsy guidance, while SPECT and 18F-choline PET have been used during disease management (Beheshti *et al.*, 2013; Manyak, 2008). The poor spatial resolution and sensitivity of such techniques, however, is a limiting factor in the detection of small tumour deposits and in the assessment of surgical margins.

[20] Prostatectomy is the surgical removal of the prostate gland.

Prostate-specific membrane antigen (PSMA) is a transmembrane protein that is expressed in a variety of cancer tissues (Silver *et al.*, 1997). In prostate cancer, PSMA is a particularly suitable target for molecular imaging and therapy because of its significant over-expression (Ghosh & Heston, 2004). Intra-operative fluorescence molecular imaging of prostate cancer has the potential to improve tumour margin assessment and to highlight lesions that would be missed using conventional techniques. In collaboration with another research group from the Nuffield Department of Surgical Sciences (Professor Freddie Hamdy *et. al.*), we investigated the possibility of using a novel NIR molecular agent to image prostate cancer by targeting PSMA.

Methods

An anti-PSMA minibody, developed by ImaginAb Inc. (Inglewood, CA, USA) and conjugated to IR800CW (LI-COR Biosciences) was obtained by our collaborators for *in vitro* fluorescence imaging of cells expressing PSMA. The excitation and emission peaks of the fluorophore were 773 nm and 792 nm respectively, as reported by the manufacturer.

A variety of human cancer cell lines were tested in this study: prostate (22Rv1 and LNCaP), bladder (Cal 29), kidney (RCC4) and pancreas (PANC-1). 22Rv1 and LNCaP cells were grown in RPMI medium containing 10% fetal bovine serum (FBS). Cal 29 cells were grown in DMEM medium with Glutamax supplemented with 10% FBS. RCC4 and PANC-1 cells were grown in DMEM medium with 10% FBS. After *in vitro* proliferation, 2×10^4 cells were seeded in 96-well plates 24 hs prior to antibody incubation. Cells were incubated in 2 μg/ml antibody in phosphate buffered saline (PBS) with 1% bovine serum albumin (BSA) at 37 ˚C and 5% CO_2. Following 1 to 4 hs incubation, cells were repeatedly washed with PBS at 37 ˚C before imaging.

Fluorescence imaging was performed using a customised microscope developed by our research group (Barber *et al.*, 2013). The microscope was used in wide-field mode with a conventional Köhler epi-illumination optical arrangement. A 785 nm laser diode (APCD-780-50, Roithner Laser Technik) with 60 mW optical power was added as NIR excitation source. The laser module was coupled to a 3 mm core diameter liquid light guide conventionally used for delivery of excitation light from a lamp (Figure 70A). Bright-field illumination was provided by a white LED.

A customised filter cube was used to select excitation and emission wavelengths. In order to have the same filtering arrangement as the FIGS systems described in this work, a laser clean-up (FF01-786/22-25, Semrock) and notch (NF03-785E-25, Semrock) filters were placed in the excitation and emission path respectively. An 801 nm single-edge dichroic beamsplitter (FF801-Di02-25×836, Semrock) was used to separate the two beams. A customised plate-supporting stage insert was used for correct positioning of the multi-well plate. Fluorescence imaging was performed using a 20×, 0.5 NA objective, 2× pixel binning and camera exposure time ranging from 1 to 2 s. A customised software interface was used for microscope control and image acquisition. Brightness levels of fluorescence images were normalised to 1 s exposure for comparison. Fluorescence and bright-field image overlays were performed using PaintShop Pro 8 (Jasc Software).

Results

Fluorescence imaging of the LNCaP cell line showed significant differences in the fluorescence emission signal between 1 and 4 hs of incubation time (Figure 70B). Differences in the fluorescence signal were also observed among two different prostate cancer cell lines (LNCaP and 22Rv1) both with 1 h (not shown) and 4 hs antibody

incubation time (Figure 70C). This suggested, as expected, different levels of PSMA expression within different prostate cancer cell lines. As expected from their almost total lack of PSMA expression, bladder (Cal 29), kidney (RCC4) and pancreas (PANC-1) cells showed significantly lower fluorescence signal even after 4 hs incubation time (Figure 70D).

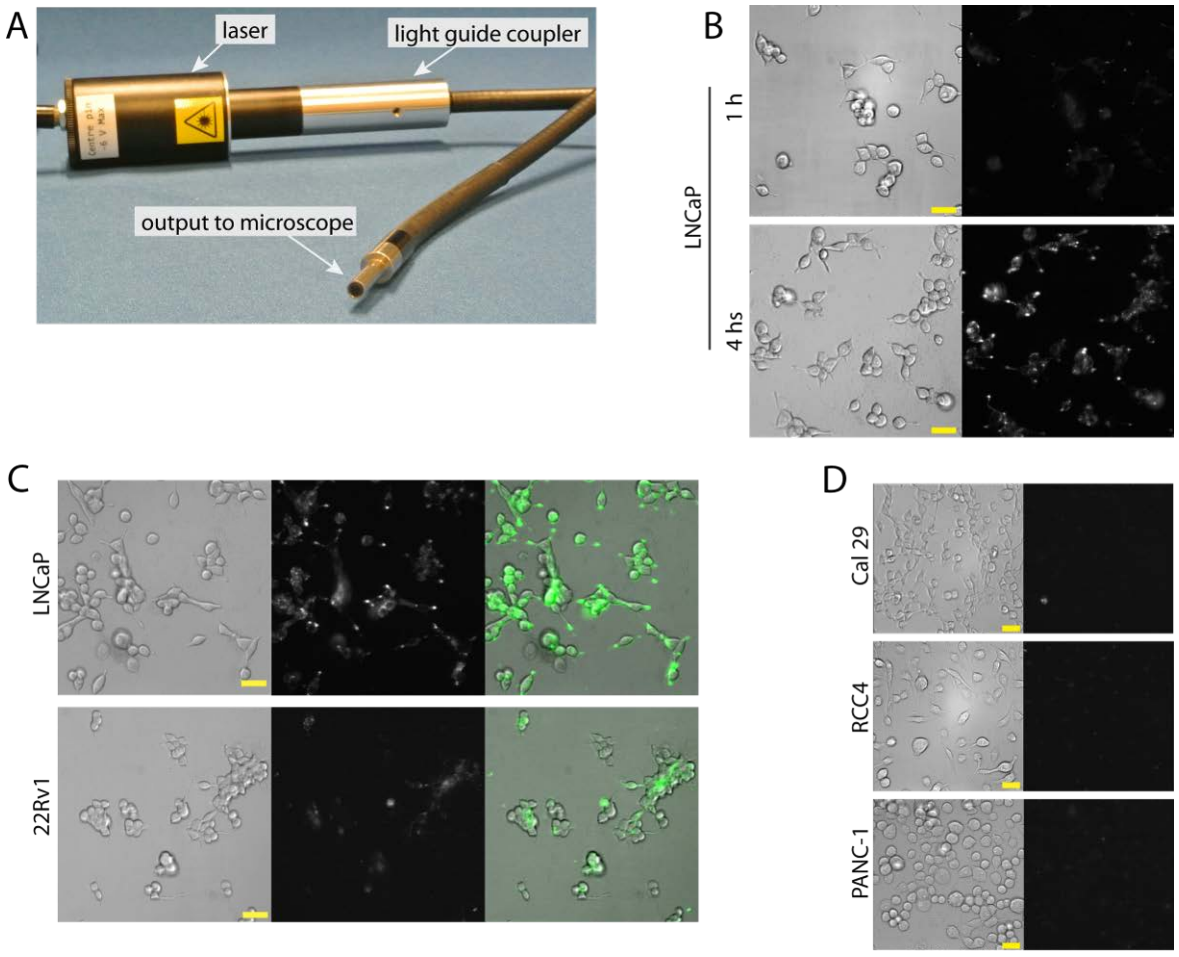

Figure 70: Fluorescence microscopy imaging of PSMA. (A) Custom-made 785 nm laser module for fluorescence excitation. (B) LNCaP prostate cancer cells imaged with bright-field (left) and fluorescence (right) at 1 and 4 hs of antibody incubation. (C) Bright-field, fluorescence and merged images of two prostate cancer cell lines after 4 hs antibody incubation. (D) Bright-field and fluorescence images at 4 hs of bladder (top), kidney (middle) and pancreas (bottom) cell lines. Scalebars: 50 µm. All fluorescence images are normalised to 1 s exposure.

4.4 Discussion of Chapter 4

In this chapter, a variety of practical applications using the FIGS systems were shown, along with a number of studies relevant for the emerging field of intra-operative fluorescence molecular imaging.

SLN detection in gynaecological cancers

The imaging systems were successfully used in a clinical study for SLN detection using non-specific fluorescence contrast agents ICG and MB. The clinical results that were presented suggest that both the laparoscopic and the wide-field imagers were effectively optimised to allow rapid clinical translation. Testing the reliability of the devices was essential towards future clinical applications using tumour-specific markers. Following optimisation of the injection technique, intra-operative SLN detection in gynaecological cancer using both devices was close to 100%. However, a larger number of cases (typically >50) are needed to further validate the superiority of this technique in comparison to conventional methods and to demonstrate the ability of the SLN to predict the metastatic status of the lymphatic basin in gynaecological cancers. These studies are ongoing at time of writing this thesis.

The clinical results presented in this chapter indicated that the imaging systems are safe and reliable for intra-operative use. Remarkably, intra-operative laparoscopic imaging of two different fluorescence dyes was demonstrated for the first time in humans. Results indicate that the two dyes can be spectrally distinguished and can therefore be used to observe independent lymphatic vasculatures.

A number of technical improvements should be considered following limitations observed during clinical use. These improvements include the use of a NIR-optimised laparoscope to increase detection light throughput, an even simpler user interface and implementation of an autofocus system for the wide-field device.

Pre-clinical imaging of c-Met in ovarian cancer

In ovarian cancer, microscopic residual chemotherapy-resistant disease constitutes a major clinical problem for patients with negative second-look, with ~50% recurrence rate within 18 months (Gadducci *et al.*, 1998). Because of its role in growth and proliferation of human cancer, the c-Met signalling pathway has been suggested as a plausible target for cancer therapy in patients with high expression of this proto-oncogene (Gherardi *et al.*, 2012). Experiments performed by our collaborators showed that over-expression of c-Met in tumour cells occurred in ~50% of ovarian cancer patients (Liu *et al.*, 2014). As a result, intra-operative assessment of c-Met expression in residual disease could be a key factor for the selection of patients suitable for c-Met targeting therapy.

Pre-clinical tests with a novel fluorescence molecular marker targeting c-Met and its potential use for intra-operative tumour detection were shown in §4.2. The wide-field imaging system provided excellent ability in detecting *in vivo* sub-millimetre deposits of cancer cells over-expressing c-Met. Moreover, real-time imaging allowed fluorescence-guided tumour resection, with significant potential for future clinical applications. Results showed retention of fluorescence signal in tumours for at least 8 hours, suggesting that clinical implementation would be possible. Although the results described here were obtained using the wide-field imaging system, the use of the camera at its lowest

sensitivity suggests that the fluorescence signal from GE137 is also likely to be suitable for laparoscopic imaging.

Targeting colorectal dysplasia using fluorescently-labelled lectins

Ex vivo detection of a novel fluorescently labelled lectin (WFA) using the FIGS systems was shown in §4.3.1. Preliminary results demonstrated that Cy5-WFA specifically binds to the MUC2 receptor that is expressed mostly in healthy mucosal tissue. Simulated fluorescence colonoscopy and wide-field fluorescence imaging confirmed the ability of Cy5-WFA to detect flat cancerous and pre-cancerous lesions that would be inevitably missed with conventional imaging modalities. Moreover, these results suggest that fluorescence can guide surgical resection of lesions during endoscopy, as demonstrated by the short exposure time (40-160 ms) used in the experiments.

The Cy5-WFA probe was verified to bind strongly to the mucosa surface, as repeated rising of up to 20 times did not affect the fluorescence signal. The main characteristic of this agent is that it binds to healthy tissue, thus creating a negative contrast mechanism to detect cancerous tissue. Although labelling cancer tissue appears to be a more intuitive approach, a positive contrast agent could potentially increase the rate of false negative results, which is undoubtedly more dangerous than false positives. From this prospective, a negative contrast agent could be considered as a safer approach for fluorescence detection of cancer.

As Cy5 dye is still awaiting approval for human use, clinical translation of the lectin-based probe will require bio-conjugation with approved fluorophores such as fluorescein. The use of a NIR fluorophore would ultimately improve fluorescence contrast due to reduced

autofluorescence. Future developments of this method will certainly consider the possibility of exploiting NIR-based contrast agents.

In vitro imaging of prostate cancer

The possibility of using a novel NIR fluorescence molecular marker to detect prostate cancer by targeting PSMA was demonstrated in §4.3.2. *In vitro* results showed a significantly higher (>>20 fold) fluorescence intensity from prostate cancer cells in comparison to cells from other organs. Differences in the fluorescence signal were observed between two different prostate cancer cell lines, LNCaP and 22Rv1. Results suggest that PSMA is expressed at higher levels in LNCaP in comparison with 22Rv1 cell line, as confirmed by previous studies (Regino *et al.*, 2009). A dramatic increase in the fluorescence signal was observed when the cells were incubated with the antibody for 4 hs before imaging. Further tests with longer incubation periods should be performed to determine signal-to-background dynamics. The use of a similar filtering arrangement for the microscope demonstrated that the FIGS devices are suitable for fluorescence imaging of this novel marker. Unfortunately, the limited availability of the marker did not allow for measurements of excitation and emission spectrum.

The wide-field FIGS system described in this work was eventually used by our collaborators in the United States for *in vivo* testing of the anti-PSMA marker. Results showed detection of 22Rv1 subcutaneous tumours in SCID and nude mice in real time, demonstrating the tremendous potential of the system to detect cancer tissue over-expressing PSMA. Moreover, detection and image-guided resection of submillimetre tumour deposits suggested that intra-operative fluorescence imaging of prostate cancer deposits is feasible.

Because of the widely recognised benefits of prostatectomy by means of keyhole surgery (Türk *et al.*, 2001), future work is needed to further validate this imaging approach during laparoscopy.

General discussion

Overview and originality of this thesis

The aim of this dissertation has been to suggest solutions to some of the limitations in conventional surgical oncology by exploiting intra-operative fluorescence imaging. This was accomplished through a theoretical characterisation of the imaging technique, the development of a novel imaging technology and a successful clinical implementation of such technology. The research has resulted in a number of original contributions to the body of knowledge on fluorescence image-guided surgery (FIGS):

- Development of a novel theoretical model to quantify and predict imaging performance in FIGS;
- Development of a graphical user interface to model practical situations in FIGS;
- Design, development and testing of FIGS imaging systems for open and minimally invasive (keyhole) surgery, designed to overcome some of the limitations of existing technologies;
- Design, prototyping and testing of a novel wide-field imaging system that exploits focus-tuneable lens technology;
- Clinical study on sentinel lymph node mapping in gynaecological cancer with first in-human laparoscopic imaging of two fluorophores during the same procedure;
- Testing of novel cancer-specific molecular markers *in vivo*, *ex vivo* and *in vitro*.

Impact of this work

Surgery is the most popular and successful way to treat cancer (Siegel *et al.*, 2012). This practice relies on the ability of the surgeon to remove the tumour effectively while preserving healthy tissue. Ultimately, the patient is cured when all the cancer cells are removed from the body. Surgery, however, is currently based on visual inspection and palpation to detect and remove lesions. Such contrast mechanisms pose a number of limitations that significantly hinder the clinical outcomes of a surgical procedure. Firstly, cancer tissue is often not distinguishable from normal tissue under direct inspection. This is particularly evident for certain types of flat lesions where the eyes and hands of the surgeons may be inadequate for complete detection (Rembacken *et al.*, 2000). Secondly, small cancerous lesions can be missed by the human eye because of its limited spatial resolution. This is the case, for example, of microscopic residual disease which are often not recognised during resection of the primary tumour (Sugarbaker, 1999). Lastly, conventional surgery is based on subjective assessment of the disease and surgeon's experience, which inevitably improves with time.

Fluorescence image-guided surgery (FIGS) is rapidly emerging as a complementary technique to conventional surgical practice that can improve surgical outcome by bringing an additional contrast mechanism to assist the surgeon's vision. This technique relies on the development of sensitive imaging systems and effective fluorescence markers appropriate for clinical use. Tumour-specific markers, in particular, are becoming increasingly attractive in surgical oncology because of their specificity at the molecular level (Hussain & Nguyen, 2014).

Tumour detection prior to the angiogenic switch is likely to have a significant impact in cancer diagnosis, as it could identify the disease before uncontrolled proliferation of

malignant cells (Naumov *et al.*, 2006). Other imaging modalities are limited to a detection threshold of ~10^9 cells (corresponding to ~1 cm^3 solid tumour) (Weissleder, 2006), despite that ~10^6 cells are believed to be sufficient for the angiogenic switch (Folkman, 1971).

In order to assess the ability of FIGS to detect pre-angiogenic cancer lesions, a theoretical model that aimed to quantify the performance of intra-operative fluorescence molecular imaging was described (Chapter 2). Modelling showed that fluorescence detection of ~10 and ~5000 cells is feasible during open and laparoscopic surgeries respectively. This result was obtained using practical parameters that are typical in real situations and by considering realistic biological data. The sensitivity of FIGS, as predicted by the model, confirmed the potential of this technique in detecting cancer before the angiogenic switch. The model also showed that detection of deep (10s of mm) samples is feasible using NIR wavelengths, although both the minimum number of cells detectable and the spatial resolution dramatically decrease with sample depth. Moreover, it confirmed the need of using sensitive imagers, particularly during keyhole surgery, where light losses in the optical system are significant.

The originality of this model relies on the relationship between biology (cell and receptor number) and imaging (number of photons and pixel counts). As the model provides a quantitative description of the complete FIGS procedure, an open-source graphical user interface (GUI) that can be used to control all the input parameters and to visualise the results was developed. This GUI was made available to the community, providing a tool to be used as guidance for the development of FIGS devices.

Modelling results on cellular sensitivity were useful to determine the technological requirements of the FIGS imaging devices that were developed in our research group and that were described in Chapter 3. The key aspect of such systems was the use of a single,

miniaturised camera to simultaneously detect bright-field and fluorescence from multiple excitation wavelengths during open and keyhole surgery. This was a significant improvement over other existing systems that typically operate at a single excitation wavelength or use bulky detectors not suitable for hand-held operation. The multi-wavelength capability of this FIGS technology offered a significant advantage as it could independently visualise different structures (for example tumour and nerves) using novel molecular contrast agents (Whitney *et al.*, 2011).

The capability of the imaging system to work in wide-field mode and in conjunction with a laparoscope offered a wide range of potential clinical applications. Due to the availability of clinically approved, non-specific fluorescence dyes, one of the most widespread uses of FIGS is for sentinel lymph node (SLN) mapping (Xiong *et al.*, 2014). The fluorescence technique is used to overcome the limitations of detection methods based on radioactive tracers, vital blue dyes or a combination of the two. In this work, the clinical use of the FIGS systems in gynaecological cancers, where the SLN concept is still unproven, was described (Chapter 4). Following a number of cases (~30) required for mastering the new technique and for injection optimisation, SLN detection rate with ICG dye approached 100% for endometrial, cervical and vulval cancers.

Multi-wavelength fluorescence detection during laparoscopy was accomplished using ICG and MB dyes. To the best of my knowledge, this was the first attempt of fluorescence imaging with multiple dyes in humans. This result demonstrated the exceptional advantages of our imaging system over most of the existing devices that operate with a single excitation channel.

In addition to assessing the feasibility of detecting SLNs in gynaecological cancers, a key aim of this clinical study was to verify the surgical usability of the imaging systems for

future applications with tumour-specific markers. Although intra-operative fluorescence molecular imaging of cancer is still at its infancy, a number of studies have shown encouraging clinical results and exceptional potential for improving cancer detection (Sturm *et al*., 2013; van Dam *et al*., 2011). In this work, the use of the FIGS systems for testing novel molecular markers for detecting cancer tissue was described. *In vivo*, *ex vivo* and *in vitro* experiments were carried out using different markers to highlight various types of cancer cells or tissues.

Pre-clinical experiments demonstrated subcutaneous ovarian cancer detection in mice, using a novel marker binding to c-Met receptors (Liu *et al.*, 2014). The proposed technology provided real-time molecular information to guide surgical resection of sub-millimetre lesions. This was a significant achievement as it confirmed the feasibility of intra-operative fluorescence molecular imaging. Although obtained with the wide-field imaging system, results from the theoretical model described in Chapter 2 indicated that comparable lesions were detectable laparoscopically following imaging optimisation (i.e. higher excitation power density and camera sensitivity). This result suggested that intra-operative fluorescence molecular imaging during laparoscopy in ovarian cancer could be exploited for detecting residual disease that is often missed during conventional observation (Gadducci *et al.*, 1998).

In separate experiments (§4.3.1 and §4.3.2), the effective use of molecular markers was demonstrated *ex vivo* in colorectal cancer tissue and *in vitro* in prostate cancer cells. In addition, further *in vivo* tests from our collaborators showed fluorescence navigation and real-time tumour resection in mice using our imaging system and a novel prostate cancer-specific molecular marker. Despite the lack of clinical results, all the experiments using targeted molecular markers presented in this work were crucial to demonstrate the high sensitivity of the FIGS imaging systems prior to clinical translation.

One of the most remarkable aspects of the technology described in this work is that the device complete design, development, testing and its clinical and pre-clinical use were fully achieved over a four-year period of time. This was made possible thanks to a technology that was guided by clinical needs as opposed to implementing complex imaging features. Such approach proved to be successful as demonstrated by the varieties of applications described in this work.

The imaging devices showed high fluorescence sensitivity as demonstrated following theoretical modelling, detection of sub-nanomolar concentrations of ICG and MB, imaging of SLNs as deep as ~20 mm and *in vivo* detection of sub-millimetre tumour deposits. The results presented here confirmed the key role that this technology can have for future developments of intra-operative fluorescence molecular imaging in oncology.

Limitations of this work

The work described in this thesis is characterised by a number of limiting factors that are summarised in this section. Despite providing a fast prediction of the performance of a FIGS imaging system, the theoretical model described in Chapter 2 uses certain approximations. These include the composition of the fluorescent sample, the characteristics of the tissue and the geometry of light collection. Moreover, a full experimental validation of the model is particularly challenging due to difficulties in estimating the correct value of some practical parameters (e.g. number of fluorophore molecules, dye dimerisation effects, tissue optical properties etc.).

The imaging systems described in Chapter 3 were designed to display raw video in real time, as this allowed more straightforward clinical translation. The systems did not make use of any post-acquisition processing algorithms that could potentially improve the SNR.

Moreover, a single miniaturised colour camera was used to collect fluorescence (and bright-field). Although beneficial in terms of size and device flexibility, the use of this camera also limited the fluorescence detection SNR.

One of the greatest weaknesses of the clinical study described in Chapter 4 was the relatively small number of patients, particularly if the learning phase is excluded (n=13). Although this proved to be adequate to validate the reliability of the imaging systems, a much greater number of cases (>50) is needed to establish its usefulness for SLN detection in gynaecological cancer. As the study is scheduled to terminate in April 2015, more women will be recruited and thus statistical relevance of the results will be improved.

Even though this work specifically focussed on FIGS applications in oncology, intra-operative fluorescence can also be exploited in a number of other medical areas. These include, among others, neurovascular surgery (Raabe *et al.*, 2003), dentistry (Lussi & Hellwig, 2006), plastic surgery (Holm *et al.*, 2003), ophthalmology (Regillo, 1999), organ transplantation (Sekijima *et al.*, 2004) and cardiac surgery (Kogon *et al.*, 2009). The technology described here can in principle be used for numerous medical applications of intra-operative fluorescence, although a number of optimisations may be required.

Future directions

The present work has focussed on the modelling and development of FIGS imaging systems, clinical applications and testing of novel molecular agents. However, it represents only an initial stage due to a large interest in the field driven by the strong clinical impact. In this section, future technological development and clinical applications related to this work will be described.

Technological developments

As mentioned in the discussion of Chapter 3, future development of the imaging technology will focus on a number of aspects. The flexibility and usability of FIGS systems can be significantly improved by including a larger number of excitation wavelengths to cover the broad spectrum of available fluorophores from 5-ALA (~405 nm excitation) to ICG (~785 nm excitation). Moreover, more powerful narrow-band excitation and illumination sources will be exploited, in particular for use during keyhole surgery. The ability to independently control red, green and blue illumination channels for bright-field illumination will allow more flexibility in adjusting the colour balance of the scene. This is critical when fluorophores emitting in the visible are used. Future FIGS systems can also be optimised to work with flexible and rigid endoscopes in order to extend the range of suitable clinical applications. Due to potentially high excitation power densities at short working distances, next-generation instruments for keyhole surgery will benefit from a distance-measuring system, based, for example, on sensing tissue diffuse reflectance, as described in §3.6.4. This arrangement can be implemented to control the excitation power as a function of laparoscope working distance, limiting the tissue exposure.

The focus-tuneable wide-field system described in §3.5 will be finalised for clinical translation in the near future. This will ultimately include an autofocus algorithm to improve practicality and reduce imaging time. Focus-tuneable lenses could also be exploited for developing a focus and zoom system to use with laparoscopes and endoscopes.

Although a conventional video camera was used in this work, future FIGS developments will require the use of ‘high definition’ sensors. These, however, require fast data transfer for displaying live video, and some form of image compression will be necessary.

Robotic surgery (Lanfranco *et al.*, 2004) will be likely to have a significant impact for future developments of FIGS systems. This is related primarily to the ability to exploit more sensitive detectors and optical arrangements that would not be suitable for manual operation. In addition, instrument stabilisation would reduce motion artefacts during long exposure imaging and effectively improve fluorescence sensitivity. This is a significant advantage over conventional fluorescence laparoscopy where long exposure times are not usually used, due to imager stabilisation difficulties.

Another potential solution for improving surgical outcomes in FIGS is the development of 'fluorescence-friendly' operating theatres, where the illumination, excitation and detection can be incorporated in the surgical lights. This will provide several advantages during open surgery, including the possibility of using more sensitive imaging systems and long working distance, large aperture zoom lenses.

Clinical applications

The gynaecological cancer clinical study presented in this work resulted in a high SLN detection rate using the FIGS systems. The clinical study will continue to recruit patients with the aim of further validating the concept of SLN in gynaecological cancer and potentially reduce unnecessary excision of lymph nodes. Although ICG provided a high detection rate, SLN mapping with MB was not quite as successful. As this has never been attempted in the clinic, future tests are necessary to assess the feasibility of using MB as a fluorescence dye for SLN mapping. In addition, the dual-dye injection and imaging technique will be further explored in endometrial cancer to quantify the occurrence of a common lymphatic drainage from separate peri-tumoural sites. This will eventually provide useful information to the injection technique during SLN mapping in endometrial cancer.

Although non-specific fluorescence dyes have shown great potential in detecting SLNs, the excised specimen still needs to undergo pathological examination to assess the presence of metastasis. This poses significant restrictions as the patient is kept in the operating theatre under anaesthesia while this examination takes place. A way to determine *in situ* the nodal involvement of cancer cells from a primary tumour would be highly desirable and beneficial. A step towards this goal will be attempted by other collaborators at King's College London (Professor Tony Ng *et. al.*) that will use the wide-field imaging system in breast cancer patients to detect metastatic cells in lymph nodes. For this purpose, the c-Met tumour-specific marker will be used. If successfully validated, this technique will have the potential to avoid needless pathological examination and improve patient outcomes.

Ureteral injury is one of the most serious complication during lower abdominal surgery (Selzman & Spirnak, 1996). As ureters are not always clearly identifiable, a safe and effective method to improve their visualisation during a surgical procedure would be highly desirable. MB has been used as fluorescence contrast agent to improve visualisation of the ureters in real time during open surgery (Verbeek *et al.*, 2013). In laparoscopy, however, the lack of tactile feedback makes the identification of the ureters particularly challenging. Fluorescence identification of the ureters has been performed during keyhole robotic surgery using ICG dye (Lee *et al.*, 2013). This contrast agent was used because of its spectral compatibility with commercially available FIGS systems. However, ICG requires direct injection in the urinary tract as its excretion does not occur renally. In order to overcome this limitation, a clinical study will be carried out by our collaborators in Oxford to detect the ureters during colorectal surgery. In fact this study is already under way at time of writing this thesis: an early result is shown in Figure 71. MB dye is injected intravenously and the fluorescence signal in the ureters measured at different time points

following 660 nm excitation. Both the wide-field and the laparoscopic systems will be used depending on the surgical requirements.

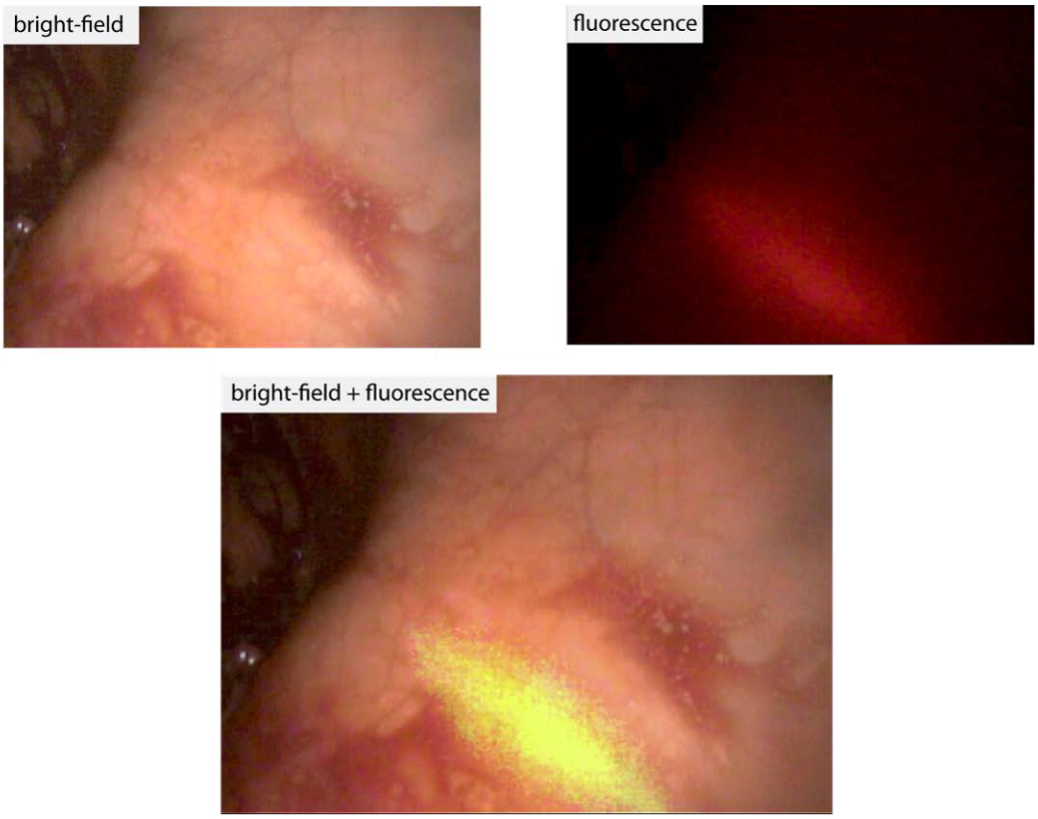

Figure 71: Intra-operative fluorescence laparoscopic detection of the ureter using MB. In this case the ureter was not visible with bright-field imaging due to its location deep in the tissue. Images courtesy of TM Yeung.

In §4.3.1, a novel fluorescently-labelled lectin that provided a negative contrast mechanism to detect cancerous lesions during colonoscopy was described. A feasibility study is planned by our collaborators in order to translate this novel molecular marker in the clinic. The aim of this study will be to detect flat lesions or early forms of colorectal cancer following topical administration of a fluorescently-labelled lectin. This can bring significant benefits in the detection of lesions that can be difficult to identify using white light endoscopy. However, this will require further developments of the FIGS system for use in conjunction with a flexible endoscope. In addition, bio-conjugation of the lectin

with fluorescence dyes suitable for human use is needed. Because of the significantly lower tissue autofluorescence, NIR dyes such as IRDye800 are strongly preferred for this purpose.

A clinical study using the anti-PSMA marker described in §4.3.2 is also among the near-future applications. The promising results *in vitro* and *in vivo* suggest the clinical usefulness of the marker. Further technological improvements of the laparoscopic system in terms of NIR light throughput, excitation power density and camera sensitivity will be considered for improving detection of small lesions at the microscopic level.

Lastly, a future version of the FIGS system that can excite in the UV-violet region (~405 nm) will be considered for intra-operative identification and resection of malignant gliomas during endoscopy using 5-ALA. This technique has shown significant benefits in terms of patient survival rate (Stummer *et al.,* 2006). However, current endoscopic systems designed to image 5-ALA do not provide white reflectance information when displaying fluorescence. As described in §3.6.1, a multi-wavelength illumination source will be exploited, with the aim of displaying false-colour bright-field images and fluorescence simultaneously. This will ultimately result in potential improvements in the safety and outcomes of the procedure.

Although much remains to be done in terms of imaging devices and contrast agents development, the future of fluorescence image-guided surgery is indeed bright.

Appendix

I. Expression of diffuse reflectance

The diffuse reflectance that is used in §2.4.2 to estimate the number of fluorescence photons that emerge from the tissue surface was computed following the approach described in (Farrell *et al.*, 1992). The diffuse reflectance was derived from the Green's function by considering a photon dipole source to satisfy the tissue-air boundary condition. This dipole consists of an isotropic source in tissue (which corresponds to the fluorescence sample) and a negative imaginary source in air. The position of this imaginary source is such that the combined fluence rate of the dipole is zero across an extrapolated boundary. The use of this boundary condition provided a simple analytical expression of the diffuse reflectance.

Using cylindrical symmetry, the diffuse reflectance $R(\rho,z_0)$ at a distance ρ from the centre following emission from an isotropic source at depth z_0 is expressed by (Farrell *et al.*, 1992):

$$R(\rho, z_0) = \frac{1}{4\pi}\left[z_0\left(\mu_{eff} + \frac{1}{r_1}\right)\frac{\exp(-\mu_{eff} r_1)}{r_1^2} + (z_0 + 2z_b)\left(\mu_{eff} + \frac{1}{r_2}\right)\frac{\exp(-\mu_{eff} r_2)}{r_2^2}\right]$$

$$r_1 = \sqrt{z_0^2 + \rho^2}$$

$$r_2 = \sqrt{(z_0 + 2z_b)^2 + \rho^2}$$

where μ_{eff} is the effective attenuation coefficient. The parameter z_b represents the distance between the air/tissue interface and the extrapolated boundary on which the overall fluence rate of the dipole is zero (Figure 72). This distance is defined as $z_b=2DA$, where D is the diffusion coefficient for light transport (§2.3.2) and $A=(1+r_d)/(1-r_d)$ is a factor that depends

on the internal reflection parameter $r_d \approx -1.44n^{-2} + 0.71n^{-1} + 0.668 + 0.064n$, where n is the refractive index of the medium (Groenhuis *et al.*, 1983). The diffuse reflectance $R(\rho,z_0)$ is expressed in unit of inverse area.

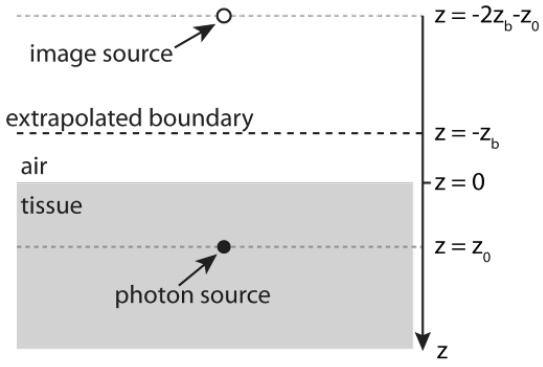

Figure 72: Schematics of the image source model used to express diffuse reflectance.

The diffuse reflectance is used in the FIGS theoretical model to compute the number of photons that escape the tissue surface following isotropic emission by a deep sample.

II. *FIFAC* software

A software tool named *FIFAC* was developed to provide a graphical interface to control the imaging parameters required by the theoretical model described in Chapter 2 and to visualise the modelled output image. The GUI was developed using *Tkinter*, the standard graphical interface of Python. The analytical calculations with multi-dimensional arrays and matrices that the model requires were accomplished using the library of functions provided by the Python extension *NumPy* (*http://www.numpy.org*). The output images were generated using the plotting library *matplotlib* (*http://matplotlib.org*). The GUI was designed to display all the imaging parameters in a single window. The analytical calculations are performed following a click on any of the three output buttons described below.

Photon image: The button labelled as ‘Photon image’ generates a grayscale map representing the number of fluorescence photons reaching each pixel of the detector during a given exposure time. Variations of parameters such as noise, quantum efficiency and gain do not affect the output image. The grayscale bar is dynamically adjusted to range from the minimum to the maximum output value.

Quantised image: The button labelled as ‘Quantised image’ generates a grayscale map representing the intensity levels (or digital counts) (Eq. (7)) for each sensor pixel. The grayscale bar is fixed according to the bit depth selected in the control panel. This image is dependent on all the imaging parameters of the control panel.

Contrast stretched image: The button ‘Contrast stretched image’ produces the same result as the previous button with the exception that the grayscale bar is adjusted according to the dynamic range of the image.

By clicking on any of the three buttons, the software also shows a photon budget of the fluorescence process (i.e. excitation fluence rate on the surface and at the sample, photon rate emitted by each fluorophore molecule and total photon rate emitted by the sample). Moreover, a number of dependent parameters are computed, for example field of view, sensor pixel size and light collection efficiency. The results displayed on the GUI are updated when any of the buttons is pushed.

Software outputs include signal-to-noise ratio (SNR) and fluorescence sample resolution. The SNR (in decibels) is calculated as the ratio between the average peak intensity of the image and the standard deviation of the noise in regions where no sample is present (Figure 73). The SNR is not computed when the ‘Photon image’ button is pressed. The sample resolution (in mm) is obtained by fitting the decay of the signal from the centre of the field of view with a Gaussian function and calculating the full width half maximum.

The output image window includes several option buttons that allow zoom/pan, reset view and save the image. It is important to note that images are always saved as 8-bit irrespectively on the sampling resolution set in the main software panel.

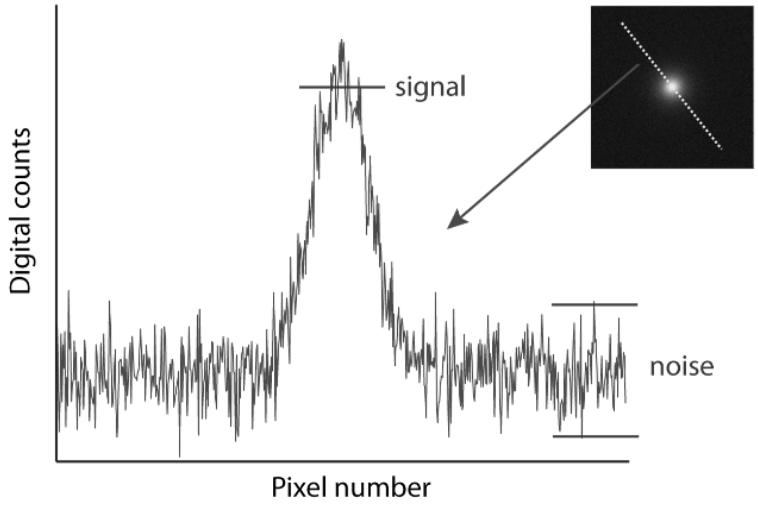

Figure 73: Schematic of SNR calculation in *FIFAC*.

III. Preparation of plasma-equivalent solution

Indocyanine green (ICG) is the most common clinically approved NIR fluorescent dye, widely used in particular in angiography and sentinel lymph node biopsy. In some of the experiments described in this thesis, ICG was diluted in an albumin-enriched physiological salt solution (APSS) to mimic its fluorescence properties in the lymphatic system. APSS was prepared as described in (Gashev *et al.*, 2002): 145 mM NaCl, 4.7 mM KCl, 2 mM $CaCl_2$, 1.17 mM $MgSO_4$, 1.2 mM NaH_2PO_4, 5 mM dextrose, 2 mM sodium pyruvate, 0.02 mM EDTA, 3 mM MOPS and 10 g/L bovine serum albumin. The compounds were diluted in distilled water and the solution mixed for 1 hour at room temperature.

IV. Étendue

Before developing an optical system of any kind, it is important to know what the theoretical limitations are. Such limitations are crucial for determining the maximum light throughput of the system. The quantity that best represents the theoretical performance of a system is known as *étendue*.

The étendue describes the angular and spatial distribution of the light flux through an optical system, providing indication on the ability of the system to transfer the flux from a source to the target. The étendue, also known as *geometrical extent G*, is defined as (Steel, 1974):

$$G = n^2 A\Omega$$

where n is the refractive index of the medium of propagation, A is the area of the entrance pupil of an optical system and Ω is the solid angle subtended at the pupil by the object or source. Alternatively, A can represent the area of the object or source and Ω the solid angle subtended by the pupil.

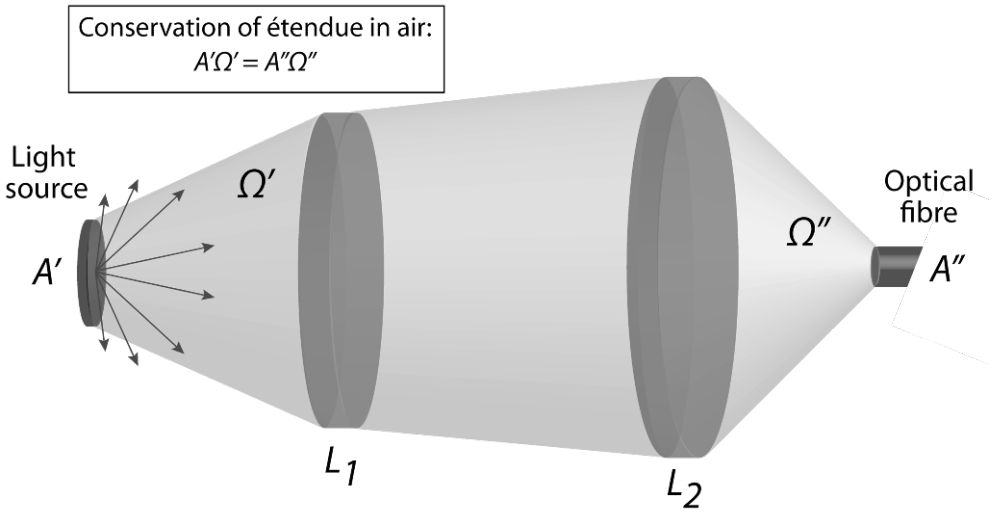

Figure 74: Schematic representation of étendue conservation. In this typical configuration, two lenses L_1 and L_2 are used to couple the light from a source of emitting area A' to an optical fibre of core diameter A''.

The étendue can be seen as the optical equivalent of entropy: in an ideal system in which light undergoes perfect reflections and refractions, étendue is conserved. In a complex optical system, the component with the lowest étendue (e.g. an optical fibre with low NA) sets the limit of the system. Figure 74 shows a typical problem of coupling light from a source to a light guide and the relevant parameters to calculate étendue.

The étendue value can never decrease in an optical system. However, it can dramatically increase if light interacts with a diffusive material. As in practical situations optical losses due to absorption, scattering, aberration and diffraction can occur, the étendue represents the theoretical limit of flux transfer capability in a system. It is therefore crucial to consider conservation of étendue when designing any illumination system.

V. Review of existing FIGS systems

The systems mentioned in this review were selected from publications in the MEDLINE database, updated to September 2014. In order to limit the number of devices described, only publications that have shown clinical results will be considered.

Commercially available systems

A summary of the commercially available systems for FIGS is shown in Table 11. One of the most popular devices for ICG fluorescence imaging during open surgery is the Photodynamic Eye (PDE) manufactured by Hamamatsu. This is a portable hand-held system with a 760 nm LED source for excitation and a CCD camera with 840 nm band-pass filter for detection (Figure 75A). Bright-field mode and/or other excitation wavelengths are not supported. The PDE has been predominantly used in the clinic for sentinel lymph node (SLN) mapping and for angiography.

Another similar system typically used for angiography is the NOVADAQ SPY, manufactured by Novadaq Technologies (Gurtner *et al.*, 2013). This device is fitted to a flexible arm for optimal positioning over the surgical bed. Excitation is provided by a 806 nm laser diode producing a power density at the sample of ~12 mW/cm^2 (Zhu *et al.*, 2014). Similarly to the PDE, a band-pass filter is used in conjunction with a CCD camera for fluorescence detection with no white reflectance capabilities. The SPY system is the only device approved by the Food and Drug Administration (FDA) for clinical use following intravenous administration of ICG.

Pulsion Medical Systems have developed the IC-View, a device that uses a 780 nm laser diode in conjunction with a band-pass filter for fluorescence imaging with a CCD camera. This system has been clinically used with ICG for SLN mapping in a variety of cancers (Hirche *et al.*, 2010a).

The HyperEye is a compact fluorescence system manufactured by Mizuho Medical Innovation (Handa *et al.*, 2010). Unlike the systems described above, the HyperEye provides a neat solution for simultaneous bright-field and ICG fluorescence using a single colour camera. An array containing visible LEDs for illumination and 760 nm LEDs for excitation is placed at the distal end of the imaging device (Figure 75B). A filter with > 90% transmittance above 820 nm and ~ 10% transmittance in the region 400-700 nm is used in front of a colour CCD camera for simultaneous view of fluorescence and bright-field. The system has been used with ICG in angiography and for SLN mapping. Early devices for intra-operative fluorescence are also the so called ‘surgical microscopes’ (e.g. Leica FL400 and Zeiss OPMI Pentero) which are typically used for 5-aminolevulinic acid fluorescence imaging of malignant gliomas (Stummer *et al.*, 2006). Such systems operate by exciting in the blue-violet region and collecting fluorescence using a long pass filter.

Device	*Manufacturer*	*Excitation*	*Filtering*	*Detection*	*Operation mode*
Photodynamic Eye (PDE)	Hamamatsu	760 nm LED, 4 mW/cm^2	840 nm band-pass	Monochrome CCD, fluorescence only	Open surgery, hand-held
SPY	Novadaq Technologies	806 nm laser diode, 12 mW/cm^2	835 nm band-pass	Monochrome CCD for fluorescence only, exposure 33 ms	Open surgery`
IC-View	Pulstion medical	780 nm laser diode, 60 mW	835 nm band-pass	CCD, colour bright-field or fluorescence	Open surgery
HyperEye	Mizuho Medical Innovation	760 nm LEDs	Custom-designed long and short pass filter	Colour CCD, fluorescence + bright-field	Open surgery
Surgical microscope	Leica, Zeiss	Xenon lamp	Blue and NIR excitation	Bright-field or fluorescence	Open surgery
Karl Storz D-Light laparoscopic system	Karl Storz	Xenon lamp with 380 – 440 nm or 690 – 780 nm band-pass filter	450 nm or 780 nm long-pass filter	Colour CCD for bright-field and fluorescence	Laparoscopy/ endoscopy
Olympus NIR laparoscope	Olympus	300 W xenon lamp	?	Colour bright-field or fluorescence	Laparoscopy/ endoscopy
FIREFLY (SPY system integrated with daVinci robot)	Novadaq Technologies-Intuitive surgical	806 nm laser diode	835 nm band-pass	Bright-field or fluorescence superimposed to monochrome bright-field, exposure 33 ms	Robotically assisted laparoscopy
PINPOINT	Novadaq Technologies	806 nm laser diode	?	Colour CCD, fluorescence and bright-field, exposure 33 ms	Laparoscopy

Table 11: Commercially available clinical FIGS systems.

A number of keyhole systems for FIGS have also been developed for commercial use. The Photodynamic Diagnostic D-Light system manufactured by Storz is a fluorescence-capable rigid endoscope that is used for autofluorescence imaging or to excite a dye absorbing in the blue-violet region. The system is a standard endoscope/laparoscope equipped with an excitation (380 – 440 nm band-pass) and emission (450 nm long-pass) filter and a 3CCD colour camera to capture fluorescence and bright-field sequentially (Thong *et al.*, 2009). The Storz D-Light system is also available with filters for ICG fluorescence imaging (Litvack *et al.*, 2012). A similar endoscope that allows successive (but not simultaneous) imaging of ICG fluorescence and bright-field is also manufactured by Olympus.

Novadaq Technologies adapted the technology of their SPY open surgery imaging system in the daVinci surgical robot (Intuitive Surgical) for laparoscopic applications. In analogy to the SPY, this system (named FIREFLY) uses an 806 nm laser diode for excitation and a 835 nm band-pass filter for collection. Fluorescence emission is displayed as false-colour overlaid to the luminance signal from the bright-field, resulting in monochromatic images of the scene with green regions indicating fluorescence.

Novadaq Technologies also developed a fluorescence laparoscopic system (PINPOINT) that uses an 806 nm laser for excitation and a colour CCD camera to simultaneously detect ICG fluorescence and bright-field. Despite the fact that no clear information on the detection system is available, a recent patent filled by Novadaq suggests that simultaneous NIR fluorescence and white-reflectance imaging is achieved by time-multiplexing white illumination and detection (Westwick *et al.*, 2013). The exposure time is fixed to 33 ms to provide video-rate images.

Research systems

A summary of systems for FIGS developed by research groups is shown in Table 12. To date, only devices for open surgery have been used clinically. Achilefu's group at Washington University in St. Louis (USA) described the development of a wearable fluorescence goggle system that uses a see-through display to visualise fluorescence on top of the actual surgical field (Liu *et al.*, 2013a). This system was used in a pilot study to detect hepatocellular carcinoma using ICG (Liu *et al.*, 2013b). Worth mentioning is also a custom-made system from Sevick-Muraca's group at University of Texas (USA) that used an intensified CCD camera to detect SLNs with ICG in breast cancer (Sevick-Muraca *et al.*, 2008).

More sophisticated intra-operative fluorescence systems for open surgery have been developed by the Frangioni's group at Harvard Medical School (USA) and by the Ntziachristos' group at Technical University of Munich (Germany).

The Frangioni's system is known as FLARE and it consists of multiple cameras to simultaneously detect two fluorescence emission wavelengths and white reflectance light from the surgical field (Troyan *et al.*, 2009). White light and LED excitation light peaked at 670 and 760 nm is delivered to the surgical field at a typical working distance of ~450 mm. Collected light is split into visible and NIR wavelengths using a dichromatic mirror for detection. The output fluorescence signal is processed and overlaid in false-colour to the white reflectance images for concurrent visualisation. A smaller version of the FLARE system (named mini-FLARE) was also developed by the same group (Figure 75C). Both the FLARE and mini-FLARE systems are not suitable for hand-held operation and their imaging head has to be supported and operated using a flexible arm. These systems have been used for SLN mapping with ICG in breast (Troyan *et al.*, 2009), vulval (Hutteman *et*

al., 2012) and cervical cancer (Schaafsma *et al.*, 2012), to detect breast cancer (Tummers *et al.*, 2014) and visualise the ureters using fluorescence from methylene blue (Verbeek *et al.*, 2013).

Device	***Institution***	***Excitation***	***Filtering***	***Detection***	***Operation mode***	***Clinical applications***
Fluorescence goggles	Washington University (USA)	760 nm LEDs	830 nm long-pass	Monochrome CMOS	Open surgery	Hepatocellular carcinoma (Liu *et al.*, 2013b)
Custom device	University of Texas (USA)	785 nm laser diode, 1.9 mW/cm^2	830 nm band-pass	Intensified CCD, fluorescence only, exposure 200 – 800 ms	Open surgery	SLN in breast cancer (Sevick-Muraca *et al.*, 2008)
FLARE and mini-FLARE	Harvard Medical School (USA)	LEDs, 670 nm at 4 mW/cm^2 and 760 nm at 14 mW/cm^2	700 nm and 800 nm band-pass	Three CCD cameras, fluorescence exposure from 100 µs to 8 s	Open surgery	SLN in breast cancer (Troyan *et al.*, 2009), vulval cancer (Hutteman *et al.*, 2012), cervical cancer (Schaafsma *et al.*, 2012)
Custom device	Technical University Munich (Germany) – SurgOptix Inc. (USA)	750 nm laser diode	795 nm band-pass	EMCCD camera for fluorescence and two CCDs for bright-field and excitation reflectance	Open surgery	Ovarian cancer (van Dam *et al.*, 2011), SLN in vulval cancer (Crane *et al.*, 2011a) and cervical cancer (Crane *et al.*, 2011b)

Table 12: Clinical FIGS systems developed by other academic research groups.

The Ntziachristos' system in Munich is similar to the FLARE in terms of design, ergonomics and image processing (Figure 75D). Unlike the FLARE, it uses a 750 nm laser diode for excitation and a halogen lamp for white-light illumination (Themelis *et al.*, 2009). Two dichroic mirrors are used to split the detected light into excitation, emission and white-reflectance channels. This system has the unique characteristic that excitation

light reflected from the tissue is collected, processed and used for light-absorption correction. This results in absorption-corrected fluorescence signal displayed in false-colour on top of the bright-field image. The Ntziachristos' system has been used for SLN detection with ICG in vulval (Crane *et al.*, 2011a) and cervical (Crane *et al.*, 2011b) cancers. The same system with a few technical adjustments was used in detecting ovarian cancer with a tumour-specific marker conjugated to fluorescein isothiocyanate (FITC) (van Dam *et al.*, 2011).

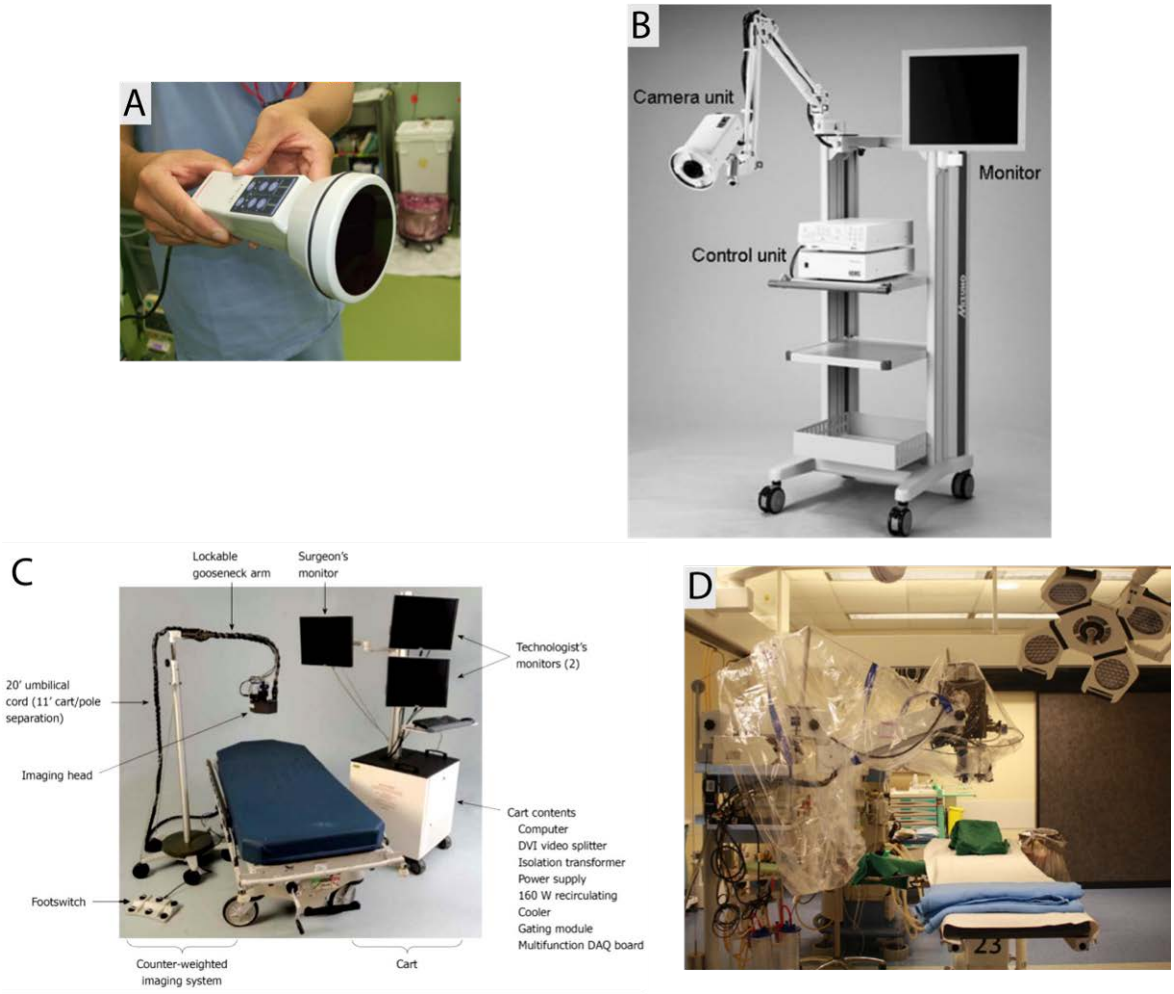

Figure 75: Images of some of the existing FIGS systems for open surgery. (A) The Photodynamic Eye by Hamamatsu (Shimada *et al.*, 2011), (B) the HyperEye by Mizuho Medical Innovation (Kubota *et al.*, 2013), (C) the mini-FLARE system from Harvard Medical School (Mieog *et al.*, 2011) and (D) the custom-made system from Technical University Munich (Crane *et al.*, 2011b). Figures reproduced with permission from Springer.

VI. Fibre bundle assembly and polishing technique

Silica fibre bundle

The silica fibre bundle used to combine multiple laser sources (§3.2.2) was developed using 300 µm core diameter, 0.37 NA multimode fibres (BFL37-300, Thorlabs). On one end of the fibre, the jacket was stripped from the fibre using an appropriate stripping tool. The fibre was then glued in a 340 µm bore FC/PC connector (30126G2-340, Thorlabs) using epoxy glue (F112, Thorlabs) and following the guidelines from the manufacturer. Once the glue set, the fibre was scored and the tip polished using increasing grades of polishing film ranging from 5 to 0.3 µm. The same procedure was repeated for 7 fibres. The other end of each fibre was cut to obtain an overall fibre length of ~300 mm, followed by stripping of ~40 mm of the jacket. The claddings from the 7 fibres were carefully placed one by one in a single 1050 µm bore FC/PC connector (30126G2-1050, Thorlabs) to form a hexagonal packing (Figure 76A). The fibres were glued to the common connector and polished with the same procedure described above. In case fewer fibres are needed, the unused ones can be shortened and left without a connector at the free fibre end. Figure 76B shows an example of a bundle that contains 6 input fibres.

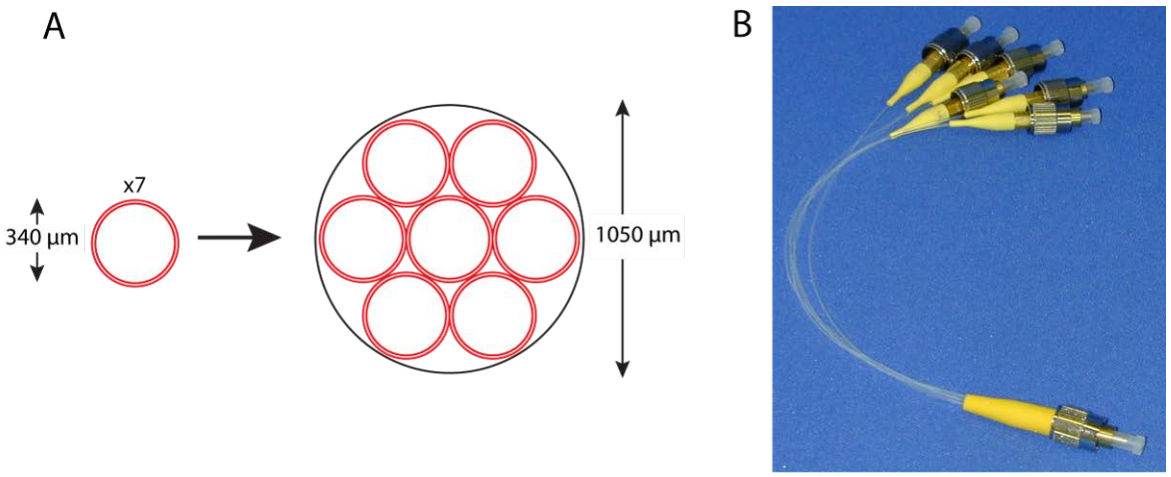

Figure 76: Schematic representation and image of the silica fibre bundle.

PMMA fibre bundle

The illumination system of the focus-tuneable wide-field imaging device used a custom-made Poly(methyl methacrylate) (PMMA) fibre bundle for delivering light from a common end to 4 separate outputs. This bundle was constructed using 0.5 mm diameter, 0.5 NA PMMA optical fibres (CK20U, Universal Fibre Optics). Seven fibres of length ~300 mm were tightly packed in a hexagonal array in a customised ferrule that consisted of a 6 mm long brass tube with 1.5 mm internal diameter and 4.8 mm external diameter (Figure 77A).

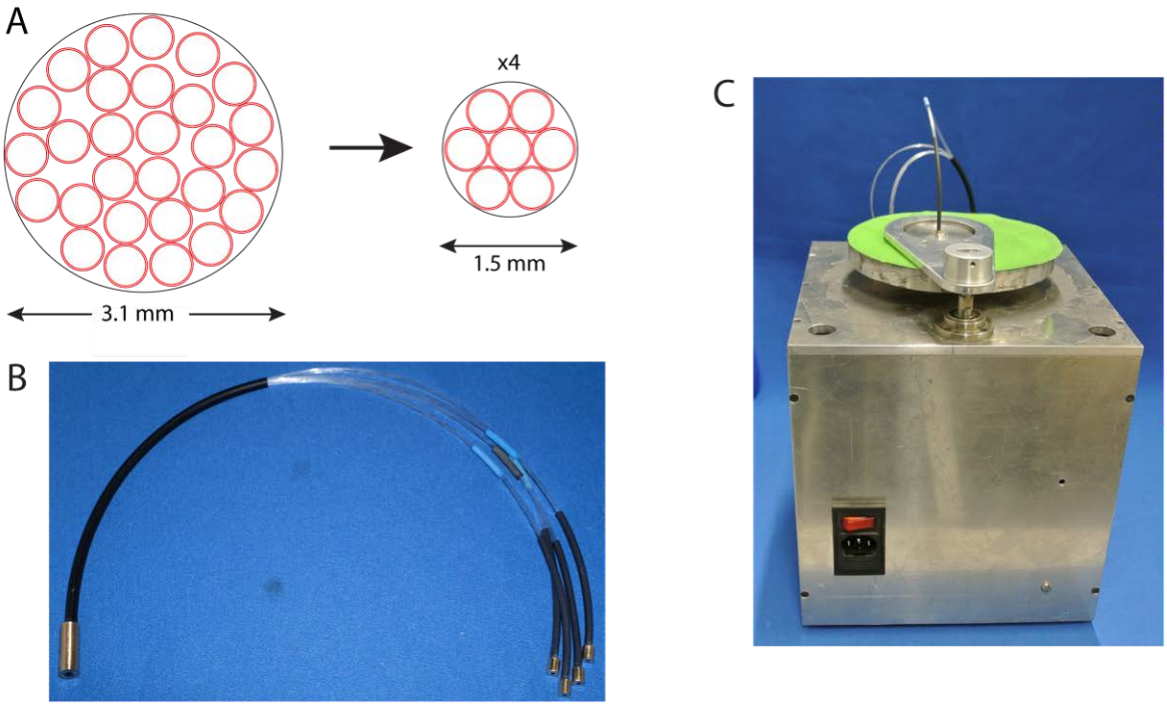

Figure 77: Polymer fibre bundle design and development. (A) Schematic diagram and (B) image of the fibre bundle. (C) Custom-made automated tool used to polish the fibre bundle.

The fibres were glued in the ferrule using UV curing glue (NOA68, Norland) together with a rubber cable sleeve for protection. The bundle of fibres in the ferrule was polished using a custom-made polishing tool that consists of a moving part that follows an arc shape and a rotating disc (Figure 77C). The moving part includes a customised holder for the brass

ferrule, while a sheet of polishing film is placed on the rotating disc. The movement is repeated back and forward and its speed is manually controlled, while the rotation speed of the disc is constant. Different grades of polishing film were used to polish the fibre bundle. The same procedure was repeated to produce 4 bundles for a total of 28 fibres (Figure 77A). At the free end, the 28 fibres were glued in a second brass ferrule (22 mm length, 3.1 mm internal diameter and 8 mm external diameter) using a similar procedure. The automated polishing of the common end was performed by replacing the ferrule holder with a larger one. The complete fibre bundle assembly is shown in Figure 77B.

References

Alex, J. C., and Krag, D. N. 1993. Gamma-probe guided localization of lymph nodes. *Surgical Oncology*, 2(3): 137–143.

Alford, R., Simpson, H. M., Duberman, J., Hill, G. C., Ogawa, M., Regino, C., Kobayashi, H., and Choyke, P. L. 2009. Toxicity of organic fluorophores used in molecular imaging: literature review. *Molecular Imaging*, 8(6): 341–54.

Allen, T. J., Hall, A., Dhillon, A. P., Owen, J. S., and Beard, P. C. 2012. Spectroscopic photoacoustic imaging of lipid-rich plaques in the human aorta in the 740 to 1400 nm wavelength range. *Journal of Biomedical Optics*, 17(6): 061209.

Amant, F., Moerman, P., Neven, P., Timmerman, D., Van Limbergen, E., and Vergote, I. 2005. Endometrial cancer. *Lancet*, 366(9484): 491–505.

ANSI. 2014a. *ANSI Standard "For the Safe Use of Lasers."*

ANSI. 2014b. *ANSI Standard "For the Safe Use of Lasers."*

Aronson, R., and Corngold, N. 1999. Photon diffusion coefficient in an absorbing medium. *Journal of the Optical Society of America A*, 16(5): 1066–71.

Arridge, S. R., and Hebden, J. C. 1997. Optical imaging in medicine: II. Modelling and reconstruction. *Physics in Medicine and Biology*, 42(5): 841–853.

Ashitate, Y., Stockdale, A., Choi, H. S., Laurence, R. G., and Frangioni, J. V. 2012. Real-time simultaneous near-infrared fluorescence imaging of bile duct and arterial anatomy. *The Journal of Surgical Research*, 176(1): 7–13.

Averette, H. E., Nguyen, H. N., Donato, D. M., Penalver, M. A., Sevin, B. U., Estape, R., and Little, W. A. 1993. Radical hysterectomy for invasive cervical cancer. A 25-year prospective experience with the Miami technique. *Cancer*, 71(4 Suppl): 1422–37.

Azhdarinia, A., Wilganowski, N., Robinson, H., Ghosh, P., Kwon, S., Lazard, Z. W., Davis, A. R., Olmsted-Davis, E., and Sevick-Muraca, E. M. 2011. Characterization of chemical, radiochemical and optical properties of a dual-labeled MMP-9 targeting peptide. *Bioorganic & Medicinal Chemistry*, 19(12): 3769–76.

Barber, P. R., Tullis, I. D. C., Pierce, G. P., Newman, R. G., Prentice, J., Rowley, M. I., Matthews, D. R., Ameer-Beg, S. M., and Vojnovic, B. 2013. The Gray Institute "open" high-content, fluorescence lifetime microscopes. *Journal of Microscopy*, 251(2): 154–67.

Barranger, E., Cortez, A., Grahek, D., Callard, P., Uzan, S., and Darai, E. 2004. Laparoscopic sentinel node procedure using a combination of patent blue and radiocolloid in women with endometrial cancer. *Annals of Surgical Oncology*, 11(3): 344–9.

Bäumler, W., Abels, C., Karrer, S., Weiss, T., Messmann, H., Landthaler, M., and Szeimies, R. M. 1999. Photo-oxidative killing of human colonic cancer cells using indocyanine green and infrared light. *British Journal of Cancer*, 80(3-4): 360–3.

Beard, P. 2011. Biomedical photoacoustic imaging. *Interface focus*, 1(4): 602–31.

Beheshti, M., Haim, S., Zakavi, R., Steinmair, M., Waldenberger, P., Kunit, T., Nader, M., Langsteger, W., and Loidl, W. 2013. Impact of 18F-choline PET/CT in prostate cancer patients with biochemical recurrence: influence of androgen deprivation therapy and correlation with PSA kinetics. *Journal of Nuclear Medicine*, 54(6): 833–40.

Benson, R. C., and Kues, H. A. 1978. Fluorescence properties of indocyanine green as related to angiography. *Physics in Medicine and Biology*, 23(1): 159–63.

Bergers, G., and Benjamin, L. E. 2003. Tumorigenesis and the angiogenic switch. *Nature Reviews Cancer*, 3(6): 401–10.

Bird-Lieberman, E. L., Neves, A. A., Lao-Sirieix, P., O'Donovan, M., Novelli, M., Lovat, L. B., Eng, W. S., Mahal, L. K., Brindle, K. M., and Fitzgerald, R. C. 2012. Molecular imaging using fluorescent lectins permits rapid endoscopic identification of dysplasia in Barrett's esophagus. *Nature Medicine*, 18(2): 315–21.

Bluestone, A. Y., Stewart, M., Lasker, J., Abdoulaev, G. S., and Hielscher, A. H. 2004. Three-dimensional optical tomographic brain imaging in small animals, part 1: hypercapnia. *Journal of Biomedical Optics*, 9(5): 1046–62.

Born, M., Wolf, E., and Bhatia, A. B. 2002. *Principles of Optics: Electromagnetic Theory of Propagation, Interference and Diffraction of Light* (p. 200). Cambridge University Press.

Bray, F., Jemal, A., Grey, N., Ferlay, J., and Forman, D. 2012. Global cancer transitions according to the Human Development Index (2008-2030): a population-based study. *The Lancet Oncology*, 13(8): 790–801.

Briganti, A., Blute, M. L., Eastham, J. H., Graefen, M., Heidenreich, A., Karnes, J. R., Montorsi, F., and Studer, U. E. 2009. Pelvic lymph node dissection in prostate cancer. *European Urology*, 55(6): 1251–65.

Burger, M. P., Hollema, H., Emanuels, A. G., Krans, M., Pras, E., and Bouma, J. 1995. The importance of the groin node status for the survival of T1 and T2 vulval carcinoma patients. *Gynecologic Oncology*, 57(3): 327–34.

Cahill, R., Anderson, M., Wang, L. M., Lindsey, I., Cunningham, C., and Mortensen, N. J. 2012. Near-infrared (NIR) laparoscopy for intraoperative lymphatic road-mapping and sentinel node identification during definitive surgical resection of early-stage colorectal neoplasia. *Surgical Endoscopy*, 26(1): 197–204.

Cancer Research UK. 2011a. Cervical cancer statistics. *http://www.cancerresearchuk.org/cancer-info/cancerstats/types/cervix/?script=true*.

Cancer Research UK. 2011b. Vulval cancer statistics. *http://www.cancerresearchuk.org/cancer-info/cancerstats/types/vulva/*.

Cancer Research UK. 2011c. Ovarian cancer statistics. *http://www.cancerresearchuk.org/cancer-info/cancerstats/types/ovary/*.

Cancer Research UK. 2011d. Bowel cancer statistics. *http://www.cancerresearchuk.org/cancer-info/cancerstats/types/bowel/*.

Cancer Research UK. 2011e. Prostate cancer statistics. *http://www.cancerresearchuk.org/cancer-info/cancerstats/types/prostate/*.

Cancer Research UK. 2013. European Age-Standardised Mortality Rates, UK, 1971-2011. *http://www.cancerresearchuk.org/cancer-info/cancerstats/mortality/all-cancers-combined/*.

Cancer Research UK. 2014. Cancer incidence in the UK in 2011. *http://publications.cancerresearchuk.org/cancerstats/statsincidence/incidence.html*.

Chambers, A. F., Groom, A. C., and MacDonald, I. C. 2002. Dissemination and growth of cancer cells in metastatic sites. *Nature Reviews Cancer*, 2(8): 563–72.

Chen, S. L., Iddings, D. M., Scheri, R. P., and Bilchik, A. J. 2008. Lymphatic mapping and sentinel node analysis: current concepts and applications. *CA: a cancer journal for clinicians*, 56(5): 292–309.

Clancy, N. T., Clark, J., Noonan, D. P., Yang, G.-Z., and Elson, D. S. 2012. Light sources for single-access surgery. *Surgical Innovation*, 19(2): 134–44.

Cody, H. 2001. Clinical aspects of sentinel node biopsy. *Breast Cancer Research*, 3(2): 104–108.

Coleman, R. E. 1991. Single photon emission computed tomography and positron emission tomography in cancer imaging. *Cancer*, 67(4): 1261–70.

Comoglio, P. M. 2001. Pathway specificity for Met signalling. *Nature Cell Biology*, 3(7): E161–2.

Comoglio, P. M., Giordano, S., and Trusolino, L. 2008. Drug development of MET inhibitors: targeting oncogene addiction and expedience. *Nature Reviews Drug Discovery*, 7(6): 504–16.

Contini, D., Martelli, F., and Zaccanti, G. 1997. Photon migration through a turbid slab described by a model based on diffusion approximation. I. Theory. *Applied Optics*, 36(19): 4587–99.

Corlu, A., Choe, R., Durduran, T., Rosen, M. A., Schweiger, M., Arridge, S. R., Schnall, M. D., and Yodh, A. G. 2007. Three-dimensional in vivo fluorescence diffuse optical tomography of breast cancer in humans. *Optics Express*, 15(11): 6696–716.

Crane, L. M., Themelis, G., Arts, H. J., Buddingh, K. T., Brouwers, A. H., Ntziachristos, V., van Dam, G. M., and van der Zee, A. G. 2011a. Intraoperative near-infrared fluorescence imaging for sentinel lymph node detection in vulvar cancer: first clinical results. *Gynecologic Oncology*, 120(2): 291–295.

Crane, L. M., Themelis, G., Pleijhuis, R. G., Harlaar, N. J., Sarantopoulos, A., Arts, H. J. G., van der Zee, A. G. J., Ntziachristos, V., Vasilis, N., and van Dam, G. M. 2011b. Intraoperative multispectral fluorescence imaging for the detection of the sentinel lymph node in cervical cancer: a novel concept. *Molecular Imaging and Biology*, 13(5): 1043–9.

Creasman, W. T., Morrow, C. P., Bundy, B. N., Homesley, H. D., Graham, J. E., and Heller, P. B. 1987. Surgical pathologic spread patterns of endometrial cancer. A Gynecologic Oncology Group Study. *Cancer*, 60(8 Suppl): 2035–41.

Dehghani, H., Eames, M. E., Yalavarthy, P. K., Davis, S. C., Srinivasan, S., Carpenter, C. M., Pogue, B. W., and Paulsen, K. D. 2008. Near infrared optical tomography using NIRFAST: Algorithm for numerical model and image reconstruction. *Communications in Numerical Methods in Engineering*, 25(6): 711–732.

Deshpande, N., Needles, A., and Willmann, J. K. 2010. Molecular ultrasound imaging: current status and future directions. *Clinical Radiology*, 65(7): 567–581.

Desmettre, T., Devoisselle, J. M., and Mordon, S. 2000. Fluorescence Properties and Metabolic Features of Indocyanine Green (ICG) as Related to Angiography. *Survey of Ophthalmology*, 45(1): 15–27.

Di Renzo, M. F., Olivero, M., Katsaros, D., Crepaldi, T., Gaglia, P., Zola, P., Sismondi, P., and Comoglio, P. M. 1994. Overexpression of the Met/HGF receptor in ovarian cancer. *International Journal of Cancer*, 58(5): 658–62.

(Ed.)Diaspro, A. 2011. *Optical Fluorescence Microscopy* (p. 244).

Dixon, J. B. 2010. Lymphatic lipid transport: sewer or subway? *Trends in Endocrinology and Metabolism*, 21(8): 480–7.

Durduran, T., Choe, R., Baker, W. B., and Yodh, A. G. 2010. Diffuse optics for tissue monitoring and tomography. *Reports on Progress in Physics*, 73(7): 76701.

Dussault, D., and Hoess, P. 2004. Noise performance comparison of ICCD with CCD and EMCCD cameras. In E. L. Dereniak, R. E. Sampson, & C. B. Johnson (Eds.), *Proc SPIE* (pp. 195–204).

Edmonson, J. M. 1991. History of the instruments for gastrointestinal endoscopy. *Gastrointestinal Endoscopy*, 37: S27–S56.

Eggebrecht, A. T., Ferradal, S. L., Robichaux-Viehoever, A., Hassanpour, M. S., Dehghani, H., Snyder, A. Z., Hershey, T., and Culver, J. P. 2014. Mapping distributed brain function and networks with diffuse optical tomography. *Nature Photonics*, 8(6): 448–454.

Elson, D., Requejo-Isidro, J., Munro, I., Reavell, F., Siegel, J., Suhling, K., Tadrous, P., Benninger, R., Lanigan, P., McGinty, J., Talbot, C., Treanor, B., Webb, S., Sandison, A., Wallace, A., Davis, D., Lever, J., Neil, M., Phillips, D., Stamp, G., et al. 2004. Time-domain fluorescence lifetime imaging applied to biological tissue. *Photochemical & Photobiological Sciences*, 3(8): 795–801.

Etzioni, R., Urban, N., Ramsey, S., McIntosh, M., Schwartz, S., Reid, B., Radich, J., Anderson, G., and Hartwell, L. 2003. The case for early detection. *Nature Reviews Cancer*, 3(4): 243–52.

Farah, C. S., McIntosh, L., Georgiou, A., and McCullough, M. J. 2012. Efficacy of tissue autofluorescence imaging (VELScope) in the visualization of oral mucosal lesions. *Head & neck*, 34(6): 856–62.

Farrell, T., Patterson, M., and Wilson, B. 1992. A diffusion theory model of spatially resolved, steady state diffuse reflectance for the noninvasive determination of tissue optical properties invivo. *Medical Physics*, 19(4): 879–88.

Fengler, J., and Westwick, P. 2009. Imaging system for combined full-color reflectance and near-infrared imaging. *US Patent: US20110063427 A1*.

Fishkin, J. B., and Gratton, E. 1993. Propagation of photon-density waves in strongly scattering media containing an absorbing semi-infinite plane bounded by a straight edge. *Journal of the Optical Society of America A*, 10(1): 127–140.

Folkman, J. 1971. Tumor Angiogenesis: Therapeutic Implications. *New England Journal of Medicine*, 285(21): 1182–1186.

Frumovitz, M., Ramirez, P. T., and Levenback, C. F. 2008. Lymphatic mapping and sentinel lymph node detection in women with cervical cancer. *Gynecologic Oncology*, 110(3 Suppl 2): S17–20.

Fujiwara, M., Mizukami, T., Suzuki, A., and Fukamizu, H. 2009. Sentinel lymph node detection in skin cancer patients using real-time fluorescence navigation with indocyanine green: preliminary experience. *Journal of Plastic Reconstructive and Aesthetic Surgery*, 62(10): E373–E378.

Furukawa, N., Oi, H., Yoshida, S., Shigetomi, H., Kanayama, S., and Kobayashi, H. 2010. The usefulness of photodynamic eye for sentinel lymph node identification in patients with cervical cancer. *Tumori*, 96(6): 936–940.

Gabriele, M. L., Wollstein, G., Ishikawa, H., Kagemann, L., Xu, J., Folio, L. S., and Schuman, J. S. 2011. Optical coherence tomography: history, current status, and laboratory work. *Investigative Ophthalmology & Visual Science*, 52(5): 2425–36.

Gadducci, A., Sartori, E., Maggino, T., Zola, P., Landoni, F., Fanucchi, A., Palai, N., Alessi, C., Ferrero, A. M., Cosio, S., and Cristofani, R. 1998. Analysis of failures after negative second-look in patients with advanced ovarian cancer: an Italian multicenter study. *Gynecologic Oncology*, 68(2): 150–5.

Gambhir, S. S. 2002. Molecular imaging of cancer with positron emission tomography. *Nature Reviews Cancer*, 2(9): 683–693.

Gashev, A. A., Davis, M. J., and Zawieja, D. C. 2002. Inhibition of the active lymph pump by flow in rat mesenteric lymphatics and thoracic duct. *The Journal of Physiology*, 540(3): 1023–1037.

Gherardi, E., Birchmeier, W., Birchmeier, C., and Vande Woude, G. 2012. Targeting MET in cancer: rationale and progress. *Nature Reviews Cancer*, 12(2): 89–103.

Ghosh, A., and Heston, W. D. W. 2004. Tumor target prostate specific membrane antigen (PSMA) and its regulation in prostate cancer. *Journal of Cellular Biochemistry*, 91(3): 528–39.

Gioux, S., Kianzad, V., Ciocan, R., Gupta, S., Oketokoun, R., and Frangioni, J. V. 2009. High-Power, Computer-Controlled, Light-Emitting Diode-Based Light Sources for Fluorescence Imaging and Image-Guided Surgery. *Molecular Imaging*, 8(3): 156–165.

Glatz, J., Symvoulidis, P., Garcia-Allende, P. B., and Ntziachristos, V. 2014. Robust overlay schemes for the fusion of fluorescence and color channels in biological imaging. *Journal of Biomedical Optics*, 19(4): 40501.

Glatz, J., Varga, J., Garcia-Allende, P. B., Koch, M., Greten, F. R., and Ntziachristos, V. 2013. Concurrent video-rate color and near-infrared fluorescence laparoscopy. *Journal of Biomedical Optics*, 18(10): 101302.

Gray, D. C., Kim, E. M., Cotero, V. E., Bajaj, A., Staudinger, V. P., Hehir, C. T., and Yazdanfar, S. 2012. Dual-mode laparoscopic fluorescence image-guided surgery using a single camera. *Biomedical Optics Express*, 3(8): 1880.

Groenhuis, R. A. J., Ferwerda, H. A., and Bosch, J. J. Ten. 1983. Scattering and absorption of turbid materials determined from reflection measurements 1: Theory. *Applied Optics*, 22(16): 2456.

Gurtner, G. C., Jones, G. E., Neligan, P. C., Newman, M. I., Phillips, B. T., Sacks, J. M., and Zenn, M. R. 2013. Intraoperative laser angiography using the SPY system: review of the literature and recommendations for use. *Annals of Surgical Innovation and Research*, 7(1): 1.

Hadley, L. N., and Dennison, D. M. 1947. Reflection and Transmission Interference Filters. *Journal of the Optical Society of America*, 37(6): 451.

Haka, A. S., Volynskaya, Z., Gardecki, J. A., Nazemi, J., Lyons, J., Hicks, D., Fitzmaurice, M., Dasari, R. R., Crowe, J. P., and Feld, M. S. 2006. In vivo margin assessment during partial mastectomy breast surgery using raman spectroscopy. *Cancer Research*, 66(6): 3317–22.

Hampl, M., Hantschmann, P., Michels, W., and Hillemanns, P. 2008. Validation of the accuracy of the sentinel lymph node procedure in patients with vulvar cancer: results of a multicenter study in Germany. *Gynecologic Oncology*, 111(2): 282–8.

Hanahan, D., and Weinberg, R. A. 2011. Hallmarks of cancer: the next generation. *Cell*, 144(5): 646–74.

Handa, T., Katare, R. G., Nishimori, H., Wariishi, S., Fukutomi, T., Yamamoto, M., Sasaguri, S., and Sato, T. 2010. New device for intraoperative graft assessment: HyperEye charge-coupled device camera system. *General Thoracic and Cardiovascular Surgery*, 58(2): 68–77.

He, X., Wang, K., and Cheng, Z. 2010. In vivo near-infrared fluorescence imaging of cancer with nanoparticle-based probes. *Wiley Interdiscip Reviews: Nanomed Nanobiotechnol*, 2(4): 349–366.

Hecht, E. 1998. *Optics* (Third Edit., p. 119). Addison-Wesley Publishing Company.

Hirche, C., Dresel, S., Krempien, R., and Hünerbein, M. 2010a. Sentinel node biopsy by indocyanine green retention fluorescence detection for inguinal lymph node staging of anal cancer: preliminary experience. *Annals of Surgical Oncology*, 17(9): 2357–62.

Hirche, C., Murawa, D., Mohr, Z., Kneif, S., and Hunerbein, M. 2010b. ICG fluorescence-guided sentinel node biopsy for axillary nodal staging in breast cancer. *Breast Cancer Research and Treatment*, 121(2): 373–378.

Hodge, K. K., McNeal, J. E., Terris, M. K., and Stamey, T. A. 1989. Random systematic versus directed ultrasound guided transrectal core biopsies of the prostate. *The Journal of Urology*, 142(1): 71–5.

Holloway, R. W., Bravo, R. A. M., Rakowski, J. A., James, J. A., Jeppson, C. N., Ingersoll, S. B., and Ahmad, S. 2012. Detection of sentinel lymph nodes in patients with endometrial cancer undergoing robotic-assisted staging: a comparison of colorimetric and fluorescence imaging. *Gynecologic Oncology*, 126(1): 25–9.

Holm, C., Mayr, M., Tegeler, J., Becker, A., Pfeiffer, U., and Mühlbauer, W. 2003. Laser-induced fluorescence of indocyanine green: plastic surgical applications. *European Journal of Plastic Surgery*, 26(1): 19–25.

Hopkins, H. 1966. Optical system having cylindrical rod-like lenses. *US Patent 3,257,902*.

Huang, D., Swanson, E., Lin, C., Schuman, J., Stinson, W., Chang, W., Hee, M., Flotte, T., Gregory, K., Puliafito, C., and Fujimoto, J. G. 1991. Optical coherence tomography. *Science*, 254(5035): 1178–1181.

Huang, Z., Teh, S. K., Zheng, W., Mo, J., Lin, K., Shao, X., Ho, K. Y., Teh, M., and Yeoh, K. G. 2009. Integrated Raman spectroscopy and trimodal wide-field imaging techniques for real-time in vivo tissue Raman measurements at endoscopy. *Optics Letters*, 34(6): 758.

Hussain, T., and Nguyen, Q. T. 2014. Molecular imaging for cancer diagnosis and surgery. *Advanced Drug Delivery Reviews*, 66: 90–100.

Hutteman, M., van der Vorst, J. R., Gaarenstroom, K. N., Peters, A. a W., Mieog, J. S. D., Schaafsma, B. E., Löwik, C. W. G. M., Frangioni, J. V, van de Velde, C. J. H., and Vahrmeijer, A. L. 2012. Optimization of near-infrared fluorescent sentinel lymph node mapping for vulvar cancer. *American Journal of Obstetrics and Gynecology*, 206(1): 89.e1–5.

Ishizawa, T., Fukushima, N., Shibahara, J., Masuda, K., Tamura, S., Aoki, T., Hasegawa, K., Beck, Y., Fukayama, M., and Kokudo, N. 2009. Real-Time Identification of Liver Cancers by Using Indocyanine Green Fluorescent Imaging. *Cancer*, 115(11): 2491–2504.

Jacques, S. L. 2013. Optical properties of biological tissues: a review. *Physics in Medicine and Biology*, 58(11): R37–R61.

Jaffer, F. A., and Weissleder, R. 2005. Molecular imaging in the clinical arena. *Journal of the American Medical Association*, 293(7): 855–62.

James, M. L., and Gambhir, S. S. 2012. A molecular imaging primer: modalities, imaging agents, and applications. *Physiological Reviews*, 92(2): 897–965.

Jemal, A., Siegel, R., Ward, E., Hao, Y., Xu, J., Murray, T., and Thun, M. J. 2008. Cancer statistics, 2008. *CA: a cancer journal for clinicians*, 58(2): 71–96.

Jewell, E. L., Huang, J. J., Abu-Rustum, N. R., Gardner, G. J., Brown, C. L., Sonoda, Y., Barakat, R. R., Levine, D. A., and Leitao, M. M. 2014. Detection of sentinel lymph nodes in minimally invasive surgery using indocyanine green and near-infrared fluorescence imaging for uterine and cervical malignancies. *Gynecologic Oncology*, 133(2): 274–7.

Kasha, M. 1950. Characterization of electronic transitions in complex molecules. *Discussions of the Faraday Society*, 9(0): 14–19.

Keereweer, S., Kerrebijn, J. D. F., van Driel, P. B. a a, Xie, B., Kaijzel, E. L., Snoeks, T. J. a, Que, I., Hutteman, M., van der Vorst, J. R., Mieog, J. S. D., Vahrmeijer, A. L., van de Velde, C. J. H., Baatenburg de Jong, R. J., and Löwik, C. W. G. M. 2011. Optical image-guided surgery--where do we stand? *Molecular Imaging and Biology*, 13(2): 199–207.

Kienle, A., Lilge, L., Patterson, M. S., Hibst, R., Steiner, R., and Wilson, B. C. 1996. Spatially resolved absolute diffuse reflectance measurements for noninvasive determination of the optical scattering and absorption coefficients of biological tissue. *Applied Optics*, 35(13): 2304–14.

Kijanka, M., Warnders, F.-J., El Khattabi, M., Lub-de Hooge, M., van Dam, G. M., Ntziachristos, V., de Vries, L., Oliveira, S., and van Bergen En Henegouwen, P. M. P. 2013. Rapid optical imaging of human breast tumour xenografts using anti-HER2 VHHs site-directly conjugated to IRDye 800CW for image-guided surgery. *European Journal of Nuclear Medicine and Molecular Imaging*, 40(11): 1718–29.

Kitai, T., Inomoto, T., Miwa, M., and Shikayama, T. 2005. Fluorescence navigation with indocyanine green for detecting sentinel lymph nodes in breast cancer. *Breast Cancer*, 12(3): 211–215.

Koehler, M. J., Speicher, M., Lange-Asschenfeldt, S., Stockfleth, E., Metz, S., Elsner, P., Kaatz, M., and König, K. 2011. Clinical application of multiphoton tomography in combination with confocal laser scanning microscopy for in vivo evaluation of skin diseases. *Experimental Dermatology*, 20(7): 589–94.

Kogon, B., Fernandez, J., Kanter, K., Kirshbom, P., Vincent, B., Maher, K., and Guzetta, N. 2009. The role of intraoperative indocyanine green fluorescence angiography in pediatric cardiac surgery. *The Annals of Thoracic Surgery*, 88(2): 632–6.

Kohl, M., Watson, R., and Cope, M. 1996. Determination of absorption coefficients in highly scattering media from changes in attenuation and phase. *Optics Letters*, 21(18): 1519–21.

Krotkov, E. 1988. Focusing. *International Journal of Computer Vision*, 1(3): 223–237.

Kubota, K., Yoshida, M., Kuroda, J., Okada, A., Ohta, K., and Kitajima, M. 2013. Application of the HyperEye Medical System for esophageal cancer surgery: a preliminary report. *Surgery Today*, 43(2): 215–20.

Lakowicz, J. R. 1999. *Principles of fluorescence spectroscopy* (p. pp 5,57). Springer.

Lalkhen, A. G., and McCluskey, A. 2008. Clinical tests: sensitivity and specificity. *Continuing Education in Anaesthesia, Critical Care & Pain*, 8(6): 221–223.

Lanfranco, A. R., Castellanos, A. E., Desai, J. P., and Meyers, W. C. 2004. Robotic surgery: a current perspective. *Annals of Surgery*, 239(1): 14–21.

Lee, A. C. H., Elson, D. S., Neil, M. A., Kumar, S., Ling, B. W., Bello, F., and Hanna, G. B. 2009. Solid-state semiconductors are better alternatives to arc-lamps for efficient and uniform illumination in minimal access surgery. *Surgical Endoscopy*, 23(3): 518–26.

Lee, Z., Simhan, J., Parker, D. C., Reilly, C., Llukani, E., Lee, D. I., Mydlo, J. H., and Eun, D. D. 2013. Novel use of indocyanine green for intraoperative, real-time localization of ureteral stenosis during robot-assisted ureteroureterostomy. *Urology*, 82(3): 729–33.

Levin, C. S. 2005. Primer on molecular imaging technology. *European Journal of Nuclear Medicine and Molecular Imaging*, 32 Suppl 2: S325–45.

Li, B., Wu, L., Li, X., Lu, H., Bai, P., Li, S., Zhang, W., and Gao, J. 2009. Sentinel lymph node identification in endometrial cancer. *Clinical Oncology and Cancer Research*, 6(2): 124–128.

Litvack, Z. N., Zada, G., and Laws, E. R. 2012. Indocyanine green fluorescence endoscopy for visual differentiation of pituitary tumor from surrounding structures. *Journal of Neurosurgery*, 116(5): 935–41.

Liu, S., Zheng, Y., Volpi, D., El-Kasti, M., Klotz, D., Tullis, I., Henricks, A., Campo, L., Myers, K., Laios, A., Thomas, P., Ng, T., Dhar, S., Becker, C., Vojnovic, B., and Ahmed, A. A. 2014. Toward operative in vivo fluorescence imaging of the c-Met proto-oncogene for personalization of therapy in ovarian cancer. *Cancer*, In press.

Liu, Y., Njuguna, R., Matthews, T., Akers, W. J., Sudlow, G. P., Mondal, S., Tang, R., Gruev, V., and Achilefu, S. 2013a. Near-infrared fluorescence goggle system with complementary metal-oxide-semiconductor imaging sensor and see-through display. *Journal of Biomedical Optics*, 18(10): 101303.

Liu, Y., Zhao, Y.-M., Akers, W., Tang, Z.-Y., Fan, J., Sun, H.-C., Ye, Q.-H., Wang, L., and Achilefu, S. 2013b. First in-human intraoperative imaging of HCC using the fluorescence goggle system and transarterial delivery of near-infrared fluorescent imaging agent: a pilot study. *Translational Research*, 162(5): 324–31.

Loughran, C. F., and Keeling, C. R. 2011. Seeding of tumour cells following breast biopsy: a literature review. *British Journal of Radiology*, 84(1006): 869–74.

Luo, S., Zhang, E., Su, Y., Cheng, T., and Shi, C. 2011. A review of NIR dyes in cancer targeting and imaging. *Biomaterials*, 32(29): 7127–38.

Lussi, A., and Hellwig, E. 2006. Performance of a new laser fluorescence device for the detection of occlusal caries in vitro. *Journal of Dentistry*, 34(7): 467–71.

Maeda, H., Wu, J., Sawa, T., Matsumura, Y., and Hori, K. 2000. Tumor vascular permeability and the EPR effect in macromolecular therapeutics: a review. *Journal of Controlled Release*, 65(1-2): 271–84.

Manyak, M. J. 2008. Indium-111 capromab pendetide in the management of recurrent prostate cancer. *Expert Review of Anticancer Therapy*, 8(2): 175–81.

Marshall, M. V, Draney, D., Sevick-Muraca, E. M., and Olive, D. M. 2010. Single-dose intravenous toxicity study of IRDye 800CW in Sprague-Dawley rats. *Molecular Imaging and Biology*, 12(6): 583–594.

Mathéron, H. M., van den Berg, N. S., Brouwer, O. R., Kleinjan, G. H., van Driel, W. J., Trum, J. W., Vegt, E., Kenter, G., van Leeuwen, F. W. B., and Valdés Olmos, R. 2013. Multimodal surgical guidance towards the sentinel node in vulvar cancer. *Gynecologic Oncology*, 131(3): 720–5.

McGinty, J., Galletly, N. P., Dunsby, C., Munro, I., Elson, D. S., Requejo-Isidro, J., Cohen, P., Ahmad, R., Forsyth, A., Thillainayagam, A. V, Neil, M. A. A., French, P. M. W., and Stamp, G. W. 2010. Wide-field fluorescence lifetime imaging of cancer. *Biomedical Optics Express*, 1(2): 627–640.

Meads, C., Sutton, A. J., Rosenthal, A. N., Małysiak, S., Kowalska, M., Zapalska, A., Rogozińska, E., Baldwin, P., Ganesan, R., Borowiack, E., Barton, P., Roberts, T., Khan, K., and Sundar, S. 2014. Sentinel lymph node biopsy in vulval cancer: systematic review and meta-analysis. *British Journal of Cancer*, 110(12): 2837–46.

Metropolis, N., and Ulam, S. 1949. The Monte Carlo Method. *Journal of the American Statistical Association*, 44(247): 335–341.

Mieog, J. S., Troyan, S. L., Hutteman, M., Donohoe, K. J., van der Vorst, J. R., Stockdale, A., Liefers, G. J., Choi, H. S., Gibbs-Strauss, S. L., Putter, H., Gioux, S., Kuppen, P. J., Ashitate, Y., Lowik, C. W., Smit, V. T., Oketokoun, R., Ngo, L. H., van de Velde, C. J., Frangioni, J. V, and Vahrmeijer, A. L. 2011. Toward Optimization of Imaging System and Lymphatic Tracer for Near-Infrared Fluorescent Sentinel Lymph Node Mapping in Breast Cancer. *Annals of Surgical Oncology*, 18(9): 2483–91.

Mistry, M., Parkin, D. M., Ahmad, A., and Sasieni, P. 2011. Cancer incidence in the United Kingdom: projections to the year 2030. *British Journal of Cancer*, 105(11): 1795–803.

Moore, D. T. 1980. Gradient-index optics: a review. *Applied Optics*, 19(7): 1035–8.

Mordon, S., Devoisselle, J. M., Soulie-Begu, S., and Desmettre, T. 1998. Indocyanine green: physicochemical factors affecting its fluorescence in vivo. *Microvascular Research*, 55(2): 146–152.

Morton, D. L., Cagle, L., Wong, J., and Economou, J. 1990. Intraoperative lymphatic mapping and selective lymphadenectomy: technical details of a new procedure for clinical stage I melanoma. *42nd annual meeting of the Society of Surgical Oncology, Washington, DC*.

Morton, D. L., Thompson, J. F., Cochran, A. J., Mozzillo, N., Elashoff, R., Essner, R., Nieweg, O. E., Roses, D. F., Hoekstra, H. J., Karakousis, C. P., Reintgen, D. S., Coventry, B. J., Glass, E. C., and Wang, H.-J. 2006. Sentinel-node biopsy or nodal observation in melanoma. *The New England Journal of Medicine*, 355(13): 1307–17.

Morton, D. L., Thompson, J. F., Essner, R., Elashoff, R., Stern, S. L., Nieweg, O. E., Roses, D. F., Karakousis, C. P., Mozzillo, N., Reintgen, D., Wang, H. J., Glass, E. C., and Cochran, A. J. 1999. Validation of the accuracy of intraoperative lymphatic mapping and sentinel lymphadenectomy for early-stage melanoma: a multicenter trial. Multicenter Selective Lymphadenectomy Trial Group. *Annals of Surgery*, 230(4): 453–65.

Morton, D. L., Wen, D. R., Wong, J. H., Economou, J. S., Cagle, L. A., Storm, F. K., Foshag, L. J., and Cochran, A. J. 1992. Technical details of intraoperative lymphatic mapping for early stage melanoma. *Archives of Surgery*, 127(4): 392–9.

Muggia, F. M., Braly, P. S., Brady, M. F., Sutton, G., Niemann, T. H., Lentz, S. L., Alvarez, R. D., Kucera, P. R., and Small, J. M. 2000. Phase III randomized study of cisplatin versus paclitaxel versus cisplatin and paclitaxel in patients with suboptimal stage III or IV ovarian cancer: a gynecologic oncology group study. *Journal of Clinical Oncology*, 18(1): 106–15.

Nakayama, A., Bianco, A. C., Zhang, C.-Y., Lowell, B. B., and Frangioni, J. V. 2003. Quantitation of brown adipose tissue perfusion in transgenic mice using near-infrared fluorescence imaging. *Molecular Imaging*, 2(1): 37–49.

National Cancer Institute. 2008. SEER Cancer Statistics Review, 1975-2005. *http://seer.cancer.gov/archive/csr/1975_2005/*.

Naumov, G. N., Akslen, L. A., and Folkman, J. 2006. Role of Angiogenesis in Human Tumor Dormancy: Animal Models of the Angiogenic Switch. *Cell Cycle*, 5(16): 1779–1787.

Nel, A., Xia, T., Mädler, L., and Li, N. 2006. Toxic potential of materials at the nanolevel. *Science*, 311(5761): 622–7.

Nguyen, Q. T., and Tsien, R. Y. 2013. Fluorescence-guided surgery with live molecular navigation - a new cutting edge. *Nature Reviews Cancer*, 13: 653–662.

Niikura, H., Okamura, C., Utsunomiya, H., Yoshinaga, K., Akahira, J., Ito, K., and Yaegashi, N. 2004. Sentinel lymph node detection in patients with endometrial cancer. *Gynecologic Oncology*, 92(2): 669–74.

Noonan, D. P., Elson, D. S., Mylonas, G. P., Darzi, A., and Yang, G.-Z. 2009. Laser-induced fluorescence and reflected white light imaging for robot-assisted MIS. *IEEE transactions on bio-medical engineering*, 56(3): 889–92.

Novak, E., and Berek, J. S. 2007. *Berek & Novak's gynecology* (Vol. 2007, p. 1696). Lippincott Williams & Wilkins.

Ntziachristos, V. 2010. Going deeper than microscopy: the optical imaging frontier in biology. *Nature Methods*, 7(8): 603–14.

Ntziachristos, V., Tung, C.-H., Bremer, C., and Weissleder, R. 2002. Fluorescence molecular tomography resolves protease activity in vivo. *Nature Medicine*, 8(7): 757–60.

Okada, E., Firbank, M., Schweiger, M., Arridge, S. R., Cope, M., and Delpy, D. T. 1997. Theoretical and experimental investigation of near-infrared light propagation in a model of the adult head. *Applied Optics*, 36(1): 21–31.

Okuyama, A. 2001. Cross dichroic prism. *US Patent US6327092 B1*.

Pace, C., Vajdos, F., Fee, L., Grimsley, G., and Gray, T. 1995. How to measure and predict the molar absorption coefficient of a protein. *Protein Science*, 4(11): 2411–23.

Pavlova, I., Williams, M., El-Naggar, A., Richards-Kortum, R., and Gillenwater, A. 2008. Understanding the biological basis of autofluorescence imaging for oral cancer detection: high-resolution fluorescence microscopy in viable tissue. *Clinical Cancer Research*, 14(8): 2396–404.

Philip, R., Penzkofer, A., Baumler, W., Szeimies, R. M., and Abels, C. 1996. Absorption and fluorescence spectroscopic investigation of indocyanine green. *Journal of Photochemistry and Photobiology a-Chemistry*, 96(1-3): 137–148.

Pichler, B. J., Judenhofer, M. S., and Pfannenberg, C. 2008. Multimodal imaging approaches: PET/CT and PET/MRI. *Handbook of Experimental Pharmacology*, (185 Pt 1): 109–32.

Prahl, S. 1999. Optical Absorption of Hemoglobin. *http://omlc.ogi.edu/spectra/hemoglobin/summary.html*.

Prahl, S. A., Keijzer, M., Jacques, S. L., and Welch, A. J. 1989. A Monte Carlo model of light propagation in tissue. *Dosimetry of Laser Radiation in Medicine and Biology*, 5: 102–111.

Pysz, M. A., Gambhir, S. S., and Willmann, J. K. 2010. Molecular imaging: current status and emerging strategies. *Clinical Radiology*, 65(7): 500–16.

Raabe, A., Beck, J., Gerlach, R., Zimmermann, M., and Seifert, V. 2003. Near-infrared indocyanine green video angiography: a new method for intraoperative assessment of vascular flow. *Neurosurgery*, 52(1): 132–9.

Ray, S. F. 2002. *Applied Photographic Optics* (pp. 128–129). Focal Press.

Regillo, C. D. 1999. The present role of indocyanine green angiography in ophthalmology. *Current Opinion in Ophthalmology*, 10(3): 189–96.

Regino, C. A. S., Wong, K. J., Milenic, D. E., Holmes, E. H., Garmestani, K., Choyke, P. L., and Brechbiel, M. W. 2009. Preclinical evaluation of a monoclonal antibody (3C6) specific for prostate-specific membrane antigen. *Current Radiopharmaceuticals*, 2(1): 9–17.

Rembacken, B., Fujii, T., Cairns, A., Dixon, M., Yoshida, S., Chalmers, D., and Axon, A. 2000. Flat and depressed colonic neoplasms: a prospective study of 1000 colonoscopies in the UK. *The Lancet*, 355(9211): 1211–1214.

Ren, H., Fox, D., Anderson, P. A., Wu, B., and Wu, S.-T. 2006. Tunable-focus liquid lens controlled using a servo motor. *Optics Express*, 14(18): 8031.

Resch-Genger, U., Grabolle, M., Cavaliere-Jaricot, S., Nitschke, R., and Nann, T. 2008. Quantum dots versus organic dyes as fluorescent labels. *Nature Methods*, 5(9): 763–75.

Ripoll, J. 2012. *Principles of Diffuse Light Propagation*. (World Scientific, Ed.) (p. 331).

Ris, F., Hompes, R., Cunningham, C., Lindsey, I., Guy, R., Jones, O., George, B., Cahill, R. A., and Mortensen, N. J. 2014. Near-infrared (NIR) perfusion angiography in minimally invasive colorectal surgery. *Surgical Endoscopy*, 28(7): 2221–6.

Roethke, M., Anastasiadis, A. G., Lichy, M., Werner, M., Wagner, P., Kruck, S., Claussen, C. D., Stenzl, A., Schlemmer, H. P., and Schilling, D. 2012. MRI-guided prostate biopsy detects clinically significant cancer: analysis of a cohort of 100 patients after previous negative TRUS biopsy. *World Journal of Urology*, 30(2): 213–8.

Rossi, E. C., Ivanova, A., and Boggess, J. F. 2012. Robotically assisted fluorescence-guided lymph node mapping with ICG for gynecologic malignancies: a feasibility study. *Gynecologic Oncology*, 124(1): 78–82.

Rossi, E. C., Jackson, A., Ivanova, A., and Boggess, J. F. 2013. Detection of sentinel nodes for endometrial cancer with robotic assisted fluorescence imaging: cervical versus hysteroscopic injection. *International Journal of Gynecological Cancer*, 23(9): 1704–11.

Sakuragi, N., Satoh, C., Takeda, N., Hareyama, H., Takeda, M., Yamamoto, R., Fujimoto, T., Oikawa, M., Fujino, T., and Fujimoto, S. 1999. Incidence and distribution pattern of pelvic and paraaortic lymph node metastasis in patients with Stages IB, IIA, and IIB cervical carcinoma treated with radical hysterectomy. *Cancer*, 85(7): 1547–54.

Saxena, V., Sadoqi, M., and Shao, J. 2003. Degradation kinetics of indocyanine green in aqueous solution. *Journal of Pharmaceutical Sciences*, 92(10): 2090–7.

Schaafsma, B. E., van der Vorst, J. R., Gaarenstroom, K. N., Peters, A. a W., Verbeek, F. P. R., de Kroon, C. D., Trimbos, J. B. M. Z., van Poelgeest, M. I. E., Frangioni, J. V, van de Velde, C. J. H., and Vahrmeijer, A. L. 2012. Randomized comparison of near-infrared fluorescence lymphatic tracers for sentinel lymph node mapping of cervical cancer. *Gynecologic Oncology*, 127(1): 126–30.

Schaafsma, B. E., Verbeek, F., Peters, A., van der Vorst, J., de Kroon, C., van Poelgeest, M., Trimbos, J., van de Velde, C., Frangioni, J., Vahrmeijer, A., and Gaarenstroom, K. 2013. Near-infrared fluorescence sentinel lymph node biopsy in vulvar cancer: a randomised comparison of lymphatic tracers. *BJOG: An International Journal of Obstetrics and Gynaecology*, 1–7.

Schauer, A., Becker, W., Reiser, M., and Possinger, K. 2005. *The sentinel lymph node concept*. Berlin/Heidelberg: Springer-Verlag.

Scholkmann, F., Kleiser, S., Metz, A. J., Zimmermann, R., Mata Pavia, J., Wolf, U., and Wolf, M. 2014. A review on continuous wave functional near-infrared spectroscopy and imaging instrumentation and methodology. *NeuroImage*, 85 Pt 1: 6–27.

Schubert, E. F. 2006. *Light-Emitting Diodes* (Vol. 4996, p. 370). Cambridge University Press.

Sekijima, M., Tojimbara, T., Sato, S., Nakamura, M., Kawase, T., Kai, K., Urashima, Y., Nakajima, I., Fuchinoue, S., and Teraoka, S. 2004. An intraoperative fluorescent imaging system in organ transplantation. *Transplantation Proceedings*, 36(7): 2188–90.

Selzman, A. A., and Spirnak, J. P. 1996. Iatrogenic ureteral injuries: a 20-year experience in treating 165 injuries. *The Journal of Urology*, 155(3): 878–81.

Semrock. 2014. Filter Spectra at Non-normal Angles of Incidence. *http://www.semrock.com/filter-spectra-at-non-normal-angles-of-incidence.aspx*.

Sevick-Muraca, E. M., Sharma, R., Rasmussen, J. C., Marshall, M. V, Wendt, J. A., Pham, H. Q., Bonefas, E., Houston, J. P., Sampath, L., Adams, K. E., Blanchard, D. K., Fisher, R. E., Chiang, S. B., Elledge, R., and Mawad, M. E. 2008. Imaging of lymph flow in breast

cancer patients after microdose administration of a near-infrared fluorophore: feasibility study. *Radiology*, 246(3): 734–741.

Sherman, A. I., and Ter-Pogossian, M. 1953. Lymph-node concentration of radioactive colloidal gold following interstitial injection. *Cancer*, 6(6): 1238–40.

Shimada, Y., Okumura, T., Nagata, T., Sawada, S., Matsui, K., Hori, R., Yoshioka, I., Yoshida, T., Osada, R., and Tsukada, K. 2011. Usefulness of blood supply visualization by indocyanine green fluorescence for reconstruction during esophagectomy. *Esophagus*, 8(4): 259–266.

Siegel, R., DeSantis, C., Virgo, K., Stein, K., Mariotto, A., Smith, T., Cooper, D., Gansler, T., Lerro, C., Fedewa, S., Lin, C., Leach, C., Cannady, R. S., Cho, H., Scoppa, S., Hachey, M., Kirch, R., Jemal, A., and Ward, E. 2012. Cancer treatment and survivorship statistics, 2012. *CA: a cancer journal for clinicians*, 62(4): 220–41.

Silver, D. A., Pellicer, I., Fair, W. R., Heston, W. D., and Cordon-Cardo, C. 1997. Prostate-specific membrane antigen expression in normal and malignant human tissues. *Clinical Cancer Research*, 3(1): 81–5.

Singh, H., Cooper, R. J., Wai Lee, C., Dempsey, L., Edwards, A., Brigadoi, S., Airantzis, D., Everdell, N., Michell, A., Holder, D., Hebden, J. C., and Austin, T. 2014. Mapping cortical haemodynamics during neonatal seizures using diffuse optical tomography: a case study. *NeuroImage: Clinical*, 5: 256–65.

Sinno, A. K., Fader, A. N., Roche, K. L., Giuntoli, R. L., and Tanner, E. J. 2014. A comparison of colorimetric versus fluorometric sentinel lymph node mapping during robotic surgery for endometrial cancer. *Gynecologic Oncology*, 134(2): 281–6.

Sjöback, R., Nygren, J., and Kubista, M. 1995. Absorption and fluorescence properties of fluorescein. *Spectrochimica Acta Part A: Molecular and Biomolecular Spectroscopy*, 51(6): L7–L21.

Sordillo, L. A., Pu, Y., Pratavieira, S., Budansky, Y., and Alfano, R. R. 2014. Deep optical imaging of tissue using the second and third near-infrared spectral windows. *Journal of Biomedical Optics*, 19(5): 056004.

Stacker, S. A., Achen, M. G., Jussila, L., Baldwin, M. E., and Alitalo, K. 2002. Lymphangiogenesis and cancer metastasis. *Nature Reviews Cancer*, 2(8): 573–83.

Steel, W. H. 1974. Luminosity, throughput, or etendue? *Applied Optics*, 13(4): 704–5.

Stokes, G. G. 1852. On the Change of Refrangibility of Light. *Philosophical Transactions of the Royal Society of London* , 142 : 463–562.

Stummer, W., Pichlmeier, U., Meinel, T., Wiestler, O. D., Zanella, F., and Reulen, H.-J. 2006. Fluorescence-guided surgery with 5-aminolevulinic acid for resection of malignant glioma: a randomised controlled multicentre phase III trial. *The Lancet Oncology*, 7(5): 392–401.

Sturm, M. B., Joshi, B. P., Lu, S., Piraka, C., Khondee, S., Elmunzer, B. J., Kwon, R. S., Beer, D. G., Appelman, H. D., Turgeon, D. K., and Wang, T. D. 2013. Targeted imaging of esophageal neoplasia with a fluorescently labeled peptide: first-in-human results. *Science translational medicine*, 5(184): 184ra61.

Sugarbaker, P. H. 1999. Successful management of microscopic residual disease in large bowel cancer. *Cancer Chemotherapy and Pharmacology*, 43: S15–25.

Swartz, M. 2001. The physiology of the lymphatic system. *Advanced Drug Delivery Reviews*, 50(1-2): 3–20.

Swindle, P., Eastham, J. A., Ohori, M., Kattan, M. W., Wheeler, T., Maru, N., Slawin, K., and Scardino, P. T. 2005. Do margins matter? The prognostic significance of positive surgical margins in radical prostatectomy specimens. *The Journal of Urology*, 174(3): 903–7.

Tagaya, N., Yamazaki, R., Nakagawa, A., Abe, A., Hamada, K., Kubota, K., and Oyama, T. 2008. Intraoperative identification of sentinel lymph nodes by near-infrared fluorescence imaging in patients with breast cancer. *American Journal of Surgery*, 195(6): 850–3.

Takahashi, K., Ikeda, N., Nonoguchi, N., Kajimoto, Y., Miyatake, S.-I., Hagiya, Y., Ogura, S.-I., Nakagawa, H., Ishikawa, T., and Kuroiwa, T. 2011. Enhanced expression of coproporphyrinogen oxidase in malignant brain tumors: CPOX expression and 5-ALA-induced fluorescence. *Neuro-oncology*, 13(11): 1234–43.

Themelis, G., Yoo, J. S., Soh, K.-S., Schulz, R., and Ntziachristos, V. 2009. Real-time intraoperative fluorescence imaging system using light-absorption correction. *Journal of Biomedical Optics*, 14(6): 064012.

Thevarajah, S., Huston, T. L., and Simmons, R. M. 2005. A comparison of the adverse reactions associated with isosulfan blue versus methylene blue dye in sentinel lymph node biopsy for breast cancer. *American Journal of Surgery*, 189(2): 236–9.

Thong, P. S. P., Olivo, M., Chin, W. W. L., Bhuvaneswari, R., Mancer, K., and Soo, K.-C. 2009. Clinical application of fluorescence endoscopic imaging using hypericin for the diagnosis of human oral cavity lesions. *British Journal of Cancer*, 101(9): 1580–4.

Tiourina, T., Arends, B., Huysmans, D., Rutten, H., Lemaire, B., and Muller, S. 1998. Evaluation of surgical gamma probes for radioguided sentinel node localisation. *European Journal of Nuclear Medicine*, 25(9): 1224–31.

Troy, T., Jekic-McMullen, D., Sambucetti, L., and Rice, B. 2004. Quantitative comparison of the sensitivity of detection of fluorescent and bioluminescent reporters in animal models. *Molecular Imaging*, 3(1): 9–23.

Troyan, S. L., Kianzad, V., Gibbs-Strauss, S. L., Gioux, S., Matsui, A., Oketokoun, R., Ngo, L., Khamene, A., Azar, F., and Frangioni, J. V. 2009. The FLARE((TM)) Intraoperative Near-Infrared Fluorescence Imaging System: A First-in-Human Clinical Trial in Breast Cancer Sentinel Lymph Node Mapping. *Annals of Surgical Oncology*, 16(10): 2943–2952.

Tsopelas, C., and Sutton, R. 2002. Why certain dyes are useful for localizing the sentinel lymph node. *Journal of Nuclear Medicine*, 43(10): 1377–82.

Tuite, E. M., and Kelly, J. M. 1993. New trends in photobiology: Photochemical interactions of methylene blue and analogues with DNA and other biological substrates. *Journal of Photochemistry and Photobiology B: Biology*, 21(2–3): 103–124.

Tummers, Q. R. J. G., Verbeek, F. P. R., Schaafsma, B. E., Boonstra, M. C., van der Vorst, J. R., Liefers, G.-J., van de Velde, C. J. H., Frangioni, J. V., and Vahrmeijer, A. L. 2014. Real-Time Intraoperative Detection of Breast Cancer using Near-infrared Fluorescence Imaging and Methylene Blue. *European Journal of Surgical Oncology*, 40(7): 850–8.

Tung, C.-H. 2004. Fluorescent peptide probes for in vivo diagnostic imaging. *Biopolymers*, 76(5): 391–403.

Türk, I., Deger, S., Winkelmann, B., Schönberger, B., and Loening, S. A. 2001. Laparoscopic Radical Prostatectomy. *European Urology*, 40(1): 46–53.

U. S. National Institutes of Health. 2014. SEER Training Modules, Lymph nodes. *http://training.seer.cancer.gov/anatomy/lymphatic/components/nodes.html*.

Umezawa, K., Matsui, A., Nakamura, Y., Citterio, D., and Suzuki, K. 2009. Bright, color-tunable fluorescent dyes in the Vis/NIR region: establishment of new “tailor-made” multicolor fluorophores based on borondipyrromethene. *Chemistry - A European Journal*, 15(5): 1096–106.

Vahrmeijer, A. L., Hutteman, M., van der Vorst, J. R., van de Velde, C. J. H., and Frangioni, J. V. 2013. Image-guided cancer surgery using near-infrared fluorescence. *Nature Reviews Clinical Oncology*, 10: 507–518.

Vakoc, B. J., Fukumura, D., Jain, R. K., and Bouma, B. E. 2012. Cancer imaging by optical coherence tomography: preclinical progress and clinical potential. *Nature Reviews Cancer*, 12(5): 363–368.

Van Dam, G. M., Themelis, G., Crane, L. M., Harlaar, N. J., Pleijhuis, R. G., Kelder, W., Sarantopoulos, A., de Jong, J. S., Arts, H. J. G., van der Zee, A. G. J., Bart, J., Low, P. S., and Ntziachristos, V. 2011. Intraoperative tumor-specific fluorescence imaging in ovarian cancer by folate receptor-α targeting: first in-human results. *Nature Medicine*, 17(10): 1315–9.

Van der Vorst, J. R., Hutteman, M., Gaarenstroom, K. N., Peters, A. A. W., Mieog, J. S. D., Schaafsma, B. E., Kuppen, P. J. K., Frangioni, J. V, van de Velde, C. J. H., and Vahrmeijer, A. L. 2011. Optimization of near-infrared fluorescent sentinel lymph node mapping in cervical cancer patients. *International Journal of Gynecological Cancer*, 21(8): 1472–8.

Van der Vorst, J. R., Schaafsma, B. E., Verbeek, F. P. R., Keereweer, S., Jansen, J. C., van der Velden, L.-A., Langeveld, A. P. M., Hutteman, M., Löwik, C. W. G. M., van de Velde, C. J. H., Frangioni, J. V, and Vahrmeijer, A. L. 2013. Near-infrared fluorescence sentinel lymph node mapping of the oral cavity in head and neck cancer patients. *Oral Oncology*, 49(1): 15–9.

Van der Zee, A. G. J., Oonk, M. H., De Hullu, J. a, Ansink, A. C., Vergote, I., Verheijen, R. H., Maggioni, A., Gaarenstroom, K. N., Baldwin, P. J., Van Dorst, E. B., Van der Velden, J., Hermans, R. H., van der Putten, H., Drouin, P., Schneider, A., and Sluiter, W. J. 2008. Sentinel node dissection is safe in the treatment of early-stage vulvar cancer. *Journal of Clinical Oncology*, 26(6): 884–9.

Venugopal, V., Park, M., Ashitate, Y., Neacsu, F., Kettenring, F., Frangioni, J. V, Gangadharan, S. P., and Gioux, S. 2013. Design and characterization of an optimized simultaneous color and near-infrared fluorescence rigid endoscopic imaging system. *Journal of Biomedical Optics*, 18(12): 126018.

Verbeek, F. P. R., van der Vorst, J. R., Schaafsma, B. E., Swijnenburg, R.-J., Gaarenstroom, K. N., Elzevier, H. W., van de Velde, C. J. H., Frangioni, J. V, and Vahrmeijer, A. L. 2013. Intraoperative Near Infrared Fluorescence Guided Identification of the Ureters Using Low Dose Methylene Blue: A First in Human Experience. *The Journal of Urology*, 190(8): 574–579.

Veronesi, U., Paganelli, G., Viale, G., Luini, A., Zurrida, S., Galimberti, V., Intra, M., Veronesi, P., Robertson, C., Maisonneuve, P., Renne, G., De Cicco, C., De Lucia, F., and Gennari, R. 2003. A randomized comparison of sentinel-node biopsy with routine axillary dissection in breast cancer. *The New England Journal of Medicine*, 349(6): 546–53.

Vojnovic, B. 2011. A medium power c.w. laser driver. *http://users.ox.ac.uk/~atdgroup/technicalnotes/A%20medium%20power%20cw%20laser%20driver.pdf*.

Vojnovic, B. 2012a. Notes on Sony CCD and CMOS 2D imaging sensors. *users.ox.ac.uk/~atdgroup/referencematerial/Sony%20CCD%20and%20CMOS%202D%20imaging%20sensors.pdf*.

Vojnovic, B. 2012b. A simple, low cost focus-tunable lens power supply. *http://users.ox.ac.uk/~atdgroup/technicalnotes/A%20simple%20focus-programmable%20lens%20power%20supply.pdf*.

Volpi, D., Tullis, I. D. C., Laios, A., Pathiraja, P. N. J., Haldar, K., Ahmed, A. A., and Vojnovic, B. 2014. A novel multiwavelength fluorescence image-guided surgery imaging system. *Proceedings of SPIE* (Vol. 8935, p. 89350G–89350G–9).

Wabnitz, H., Willenbrock, R., Neukammer, J., Sukowski, U., and Rinneberg, H. H. 1993. Spatial resolution in photon diffusion imaging from measurements of time-resolved transmittance. *Proceedings of SPIE*, 48–61.

Wachsmann-Hogiu, S., Weeks, T., and Huser, T. 2009. Chemical analysis in vivo and in vitro by Raman spectroscopy-from single cells to humans. *Current Opinion in Biotechnology*, 20(1): 63–73.

Wang, L. H., Jacques, S. L., and Zheng, L. Q. 1995. MCML - Monte-Carlo Modeling of Light Transport in Multilayered Tissues. *Computer Methods and Programs in Biomedicine*, 47(2): 131–146.

Wang, L., and Jacques, S. 1993. Hybrid model of Monte Carlo simulation and diffusion theory for light reflectance by turbid media. *Journal of the Optical Society of America A*, 10(8): 1746–52.

Wang, L., and Jacques, S. 2000. Source of error in calculation of optical diffuse reflectance from turbid media using diffusion theory. *Computer Methods and Programs in Biomedicine*, 61(3): 163–70.

Wang, M., Abbineni, G., Clevenger, A., Mao, C., and Xu, S. 2011. Upconversion nanoparticles: synthesis, surface modification and biological applications. *Nanomedicine*, 7: 710–729.

Wang, T. D., Friedland, S., Sahbaie, P., Soetikno, R., Hsiung, P.-L., Liu, J. T. C., Crawford, J. M., and Contag, C. H. 2007. Functional imaging of colonic mucosa with a fibered confocal microscope for real-time in vivo pathology. *Clinical Gastroenterology and Hepatology*, 5(11): 1300–5.

Wang, and Wu, H. 2007. *Biomedical Optics - Principles and Imaging*. Wiley-Interscience.

Weis, S. M., and Cheresh, D. A. 2011. Tumor angiogenesis: molecular pathways and therapeutic targets. *Nature Medicine*, 17(11): 1359–1370.

Weiss, L. M. 2009. Lymph Nodes. *eLS*. John Wiley & Sons, Ltd.

Weissleder, R. 2006. Molecular imaging in cancer. *Science*, 312(5777): 1168–71.

Weissleder, R., and Pittet, M. J. 2008. Imaging in the era of molecular oncology. *Nature*, 452(7187): 580–9.

Westwick, P., Potkins, D., and Fengler, J. 2013. Imaging system with a single color image sensor for simultaneous fluorescence and color video endoscopy. *US Patent 8,498,695*.

Whitney, M., Crisp, J. L., Nguyen, L. T., Friedman, B., Gross, L., Steinbach, P., Tsien, R. Y., and Nguyen, Q. T. 2011. Fluorescent peptides highlight peripheral nerves during surgery in mice. *Nature Biotechnology*, 29(4): 352–6.

Wilson, B., and Adam, G. 1983. A Monte Carlo model for the absorption and flux distributions of light in tissue. *Medical Physics*, 10(6): 824–830.

World Health Organization. 2013. World health statistics 2013. *http://www.who.int/gho/publications/world_health_statistics/EN_WHS2013_Full.pdf?ua=1*.

Xia, J., and Yao, G. 2007. Angular distribution of diffuse reflectance in biological tissue. *Applied Optics*, 46(26): 6552–60.

Xiong, L., Gazyakan, E., Yang, W., Engel, H., Hünerbein, M., Kneser, U., and Hirche, C. 2014. Indocyanine green fluorescence-guided sentinel node biopsy: A meta-analysis on detection rate and diagnostic performance. *European Journal of Surgical Oncology*, 40(7): 843–9.

Yoo, K. M., Liu, F., and Alfano, R. R. 1990. When does the diffusion approximation fail to describe photon transport in random media? *Physical Review Letters*, 64(22): 76701.

Zhu, B., Rasmussen, J. C., and Sevick-Muraca, E. M. 2014. A matter of collection and detection for intraoperative and noninvasive near-infrared fluorescence molecular imaging: To see or not to see? *Medical Physics*, 41(2): 022105.

List of Publications

Volpi, D., Tullis, I. D. C., Laios, A., Pathiraja, P. N. J., Haldar, K., Ahmed, A. A., and Vojnovic, B. 2014. A novel multiwavelength fluorescence image-guided surgery imaging system. *Proceedings of SPIE* (Vol. 8935, p. 89350G–89350G–9).

Liu, S., Zheng, Y., **Volpi, D.**, El-Kasti, M., Klotz, D., Tullis, I., Henricks, A., Campo, L., Myers, K., Laios, A., Thomas, P., Ng, T., Dhar, S., Becker, C., Vojnovic, B., and Ahmed, A. A. 2014. Toward operative in vivo fluorescence imaging of the c-Met proto-oncogene for personalization of therapy in ovarian cancer. *Cancer*, In press.

Index